AGH UNIVERSITY OF SCIENCE AND TECHNOLOGY

FIELD OF SCIENCE
ENGINEERING AND TECHNOLOGY

SCIENTIFIC DISCIPLINE
AUTOMATION, ELECTRONICS, ELECTRICAL ENGINEERING AND SPACE TECHNOLOGIES

DOCTORAL THESIS

Axial Active Magnetic Suspension Systems

Author: Bartłomiej Sikora M.Sc.Eng.

Supervisor: Adam Piłat Ph.D., D.Sc., prof. AGH

Completed in:
AGH University of Science and Technology
Faculty of Electrical Engineering, Automatics, Computer Science, and Biomedical Engineering
Department of Automatic Control and Robotics

Krakow, 2023

AKADEMIA GÓRNICZO-HUTNICZA IM. STANISŁAWA STASZICA W KRAKOWIE

DZIEDZINA
NAUK INŻYNIERYJNO-TECHNICZNYCH

DYSCYPLINA

AUTOMATYKA, ELEKTRONIKA, ELEKTROTECHNIKA I TECHNOLOGIE KOSMICZNE

ROZPRAWA DOKTORSKA

Osiowe aktywne systemy zawieszenia magnetycznego

Autor: mgr inż. Bartłomiej Sikora

Promotor rozprawy: dr hab. inż. Adam Piłat, prof. AGH

Praca wykonana:
Akademia Górniczo-Hutnicza im. Stanisława Staszica w Krakowie
Wydział Elektrotechniki, Automatyki, Informatyki i Inżynierii Biomedycznej
Katedra Automatyki i Robotyki

Kraków, 2023

Dziękuję Prof. Adamowi Piłatowi za życzliwą pomoc i wieloletnią współpracę, dzięki której mogłem zrealizować założony plan badawczy przedstawiony w poniższej rozprawie doktorskiej. Dziękuję również za nieoceniony wkład merytoryczny i inspirowanie do podejmowania nowych wyzwań, a także za towarzyszenie mi w rozwoju akademickim, dzielenie sukcesów i porażek na drodze poszukiwania naukowej prawdy i niespotykaną serdeczność, która nieustannie motywuje do pracy.

Abstract

The doctoral dissertation presents the concept of a novel actuator with six pole pieces (6pAAMB) that operates as an axial active magnetic suspension system. The dissertation is interdisciplinary, presenting a number of research on virtual and rapid prototyping of the axial electromagnetic actuators. The structure of the dissertation is modular. Its scope covers numerous fields of science around the author's interests, the effect of which is the coherent line of reasoning leading from the application need and idea, through testing and verification of various concepts, to the design procedure, including numerical modeling, analytical calculations, manufacturing, quality check, identification and control application. The dissertation is divided into the introductory part (Chapters 2-5) containing preliminary research and the main part (Chapters 6-13) discussing the 6pAAMB configuration.

Chapter 2 includes research on a magnetic levitation system with two antiparallel electromagnetic actuators. The research carried out confirmed that the dynamical properties of the lateral motion can be configured by stretching control. Chapter 3 focuses on the magnetic levitation thermal model. It extends the dynamic equations of magnetic levitation systems by using the nonlinear temperature-dependent heating transfer model. In Chapter 4 the concept of an electromagnet with a porous core is studied together with the prototyping procedure, using a finite element method. The concept, design, model and prototype of the hybrid axial magnetic bearing is presented in Chapter 5.

Chapter 6 in a nutshell introduces the reader to the concept of an axial actuator with a few pole pieces that is capable of axial active levitation with the function of spatial orientation of the rotor in the active bearing space. Chapter 7 presents a numerical model of the axial magnetic bearing with six cylindrical poles. The proposed design allows us to suppress the tilting of the disc with the use of a few axial force components. An unintended actuator defect was the motivation for Chapter 8. A run-up experiment showed that the applied 6pAAMB configuration requires a quality test. As a consequence, the author proposes an original diagnostic method of the disc-type electromagnetic actuator based on the fusion of distance, current and control signal measurements, according to a specific scenario. The algorithm, which is used for actuator fault diagnosis, indicates differences between the heights of individual pole pieces with adequate accuracy. Introducing an interdisciplinary approach to the design of active magnetic bearings, the slim-type 6pAAMB actuator was tested and adapted to the vertical rotor-shaft configuration in Chapter 9. Chapter 10 presents the 6pAAMB analytical model, which was developed to provide the 3D axial magnetic induction distribution. The model utilizes the magnetic vector potential formulation and Schwarz–Christoffel mapping. The research covers deliberations on the end effect influence and the conjugate complex permeance function. The main advantage of the proposed model is the significantly shorter computation time compared to the numerical one with comparable convergence. Chapter 11 presents the configuration of a passive radial bearing that supports the lateral stabilization of the levitating rotor in 6pAAMB. Several experiments showing the properties of the proposed solution are presented. A proprietary magnetic coupling is used to accelerate the rotor to a speed of 4000 rpm without contact. Chapter 12 elaborates a comprehensive approach to identify the parameters of the 6pAAMB actuator with current-driven electromagnets. The coil parameters were measured with a precise indication of the differences. The thermal reliability of the bearing was tested. The study extends the crucial aspect of measuring and calculating the electromagnetic force through several methods with decent convergence between them. In general, the proposed mechatronic actuator is capable of increasing the stability range of levitating rotors and is characterized by favorable dynamic properties, which was demonstrated in the shaker test with external harmonic excitation. A complete description of the actuator with uncertainties in the parameters was obtained by accessible in situ identification. Finally, Chapter 13 focuses on presenting the possibility of stabilizing the disc at a selected point in the active space of the bearing with the use of the developed 6pAAMB actuator.

As a result of scientific research, the main statement was confirmed, showing the exclusive feature of the actuator, which is the possibility of spatial positioning of the levitating object. The issues presented in the above dissertation summarize the interdisciplinary course of designing, manufacturing, identifying and controlling the levitation object by means of an axial active magnetic bearing with six pole pieces. The reader may consider this as the blueprint for the design of an axial actuator with a few pole pieces. The author considers the above as the introduction and the invitation to continue his scientific research.

Streszczenie

W rozprawie doktorskiej przedstawiono koncepcję nowatorskiego siłownika z sześcioma nabiegunnikami (6pAAMB) w aplikacji osiowego aktywnego układu zawieszenia magnetycznego. Rozprawa ma charakter interdyscyplinarny, prezentując szereg badań nad wirtualnym i szybkim prototypowaniem osiowych siłowników elektromagnetycznych. Struktura rozprawy ma charakter modułowy. Swoim zakresem obejmuje wiele dziedzin nauki wokół zainteresowań autora, czego efektem jest spójny tok rozumowania prowadzący od potrzeby i pomysłu aplikacji, poprzez testowanie i weryfikację różnych koncepcji, aż po procedurę projektową, w tym modelowanie numeryczne, obliczenia analityczne, konstrukcję, kontrolę jakości, identyfikację i sterowanie. Rozprawa podzielona jest na część wstępną (Rozdziały 2-5) oraz część główną (Rozdziały 6-13).

Rozdział 2 zawiera badania nad systemem lewitacji magnetycznej z dwoma przeciwsobnymi siłownikami elektromagnetycznymi. Przeprowadzone badania potwierdziły, że właściwości dynamiczne ruchu poprzecznego można konfigurować poprzez sterowanie siłą osiową. Rozdział 3 skupia się na modelu termicznym lewitacji magnetycznej. Równania dynamiki systemu lewitacji magnetycznej rozszerzono o przepływ ciepła za pomocą nieliniowego modelu zależnego od temperatury. W rozdziale 4 omówiono koncepcję elektromagnesu z porowatym rdzeniem wraz z procedurą prototypowania wspomaganą metodą elementów skończonych. Koncepcję, konstrukcję, model i prototyp hybrydowego osiowego łożyska magnetycznego przedstawiono w rozdziale 5.

Rozdział 6 w skrócie zapoznaje czytelnika z koncepcją siłownika osiowego z kilkoma nabiegunnikami, który jest zdolny do osiowej lewitacji z funkcją orientacji przestrzennej wirnika w aktywnej przestrzeni łożyska. Rozdział 7 przedstawia numeryczny model osiowego łożyska magnetycznego z sześcioma cylindrycznymi nabiegunnikami. Zaproponowana konstrukcja pozwala na kontrolę kąta nachylenia wirnika za pomocą kilku składowych siły osiowej. Niezamierzony defekt siłownika stał się motywacją do napisania rozdziału 8. Eksperymenty uruchomieniowe wykazały, że zastosowana konfiguracja 6pAAMB wymaga kontroli jakości. W konsekwencji autor proponuje metodę diagnostyki osiowego siłownika elektromagnetycznego, opartą na fuzji pomiarów odległości, prądu i sygnału sterującego, według określonego scenariusza. Algorytm, który służy do diagnostyki uszkodzeń siłowników, z satysfakcjonującą dokładnością podaje różnice pomiędzy wysokościami poszczególnych nabiegunników. Wprowadzając interdyscyplinarne podejście do projektowania aktywnych łożysk magnetycznych, w rozdziale 9 przetestowano i zaadaptowano siłownik 6pAAMB w pionowej konfiguracji wirnik-wał. Rozdział 10 przedstawia model analityczny 6pAAMB, który został opracowany w celu uzyskania trójwymiarowego rozkładu składowej osiowej indukcji magnetycznej. Model wykorzystuje opis wektorowy potencjału magnetycznego i mapowanie Schwarza-Christoffela. Badania obejmują rozważania na temat wpływu efektu końcowego oraz sprzężonej funkcji permeancji. Główną zaletą proponowanego modelu jest znacznie krótszy czas obliczeń w porównaniu z modelem numerycznym przy ich zbieżności. Rozdział 11 przedstawia konfigurację pasywnego łożyska promieniowego, które wspomaga stabilizację poprzeczną lewitującego wirnika. Omówiono kilka eksperymentów pokazujących właściwości proponowanego rozwiązania. Autorskie sprzęgło magnetyczne służy do bezkontaktowego przyspieszenia wirnika do prędkości 4000 obr./min. W rozdziale 12 omówiono kompleksowe podejście do identyfikacji parametrów siłownika 6pAAMB z elektromagnesami sterowanymi prądowo. Zmierzono parametry cewek z dokładnym wskazaniem różnic. Zbadano niezawodność termiczną łożyska. Badania obejmują analizę siły elektromagnetycznej kilkoma metodami z zadawalającą zbieżnością między nimi. Ogólnie rzecz biorąc, zaproponowany siłownik mechatroniczny jest w stanie zwiększyć zakres stabilności lewitujących wirników i charakteryzuje się korzystnymi właściwościami dynamicznymi, co wykazano w testach z zewnętrznym wymuszeniem harmonicznym. Pełen opis siłownika wraz z niepewnościami parametrów uzyskano dzięki identyfikacji in situ. Na koniec rozdział 13 skupia się na przedstawieniu możliwości stabilizacji wirnika w wybranym punkcie przestrzeni aktywnej łożyska z wykorzystaniem opracowanego siłownika 6pAAMB.

W wyniku badań naukowych potwierdzono główną tezę, demonstrując zasadniczą cechę siłownika, jaką jest możliwość przestrzennego pozycjonowania lewitującego obiektu. Zagadnienia przedstawione w powyższej rozprawie podsumowują interdyscyplinarny przebieg projektowania, wytwarzania, identyfikacji i sterowania obiektem lewitacji za pomocą osiowego aktywnego łożyska magnetycznego z sześcioma nabiegunnikami. Czytelnik może uznać powyższe za schemat projektowania siłownika osiowego z kilkoma nabiegunnikami. Autor traktuje tę pracę jako wstęp i zaproszenie do dalszych badań naukowych.

Table of Contents

List of Acronyms

6pAAMB	six pole axial active magnetic bearing
3D	three-dimensional
2D	two-dimensional
AAMB	axial active magnetic bearing
AFPMM	axial flux permanent magnet machine
AMB	active magnetic bearing
AMS	active magnetic suspension
AC	alternating current
CAD	computer aided design
CNC	computerized numerical control
DAC	digital-to-analog
DC	direct current
DoF	degrees of freedom
FEM	finite element method
HAMB	hybrid axial magnetic bearing
MAGLERS	Magnetic Levitation Research Systems
MEC	magnetic equivalent circuit
MLS2EM	magnetic levitation system with two electromagnets
MLS1EM	magnetic levitation system with one electromagnet
PAC	programmable analog controller
PD	proportional–derivative
PID	proportional–integral–derivative
PMs	permanent magnets
PWM	pulse-width modulation
PMB	passive magnetic bearing
RMSE	root mean square error
RPMB	radial passive magnetic bearing
SC	Schwarz-Christoffel
SE	static eccentricity

Chapter 1

Introduction

1.1. Research motivation

Issues related to magnetic bearings are still a real engineering and technological challenge due to the extremely demanding needs of the aviation and military industries or the increasingly popular innovative space technologies [1]. It is worth mentioning the feat of the US Air Force, which already in 2016 set a speed record of 622mph propelling rocket-powered magnetically levitated sled on a nearly frictionless track. It is anticipated that automatic control systems in modern robotics, such as actuators, drives, joints and gears will benefit from solutions of active magnetic levitation technology, which offers unrivaled technical advantages. Contactless operation, precise control, no lubrication and low maintenance cost are superior features compared to mechanical bearings. Active magnetic levitation performs the task of stabilizing the object, often in motion, usually a rotating one. For applications such as centrifuges [2], computerized numerical control (CNC) tools [3], turbocompressor drive systems [4], [5], molecular pumps [6], to name a few, the urgency towards operational stability, higher electrical power density and compact design sets the current development trend [7]. Today, especially, it is important to minimize energy consumption and ensure stable operation of industrial machines. The future development of magnetic levitation is also in energy storage [8], [9], transport [10], high-speed machines [11], [12] or medical applications, an example of which is a fully magnetically suspended pump for advanced heart failure [13].

The author of this dissertation during his PhD studies participated in a few projects, such as a high-power generator for hydroelectric plants or a prototype of an axial generator for low power wind turbines. In various studies the author has focused on the design of axial electric drives. These projects introduced numerous technological difficulties related to the design of the drive, the shape of the rotor, the magnetic circuit optimization, uneven distribution of peripheral forces or wobbling of the rotor. On the basis of

these experiences, possible development trends were observed in the design and identification of axial actuators, together with their extended potential in magnetically levitated rotors. This constitutes the motivation for the doctoral dissertation, in which the author will tackle its subject in the course of an interdisciplinary approach, proposing a new solution for an axial actuator with a few pole pieces.

1.2. Up-to-date magnetic levitation technology trends

Few companies in the world have established their brands based on magnetic levitation technology. This is due to a specific market where most implementations require close collaboration with customers during project design and development to provide the expected reliable bearing performance. Waukesha Bearings[1] is one of those companies that offers magnetic bearings, including axial ones, that position a rotor axially using electromagnetic forces pulling in opposition on the collar. Disc-shaped electromagnets are located on both sides of the collar, which is the common axial bearing configuration. Looking at industrial implementations and scientific prototypes, the main emphasis is on radial stabilization with the axial one as a support. Rotating machines normally also require axial support in addition to radial stabilization. The structure of a conventional axial magnetic bearing provides a single axial force vector. Another company Calentix Technologies[2] selects a unique patented magnetic bearing design that combines the functions of axial and radial bearings in one device. The papers cited below, to which the reader may refer, briefly present the current configurations, research methodology and mathematical models that can be utilized among electromagnetic actuators and machines, in particular with axial flow of magnetic flux. A detailed discussion of the key issues during the prototyping of axial magnetic actuators will be included in the individual chapters of the dissertation.

In [14], [15] the electromagnetic actuator composed of several coils and the 6-degrees of freedom (DoF) contactless operation of a magnetized object were discussed. The design of active magnetic bearing (AMB) is constantly evolving, starting with a structure that uses permanent magnets (PMs) [16], [17], a classic active configuration, which contains a pair of cylindrical electromagnets [18], by inserting PMs into the magnetic circuit [19], up to a hybrid design, in which the functionality of the axial and radial bearings is combined [20]. In [21] a novel structure with a cylindrical rotor core was presented. A conical AMB with claw structure suitable for use in a limited radial space is presented in [22]. The design and optimization of AMB was examined in terms of its rotor dynamics [23] and geometry [24] with a new graphical approach to the stator shape design. The competitive design of an axial active magnetic bearing (AAMB) that meets the application requirements is the subject of numerous investigations. The emphasis is on self-bearing drives with active axial suspension [25]. Among the attractive solutions, actuators can be found that utilize Halbach arrays [26]. Typically, AAMBs provide a single electromagnetic force component, which is not sufficient to reduce the lateral vibrations of the levitating

[1] *https://www.waukbearing.com/en.html*
[2] *https://www.calnetix.com/*

object, although it is possible to some extent [27]. There are known axial stabilization systems containing PMs (with a typical repulsive effect), where a few electromagnetic actuators are used [28]. In most cases, AMBs are designed based on finite element method (FEM) modeling. Especially in AAMBs, a three-dimensional (3D) FEM model is desired, but requires substantial computational resources. In [29] a dynamic model of active magnetic suspension (AMS) with the embedded controller was developed in COMSOL Multiphysics. To efficiently model AMBs, numerous analytical methods are used during the initial design stage. A complete comparison of the three analytical methods for the cogging torque in axial flux permanent magnet machine (AFPMM) can be found in [30]. The AFPMM slotless model is presented in [31]. In [32] an optimization of the PMs design based on Schwarz-Christoffel (SC) mapping was systematized, which was used further to analyze the magnetic field distribution of motor PMs [33]. The author also utilized this method with a few changes to analyze the magnetic field distribution and end effects in the designed actuator. An improved subdomain technique was presented in [34] while such a model of PMs biased radial AMB can be found in [35]. In [36] a quasi-3D AFPMM model was developed containing the analysis of the end effects.

Subsequent numerous papers deal with a new approach to modeling axial machines, including the description of their eccentricity, optimization of the magnetic field flux, hybrid zero-power systems, the considerations of chaotic rotor motion or various modeling methodologies with the use of analytical and numerical tools.

1.3. Aim of dissertation and main statement

The subject of the doctoral dissertation are **Axial Active Magnetic Suspension Systems**. The aim is the design, implementation and identification of the novel axial actuator with a few pole pieces, which operates as a levitation device capable of setting the tilt of the rotor and enabling control of the rotor position in the levitation space. The dissertation is interdisciplinary, referring to various issues of electromagnetic field theory, mechanical engineering, machine dynamics, control applications and material properties. This is in part due to the need to engage numerous fields of science to achieve the goals set for the dissertation, as well as the educational background of the author, who graduated from both Electrical Engineering [37], Mechanical and Material Engineering [38]. The structure of the dissertation is modular, where each of the chapters sets out a unified thought devoted to a selected issue of designing axial magnetic suspension systems. Modularity allows for a comprehensive approach to the topic of the dissertation, presenting a consistent line of reasoning heading for the confirmation of the main statement, which is formulated as follows: **axial active magnetic bearing with a few pole pieces allows for setting the spatial orientation of the levitating object.**

1.4. Dissertation overview

Proving the main statement required extensive research, the effects of which are described in the following twelve chapters. Below are brief descriptions of their content.

Chapter 2 contains research on a magnetic levitation system with two electromagnetic actuators in an E-shaped configuration, located opposite each other. The object of the levitation is a metal sphere. The influence of current and proportional–derivative (PD) controller settings on lateral motion of the sphere was considered. Simulation models in conjunction with experimental studies are validated with the help of image processing. The research carried out confirmed that the dynamical properties of the lateral motion can be configured by stretching control. The results were published in [27]. The author's contribution is 33%.

Chapter 3 considers thermal effects in the axial pot core actuator. This chapter focuses on the magnetic levitation thermal model and the effects associated with losses due to electromagnet heating. A slight change in the inductance of the electromagnet and its dynamics as a function of temperature were observed during the long-term stabilization of the sphere. An extension of these considerations, which will be included in the MAGLERS[3] team paper, is the nonlinear mathematical model of axial levitation with an E-type electromagnet, which takes into account the effect of temperature on the position of the levitating object.

Chapter 4 evaluates the concept of electromagnets with a porous core. The core was manufactured manually. The aim of this chapter is to provide an initial analysis of the proposed powder core together with the prototyping procedure, using a finite element method. The assessment of the convergence of the numerical model with the experimental data allowed for the estimation of the magnetic properties of the produced core. This chapter emphasizes the importance of careful material selection in the design of electromagnetic applications. The results were published in [23]. The author's contribution is 50%.

Chapter 5 implements from scratch the concept, design and prototype of hybrid axial magnetic bearing (HAMB). The numerical model was developed in COMSOL Multiphysics. The manufactured stator and rotor were tested on a laboratory test rig. Initial tests were carried out in differential mode with voltage control. The advantages of the hybrid actuator configuration and favorable force characteristics were demonstrated, as well as the need to develop a 3D model taking into account the mutual coupling between its active and passive part. The results were published in [39]. The author's contribution is 50%.

Chapter 6 is the first to introduce six pole axial active magnetic bearing (6pAAMB). In principle, this configuration stabilizes the motion of the rotor in the axial direction and provides the possibility of disc tilt control. The geometry of the actuator is presented with variants of coil connections. The features of the axial actuator are discussed.

Chapter 7 develops a numerical model of the axial magnetic bearing with six cylindrical poles. The model evaluates several configuration variants. The influence of changes in current and rotor position on force characteristics was investigated. The model confirms the possibility of controlling disc wobbling

[3] Magnetic Levitation Reserach Systems; *http://www.maglev.agh.edu.pl/*

with the use of a few axial force components that are capable of actively compensating for the axial load. The chapter shows the advantage of striving to design a virtual prototype that allows for reliable multiparametric optimization of the system according to the criteria of cost, performance, operation or production. Before a real device is manufactured, the accurate numerical model will provide essential knowledge about the performance of the axial magnetic bearing. The results were published in [40]. The author's contribution is 50%.

Chapter 8 develops an original diagnostic method of the disc-type electromagnetic actuator by assessing the quality of its active surface. This chapter is an extension of the identification of AAMBs. The prototype manufactured on the basis of numerical analysis did not meet the operational requirements. A run-up experiment showed that 6pAAMB demands a quality test. The algorithm, which is used for actuator fault diagnosis, indicates differences between the heights of individual pole pieces with 50μm accuracy. The experimental results have been verified using the coordinate measuring machine. Finally, a scan of the actuator with a laser profiler is presented.

Chapter 9 describes several variants of laboratory test rig supported by two active magnetic bearings, the axial active magnetic bearing alone or in combination with radial passive magnetic bearing (RPMB). The concept of a slim-type AAMB with six cylindrical poles was tested and adapted to the vertical rotor-shaft configuration through an interdisciplinary approach to the design process. The results were published in [23]. Primarily, this chapter contains seemingly incomplete but immensely important research, which in the PhD timeline coincided with the pandemic. The prototypes of the test stands built at that time showed the overarching features of the proposed configuration of the axial actuator together with some limitations and further recommendations. In the next iteration of the research, a new prototype was described and implemented, current control was applied and the test stand was improved, including the measuring system and overall stability of the system.

Chapter 10 presents the second iteration of the novel six pole axial active magnetic bearing, which was manufactured and investigated experimentally. The developed analytical model utilizes the magnetic vector potential formulation and Schwarz–Christoffel mapping. The research covers in-depth deliberations on the end effect influence and the conjugate complex permeance function. The chapter guides the reader through the steps of mathematical analysis, discussing in detail the tools used to describe 6pAAMB. The main advantage of the proposed analytical model is the significantly shorter computation time compared to the numerical one, which is useful from the point of view of modeling and building controllers, especially in the case of optimization procedures. The results were published in [41]. The author's contribution is 50%.

Chapter 11 describes the consequences of combining the designed axial actuator with a radial passive magnetic bearing. The reliable operation of passive magnetic bearings depends on the properly adjusted force characteristics and mutual interactions between the active actuator and permanent magnets. In this chapter, several experiments have been designed to identify the rotor dynamics in the abovementioned system. Finally, a proprietary magnetic coupling was used to accelerate the rotor to a speed of 4000 rpm in a full levitation mode.

Chapter 12 elaborates a comprehensive approach to identify the parameters of the novel six-pole axial active magnetic bearing actuator with current-driven electromagnets. The reader can explore a number of identification methods that provide a holistic view of the actuator. This research emphasizes the accessible in situ identification of 6pAAMB using various measurement methods to obtain a complete description of the actuator with uncertainties in its parameters. In general, the proposed mechatronic actuator is capable of increasing the stability range of rigid or flexible rotors and is characterized by favorable dynamic properties. The results will be published in [42]. The author's contribution is 50%.

Chapter 13 summarizes the interdisciplinary design of the 6pAAMB . Stabilization experiments were performed in a control system consisting of three local proportional–integral–derivative (PID) controllers, obtaining a set of equilibrium points and transient states of the rotor with satisfactory repeatability. Raw experimental data were used in numerical calculations to formulate model equations that describe the rotor in steady state. A detailed analysis of the electromagnetic force and torque distribution was provided. The tilt of the rotor around the x axis with variable PD settings illustrates the influence of the controller on the dynamics of the spatial orientation of the rotor. This chapter is the closure of the presented scientific course to confirm the main statement of the dissertation.

1.5. Dissertation in numbers

In the course of developing the scientific research included in the following dissertation, 9 articles have been published. The author also participated in 5 conferences and technical workshops. The result of completed experimental studies is more than 10 various test stands, HAMB prototype, 2 versions of 6pAAMB prototype and various RPMB variants. During prototyping, 3D printing technology, CNC machining and laser cutting were utilized. Approximately 15 rolls of filament were printed during the more than 1500 hours of the 3D printer Zortrax M200. The dissertation refers to nearly 150 literature items, a large part of which are the latest achievements in the field of magnetic levitation. The interdisciplinary scope of research required the use of tools from many fields of science, i.e. computer aided design (CAD), development of numerical models using FEM methods, extended mathematical calculations and advanced measurement methods, which required the use of more than 20 different computer applications. The dissertation is well illustrated for a better overview, guiding the reader along the main line of reasoning. All charts and illustrations were prepared almost entirely by the author. It is also worth mentioning that during his doctoral studies, the author completed the KIC InnoEnergy PhD School program, participating in 7 international business trainings and conferences throughout Europe, focused on networking and pioneering changes in sustainable green energy toward innovation and business. The author completed a 4-month internship at Uppsala University, developing numerical models for a high-power hydrogenerator. The author cordially invites You to read his dissertation, which is the result of the above-mentioned activities.

Chapter 2

Investigation of lateral motion in levitation system with opposite electromagnets

This chapter contains research on a magnetic levitation system with two electromagnetic actuators in an E-shaped configuration, located antiparallel. The section presents the influence of the coil current in the operating point on the lateral stiffness and damping of the levitating sphere, under the external static and dynamic load. The numerical model and experimental research, validated with support from image processing, are presented. The lateral displacement is identified. The research carried out confirmed that the dynamical properties of the lateral motion can be configured by stretching control.

2.1. Research inspiration

To illustrate the conducted research, imagine two boys pulling both ends of a rope, each in the opposite direction. In the middle of the rope, a ball was fixed through its axis. The third boy tries to move the ball by applying force perpendicular to the plane of the rope. Can two boys pull the rope so tightly that the third boy cannot move the ball?

This research was motivated by the differential mode PD controller achieved for magnetic levitation system with two electromagnets (MLS2EM) [43]. Furthermore, the plenary talk given by Prof. Takeshi Mizuno from Saitama University, Japan, during the 16^{th} International Symposium on Magnetic Bearings (ISMB16) described the possibility of lateral vibration control by switching stiffness. Active magnetic levitation systems allow to counteract the gravitational force. Typically, a solution with a single electromagnetic actuator, which may be supported by a permanent magnet, is used [44]. The application of two electromagnets, placed opposite each other [45], allows research on stabilizing regulators [46], fuzzy logic controllers [47], up to model predictive control [48]. Using two actuators, a common configuration of a single-axis active magnetic bearing may be applied. Its mathematical model and control methods are widely known [29]. The FEM design approach may provide a model that is similar to the experimental one, thus useful in virtual prototyping [49]. However, effective control of a levitated rotor

requires a multidimensional regulator. The static and dynamic regulator configuration, which is embedded in the hardware layer of an industrial programmable analog controller (PAC), is presented in [50]. Research on the state observation of the single-axis magnetic bearing with additional axial load is conducted [51]. The extended magnetic levitation system by an additional electromagnet leads to improved stability with a PID controller with 2-DoF [52]. This chapter describes the implementation of the configurable load, which acts on the levitating sphere in the axis perpendicular to its axial motion. The scientific novelty is included in the extended analysis of MLS2EM lateral stiffness and damping, by investigating lateral motion of the sphere, involving FEM, image processing and experimental procedures. The following questions arise. Does a control in a single axis, with both electromagnets in E configuration, located axially and antiparallel, allow one to minimize a motion in a perpendicular axis? What is the distribution of the electromagnetic force for a variable position of the sphere in the levitating space? How do the dynamic properties of a closed-loop system change when increasing the control of the electromagnetic actuators?

2.2. Magnetic levitation system with two electromagnets

Analytical model

The laboratory test rig MLS2EM consists of two electromagnets operating in differential mode. The widespread configuration of the electromagnetic actuator in the system consists of the core in a shape of a horseshoe and two windings located on both pole pieces. The mathematical model of the single-axis magnetic levitation system [53] with hardware coil current regulators (Fig. 2.1a) can be expressed by the following set of equations:

$$\begin{cases} \dot{x}_1 = x_2 \\ \dot{x}_2 = \dfrac{1}{2m_s}\left(\dfrac{dL(x_1)}{dx_1}\cdot x_3^2 - \dfrac{dL(x_t - x_1)}{d(x_t - x_1)}\cdot x_4^2 + F_g\right) \\ \dot{x}_3 = \dfrac{1}{T_3}\cdot(k_3(u_1 + u_{c3}) - x_3) \\ \dot{x}_4 = \dfrac{1}{T_4}\cdot(k_4(u_2 + u_{c4}) - x_4) \end{cases} \tag{2.1}$$

where state variables x_1, x_2, x_3, x_4 are, respectively, axial position and velocity of the sphere, current of the top and bottom electromagnets. The control applied to the actuator units stands as u_1 and u_2. Table 2.1 shows the key parameters of the real MLS2EM system, which were identified experimentally. Figure 2.2 presents the derivative of the coil inductance over the axial position of the sphere and the electromagnetic force versus the position of the sphere for different current values.

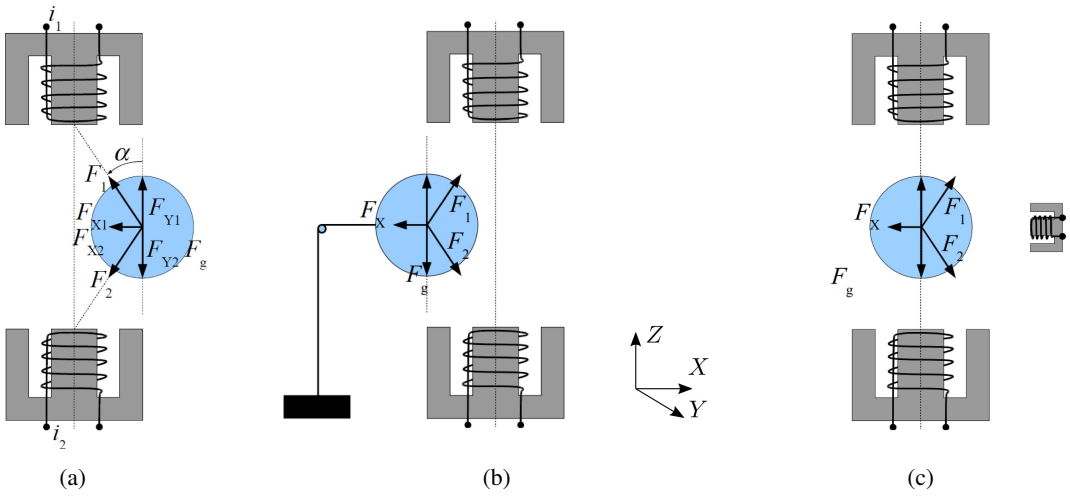

Fig. 2.1. Distribution of the electromagnetic force components, when (a) the sphere is displaced horizontally from the center - steady-state levitation point; (b) levitation scenario under the static load - the mass hanging on the thread; (c) levitation scenario under the dynamic load - the horizontally located electromagnet, which generates variable lateral force.

Table 2.1. Parameters of the real MLS2EM system.

Parameter	Symbol	Value
mass of the sphere	m_s	38.7g
mass of the static load	m_l	8.5g
total air gap	x_1^t	21mm
external sphere radius	R_e	29.5mm
number of coil turns	N_T	640
resistance of the coil	R	4.3Ω
time constant of the electromagnet	T_3, T_4	10ms
gain coefficient	k_3, k_4	0.64A/V
constant coil voltage	u_{c3}, u_{c4}	0.045V
constant coil current	i_{03}, i_{04}	0.23A
derivative of the coil inductance	$\frac{dL(x_1)}{dx_1} = a \cdot e^{bx_1}$	a= 6.996, b=-171.5

Numerical model

The 3D numerical model of the MLS2EM system was developed in COMSOL Multipysics (Fig. 2.3a) to calculate the components of electromagnetic force with respect to the displacement of the levitating object and the applied coil current. A single set of calculations is presented in Figs. 2.3c and 2.3d. Note that the axial force depends on the object's displacement and, therefore, the control of dynamical properties in the lateral direction is possible. An initial comparison was made between the numerical and experimental setup to check the convergence (see Fig. 2.3b). The modeled sphere is, in fact, two sheets of metal that are pressed together. The model does not take into account the core lamination and magnetization curve. The imperfect manufacturing of the sphere, which can levitate at an angle, causes an uncertainty error of the sensor measurement.

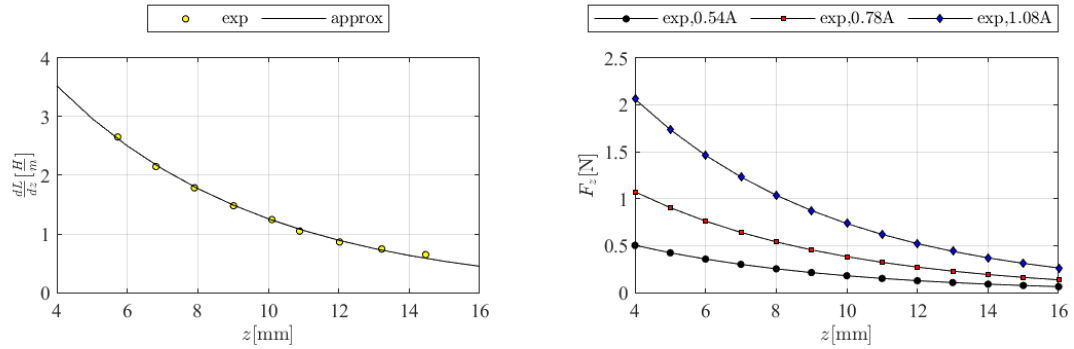

Fig. 2.2. Derivative of the inductance over the sphere's axial position (a) and the electromagnetic force characteristic from experiments of PD stabilization, close to the MLS2EM operational point.

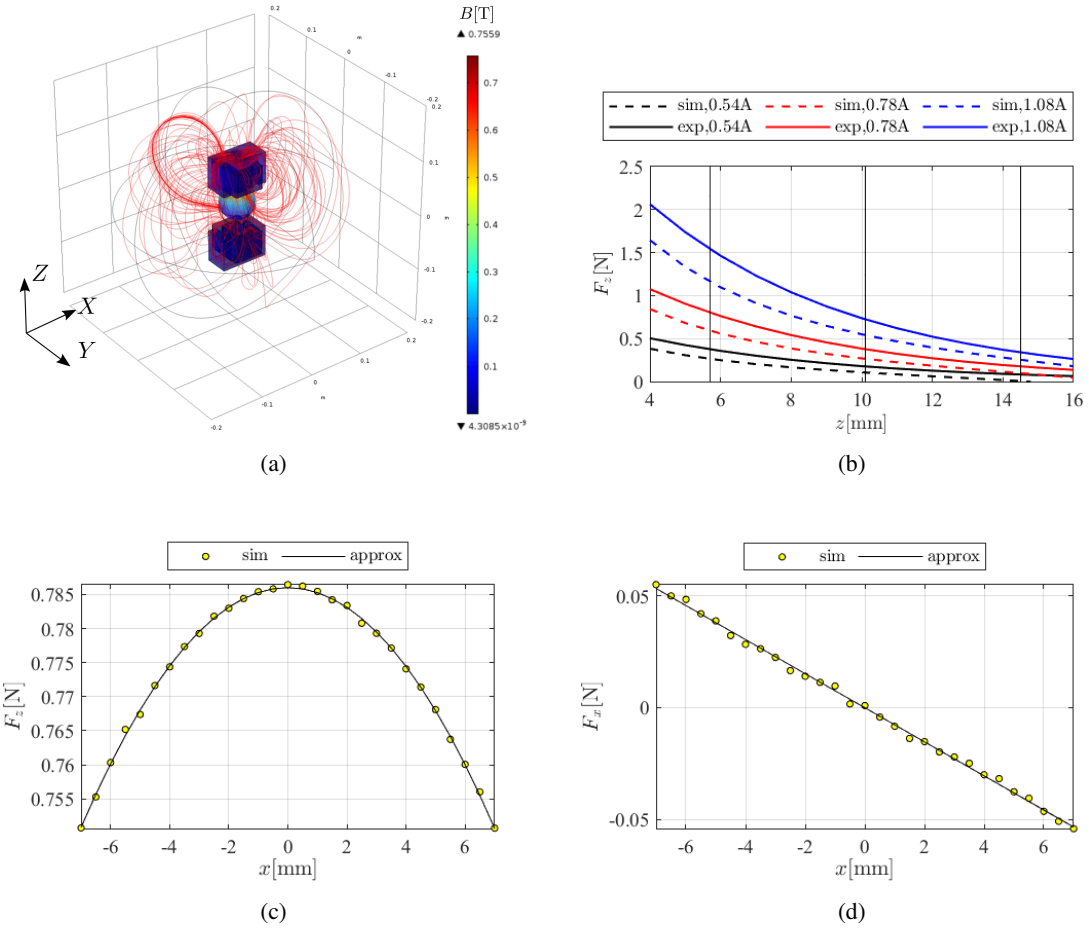

Fig. 2.3. Numerical analysis: (a) 3D model of MLS2EM for 1 A current in the upper electromagnet; (b) comparison between the electromagnetic force from the identification and the numerical model, for a few selected operational points; (c) the axial and (d) lateral electromagnetic force versus lateral displacement of the sphere.

The laboratory test rig MLS2EM [45] was modified to meet the planned research requirements, as follows (see 2.4a):

– a power amplifier with a current controller (with an internal hardware feedback loop, in order to maintain the current set value) was applied,
– static load in the form of a mass hanging on a thread,
– a side electromagnet was used to excitate a lateral motion of the levitated sphere,
– a camera was used for additional observation of the sphere motion.

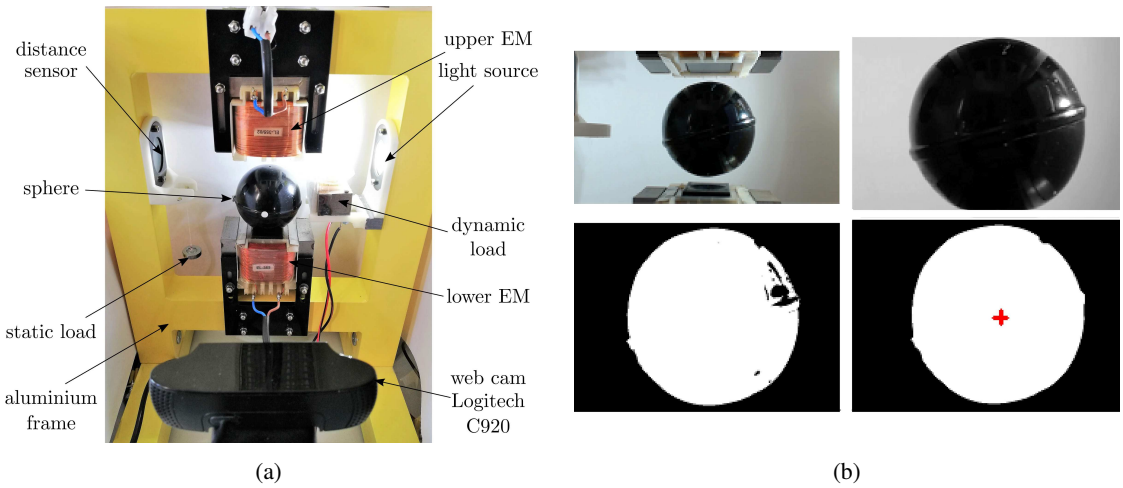

Fig. 2.4. Experimental research on (a) upgraded MLS2EM test-rig [45] and (b) operation example of the sphere's displacement detection, based on recorded video file.

Method of sphere motion detection

In order to determine the horizontal displacement of the sphere, the additional sensor must be used. The Logitech C920 camera was used, as a tool for global observation of the sphere's location. This camera does not allow one to close the real-time video feedback in a control loop. Also, limited data acquisition and transfer to 30 frames per second (fps), at resolution of 1080x720, narrows the possible observation range of the sphere's motion. Therefore, the recorded video material is analyzed offline to reconstruct the motion of the sphere in the levitating space. The red-green-blue (RGB) image is transformed into a monochrome image and then binarized. The sphere surface is covered, to obtain the full circle shape. The center of mass is then determined, which is the representation of its center.

An image was recorded and stored with a frequency of 30 fps, regardless of the experiment carried out in real time, with a sampling frequency of 1 kHz (T_0=1 ms) under supervision of Simulink Real-Time desktop running in MATLAB / Simulink, on Windows 7. After the registration of the video material and experimental data, the content of files was processed in order to obtain particular sphere's displacements. The waveforms were synchronized on the basis of the alignment of the sphere's displacement in the vertical direction (axial alignment of electromagnets). The PD (2.2) and PID (2.3) stabilizing controllers were performed in differential mode to keep the sphere levitating in the center between the electromagnets.

$$u_{PD}(k) = (K_p + K_d {T_0}^{-1})e(k) - K_d {T_0}^{-1} e(k-1) \tag{2.2}$$

$$u_{PID}(k) = (K_p + K_d {T_0}^{-1})e(k) + K_i T_0 \sum_{j=0}^{k} e(j) - K_d {T_0}^{-1} e(k-1) \tag{2.3}$$

$$u_1(k) = u_{10} + u_{PD}(k) \tag{2.4}$$

$$u_2(k) = u_{20} - u_{PD}(k) \tag{2.5}$$

where: $e(k) = x_{10}(k) - w$, u_{10}, u_{20} - is a steady-state control applied to the upper and lower electromagnets, respectively, T_0 is the sampling period (1 ms), K_p, K_i, K_d are proportional, integral and derivative parameters of the stabilizing controller. Choosing the values of K_p, K_d, u_{10} and u_{20}, the dynamical properties of the levitation system can be set. Due to the current feedback applied in the hardware, the control signal is proportional to the coil current and therefore its time diagrams will be omitted.

2.3. Analysis and estimation of lateral displacement

Based on image processing, a waveform is obtained that represents the vertical and horizontal displacement of the sphere. From the control theory point of view, according to the dynamics of the active magnetic levitation system, it is particularly interesting to know the dynamic properties in the horizontal axis, when controlling the vertical axis motion of the sphere. The low image acquisition frequency strongly affects the quality of the reconstructed displacement signal. It is assumed that the dynamical motion of the levitating sphere in a horizontal axis is described by the second-order linear system. Therefore, the lateral oscillatory motion can be formulated in the form of equation (11.3). To more accurately determine the frequency of horizontal vibrations of the sphere and the damping coefficient, the experimental data were approximated by (11.3).

$$x(t) = A \cdot e^{-\delta \cdot t} \cdot sin(\omega t + \phi) \tag{2.6}$$

where A, δ, ω and ϕ denote, respectively, the amplitude of vibration, the exponential coefficient that provides the vibration attenuation, the signal frequency and its phase shift. The approximation procedure based on (11.3) and scaled with the resolution values of the Logitech C920 (the resolution in the x- and y- axes is 107.6 μm and 109.80 μm) were used to identify the lateral motion of the levitating object.

2.3.1. Investigation of lateral motion under static load

Aim of this experiment was to levitate the sphere with the attached mass (see Fig. 2.1b) and increase the control of the upper and lower electromagnets. On the basis of the control change analysis and as a consequence of the linear steady-state current change, one can observe the effect of the electromagnetic force change affecting the levitating sphere. The rising electromagnetic force will cause attraction

of the sphere towards the axis of electromagnets. When the force value is reduced, the sphere moves toward the static load. This experiment allows one to scale the electromagnetic force on the basis of the external load (see Figs. 2.5a, 2.5c, 2.5e). Note that due to the stabilization given by the controller, the sphere is kept close to the desired position.

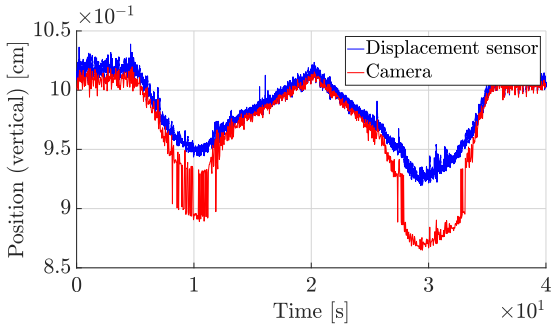

(a) Displacement in vertical axis of the sphere.

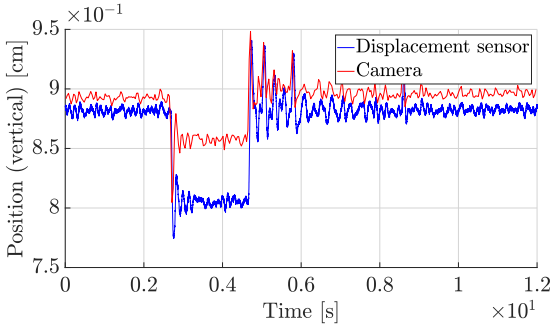

(b) Displacement in vertical axis of the sphere.

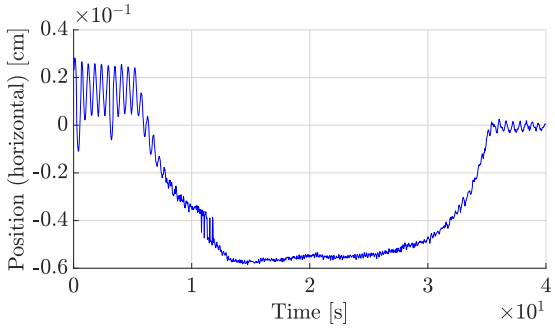

(c) Displacement in horizontal axis of the sphere.

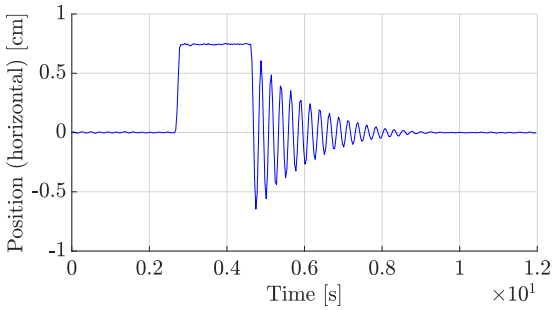

(d) Displacement in horizontal axis of the sphere.

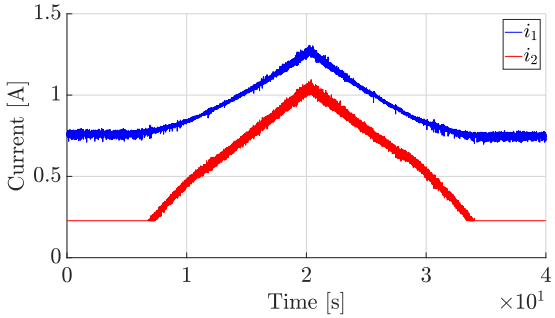

(e) Coil current in the static load experiment.

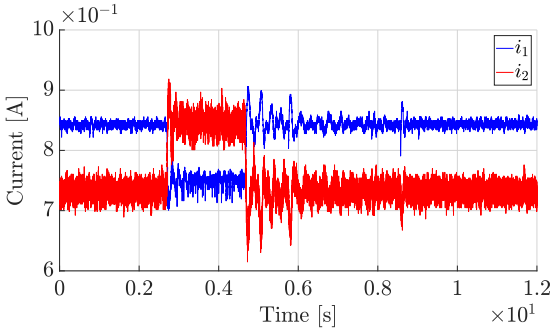

(f) Coil current in the dynamic load mode.

Fig. 2.5. Comparison between static (a, c, e) and dynamic (b, d, f) excitation impact on the levitating sphere.

2.3.2. Investigation of lateral motion under dynmic load

Aim of this experiment was to levitate the sphere, turn on and off the external excitation in the horizontal axis, using an electromagnet (see Fig. 2.1c). With this noncontact method, the sphere will be pulled out from the center position. The angle α (see Fig. 2.1a) appears and the forces F_1 and F_2 have horizontal and vertical components. When the external force is applied, the sphere returns to the

central position (see Figs. 2.5b, 2.5d, 2.5f). The dynamics of motion depends on the stabilizing controller and its parameters. Two experimental results were compared for the modified steady-state control. The controller parameters were established as follows: $K_p = 250$, $K_d = 2$, while the steady state current was applied as i_{10}=0.76 A, i_{20}=0.23 A for scenario Scn_A and i_{10}=1.44 A, i_{20}=1.18 A for scenario Scn_B. Horizontal displacements were recorded, analyzed, and fitted with the proposed analytical response. The coefficients of the equation (11.3) are listed in Table 2.2. The stretching action of electromagnetic forces results in system dynamics.

Table 2.2. Results of experimental data approximation.

Scenario	A	δ	ω	ϕ
Scn_A	1.6364	0.3603	10.5241	2.6562
Scn_B	-0.8946	0.8788	41.4604	-0.0323

Generalization

On the basis of conducted research, the author proposes the generalization (2.7) of the active magnetic levitation system to the 3D model, when the model consists of a single electromagnet or two electromagnets, located opposite each other, with controlled axial motion of a levitating object.

$$\begin{cases} M\ddot{x} = F(x,i) + G \\ \dot{i} = f_i(x,i,u) \end{cases} \tag{2.7}$$

where: x is a displacement vector, i is a coil current vector, u is a control vector, f_i is a function that describes the dynamics of electromagnetic actuators, M is a mass matrix, $F(\cdot)$ is a force matrix and G is a gravity matrix.

Summary of results

This research demonstrated that it is possible to minimize the design of an active magnetic levitation to the configuration with two electromagnets if the stretching forces are sufficient to stabilize the levitating object under external disturbances. This chapter outlined the general concept in which the simplified single axis AMB allows us to influence to some extent the position of the levitating object in the inactive axes. This approach can be targeted in two ways. The geometry of a radial AMB can be significantly reduced to a uniaxial configuration with a properly designed stiffness. It is also possible to develop a new axial bearing that will be able to control the dynamics of the axial motion to the extent that it can support the task of radial stabilization in a more controlled manner. In both cases, the impact of external disturbances should be investigated. Increasing the stiffness of AMB is equivalent to higher current flow, which generates heat. Thermal phenomena should therefore be treated not only as an important part of actuator design process, but also as a disturbance affecting its operation including its dynamic.

Chapter 3

Axial active magnetic levitation extended by heat transfer

Active magnetic levitation systems are typically modeled as an interaction of motion dynamics and electromagnetic circuit dynamics. Thermal effects are often neglected or taken into account in the form of coefficients, which do not translate into the real-time dynamic system. This chapter focuses on the magnetic levitation thermal model and the effects associated with losses due to electromagnet heating. The following sections extend the dynamic model of magnetic levitation systems by using the heating transfer model. On the basis of the experimental research carried out on cylindrical and E-shaped electromagnets, a nonlinear temperature-dependent model was developed. Temperature effects were observed during long-term stabilization of the sphere.

3.1. Motivation and thermal analysis review

The impact of a temperature increase on the performance of an electromagnetic actuator depends on several factors, such as its operating conditions, a cooling system or an implemented regulator. An illustrative example may be a CNC machine with an electromagnetic holder for a cutting tool. Under the influence of cutting forces on a material, the clamping force of a tool must increase to maintain the stability of the manufacturing process. A rise in the driven current gives rise to a temperature, which lowers a magnetic field and a force itself. In a medium-sized company with, e.g. 20 machines of this type, a poorly designed actuator causes either a machine or a tool failure and downtime or a significant increase in a power demand due to a higher current. Both variants accelerate financial losses. Therefore, it is necessary to address thermal phenomena in electromagnetic actuator design and regulator synthesis, taking into account the direct impact of thermal phenomena on its parameters.

Various control methods are successfully utilized to stabilize a levitating object, e.g., linear and nonlinear, robust, adaptive, self-learning and self-measuring. To a large extent, most studies contain the results of short-term experiments [54]. often forgoing discussion on machine failure due to thermal

phenomena. Numerical simulations, especially 3D, can take into account complex geometry, operating conditions, and applied load at a very accurate point. In [55] a transient real-time 3D thermal model was introduced for a moving magnet planar actuator. The results have been verified by measurements using an infrared camera. The model may be running in real time due to a 0.1 ms single-step computational time. Thermal phenomena will greatly affect the performance of high-temperature superconductor due to electromagnetic parameters strongly dependent on local temperature [56], [57]. The analysis of a magnetically levitated gravity compensator was carried out in [58], where innovation is the inclusion of the thermal radiation effect in a fairly simple model, which is suitable for optimizing the design of AMB. Furthermore, medicine utilizes thermal models, e.g., in [59] numerical analysis supports the magnetic hyperthermia procedure. A well-known approach is a static lumped thermal network. Therefore, a thermal analysis was carried out in [60] for a radial active magnetic bearing and in [61] to analyze analytically the thermal structure of a catcher bearing using thermal resistance equations. In [62] a new design tool for high-temperature magnetic bearings was also developed, which allows their layout and optimization based on the reluctance model. Often, publications with an emphasis on material properties develop an analytical description of magnetic field parameters under heat treatment. In [63], a comprehensive model was proposed that predicts magnetization through temperature. In [64] magnetic properties of the silicon steel lamination were modeled taking into account the influence of temperature. Numerous studies present experimental measurement methods, using temperature sensors and thermal cameras to verify model calculations. In [65] the effects of increased temperature on the control performance of magnetically levitated planar actuators with a moving magnet in a high-precision field were studied. In [66] an experimental validation of the actuator operating in a high temperature environment of up to 500°C was carried out. The paper [67] describes the dynamic changes of the permanent magnet harvester model at different ambient temperatures. The influence of temperature, e.g. on the position of the oscillating mass and on the frequency of the mass oscillation.

Some research, including this one, discusses the change in the inductance of the electromagnet as a function of temperature. The measurements in [68] showed a slight decrease in the inductance of the coil with the core with increasing temperature. This change is approximately linear and was confirmed by FEM simulations. In [69] almost no correlation was reported between the inductance of a miniature coil without core and temperature over a wide temperature range. Following [70] the change in inductance of the ferrite core coil was indicated according to the direct current flowing through it. No influence of current values on the inductance of the coil with a powder core and its change in a ferrite toroidal core was observed. Inductance is determined by the conductor geometry (neglible thermal expansion) and the properties of the ferrite core material (temperature coefficient). The temperature coefficient of an inductor depends on several factors that may be additive or subtractive over a given temperature range. It is important to consider that aircore inductors have effectively very low temperature coefficient compared to ferrite core ones, which are frequency and direct current dependent.

3.2. Cylindrical electromagnet thermal study

3.2.1. Test stand for thermal research

The section presents a developed test stand and properly designed experiments to identify the effect of temperature on the active magnetic levitation system. Research was carried out in both the open-loop and closed-loop systems. The ultimate goal was to propose a set of mathematical equations that would be useful for control synthesis. The first version of the stand examined the cylindrical core (Fig. 3.1). The electromagnet with dimensions (Fig. 3.1d) was placed in a 3D printed housing (material Z-ULTRAT). In the housing there is a window for a thermal camera and channels for thermocouples (Figs. 3.1a-3.1b). The flux of the magnetic field is measured by the ASONIK probe[1]. The KEYENCE distance sensor with the EX-110V sensor head with a range of up to 2 mm measures the position of the sphere. Zero in the coordinate system is on the central axis of the electromagnet, on its center pole plane (Fig. 3.1c). The system is enclosed with plexiglass plates to minimize reflections and the influence of the environment on camera measurement.

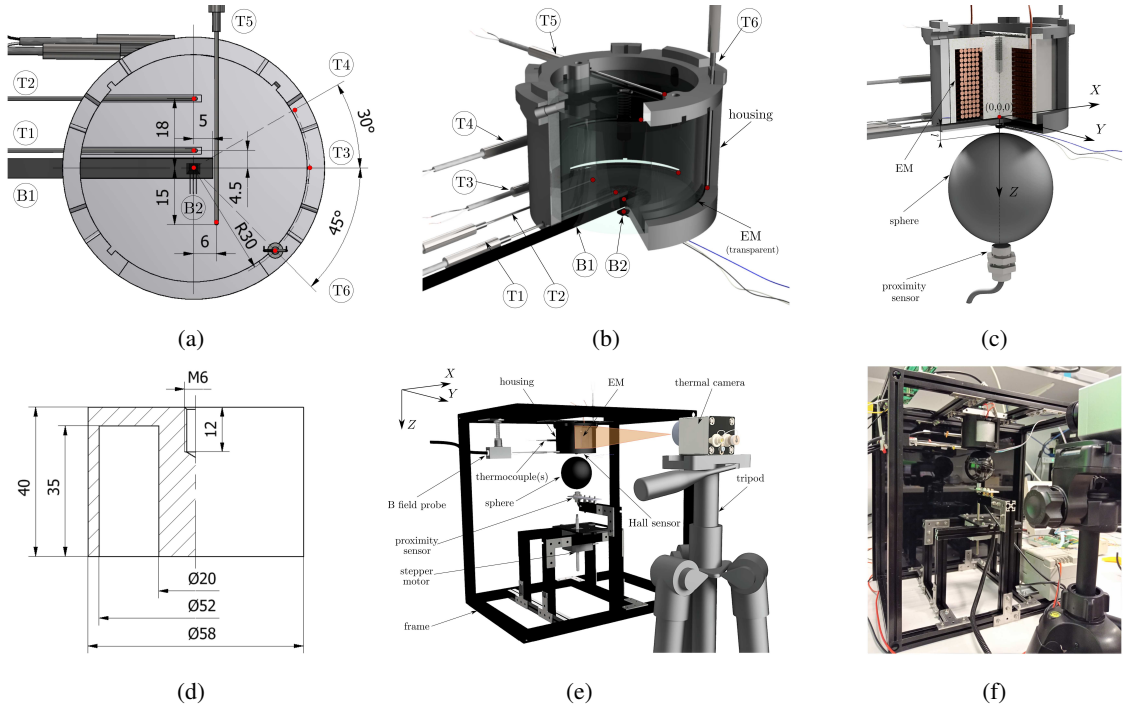

Fig. 3.1. Thermal research with cylindrical core magnetic levitation system with one electromagnet (MLS1EM).

3.2.2. Thermal measurements

Long-term studies of 48 g sphere levitation were carried out with the regulator PD and PID. Data processing and acquisition from a fixed starting point were developed for each experiment. The temperature was measured at a few points through thermocouples and a thermal camera. A numerical model of

[1]The $B2$ sensor, i.e. the SS495A Honeywell Hall sensor used in the stand operated at the limit of its measurable magnetic field range equaled 67 mT, therefore, measurements with it are not included.

a cylindrical core heat exchange was developed, which demonstrated convergence with the measurement data. The results are not included here because of the purpose of the chapter, which is to emphasize the impact of thermal effects on the levitation system and the regulator synthesis procedure. The Magnetic Levitation Research Systems (MAGLERS) team, of which the author is a member, conducts experiments on magnetic levitation thermal design with robust controllers. In Figure 3.2 there is a comparison between PD and PID levitating sphere control in a long-term experiment of 5 hours. One may observe a decrease in current and magnetic induction as the control increases and the sphere descends. Figure 3.4 shows the derivative of the inductance as a function of the axial position, current, temperature and time. The derivative was determined by the indirect method from the equilibrium points of the sphere during the experiment. The fall of the sphere and thus the increase in the levitation distance occurs as a result of the magnetic field reduction owing to temperature. This has a direct effect on the current decrease and therefore the derivative of the inductance decreases with time as the sphere distance and temperature rise.

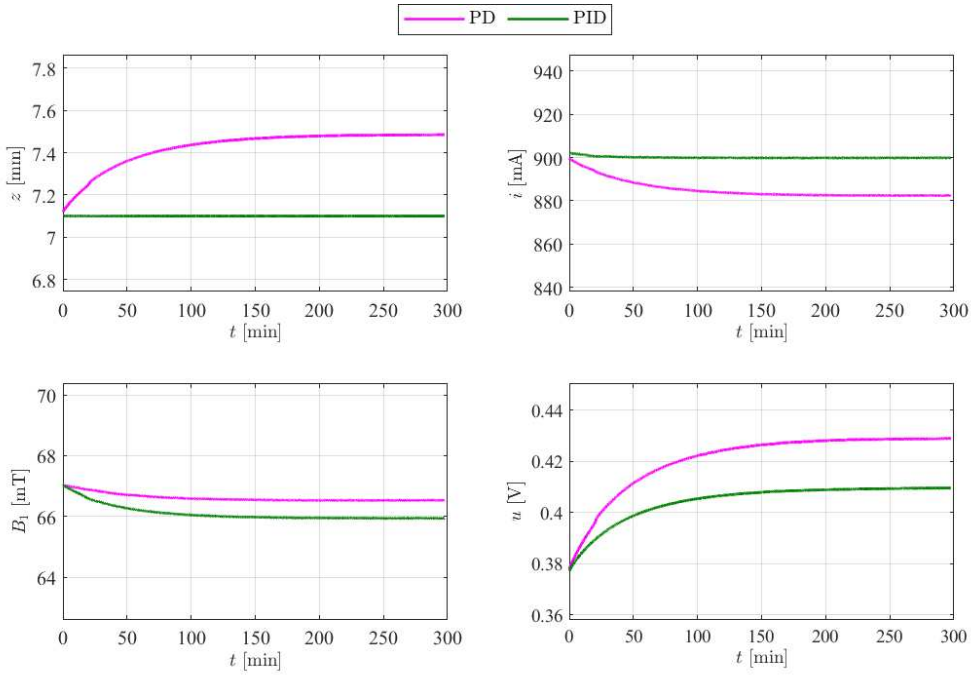

Fig. 3.2. Long-term static levitation with the cylindrical core MLS1EM.

The influence of temperature on the coil inductance seemed debatable and required verification by additional experiments. Figure 3.3 shows the measurement of inductance by several methods, that is, the technical method with an accurate current measurement by two RIGOL DM3068 6.5-digit multimeters, the direct measurement of inductance with the GW Instek LCR-821 meter and also with the voltage pulse-width modulation (PWM) signal, which allows estimation of time constant. Data were approximated by functions that were then differentiated and compared with the results of the indirect method. The observation of derivative inductance under the influence of temperature presents values comparable to those of other methods, but with a downward trend. This indicates the necessity of including thermal effects during the identification of the electromagnet inductance with a given power supply unit.

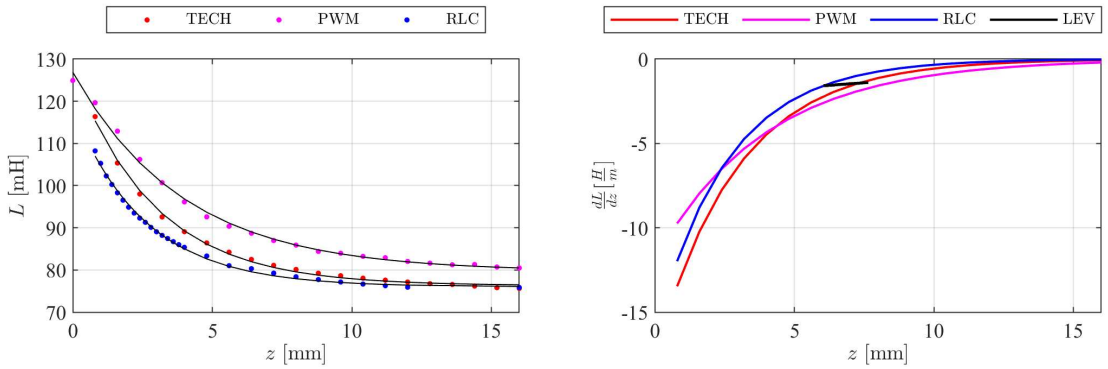

(a) (b)

Fig. 3.3. Identification of the inductance in the cylindrical core electromagnet.

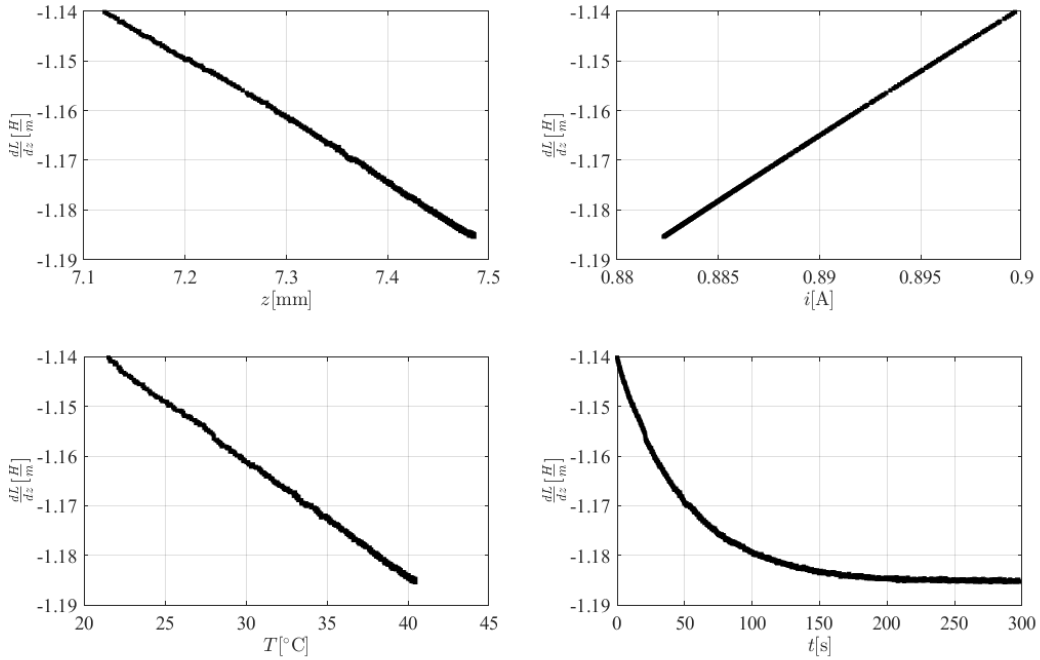

Fig. 3.4. Inductance derivative over axial position in function of different parameters for long-term experiment.

In addition to the inclusion of thermal effects in the magnetic levitation model, dynamic experiments consisting of a temporarily applied zero control were carried out. Changes in the position of the sphere and the settings of P and D were registered for the PD and PID controllers. However, the sphere is not perfect and was often levitated at an angle, making both repeatability and comparison between experiments impossible. Dynamic measurement was reduced to applying zero control at the beginning and end of the long-term experiment. The results were normalized and shown in Figure 3.5. The test was repeated five times with a satisfactory distribution of results in the range of $\pm 5\%$. You can see the influence of temperature on the overshoot value even with a temperature difference of less than 20°C.

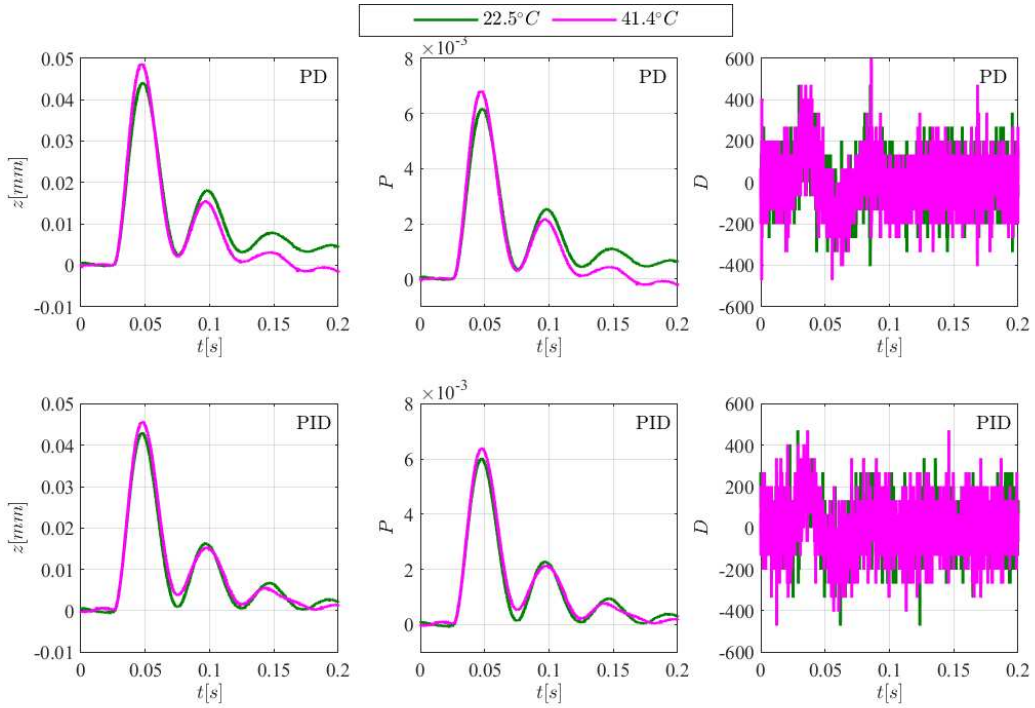

Fig. 3.5. Dynamic experiment with control switch-off for the PD and PID regulator (normalized data).

3.2.3. Mathematical model

The 4th order nonlinear mathematical model of the cylindrical core MLS1EM with the PWM coil current regulator, taking into account the influence of the core temperature, can be expressed by the following set of equations:

$$\begin{cases} \dot{x}_1 = x_2 \\ \dot{x}_2 = \dfrac{1}{2m_s}\left(\dfrac{dL(x_1)}{dx_1}\cdot x_3^2 + F_g\right) \\ \dot{x_3} = \dfrac{R_0(1+\alpha\left[x_3 - T_{ref}\right])x_4^2}{\epsilon} - \lambda(x_3 - T_a) \\ \dot{x_4} = \dfrac{1}{L(x_1)}\left(-\dfrac{dL(x_1)}{dx_1}x_2x_4 - R_0(1+\alpha\left[x_3 - T_{ref}\right])x_4 + u\right) \end{cases} \tag{3.1}$$

where state variables x_1, x_2, x_3, x_4 are, respectively, the axial position and velocity of the sphere, the core temperature and the coil current; F_g - the force of gravity, m_s - mass of the sphere, $L(x_1)$ - inductance versus the position of the sphere, R_0 - resistance of the coil at reference temperature, α - coefficient of linear thermal expansion for the coil, λ - generalized thermal conductivity, ϵ - heat capacity, T_{ref} - reference temperature and T_a - ambient temperature, u - applied control signal. Table 3.1 shows, among others, the key thermal parameters of the prototyped system, which were identified experimentally.

Table 3.1. Parameters of the test stand with cylindrical electromagnet.

Parameter	Symbol	Value
mass of the sphere	m_s	47.0g
total air gap	x_1^t	8mm
resistance of the coil	R	4.57Ω
coefficient of linear thermal expansion	α	0.0049K^{-1}
generalized thermal conductivity	λ	5.3830·10^{-4}
heat capacity	ϵ	402.66JK^{-1}

The proposed model (3.1) showed convergence in the vicinity of the operating point assumed at x_1 = 6.5 mm, x_2 = 0 m/s, x_3 = 25°C, x_4 = 1 A. The experiments carried out led to a discussion on the influence of temperature on the inductance of the electromagnet and the dynamics of AMS. However, the inability to ensure a constant position of the sphere without skewing it during levitation and the related measurement uncertainties of the distance sensor mounted below the sphere and the magnetic field sensors in the electromagnet housing caused the decision to continue further research on the E-shaped electromagnet from the test stand described in Chapter 2. As part of these studies, the MAGLERS team developed the 5$^{\text{th}}$ order nonlinear mathematical model with an additional state variable, which is the coil temperature. A detailed description of this research will be published in an upcoming paper.

Summary of results

During the experiments, the effect of temperature on the control and magnetic field distribution in the cylindrical core MLS1EM was observed. The chapter focused on descriptions of thermal effects in an active magnetic suspension with a cylindrical actuator and a levitating sphere stabilized by a PD and PID controller. The conducted long-term experiments, in addition to expected conclusions about the thermal design of the actuator, demonstrated the influence of temperature on the AMS regulator. The mathematical model of AMS extended by heat transfer allows for the synthesis of a thermally robust controller. Understanding the influence of temperature on the dynamics of the designed system in connection with its geometry and electromagnet parameters provides important suggestions for improvements at the actuator design stage. The quality of the magnetic levitation system can be influenced not only by external disturbances, such as forced vibrations or physical phenomena, such as heat transfer, but also by the selection of the material and geometry of the core.

Chapter 4

Porous core electromagnet design for levitation applications

A concept of electromagnet with the porous core is studied. The form of the electromagnet core was prepared by 3D printing. The core was manufactured manually using iron filings mixed with epoxy resin and left to dry at ambient temperature and air pressure. The aim of this chapter is to provide an initial analysis of the proposed powder core together with the prototyping procedure, by using a finite element method and to compare these results with experimental measurements of the manually manufactured electromagnet. The material property of the numerical model was adjusted to fit the experimental results. Finally, the electromagnet was tested in the levitation real–time experiment.

4.1. Powder core concept

The motivation behind the idea of a porous core was an attempt to propose a novel electromagnetic core configuration applied to active magnetic levitation systems and other devices, where the driven magnetic field provides a source of electromagnetic force. The method of automatic design approach developed for magnetic bearing [24] allows one to generate an optional shape of the magnetic bearing stator, including optimally contoured pole shoes, to maximize the electromagnetic force and minimize the value of magnetic flux density at the corners of the stator. The manufacture of such bearings is restricted due to a technological process, which may be carried out using cutting methods of the laminated electrical steel sheets. Powder cores, which are compacted from resin coated powder, are an excellent solution for high-frequency applications with the objective of downsizing. As the idea of renewable sources and clean energy is promoted, there is a strong need to increase the efficiency of electromagnetic converters and actuators. Development of powder cores tends toward better magnetic properties in a wide range of frequencies and allows for shape of the core geometry during the manufacturing process. The magnetic core is an essential electromagnetic conversion part, which needs to provide sustainable operation. The soft magnetic powder cores have a higher magnetic flux density and lower core losses. Recently, a great

deal of research has been aimed at the development of new soft magnetic materials, which are widely used in alternating current (AC) and direct current (DC) motor applications. Sufficient high-frequency magnetic properties and low eddy current losses cause these materials to have superior advantages [71]. In other applications, to prepare the NiCuZn ferrite core, a gel casting procedure was applied [72]. Using this method, it is possible to magnify the permeability value, which improves the magnetic properties of the core. Soft magnetic composites also match new trends in motor applications [73]. It is a forthcoming evolution in powder metallurgy, which may be noticed to be popular in the automotive industry and electrical appliances. However, these materials often require special heat treatment or a sintering procedure. A specified coat for a composite must also be used. Such a procedure includes pressing and forming a powder with a given insulation shell. This modification of the magnetic composition has been shown to lead to substantially more efficient results during its operation [74]. With this research, the manufacturing of the electromagnet will be done manually.

4.1.1. Design and manufacturing of porous core

An attempt was made to develop the core of an electromagnetic actuator using iron filings. Being aware of the lack of specialized equipment to produce a composite with distributed air gaps, characterized by relatively high relative permeability compared to professionally produced powder cores, the author decided to develop and verify the method of producing the core for the electromagnetic actuator. The research involved the use of 3D printing technology to develop the mold. Figure 4.1b shows the cross section of the core and the 3D design of the electromagnet. To obtain an electromagnet, it is necessary to design a winding. For this purpose, 3D printing technology was reused and a bobbin was designed, which consists of two parts screwed together, as shown in Fig. 4.1e.

Table 4.1. Parameters of the manufactured powder core electromagnet.

Parameter	Symbol	Value
mass of the iron filings	m_f	142.0g
density of the iron filings	ρ_f	7.15g/cm^3
mass of the solid iron core	m_s	189.8g
diameter of the coil wire	d_w	0.5mm
number of coil turns	N_T	465
resistance of the coil	R	3.2Ω
inductance of the coil at $z \to \infty$	L_0	6.04mH
relative permeability of the core	μ_r	9.1

The proposed electromagnet model is cylindrical in shape with a powder core placed from the bottom side in a housing, which is made of ABS[1]. From the top side there is a multi-turn circular coil with 465 turns and a diameter of single enamelled wire equal to 0.5 mm. The powder core was made of iron filings combined with a two-component glue. The core and winding were prepared manually. An amount of 142 g of iron filings was mixed with pre-prepared two-component adhesive and then filled

[1] Acrylonitrile butadiene styrene, a common thermoplastic polymer used in 3D printing technology.

into the core mold by manually compressing the material. The upper surface was then aligned with the edge of the mold. The core was cured at room temperature for 24 hours. The bobbin was assembled and the coil was manually wounded, using a glue to join the winding layers. The final result is presented in Fig. 4.1c. Configuration details are listed in Tab. 4.1.

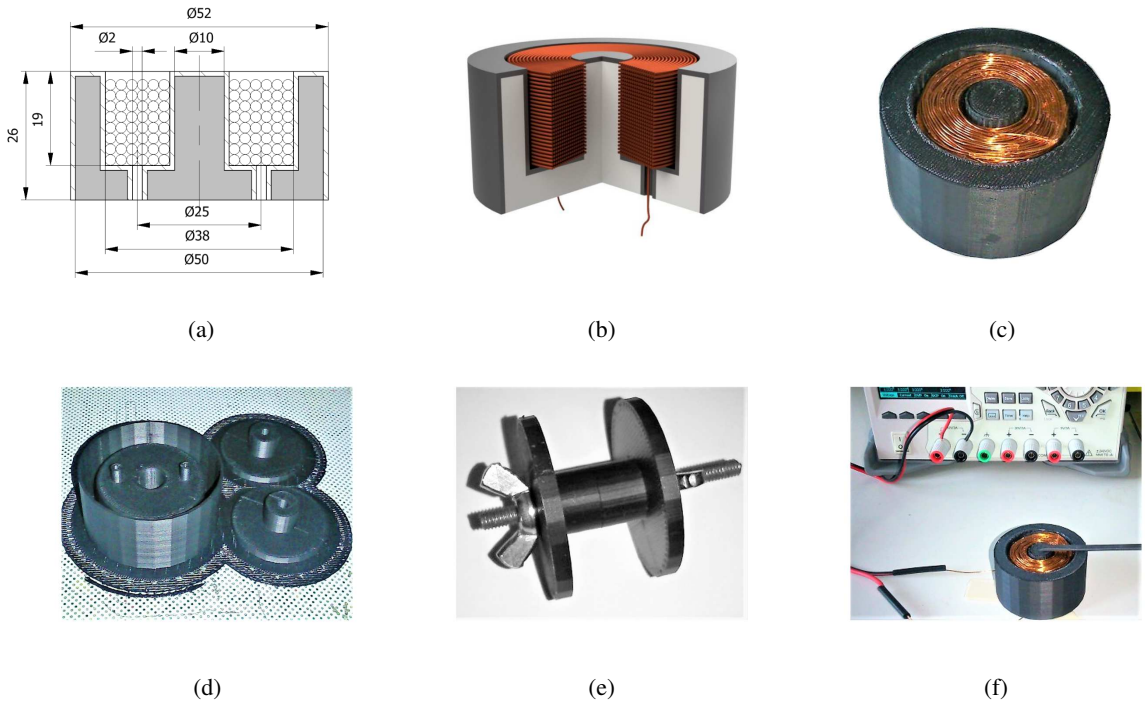

Fig. 4.1. Design and manufacturing of a powder core using a non-industrial method for preliminary tests.

4.1.2. Identification and experimental validation of porous core

In order to identify the electromagnetic actuator, the adjustable power supply RIGOL DP832 was used, with a current limit set to 3 A, a maximum voltage of 12 V, and a regulated current that feeds the electromagnet. Research has also been carried out with the use of SMS-102 magnetic field sensors. The thickness of the probe is 1.2 mm plus the thickness of the insulating casing; therefore, the exact location of the Hall sensor that measures the magnetic field is subject to a position error of ± 0.6 mm. When the probe touches the electromagnet, the total distance between the Hall probe and the porous core is approximately 2.6 mm$\pm$0.6 mm (see Fig. 4.1f). Therefore, the magnetic flux density measurement can vary with respect to the real value. Two sets of measurements have been performed to determine the magnetic flux density as a function of the control and the distance from the electromagnet.

In the first case, the magnetic flux density was examined with respect to the coil current (see Fig. 4.2a). As a result of the heat generated, the first set of measurements was terminated. The conclusion is clear that due to constructional aspects, the winding must be designed with a temperature excess in relation to the desired operational point (see Chapter 3). In the second set of measurements, the power supply was turned on for the long term. The current was set to 1 A. The nominal temperature of the operating mode was reached. The distribution of the magnetic flux density as a function of position was

examined (see Fig. 4.2b) by using a robotized setup for magnetic field investigation [46]. The supply voltage was set in the range 0-4 V with a resolution of 0.1 V. The coil current was measured using a built-in power supply current sensor. The selected results are summarized in the Tab. 4.2. The magnetic flux density was measured in the axial direction. One can find that the characteristic can be approximated by linear function:

$$B_z(i) = 22.8548i + 0.0968 \tag{4.1}$$

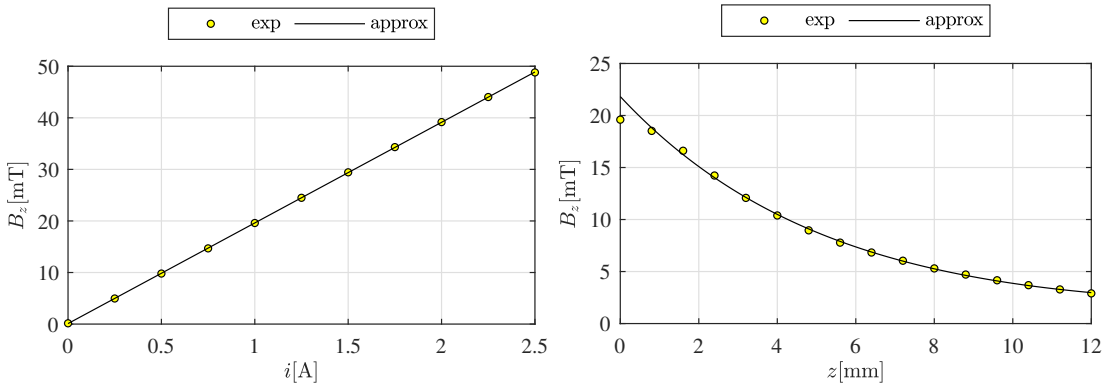

(a) (b)

Fig. 4.2. Magnetic flux density versus: (a) current and (b)position.

The second set of measurements presents the magnetic flux density in the z axis for the variable distance between the magnetic sensor probe and the surface of the electromagnet. The fitted curve results in root mean square error (RMSE) equal to 0.1744 and 0.9990 goodness of fit.

$$B_z(z) = 21.65\exp^{-0.1876z} + 0.1694\exp^{0.1174z} \tag{4.2}$$

The characteristics 4.1 and 4.2 are expressed in units as in Fig. 4.2.

Table 4.2. Magnetic flux density for: (a) different current and (b) position values.

(a)

u[V]	i[A]	p[W]	B_z[mT]
0	0	0	0.06
0.5	0.16	0.080	3.72
1.0	0.32	0.320	7.37
1.5	0.48	0.720	11.01
2.0	0.63	1.260	14.52
2.5	0.77	1.925	18.05
3.0	0.91	2.721	20.98
3.5	1.03	3.595	23.76
4.0	1.13	4.509	25.76

(b)

M5 pitch	z[mm]	B_z[mT]
0	0	19.60
1	0.8	18.52
2	1.6	16.61
3	2.4	14.23
4	3.2	12.08
6	4.8	8.96
8	6.4	6.83
10	8.0	5.30
12	9.6	4.16

4.2. Modeling powder core electromagnet

Numerical model

Designing electromagnetic actuators for their application in target devices, formulation of mathematical models and control syntheses requires the development of their numerical model. This model is subject to simulation research and the so-called virtual prototype. The actuator model was developed in the COMSOL Multiphysics program. The core of the electromagnet is the geometry of the inside of the mold, and the winding is modeled as a ring with radii: 8 mm, 17.5 mm and 16 mm height. The purpose of the modeling is to determine the parameter that will represent the magnetic properties of the material. Two models have been prepared, without and with the metal sphere (Fig. 4.3). The first describes the magnetic flux distribution in the magnetic circuit of the proposed electromagnet and the second represents the experimental investigation stage (see Chapter 2) of the operation mode of the magnetic levitation test rig.

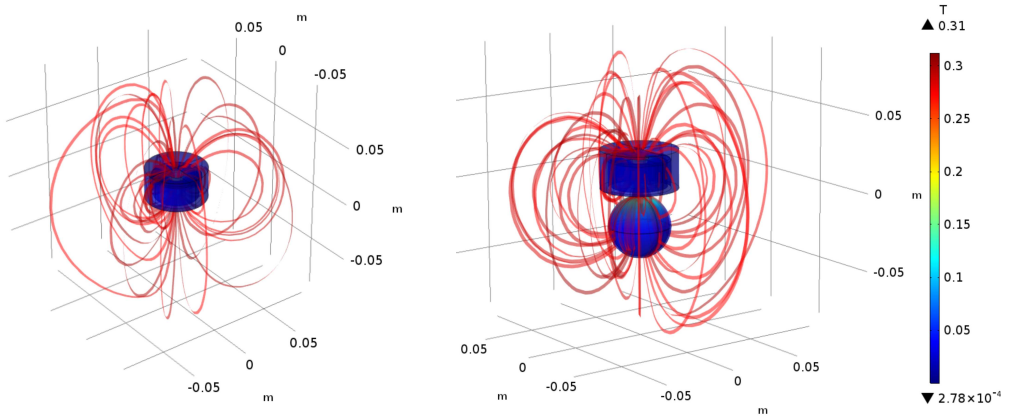

(a) (b)

Fig. 4.3. The numerical model of an electromagnetic actuator with visualization of the normalized magnetic flux density and its streamlines for electromagnet: (a) without and (b) with metal sphere located at distance 5 mm and coil current 2 A.

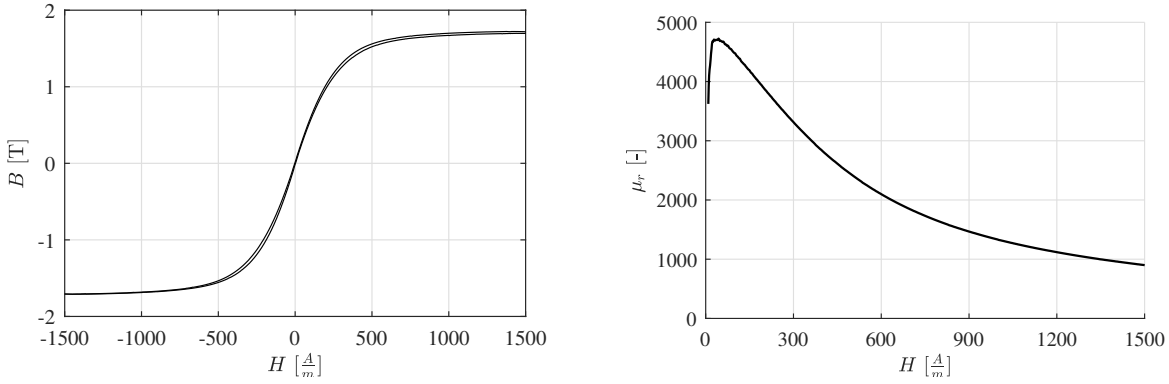

(a) (b)

Fig. 4.4. Measured magnetization characteristics of iron filing sample (cf. section 7.5): (a) hysteresis loop B-H, (b) relative permeability μ_r.

Figure 4.4 provides the magnetic properties of the iron filings. The details of the measurement method are discussed in section 7.5 related to the material properties in numerical modeling of 6pAAMB. The properties of the fabricated core are unknown. To fit the simulation data with the experiments, the relative permeability of the core was adjusted. The goal was to minimize RMSE in the optimization procedure to fit the model output to the measurement data. The final value is 9.1. The characteristics obtained via a parametric solution of the time-invariant numerical model resulted in stationary characteristics of the magnetic flux density. Two models with different mesh density were considered and computed (see Fig. 4.5a): normal mesh (n.m.), extra fine mesh (e.f.m.). The simulation data were approximated by linear functions given in the form of (4.3) and (4.4). When comparing the experimental and simulation results, the error plot was presented, Fig. 4.5b. The simulation results are sensitive to the chosen mesh density.

$$B_{zn.m.}(i) = 23.0682i \tag{4.3}$$

$$B_{zie.f.m.}(i) = 22.6741i \tag{4.4}$$

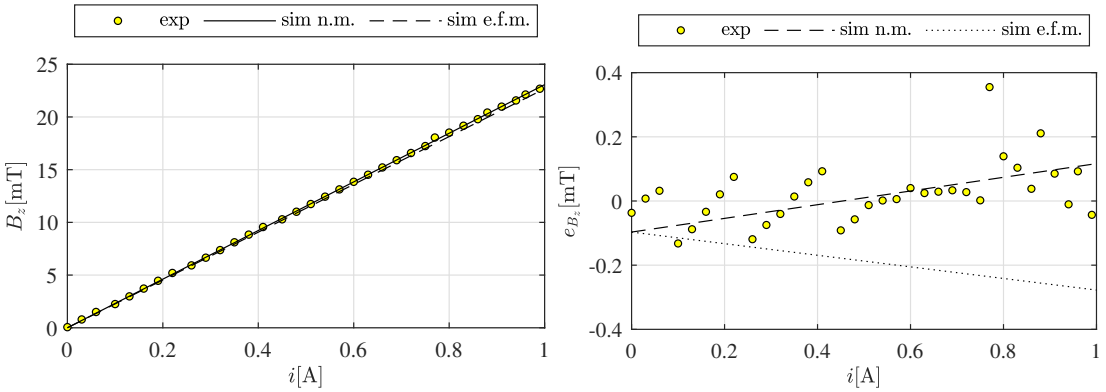

(a) (b)

Fig. 4.5. Magnetic flux density versus current: experimental and simulation results (a), difference between them for variable mesh resolution (b).

Equations (4.5) show the formulas for the errors between the particular characteristics of Fig. 4.5b. It has been shown that the type of selected mesh and its parameters influence the simulation results.

$$\begin{aligned} e_{exp}(i) &= B_z^{exp} - B_z \\ e_{n.m.}(i) &= B_z^{n.m.} - B_z \\ e_{e.f.m.}(i) &= B_z^{e.f.m.} - B_z \end{aligned} \tag{4.5}$$

where: e_{exp} - difference between measured data and approximation, $e_{n.m.}$ - difference between data obtained from numerical normal mesh discretization and approximation, $e_{e.f.m.}$ - difference between data obtained from numerical extra fine mesh discretization and approximation.

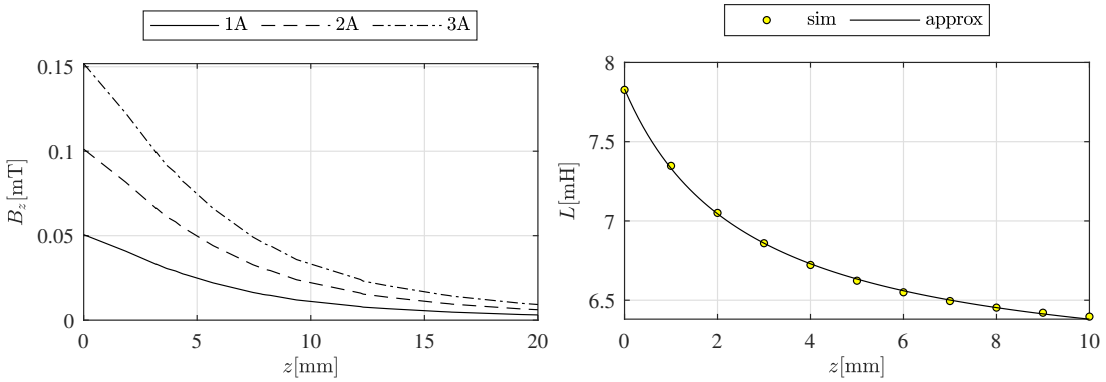

(a) (b)

Fig. 4.6. Magnetic flux density with the sphere versus position, for different current values (a) and inductance versus sphere's position (b).

Levitation

Finally, MLS1EM [45] was upgraded with the manufactured core to perform a control task. The AAMB system can be controlled by a computer with MATLAB/Simulink supported by the real-time kernel or PAC that runs the control algorithm in a hardware layer. The 18.6 g ferromagnetic sphere with a diameter of 20 mm was set in levitation mode at a distance of 5 mm. The discrete in time controller (K_1=1400, K_2=1000) in the form (4.6) drives the PWM duty of the 10 kHz signal in sample k to control the electromagnet with a coil current i_0 = 2.38 A to stabilize the sphere with a sampling frequency of 1 kHz, minimizing the error $e(k) = x(k) - x_0$.

$$u(k) = u_0(k) + K_1 e(k) - K_2 e(k-1) \tag{4.6}$$

Summary of results

An original method for rapid prototyping of the powder core AAMB was discussed. Powder cores eliminate the influence of eddy currents and are generally used in high-frequency applications. The manufactured electromagnet did not meet the expected requirements. The relative magnetic permeability was 9.1, more than 100 times less than the saturated iron filings alone. The inductance of the core without the armature is 6.04 mH and is more than 12 times lower compared to that of the twin electromagnet with a solid core, which operates at 0.5 A under the same conditions. Although the idea of using 3D printing technology to obtain a core mold is justified, the powder core requires different material and technological solutions. The efficiency of its magnetic circuit depends on the degree of packing of the iron filings and the type of bonding agent. The lack of access to industrial facilities that enable the powder core manufacturing process to be optimized prompts the author to continue searching for energy-optimized solutions. The answer may be the zero-power control of magnetic levitation that uses PMs and electromagnets.

Chapter 5

Hybrid axial active magnetic bearing

This chapter presents the concept, design, model and prototype of the hybrid axial magnetic bearing. The numerical model developed in COMSOL Multiphysics was analyzed. The manufactured stator and rotor were tested on a laboratory test rig.

5.1. Design

To achieve full rotor levitation, in addition to the radial magnetic bearing, the axial bearing must be applied. Both functions, which are performed by thrust and journal bearings, can be integrated into a single machine. Novel structures of PMs-biased AMBs are widely used in flywheels and aerospace systems [75]–[77]. High-speed machinery especially requires the design of the structure and optimization of thrust magnetic bearings for its applications [78]. In [21] basic characteristics of an active thrust magnetic bearing with a cylindrical rotor may be found. HAMB with gimballing control ability for the momentum flywheel is presented in [79]. For the radial design [80] a comparison of two simulation models developed for the transient states of hybrid magnetic bearings is provided.

This chapter is focused on the hybrid axial magnetic bearing analysis carried out based on two-dimensional (2D) axisymmetric model in COMSOL Multiphysics. The motivation for HAMB design was the test stand with flexible shaft and radial bearing (see Chapter 9). This configuration assumed a vertically oriented rotor-shaft assembly. In that case, the axial magnetic bearing should have the ability to compensate for the gravitational force acting on the rotor. In the proposed solution, PMs were used to introduce the bias flux. The structure of HAMB was limited by the dimensions and layout of the existing test stand housing. A measuring path was provided for the proximity sensors.The magnetic circuit of the proposed configuration should support the self-centering of the disc. Figure 5.1a presents the 3D model of HAMB. The design includes two actuators, which operate in differential mode. The armature, in the form of a disc (Fig. 5.1b), is placed inside them, with an air gap equal to 500 μm on each side. Ring-shaped PMs, placed both in the actuators and in the disc, provide bias flux.

Table 5.1. Parameters of NdFeB PMs and the electromagnet.

Parameter	Symbol	Value
inner magnet diameter	D_{in}	16mm
outer magnet diameter	D_{out}	32mm
magnet height	h	3mm
remanent induction	B_r	1.21T
maximum load	L_{max}	8.6kg
number of coil turns	N_T	125
resistance of the coil	R	2.9Ω
inductance of the coil at $z \to \infty$	L_0	3.96mH

The designed actuator contains PMs and the electromagnet in the form of a circular coil[1] wound around the stator (Fig. 5.1b). The coil consists of 125 turns of cooper wire with enameled diameter equal to 0.5 mm.

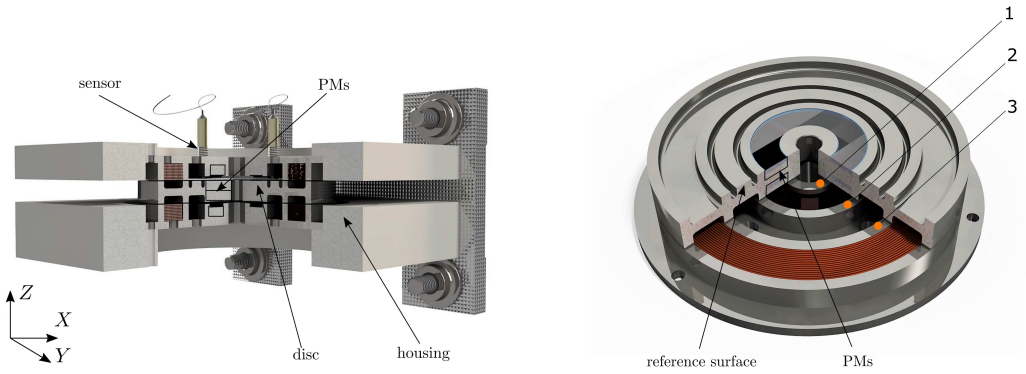

(a) (b)

Fig. 5.1. 3D CAD of HAMB (three–quarters view)(a); the HAMB disc and actuator with measuring points (b).

5.2. Numerical model

Characteristics of the normal magnetic induction vector and the electromagnetic force acting on the disc as a function of position and current (with the top HAMB actuator) were provided from simulation, using finite element analysis in COMSOL Multiphysics. The simulation model was 2D axisymmetric to reduce computational time. Meshing was extremely fine, with a maximum element size of 0.25 mm. The complete mesh consists of 90330 domain elements and 2741 boundary elements. Structural steel was assigned as a material to the stator and disc. The relative permeability was set to 500. Stationary simulation with parametric sweep was performed. First, a single bottom actuator was simulated to identify and compare with the real experiment. Then the entire HAMB was simulated and the magnetic

[1]The inductance of the coil without armature was calculated from the total magnetic energy excluding PMs. Technical details are listed in Table 5.1. For a current of 3 A, the total magnetic energy of HAMB without the disc is 0.39 J, with a corresponding inductance of 87.3 mH.

field distribution with the net force characteristic was obtained (Fig. 5.2). In case of 1. (Fig. 5.4d) and 2. (Fig. 5.4e) measuring point, the simulation returns characteristics of magnetic induction that are similar to each other for different current values. For a single actuator without disc, the electromagnet has negligible influence on the flux provided by PMs. A position equal to 0 mm denotes the disc surface for the corresponding points depicted in Figure 5.1b. Figure 5.2a presents the net electromagnetic force acting on the disc in HAMB. The characteristic of the force provided by PMs may be approximated by a linear function. For the same air gap on each side of the disc, HAMB generates a force of 20 N, which compensates the gravitational force of the disc. When both electromagnets operate in differential mode, the net force adopts a linear characteristic in the range of 0.3 to 0.7 mm.

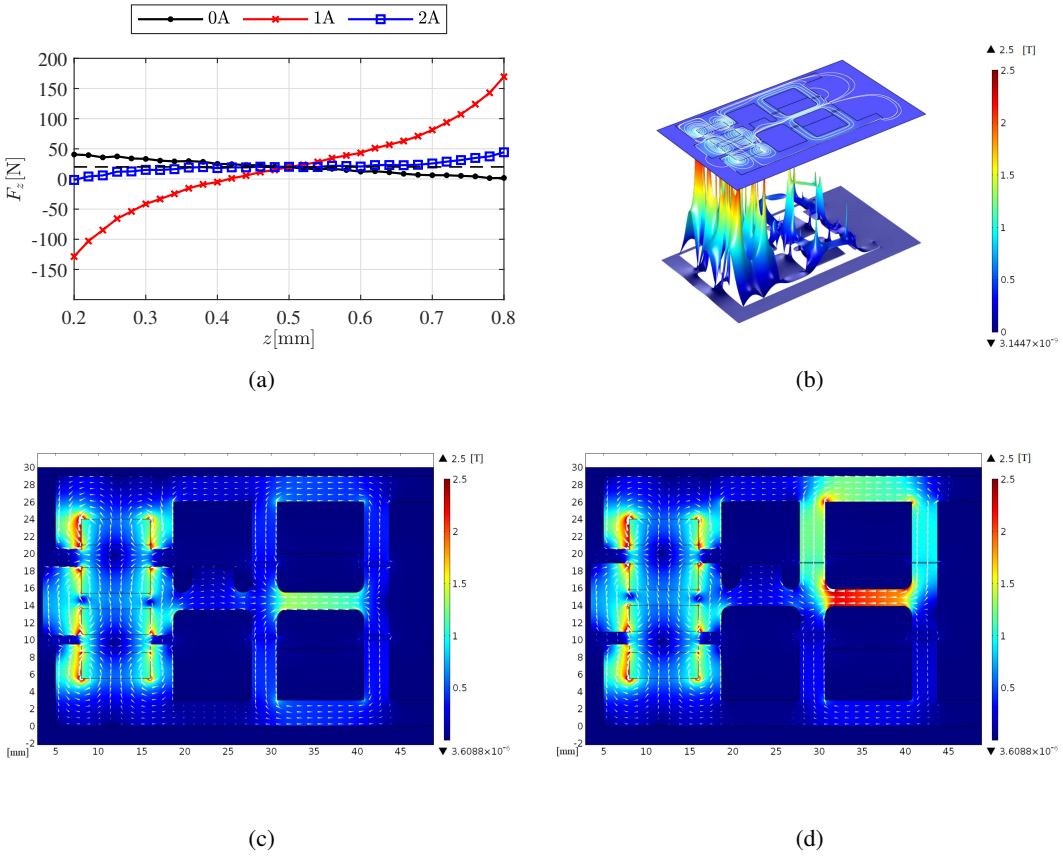

Fig. 5.2. Net electromagnetic force acting on the disc with both actuators operate in differential mode, driven by the same current with 1 mm total air gap (a); magnetic induction distribution: height representation (b); disc in the air gap midspan, both actuators driven by 2 A current (c); disc almost sticked to the top electromagnet (0.1 mm air gap), both actuators driven by 2 A current (d).

5.3. Prototype

The manufactured HAMB consists of two actuators and the disc with PMs. Structural steel S355JR was used. The upper and lower actuators differ from each other in height of the stator part, which surrounds PMs. This solution enables the initial force to compensate for gravity. The measurement system consists of four position sensors EX-201 from KEYENCE (located in the mounting holes of the upper

actuator), with sensor head diameter equal to 5.4 mm, measurement range from 0 to 1 mm, analog output from 0 to 10 V and frequency response up to 18 kHz. Fusion of these sensors allows one to obtain a complete observation of the disc. The reference surface (indicated in Fig. 5.1b) with a width equal to 5 mm can be shifted when the disc is wobbling. This may lead to measurement errors. HAMB geometry should support disc centering in the bearing space, thus a radial magnetic bearing can be favorably miniaturized. The system is mounted on 40x40 aluminum Bosch Rexrot profiles. The disc is connected to a long flexible shaft by a pressed fit.

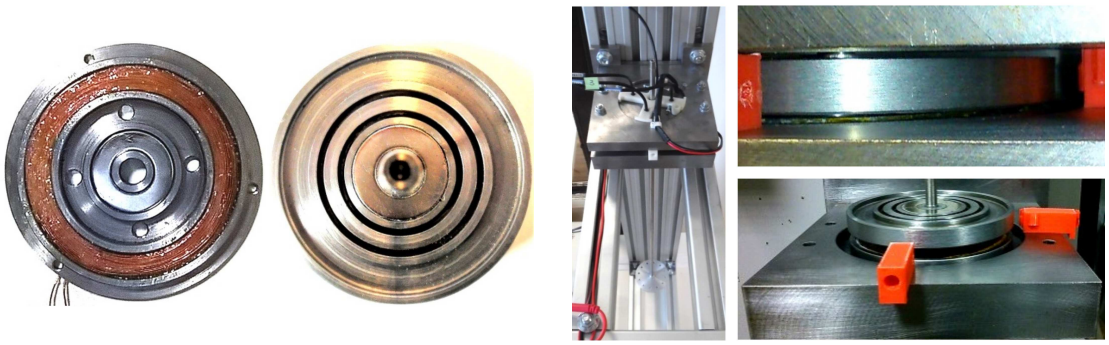

(a) (b)

Fig. 5.3. Manufactured HAMB upper actuator and disc (a); assembled laboratory HAMB test rig with disc located between both actuators (b).

5.4. Identification and experiments

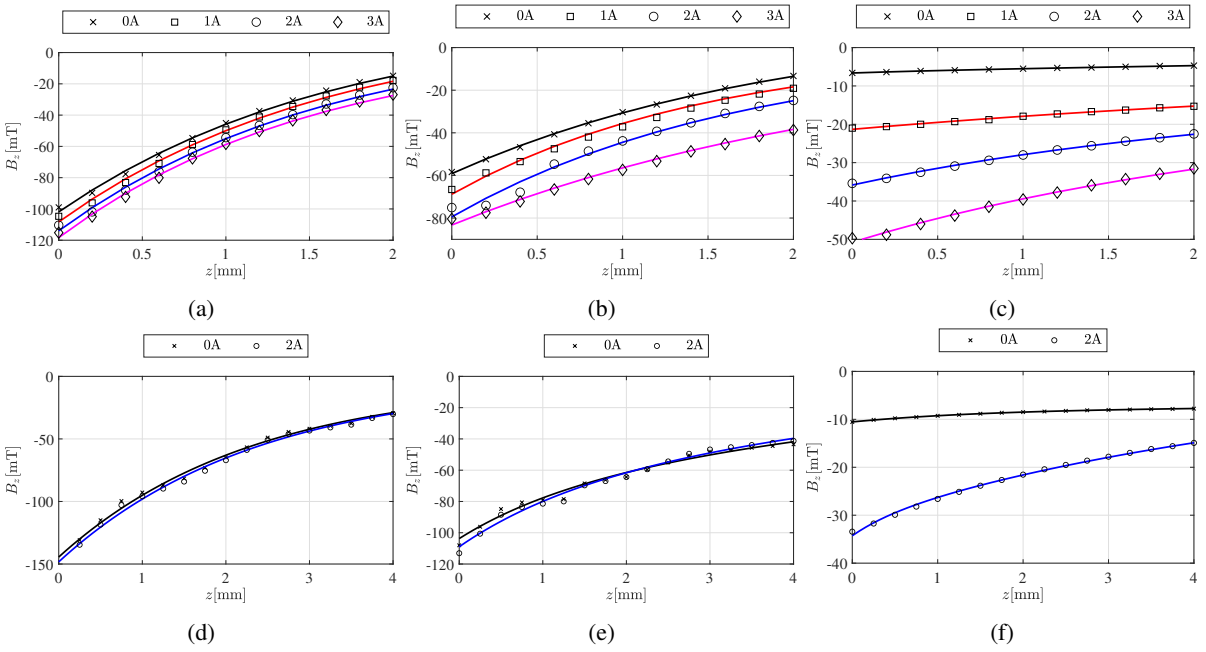

Fig. 5.4. Magnetic induction versus position with various current values for, respectively, 1st(a,d), 2nd(b,e), 3rd(c,f) measuring point; experimental data (a-c), simulation (d-f).

Magnetic induction versus position and current was measured using the SMS-102 ASONIK hall effect meter (Fig. 5.5). To determine the current characteristic, the RIGOL DP832 adjustable power supply was used, with the current limit set to 3 A, which feeds the electromagnet. Magnetic induction measurements were performed with the use of the robotized setup for magnetic field investigation [46]. Characteristics show a trend comparable to simulations; however, it is visible that the magnetic field of the electromagnet influences the magnetic field around PMs (Figs. 5.4a, 5.4a), which was not demonstrated in simulations. The third measuring point of the bottom actuator returns similar results from a real experiment and simulation. The teslameter probe has a thickness of 2.4 mm and may introduce errors resulting from measurement inaccuracy. The current characteristic is linear, without offset and with a coefficient between current and voltage equal to 0.3658 A/V. The control system is a differential PID regulator. The error is the difference between the desired and measured values of the position. The aim of this experiment was to check whether the operation of the electromagnet compensates for the disc misalignment, as a result of the lateral forces generated by PMs. The assumption was formulated that the disc will be centered by the forces of electromagnets. The graphs show the behavior of the disc under different conditions, but do not reflect the desired operating mode of the PID regulator, which was manually tuned in that case. Current control was implemented in the HAMB system. This choice deals with issues related to the slow response of the actuator in the voltage-mode control.

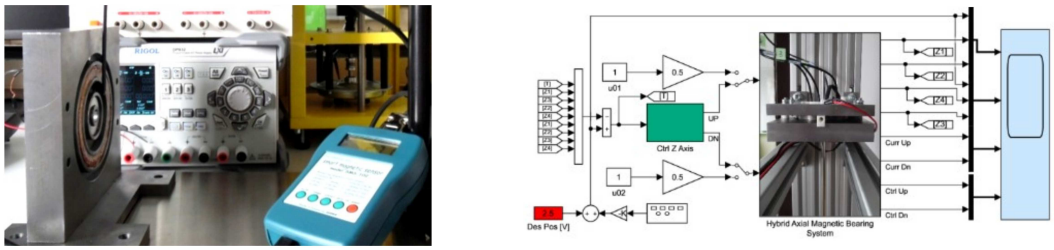

(a) (b)

Fig. 5.5. Measurement of the axial magnetic field in HAMB (a); rapid prototyping of the control system (b).

In Figure 5.6b, in 2.25 s the disc is in the lower electromagnet and a current drop may be observed due to the change in inductance. In Figure 5.6c, when the lower actuator attracted a disc, the algorithm feeds the maximum current to the upper electromagnet. Afterwards, the control algorithm is switched on, the current from the bottom electromagnet drops to 0 A and the upper electromagnet acts on the disc. In Figure 5.6d disc is attracted to the upper electromagnet and then the control algorithm is activated. Four sensors converge to the desired value; the disc is skewed. Next, the power is off, control from the upper electromagnet remains and both currents drop to 0. Despite the lack of power, the disc levitates, lowering its location a bit. Finally, the power is on and both currents reach steady levels. Figures 5.6g-5.6i show waveforms of the position, current and control for sine excitations. Clearly, the disc is skewed and wobbles in the bearing space. The system responds with a phase shift with respect to the control signal.

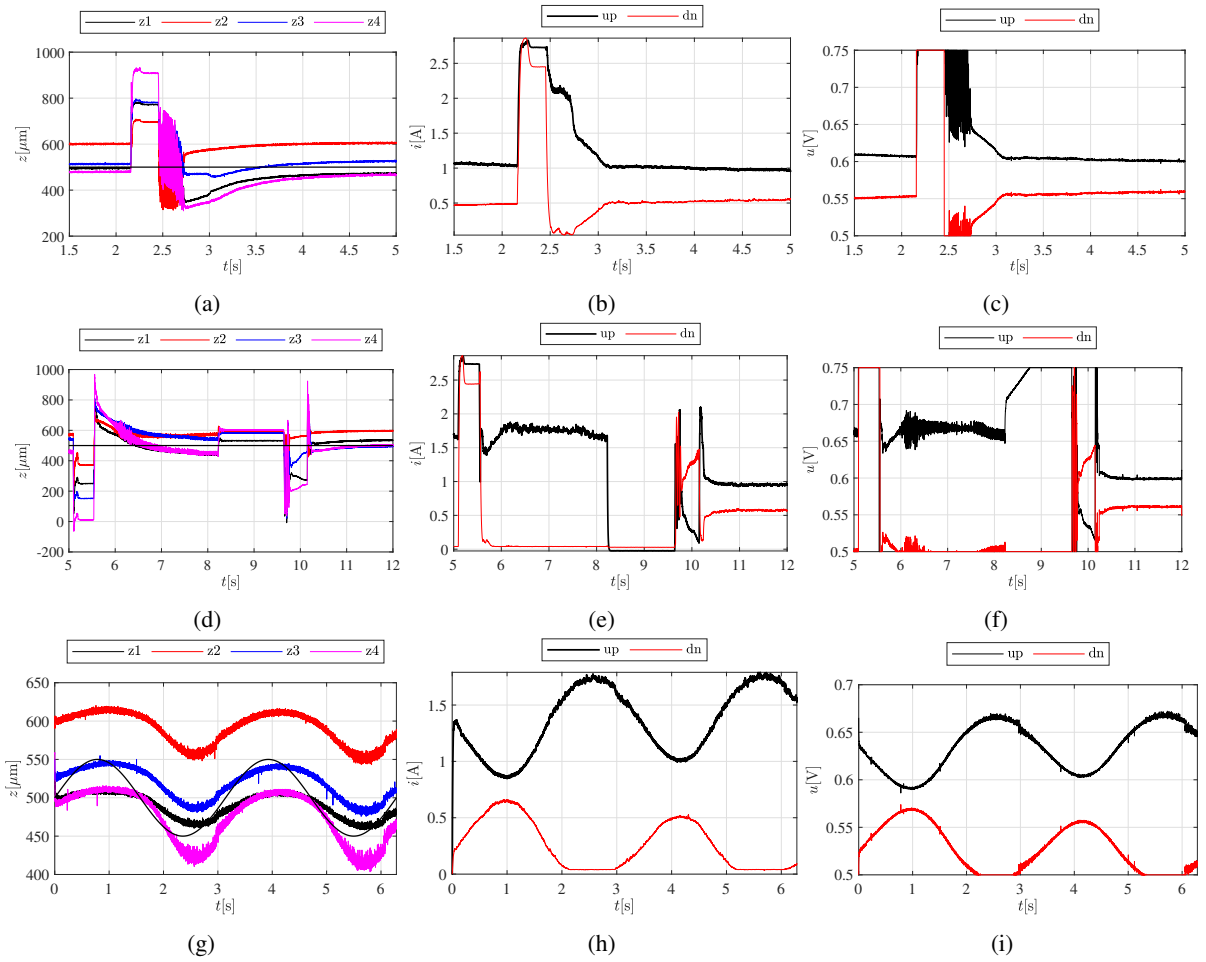

Fig. 5.6. Experimental waveforms: 1st scenario: firstly bottom electromagnet attracted disc, then control algorithm is switched on (a-c); 2nd scenario: firstly top electromagnet attracted disc, then control algorithm is toogled on–off–on (d-f); 3rd scenario: sine excitation (g-i); from the left column, position, current and control signal respectively.

Summary of results

By using the PMs-biased configuration in the implemented concept of AAMB, the power consumption was reduced. At the same time, a significant force from PMs caused frequent skewing of the disc, thus the task of radial stabilization requires the support of a radial active magnetic bearing. The magnetic flux path of HAMB was adjusted to compensate for the gravity load at the desired operating point. Despite the satisfactory convergence of the simulation with the experiment, it is recommended to develop a 3D model for the optimal actuator design due to the limitations of axisymmetric modeling. Finally, HAMB was started with PAC support and MATLAB/Simulink in real-time mode. Lateral forces were not observed in the 2D simulations and the experiment did not confirm the self-centering of the 5-DoF levitating disc. On the basis of experiments, it is suggested to develop a solution with a few controlled axial force components to suppress a tilt motion of the disc.

Chapter 6

Concept of axial active magnetic bearing with six poles

This short chapter introduces the reader to the concept of an axial actuator with a few pole pieces that is capable of axial active levitation with the function of spatial orientation of the rotor in the active bearing space. Rotor tilt angle control allows the rotor plane to remain in the axis in case of a nonuniform load distribution on the surface of the rotor. Below are some novel design solutions for AAMBs.

6.1. The actuator with six cylindrical poles

The axial active magnetic bearing with six cylindrical poles was designed to prevent movement of the shaft in the axial direction. In principle, it has a feature to control disc tilting. The actuator, made of low-carbon steel S355JR with a stator thickness of 4 mm, consists of six poles in the form of pins, each with a height of 6 mm, placed around the circumference every 60°, with circular coils (Fig. 6.1). The electromagnet is created by six coils with windings placed around each pole piece. The set of parameters is given in Table 6.1. The coils can be connected in parallel or in series. In addition, they can be divided into groups, introducing additional components of the axial force to suppress the motion of the disc tilt.

The project concerns an axial active magnetic suspension with a slim and simple design, with the ability to provide a few vectors of electromagnetic force. The idea behind the proposed bearing structure was to introduce an actuator in an axial configuration with many pole pieces, with the possibility of adjusting the rotor tilt angles and with the function of supporting the radial bearing. A major emphasis is placed on AAMB design, identification and utilization for passive hybrid support configurations. The project has the potential to provide the technological basis for the adaptive magnetic suspension of vertical wind turbines and kinetic energy stores with configurable elasticity and damping values. The design of the first prototype assumed a simplified manufacturing process that involved the use of only a lathe.

The two-stage pins are mounted with an interference fit in the stator yoke. There are mounting holes for the connection cables and the rotor axis. The adopted round shape of the bobbins allowed the coils to be manually wound with satisfactory accuracy. In the following chapters, the benefits of the proposed structure and numerous problems resulting from assembly issues will be presented.

Table 6.1. Parameters of the 6pAAMB prototype with cylindrical poles.

Parameter	Symbol	Value
disc mass	m	117g
nominal air gap	z_0	0.5mm
nominal current	i_0	1A
number of turns for a single coil	N_t	50
coil's resistance	R	0.6Ω
actuator's inductance for nominal values	$L(z_0,i_0)$	89.21mH
pole piece cross-section	S	254.5mm^2
average flux path between pole pieces	l	77mm
relative permeability of S355JR steel	μ_r	500

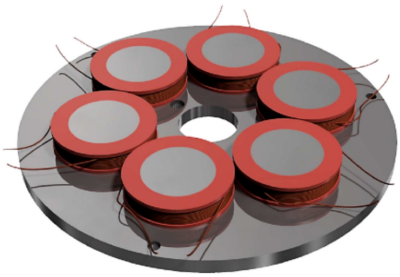

(a) 3D isometric model.

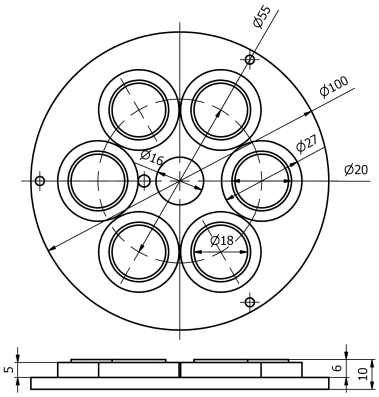

(b) Geometry of the stator.

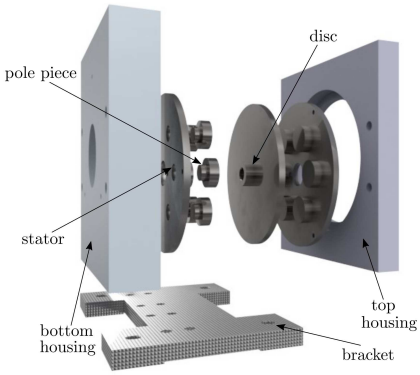

(c) Assembly exploded drawing.

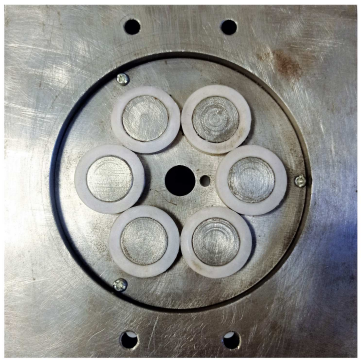

(d) Manufactured stator in housing.

Fig. 6.1. Axial active magnetic bearing prototype with six cylindrical poles.

6.2. The actuator with six trapezoidal-shaped poles

The next version of the actuator prototype introduced a significant change in the form of the trapezoidal shape of the pole pieces (Fig. 6.2). This configuration requires the use of a milling or CNC machine. The advantage is the full use of the stator space, giving the possibility of optimizing the height of the actuator in relation to the previous one with cylindrical pole pieces while maintaining the load capacity. The proposed variant is also distinguished by its modularity. One can assemble an actuator from 3, 4 or 6 pole pieces, implementing selected features for a given application. In addition, a Hall sensor can be placed in the mounting space of the screw, which introduces measurement functionalities.

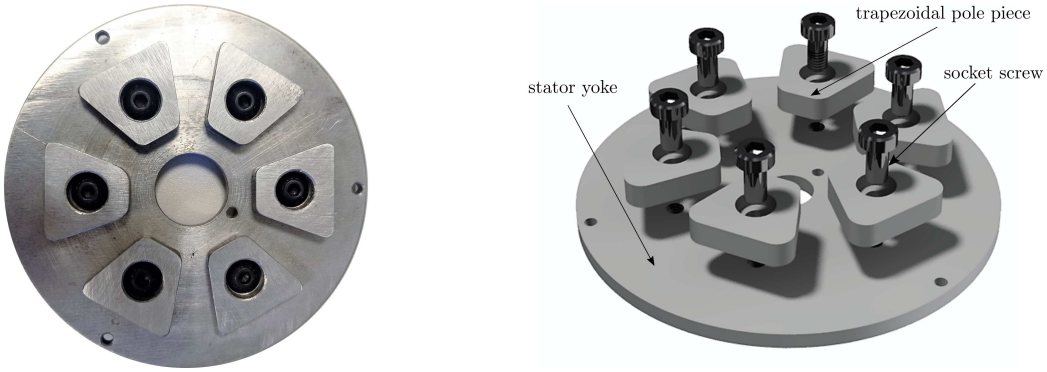

(a) Manufactured stator prototype.

(b) Stator exploded drawing.

Fig. 6.2. Axial active magnetic bearing prototype with six modular trapezoidal-shaped poles (1st iteration).

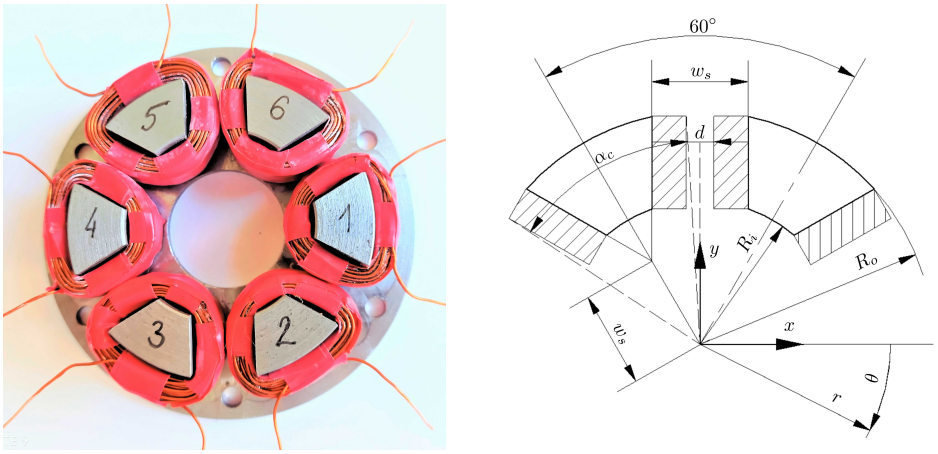

(a) Manufactured stator prototype.

(b) Geometry of the stator.

Fig. 6.3. Axial active magnetic bearing prototype with six trapezoidal-shaped poles (2nd iteration).

The second iteration of this prototype is the single-piece solid core stator (Fig. 6.3a). This version was intended for increased loads with an air gap up to 3 mm. The increased axial clearance allows to demonstrate the key configuration features in case of skewed rotor. In general, the presented actuator has the ability to control the static and dynamic eccentricity of the rotor due to its tilting motion [28]

or misalignment of the montage [81]. The actuator, made of C45 carbon steel with a yoke thickness of 3 mm, consists of six poles, each of 20 mm height, located every 60° on a perimeter (Fig. 6.3b), with coils wounded around them. Three pairs of adjacent concentrated coils alternately polarized make up the electromagnets. The set of parameters is given in Table 6.2. Electromagnets introduce three components of the axial electromagnetic force, controlled separately.

Table 6.2. Parameters of the 6pAAMB prototype with trapezoidal-shaped pole pieces.

Parameter	Symbol	Value
inner pole radius	R_i	21mm
outer pole radius	R_o	34mm
slot opening	w_s	14mm
distance between two coil sides	d	0.5mm
total air gap length	l_{max}	3mm
pole height	h_s	20mm
number of turns in a single coil	N_t	125
current in a k^{th} pair of coils	i_k	[1.00,1.66,2.00]A
slot opening arc segment	w_{so}	$r \cdot \arccos(1 - \frac{w_s^2}{2r^2})$
coil side arc segment[1]	w_c	$0.5 \cdot (w_{so} - d)$
pole arc segment	w_p	$\frac{\pi r}{3} - w_{so}$
coil span angle	α_c	$w_p + 2w_c$
circumferential coordinate	u	$\theta \cdot r$
cartesian coordinate system	(x, y, z)	
cylindrical coordinate system	(r, θ, z)	
nominal air gap	z_0	2.2mm
nominal current	i_0	1A
coil's resistance	R	1.34Ω
actuator's inductance for nominal values[2]	$L(z_0,i_0)$	142.04mH

Summary of results

Novel configurations of electromagnetic actuators for AAMB were presented. A special feature of the described prototypes is six pole pieces that allow for the arrangement of at least three electromagnets generating separate vectors of the axial electromagnetic force. Subsequent chapters include a comprehensive interdisciplinary approach in modeling and identification of the original concept of the six-pole AAMB actuator, hereinafter referred to as 6pAAMB.

[1] It is assumed, that a line segment is close to an arc segment and the difference is negligible (see Fig.6.3).

[2] The inductance in Tab. 6.1, 6.2 was calculated from the numerical model 3D for 1 A nominal current; 6pAAMB with cylindrical pole pieces has inductance of 760.23, 89.21 and 13.72 mH for 0, 0.5 mm and $z \to \infty$ respectively; 6pAAMB with trapezoidal pole pieces has inductance of 16.50 H, 142.04 mH and 79.48 mH for 0, 2.2 mm and $z \to \infty$ respectively.

Chapter 7

Numerical model of axial magnetic bearing with six cylindrical poles

The chapter presents a numerical model of the novel design of the axial magnetic bearing with six cylindrical poles. The motivation behind this idea was to eliminate vibrations in rotating machinery due to axial load. The common conception of such a bearing provides only a single component of the electromagnetic force, which is not enough to reduce the transverse and lateral vibrations of the armature. The proposed design allows us to suppress the tilting of the disc with the use of a few axial force components that are capable of actively compensating the axial load and stabilizing the disc in a balanced position. Before a real device is manufactured, a virtual prototype should be prepared. The accurate numerical model will provide essential knowledge about the performance of the axial magnetic bearing.

7.1. Review of numerical approach in levitation applications

Numerical modeling is commonly used in the design of electromagnetic actuators to optimize their geometry, magnetic circuit or even control system. Numerical programs such as open-source FEMM [82] or licensed COMSOL Multiphysics allow one to develop models, often multiphysics with complex 3D geometry. Simulation engineers strive to prepare the so-called digital twins, virtual prototypes, on which online tests may be carried out without generating a financial burden before the construction of the real prototype. In summary, in the blog article [83] the methods for modeling magnetic bearings in COMSOL Multiphysics are clearly described. The numerical model can also verify experiments carried out in a real system [41], support analytical models [24] or even regulators synthesize for a real-time application [46]. In [84], the unbalanced magnetic pull has been the subject of research. The phenomenon was canceled by applying independent excitation currents to different groups of rotor poles performed on a 12-pole synchronous machine, which was verified numerically. In [85] a very interesting way to include lamination in the stators was presented using a homogenization approach.

Virtually every magnetic levitation system project requires the use of numerical tools at some stage in the design process to streamline the product design and manufacturing process. Radial magnetic bearing models were developed in [86], [87] and [88]. The analysis and design of permanent magnet biased magnetic bearing was carried out in [89], [90] and [91], where a new 5-DoF AC/DC hybrid magnetic bearing was investigated to reduce the volume, weight, manufacturing and operation cost of magnetic suspension motors. In the case of actuators and machines with axial magnetic flux, it is not possible to directly reduce the model to 2D. As a result, a complete 3D model is required, which incurs the costs of computational time and the preparation of an often complicated model. The dynamic characteristics of the asymmetric triaxial magnetic control bearing were described in [92]. Examples of axial actuator modeling can be found in [93], [94] with an optimization procedure or in [95], where a conical passive magnetic bearing of constant stiffness was presented. There are a few tips to keep in mind when modeling magnetic circuits:

1. assume small nonzero air conductivity to avoid creating singular matrix during computing,
2. in time domain, to improve convergence, set the discretization of the magnetic vector potential to linear,
3. remember about the closed current path using appropriate modeling techniques,
4. add air domain around the conductor,
5. use frequency domain in case of periodic signal,
6. ensure current continuity equation in the modelling domain,
7. in case of 3D inductor, the skin effect is included in impedance boundary condition,
8. if skin depth is less than half a thickness of the conductor, consider using a boundary layer mesh,
9. multi-turn coil domain can be used as long as the skin depth is much larger than the wire diameter.

7.2. Numerical model with top electromagnet

In the 3D models designed in COMSOL Multiphysics, the electromagnetic force was calculated, using Maxwell's stress tensor integrated on the exterior surfaces of the selected disc domain. It is the most general method, as it requires an air or vacuum domain around the armature because the Maxwell stress tensor is defined on the boundary of the material and distributed to the determined domain through its structure. This method is also very sensitive to mesh, which should be refined inside and symmetric around the calculated domain.

7.2.1. Disc tilt setting with top electromagnet

The first set of simulations concerns the disc tilt setting with only a single top electromagnet of AAMB, with the constant air gap z equal to 1 mm. The disc was rotated around its two orthogonal axes of the plane, which is perpendicular to the axial direction (see Fig. **??**). Rotation was determined by two angles: α and β, which vary from -0.5° to 0.5°. A 3D vector of the electromagnetic force was obtained (Figs. 7.1, 7.2a).

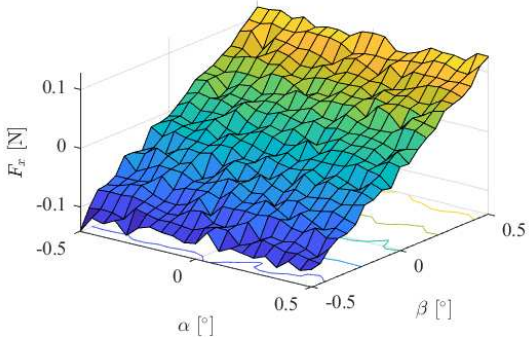

(a) The x component, 2 A current and 1 mm air gap.

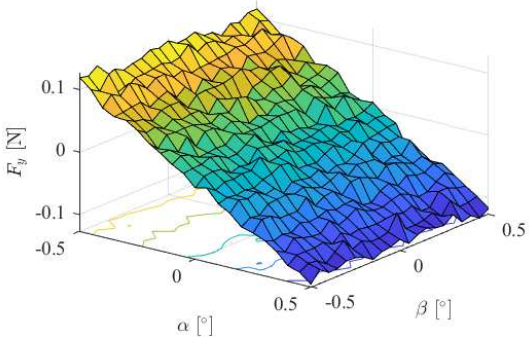

(b) The y component, 2 A current and 1 mm air gap.

Fig. 7.1. The components of electromagnetic force in the $x - y$ plane versus disc tilt angles.

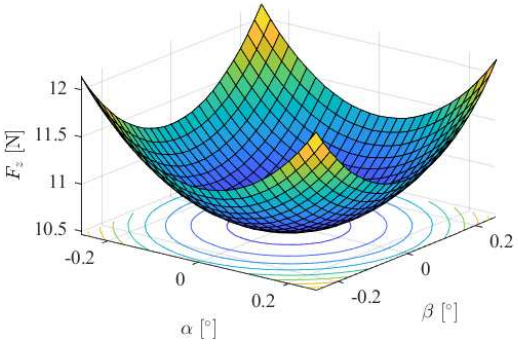

(a) 2 A current and 1 mm air gap.

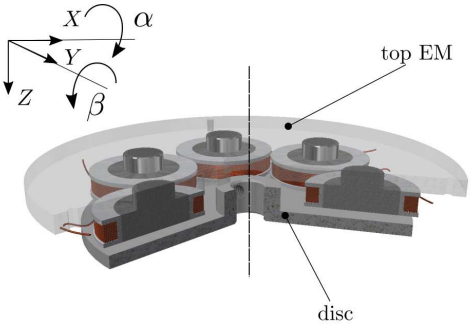

(b) Top electromagnet isometric cross-section.

Fig. 7.2. The axial electromagnetic force versus disc tilting angles (a) and top electromagnet diagram (b).

7.2.2. Axial displacement of disc with top electromagnet

In second set of simulations, the motion of the disc was constrained axially. The total air gap between two AAMBs is 1 mm and the position of the disc in the middle of this distance corresponds to 0.5 mm (Fig. 7.3a). The nonlinear characteristics of the electromagnetic force can be found with respect to the coil current and disc displacement. Analysis of the data obtained allowed us to propose a mathematical function (7.1) corresponding to a fixed coil current.

$$F_z(z) = ae^{bz} + ce^{dz} \tag{7.1}$$

The electromagnetic force versus current (Fig. 7.3b) may be approximated by a second-order polynomial. The coefficients for some disc displacements are presented in Table 7.1.

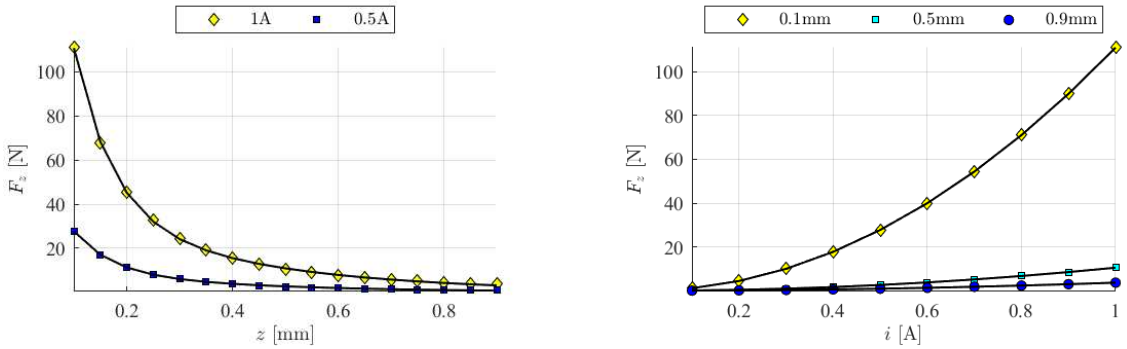

(a) (b)

Fig. 7.3. The axial component of the electromagnetic force F_z in the function of: (a) air gap z and (b) current i.

Table 7.1. Coefficients of approximation functions (Fig. 7.3a) for i = 1 A.

Parameter	a	b	c	d
Value	-297.90	-13750	-47.94	-3021

Table 7.2. Coefficients of approximation function (Fig. 7.3b)

z[mm]	0.1	0.5	0.9
Coefficient pi^2	111	10.51	3.68

Finally, the electromagnetic force can be represented by an analytical monotonic function (see Fig. 7.4a) expressed by the formula below. The coefficients are presented in Table 7.3 with a R^2 error equal to 0.98.

$$F_z(z,i) = ae^{-bz} \cdot i^2 \tag{7.2}$$

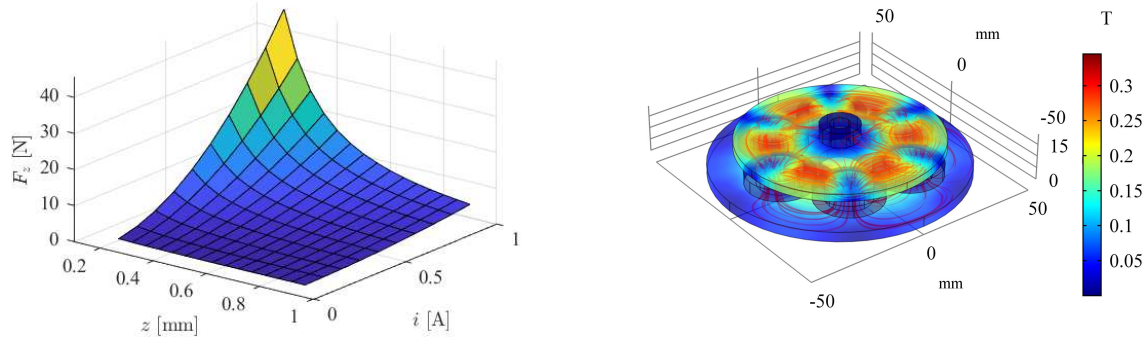

(a) (b)

Fig. 7.4. The electromagnetic force F_z in the function of air gap z and current i (a) and the magnetic field distribution in the disc for z = 500 μm and i = 1 A ($B_{\max}$ = 0.3 T).

Table 7.3. Coefficients of approximation function (Fig. 7.4a)

Parameter	a	b
Value	213.10	-7117

The main parameters determining the behavior of the armature in the magnetic levitation space are the current and displacement stiffness, respectively, k_i and k_z (7.3). Both are crucial in the control system design procedure of magnetic levitation systems (see Fig. 7.5). Fig. 7.6a presents the inductance L in relation to the displacement z. The function is described in equation (7.4).

$$k_i = \frac{\partial F_z(z,i)}{\partial i}, k_z = \frac{\partial F_z(z,i)}{\partial z} \tag{7.3}$$

$$L(z) = ae^{-bz} + c \tag{7.4}$$

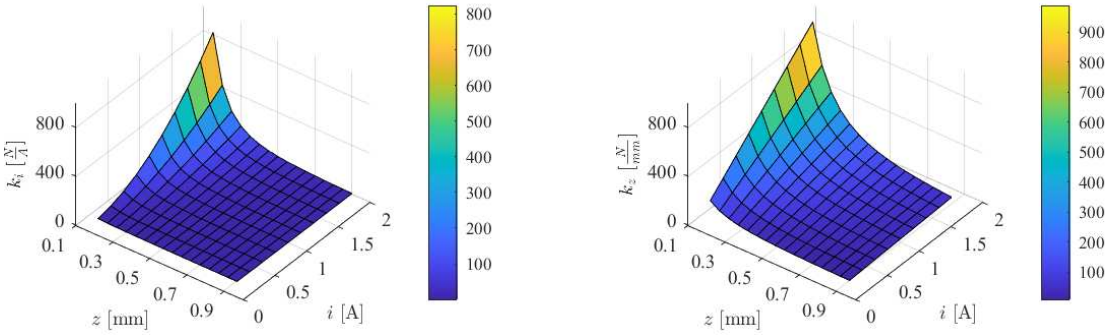

(a) (b)

Fig. 7.5. The current stiffness k_i (a) and displacement stiffness k_i (b) in the function of air gap z and current i.

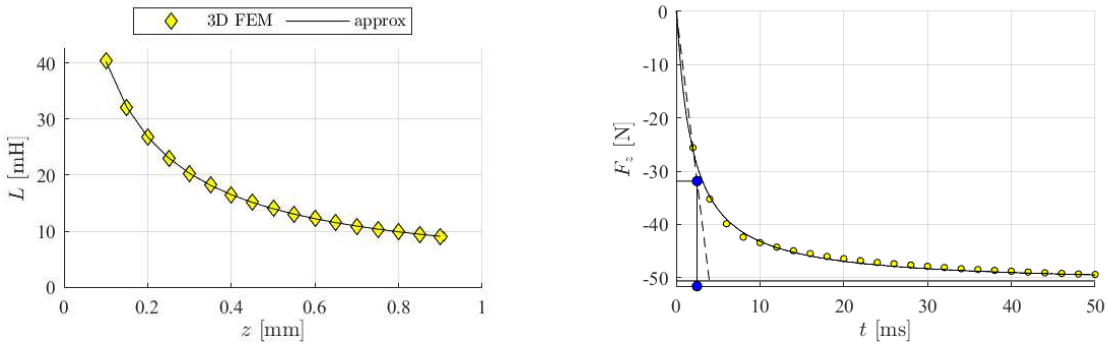

(a) (b)

Fig. 7.6. The electromagnet inductance $L(z)$ (a) and $F_z(t)$ for 1 A current and 0.2 mm air gap (b).

The R^2 error of the approximation (7.4) is equal to 0.996 and the coefficients are as follows: a = 49.29, b = 4.931 and c = 9.24, assuming z in [mm] and $L(z)$ in [mH] (Fig. 7.6a). Figure 7.6b shows a time-domain simulation of the force rise time after a 1 A step current with a 2.5 ms time constant.

7.3. Numerical model with both electromagnets

7.3.1. Disc tilt setting with top and bottom electromagnet

In this analysis, the zero value electromagnetic force is expected. However, because of the selected force calculation method, an outcome is sensitive to discretization of the levitation region. In the case considered, the geometric dimensions of the magnetic bearing structure are significantly larger relative to the air gap. This is often a cause of numerical errors (see Fig. 7.7a-7.7c). In the case of both identical electromagnets, driven by the same current, with the disc located in the middle of the total air gap, all the forces should balance each other (Fig. 7.7d). Figs. 7.7a and 7.7b show the numerical noise, which varies from -0.05 N to 0.05 N for the x and y component of the force. In Fig. 7.7c numerical errors appear for large tilt angles. The reason is the decreasing air gap and nonadaptive mesh, which cause disturbed calculations and convergence difficulties. For a small air gap, the results are uncertain and simulation is time consuming. Table 7.4 presents custom mesh settings. To improve convergence, linear discretization of the magnetic vector potential was selected. The conductivity of the air region was set at 0.1 S/m to avoid singularity error. The magnetic bearing geometry was surrounded by an air sphere with radius of 75 mm.

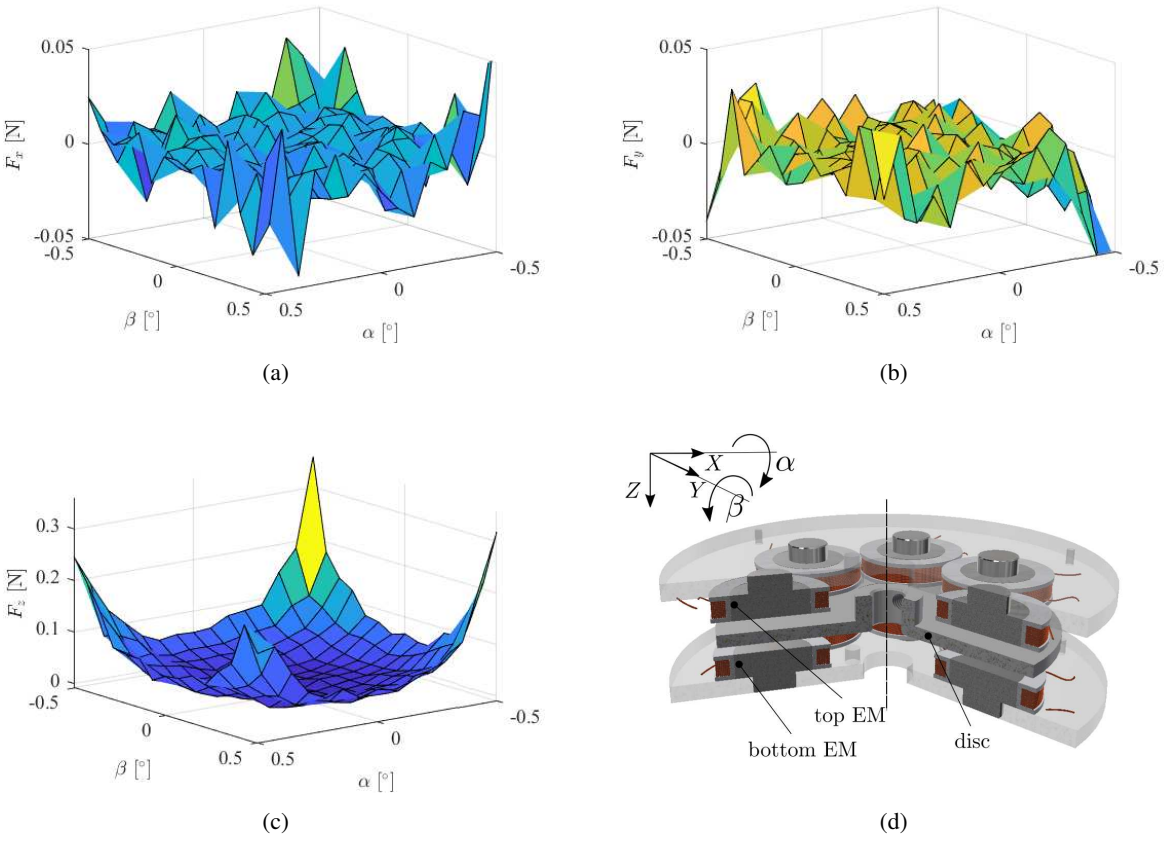

Fig. 7.7. The x (a), y (b) and z (c) component of the electromagnetic force F_z in the function of disc tilting angles, for 1 A current and 0.5 mm air gap on each side of the disc; diagram of the top and bottom electromagnet (d).

Table 7.4. Mesh settings from the 3D numerical model.

Parameter	Value
maximum element size	8.25mm
minimum element size	0.08mm
curvature factor	0.4mm
resolution of narrow regions	0.7
maximum element growth rate	1.4
number of mesh elements	379 412

7.3.2. Axial displacement of disc with top and bottom electromagnet

The retrieved data are well approximated by the functions (7.5,7.6) for the fixed position of the disc.

$$F_z(i) = p_1 i^2 + p_2 \tag{7.5}$$

$$F_z(i) = \frac{p_1 i^2 + p_2}{a e^{bz} + c e^{dz}} \tag{7.6}$$

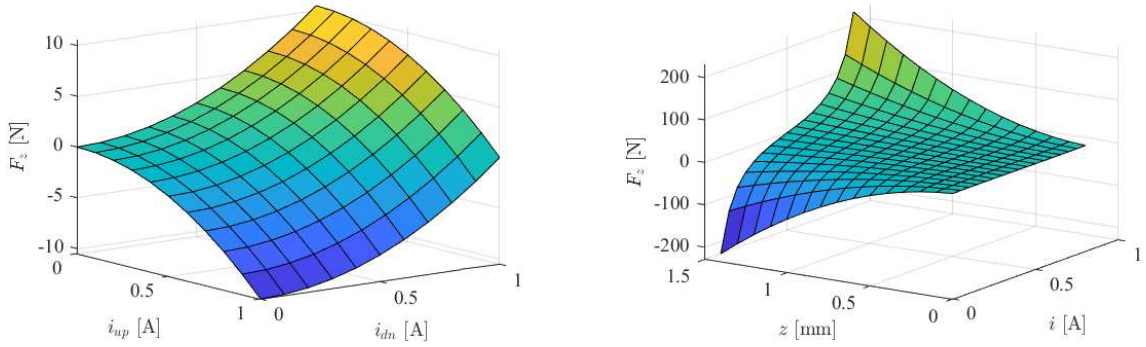

(a) (b)

Fig. 7.8. The axial component of the electromagnetic force F_z versus currents of bottom i_{dn} and top i_{up} electromagnet, for air gap z = 0.5 mm (a); versus air gap z and current i identical for both electromagnets (b).

The axial electromagnetic force (Fig. 7.9a) can be approximated using functions (7.1,7.5). In the subsequent simulation, the bottom electromagnet was powered by a bias current of 0.5 A and the top electromagnet was driven by the sum of a bias current and a load current, which varies from 0 to 1 A. Calculations were performed for a variable location of the disc in the air gap (see Fig. 7.10a). Setting the bias current determines the linearity range of the force (see Fig. 7.10b). Fig. 7.10b shows that the linearity range of the electromagnetic force moves toward the bottom electromagnet and decreases, compared to Fig. 7.9a. The nonlinear force character, hard on the top electromagnet, occurs for larger values of the load current. Furthermore, the range of a linear characteristic is slightly shorter, less than 5% (see Fig. 7.10b). For a load current equal to 1 A, it is from 0.25 mm to 0.55 mm.

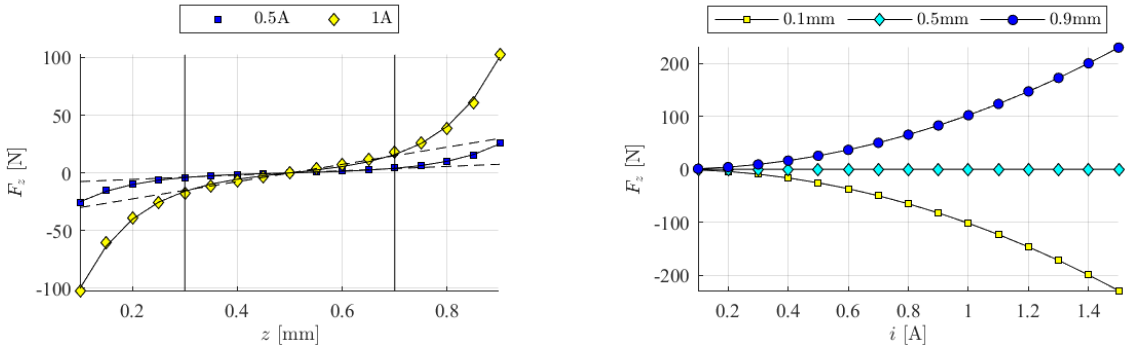

(a) (b)

Fig. 7.9. The axial component of the electromagnetic force F_z versus air gap z (a), versus current i (b), where current i is identical for both electromagnets.

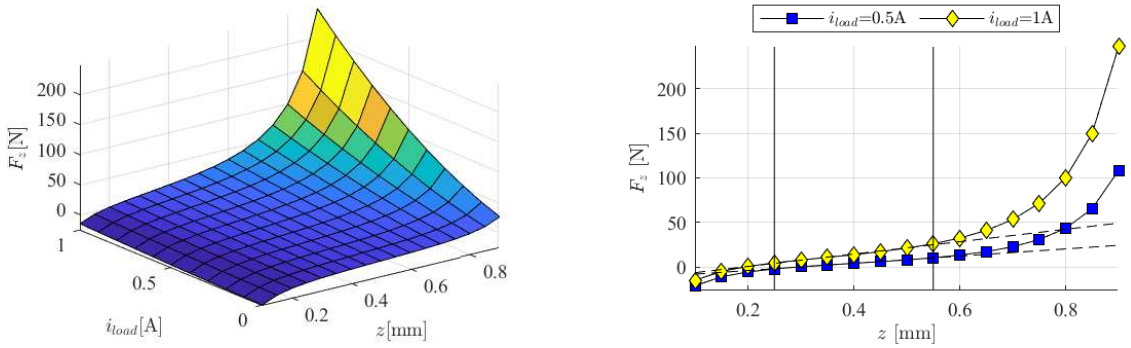

(a) (b)

Fig. 7.10. The axial component of the electromagnetic force F_z in the function of air gap z and load current (a), versus air gap z (b), for bias current equals to 0.5 A.

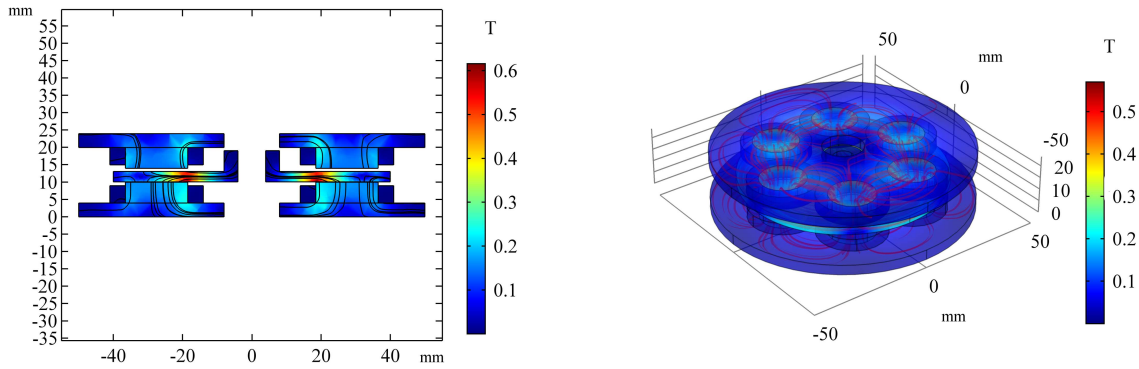

(a) (b)

Fig. 7.11. Magnetic field distribution for air gap z = 0.5 mm and current of the bottom and top electromagnet,respectively, 1 A bias and 1.5 A (a); 3D magnetic field distribution and its streamlines for the axial active magnetic bearing (b).

7.4. Eddy currents calculation

Finally, eddy currents were calculated due to the solid form of the electromagnet poles and the armature. Three simulation scenarios were chosen to observe the consequences of increased frequency. Typically, AMB operates at a constant current level, with a change corresponding to the time reaction resulting from the axial motion of the rotor. In fact, there is no oscillatory motion, rather a motion with damping characteristics. But let us assume that a coil current will be harmonic with frequencies such as 10 Hz, 100 Hz, 1000 Hz. With a numerical model, it is possible to analyze the induced eddy currents in the pole. Figure 7.12 shows the distribution of the eddy currents on the surface of the poles. One can find a tendency of growth and concentration of eddy currents on the outer edges of the poles with respect to the increasing frequency. Figure 7.13 demonstrates a more than thirty-fold increase in eddy currents on the disc surface with a ten-fold increase in the frequency of the control current.

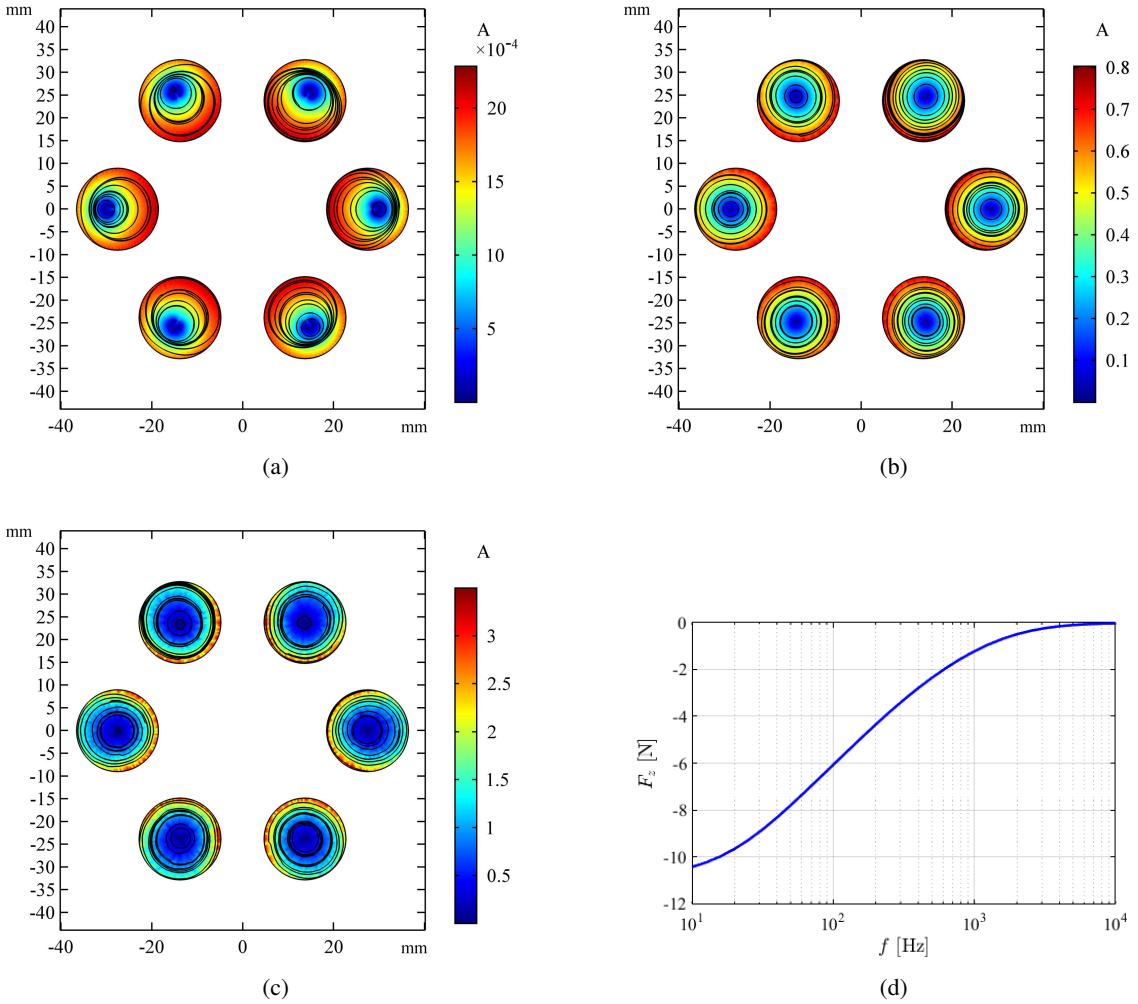

Fig. 7.12. Eddy currents on the pole pieces surface for frequency 10 Hz (a), 100 Hz (b), 1000 Hz (c) and the axial electromagnetic force F_z versus frequency f (logarithmic scale) for 1 A current and 0.5 mm air gap (d).

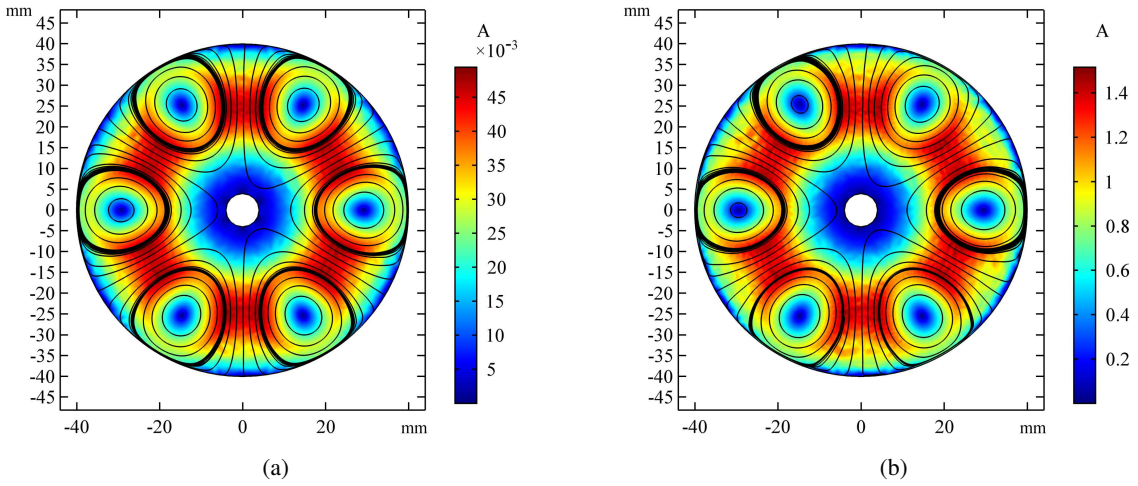

Fig. 7.13. Eddy currents on disc's surface for frequency 10 Hz (a), 100 Hz (b).

Finally, the developed AAMB numerical model was examined with respect to the tilt simulation. The disc was rotated at specified angles α and β. From the simulation results, presented in Fig. 7.14, one can read that the magnetic flux density changes with respect to the disc orientation. The parallel disc location, with respect to the AAMB poles and the magnetic flux distribution with marked poles, is presented in Fig. 7.14a. One can analyze the control configuration of the cylinder electromagnets. When the disc is tilted, the magnetic flux density reflects the disc orientation. The practical application of this solution is the sensing feature of the proposed configuration. The values of the magnetic flux density are presented in detail in Table 7.5. The examined configuration operates in a relatively small value of the magnetic flux density; therefore, nonlinear aspects should be considered in future research. During the modeling procedure of the electromagnetic actuator, magnetic saturation should be taken into account. Saturation will occur especially in thinner ferromagnetic elements. The limits of induced magnetism in an armature must be investigated. The shape, size and configuration of the electromagnet will influence the practical limitations of the application.

Table 7.5. Magnetic flux density B_z on poles' surfaces: average, maximum and minimum values for poles 1, 2, 3 (see Fig. 7.14 for numbering).

α[°]	β[°]	$\bar{B}$[mT]			$B_{\max}$[mT]			$B_{\min}$[mT]		
		B_{z_1}	B_{z_2}	B_{z_3}	B_{z_1}	B_{z_2}	B_{z_3}	B_{z_1}	B_{z_2}	B_{z_3}
-0.5	-0.5	-115	86	-92	-77	140	-63	-187	58	-151
-0.5	0	-98	98	-134	-70	151	-93	-149	69	-205
-0.5	0.5	-86	115	-234	-60	183	-146	-140	78	-405
0	-0.5	-168	109	-94	-119	167	-68	-242	75	-151
0	0	-131	131	-131	-105	179	-104	-177	104	-182
0	0.5	-109	168	-216	-75	248	-160	-170	117	-342
0.5	-0.5	-291	165	-92	-172	257	-64	-617	104	-151
0.5	0	-202	202	-134	-145	295	-93	-293	153	-200
0.5	0.5	-165	291	-234	-113	645	-150	-254	179	-414

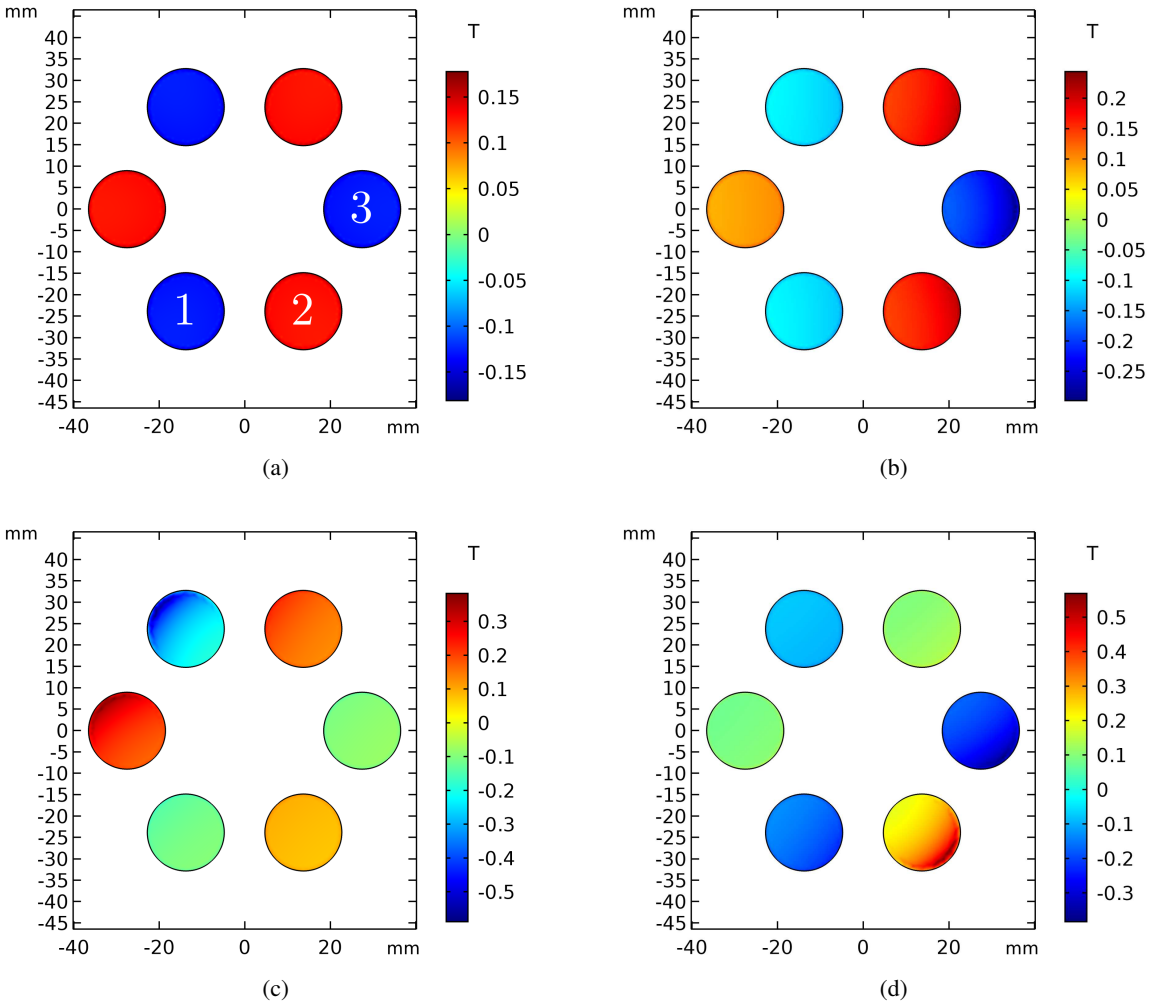

Fig. 7.14. Axial component of the magnetic flux density B_z on pole piece surface, for different angles α and β of disc's rotation: 0°,0° (a), 0°,0.5° (b), -0.5°,-0.5° (c), 0.5°,0.5° (d).

7.5. Magnetic properties measurement

Often during the prototyping of electromagnetic actuators, a core is manufactured by machining in widely available materials, for example, structural steel, for which the supplier generally does not provide magnetic properties. The core of 6pAAMB was manufactured with laser cutting and machining. The material was S355J2 steel, which is commonly used in welded steel structures. Thanks to Antoni Zywczak, BEng, Ph.D. at the Academic Center for Materials and Nanotechnology, the magnetic properties measurement of the S355J2 steel sample was carried out using the LakeShore Type 7407 Vibration Magnetometer, which measures, among others, the magnetization as a function of the external magnetic field. It works on the basis of the vibrating sample method and quadrature change detection in the magnetic flux induced by it. It enables testing of solid samples, single crystals, thin films, powders and liquids. Samples with linear dimensions less than 10 mm and a mass of 10 g at room temperature can

be measured. The required sample was prepared. The measurement result is shown in Fig. 7.15. Similar measurements were made for a sample of iron filings from which the powder core (see Chapter 4) was manufactured. The obtained characteristics were imported to the developed 3D numerical model.

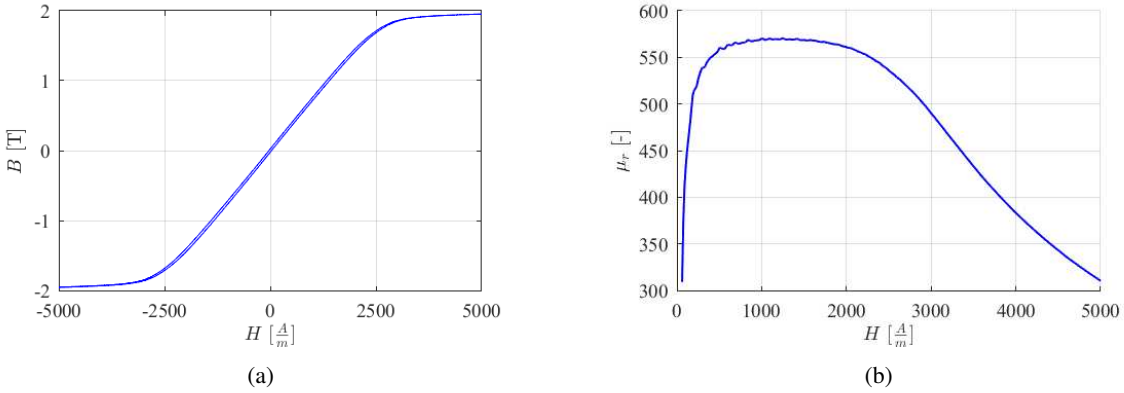

(a) (b)

Fig. 7.15. Magnetization characteristics of S355J2 steel: hysteresis loop B-H (a), relative permeability μ_r(b).

Summary of results

The effect of this chapter was a virtual twin of 6pAAMB, from which the user can collect various characteristics necessary for further optimization of the design, selection of the power system and regulator synthesis. Numerous functions were obtained that describe the key AAMB parameters versus the current and spatial position of the disc. As a result of simulation research, the first version of the prototype was manufactured. The chapter discussed the AAMB sandwich configuration with the disc between the top and bottom 6pAAMB actuator, while the author notes that later in the dissertation emphasis will be placed on the configuration with a single actuator. Numerical modeling is a very useful tool which is critical for designing and optimizing a device, and even for synthesis of regulators through the support of experimental identification. However, if there are disturbances or uncertainties in a given device, they can limit the effective use of FEM. In the next chapter the reader will see how actuator mounting errors forced experimental identification of the 6pAAMB system based on the proprietary fault detection algorithm.

Chapter 8

Quality performance of the axial magnetic bearing

This chapter is an extension of the identification of axial active magnetic bearings. A run-up experiment showed that the applied novel six pole axial active magnetic bearing configuration demands a quality test. The designed and manufactured actuator did not meet the operational requirements, therefore, the validation steps were necessary to be realized. The expected AAMB life calculation is at risk of a dramatic decline if a stator or a rotor is not aligned with the geometric tolerances, as a result of machining inaccuracies or assembly faults. As a consequence, the author proposes an original diagnostic method of the disc-type electromagnetic actuator based on the fusion of distance, current and control signal measurements, according to a specific scenario. The algorithm, which is used for actuator fault diagnosis, indicates differences between the heights of individual pole pieces with adequate accuracy. The calculated results were verified using the coordinate measuring machine.

8.1. Review of fault diagnosis for rotating machinery

Active magnetic bearings are successfully applied in industrial turbomachines due to their frictionless suspension and contactless operating principle. A reverse application of the active magnetic suspension system may be the diagnosis of faults based on the performance of the levitated object or the operation of the entire machine. In [96] active magnetic bearing was used as a diagnosis and identification tool. The application requires accurate force measurement and the development of state-space models to utilize the diagnostic procedure. In [97] research combines two methodologies, using parameter and state estimators to detect sensor and actuator faults in AMB or rotor systems. The linearized system dynamic model and state observers are established for a real-time diagnosis to determine machine fault symptoms from the fusion of position and current sensors. The details of the housings and mounting of AMBs to provide proper assembly of the components are important issues, as mentioned in [98]. In AFPMMs, static eccentricity (SE) causes asymmetric air gaps and leads to mechanical failures, which represents up to 60% of all faults. Analytical models are used successfully in modeling SE [99]. Based on the estimation of the SE factor, an appropriate criterion of [100] has been presented for fault detection using the back electromotive force (bEMF) of the coils. Its development into an online method, which allows SE fault detection and calculation of the minimum value of the air gap, was presented in [101]. Many diagnostic procedures are focused on the vibration response from frequency excitation. In [102] the axial

frequency spectrum has been shown to be an effective method for diagnosing axial displacement faults. In [103] a vibration image was constructed from multiple sensor channels with feature extraction and classification via the two-layer Ada Boost algorithm. An example of a signal fusion diagnosis supported by a machine learning algorithm is covered in [104]. Assembly and manufacturing imperfections are responsible for most rotor faults in AFPMMs. In [105] an assessment of AFPMM performance was provided based on the temperature distribution in the stator winding. Rotor faults may be classified into three categories: a shift in the rotor surface along the axial direction, a horizontal shift of the rotor geometry axis with respect to the stator axis or rotor inclined surface. The detection of defects and its determination of type based on voltage signals extracted from the controller was described in [106]. Enhanced rotating machine fault diagnosis based on empirical mode decomposition (EMD) was developed in [107], where fault information and different noise are adaptively fused using a nonlinear manifold learning method. Diagnostic methods for assessing the performance quality of rotary machines and electromagnetic actuators are constantly developed on the basis of mathematical tools, modern measuring techniques, signal fusion and machine learning algorithms.

8.2. Axial magnetic bearing fault detection based on signal fusion

A magnetic levitation research system was configured, consisting of the axial actuator with six cylindrical pole pieces and the disc in the housing. Feedback was provided by a proximity sensor. To implement the control algorithm, identification experiments were carried out. The regulator, which stabilized the disc, was designed and set in operation mode [29]. During the experiments, it was observed that the disc did not levitate in a horizontal position despite the fact that the experimental setup was properly leveled. The surface of the armature was a plane at an angle to the horizontal reference surface of the AAMB housing. While one side of the disc was pulled up by the electromagnet, the other touched the base surface. When experiments were carried out on 6pAAMB, it was noticed that the precision of a component is crucial. Especially electromagnetic actuators demand very high-precision manufacturing. Shortening the working life of AMBs, caused by misalignment, can be a significant cost driver for both the machine builder and the owner. Machine builders suffer from higher warranty costs in case of bearings fail prematurely. It is worth highlighting the tangible cost of a damaged reputation for quality, too. Machine owners, meanwhile, must contend not only with the cost of buying and installing new bearings but also with any downtime costs, which may be a reason for huge production losses and the necessity of including such situations in the company's flow of material.

8.2.1. Motivation

During the AAMB design process, most of the assembly steps were completed by the designer, causing an inequality in the electromagnet plane. Some pole pieces were not embedded in the stator with the required precision. The following considerations aim to present the method of automatic detection of the faulty assembled construction of the electromagnet. From a control theory point of view, this issue is

very crucial due to the fact that such a bearing should support the levitated rotor. This section presents results of experiments, which were inspired by an imprecise montage of the AAMB pole pieces and an unintended observation during a levitation experiment in the faulty assembled axial magnetic bearing stator. As a result of the above, an automatic fault diagnostics procedure was developed to validate the performance of disc-type machines.

8.2.2. Experimental setup

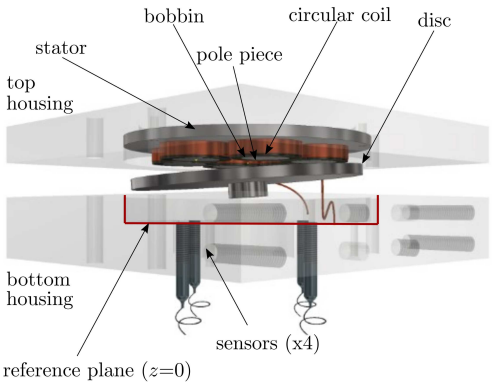

(a) 3D model of the 6pAAMB system.

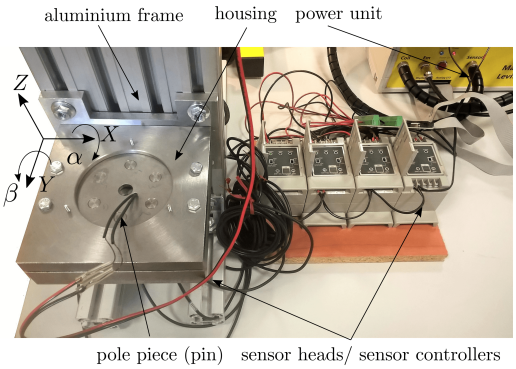

(b) Configured setup for the 6pAAMB fault detection.

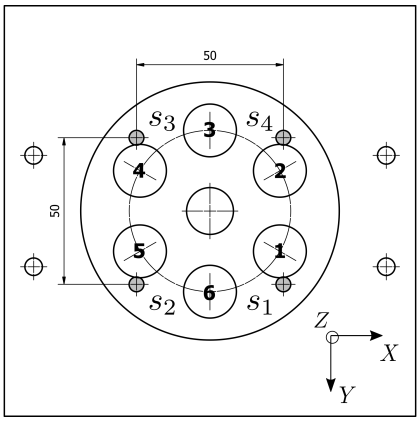

(c) Sensors and pole pieces locations (top view).

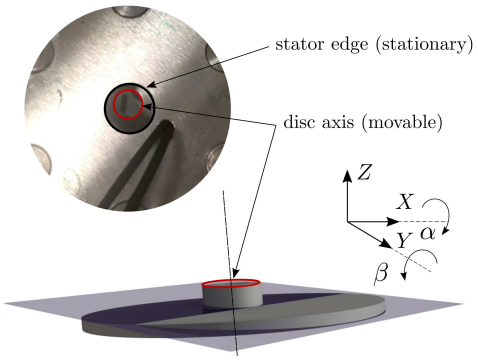

(d) The adopted coordinate system of the disc.

Fig. 8.1. Configuration of the 6pAAMB test system used to determine bearing's assembly defects.

Figure 8.1 presents the configured 6pAAMB setup with the power unit, proximity sensors with signal conditioning units and computer interface board. The 6pAAMB housing is mounted on structural aluminum profiles. For the development of the diagnostic procedure, 4 distance sensors (Fig. 8.1c) were installed. Sensors, which measure position of the levitated disc, are inductive gauging type from Keyence EX-201 series with a 1 mm measuring range. Fig. 8.1d shows the adopted coordinate system and example fault in the form of a shift of the rotor axis relative to the stator axis. The maximum air gap between the disc and the surface of the pole pieces is 1mm. In the designed control system, the RT-DAC4/PCI

(www.inteco.pl) was used, which is a multifunctional analog and digital I/O board dedicated to real-time data acquisition and control compatible with the MATLAB/Simulink software.

8.2.3. Axial magnetic bearing self-identification

The applied semi-automatic procedure aimed at self-identification of the system consists of a few simple measurements, which have been automated and allow determining parameters of the object and the controller. This identification step is necessary to perform the proposed diagnosis algorithm and is proceeded in the following manner:

1. current scaling and resistance measurement,
2. inductance measurement - indirect method, using a time constant estimation:
   (a) set low frequency of the PWM signal,
   (b) measure current value of the system,
   (c) perform RL series circuit analysis,
3. electromagnetic force estimation - indirect approach based on open loop measurements[1],
4. synthesis of the PID controller for closed loop experiments,
5. automated scope of experiments in a closed loop according to the proposed scenario.

The proposed measurement method used 4 inductive gauging sensors:

– experiment and analysis of pulling up the disc,
– experiment and analysis of levitating the disc,
– experiment and analysis of pulling down the disc.

Figure 8.2 presents the open-loop experiment with ramp control signal. The air gap is equal to 1mm. Referring to sensor location (Fig. 8.1c), the electromagnet attraction force has been observed at first in positions 2 and 3, then 4 and 1. Further observations provided the following conclusions:

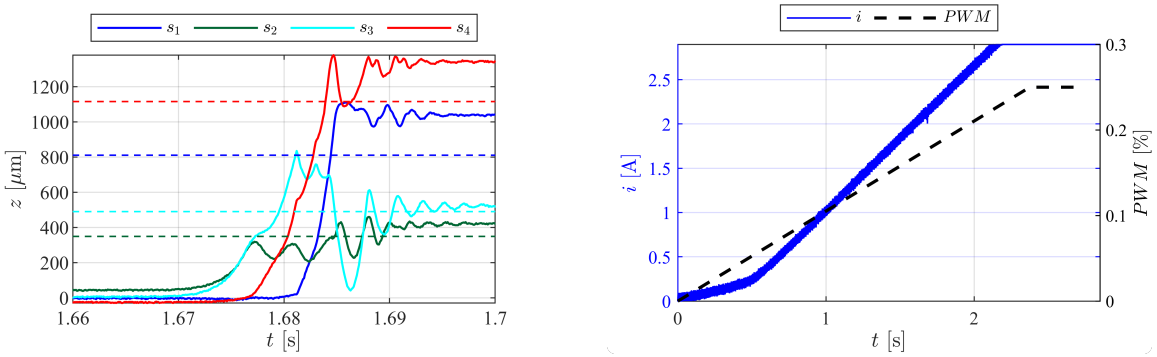

(a) Position waveforms.

(b) Current and control waveforms.

Fig. 8.2. Open loop experiment of the 6pAAMB with ramp control signal.

[1]Measurement of the coil's terminals voltage, current and position of the disc with coil's sinusoidal voltage supply.

– sensors 2,3 first measure rising disc position, pointing to the minimum gap on piece pole 4 or 5,
– sensors 1,4 are out of range, indicating disc skew and a minimum air gap on piece pole 1 or 2,
– sensor 3, after an initial rise, descends, indicating a rebound from a neighboring piece pole 3 or 5,
– sensor 2 returns the lowest position, indicating piece pole 5 as potentially the most protruded,
– the disc is lifted with a current of around 2.1 A.

Table 8.1. Identification results.

Symbol	Parameter		Value	
k	gain coefficient		$0.3174\Omega^{-1}$	
u_c	constant voltage on the coil's terminals		-0.876V	
m	mass of the disc		0.220kg	
R	resistance of the AAMB coils in series		0.510Ω	
T	time constant (f_s=2kHz, f_{pwm}=0.5Hz, PWMmode=1, Prescaler=0)			
	graphical approach		gaussian normal equation	
	with disc	without disc	with disc	without disc
$T_{up}[\mu s]$	800	400	1130	330
$T_{dn}[\mu s]$	550	350	300	150

Table 8.2. Estimated function coefficients.

Function	General form $f(x)$	Coefficients			
		p_1	p_2	p_3	p_4
$U_s = f(PWM)$[V]	$p_1x^3 + p_2x^2 + p_3x + p_4$	-457.30	222.20	7.64	0.74
$L = f(z)$[mH]	$\frac{p_1x^2+p_2x+p_3}{x+p_4}$	$3.99{\cdot}10^{-5}$	$5.34{\cdot}10^{-4}$	$3.35{\cdot}10^{-3}$	1.68
	$p_1x^3 + p_2x^2 + p_3x + p_4$	$-6.67{\cdot}10^{-5}$	$9.87{\cdot}10^{-5}$	$-4.88{\cdot}10^{-4}$	$1.87{\cdot}10^{-3}$

The setup developed in the initial design phase is an example of a single-axis AMS with a distributed coil wounded around six pole pieces. Equations (8.1) describe system dynamics by using Newton's second law of motion with Faraday and Kirchhoff's laws.

$$\begin{cases} \frac{dz}{dt} &= v \\ \frac{dv}{dt} &= \frac{1}{2m}\frac{dL(z)}{dz}i^2 + g \\ \frac{di}{dt} &= \frac{1}{L}(-\frac{dL}{dz}\frac{dz}{dt}i - Ri + u) \end{cases} \tag{8.1}$$

where z,v,i are state variables, respectively, axial position, velocity and current; m,R,u denote, respectively, disc mass, coil resistance, and control voltage; L is the electromagnet inductance and g is gravity. The system reacts below the sampling period T_s=1 ms adopted in the target experiments, but when closer to the rising and falling edges of the current waveform, one may notice that it is similar to the response of the first-order system. The rising edge time constant differs from the falling edge one due to a nonlinearity of an electronics. At this stage, the phenomenon was neglected by simplifying the current equation to the linear formula:

$$\frac{di}{dt} = -\frac{1}{T}i + \frac{k}{T}(u + u_c) \tag{8.2}$$

where T,k and u_c are, respectively, the time constant, the gain coefficient, and the constant residual coil voltage. The time constant T will be calculated from the step response of the digitized current equation with a given quality factor:

$$\begin{cases} i(k+1) &= a_d i(k) + b_d(u(k)+u_c) \quad k=0,1,2... \\ a_d &= e^{-\frac{T_s}{T}} \\ b_d &= k\left(1-e^{-\frac{T_s}{T}}\right) \\ J(a_d,b_d) &= \frac{1}{2}\sum_{k=1}^{N}\left(i(k)-I(k)\right)^2 \end{cases} \tag{8.3}$$

where $I(k)$ denotes the current measured value in kT_s. The time constant is determined graphically and by finding the solution of the Gaussian normal equation for the minimum of the quality factor of (8.3). The resistance of the connected in series coils was measured by a technical method with accurate current measurement. According to (8.2) it is possible to control the current in the coil regardless of other state variables. Refer to [108] for a detailed description of the identification methods, the results of which are presented in Tables 8.1 and 8.2, allowing the synthesis of regulators (Fig. 8.3). Most of the steps mentioned above were automated in the form of scripts in the MATLAB/Simulink environment.

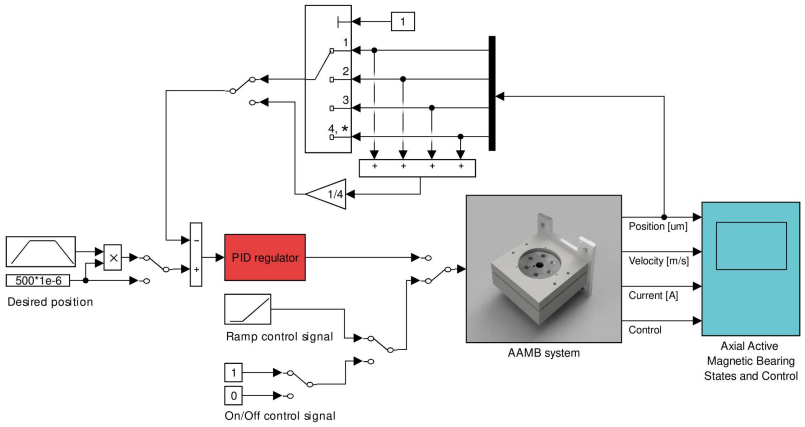

Fig. 8.3. Rapid prototyping of a single axis control system for the 6pAAMB in MATLAB/Simulink.

8.2.4. Axial magnetic bearing investigation in closed loop

Research was carried out on the test stand equipped with four distance sensors. The pole pieces coils were connected alternately in series, forming three pairs of C-type electromagnets. First, sensor calibration is performed by determining the limit values (disc in the reference plane and at maximum attraction force). By setting the constant distance between the disc reference plane (lower housing) and the stator reference plane (upper housing), scaling was done. The experiment duration was set to 10 seconds, with 1ms sampling. The disc was stabilized sequentially for feedback from each sensor and for the sum of all sensors divided by their number. For each variant, 5 experiments were carried out, from which the mean values of the state variables with the disc in a stable position were calculated (see Table 8.3).

Table 8.3. Sample set of closed loop experiments for feedback from the 1st sensor.

exp	z[μm]				PWM[%]	i_f[A]
	1	2	3	4		
1	375.5	236.0	1.9	247.0	0.1552	1.8093
2	378.6	245.7	1.7	248.3		
3	353.0	242.4	-0.1	240.8		
4	401.7	230.5	-0.2	263.3		
5	394.7	223.9	2.0	237.5		
avg	380.7	255.5	1.1	247.3		

Figure 8.4 shows waveforms from experiment no. 1 – levitation of the disc with feedback control signal from the 1st sensor. The desired value equals 500 μm with the 1 mm air gap. The attraction force generated by the electromagnet has been observed at first in position 2, then respectively 1, 3 and 4. Current and control waveforms were filtered with a 2nd order IIR Butherworth low-pass filter with cutoff frequency 0.3. Additionally pos. 1 indicates two stages when pulling up and slowly increases during stabilization; at pos.2 the disc is stabilized at 250 μm; pos.3 shows only small movement throughout the experiment; pos. 4 gently falls (about 25 μ m) during the pulling stage, but apart from that, it is similar to pos. 1, with a maximum value around 250 μm. During this experiment, a gentle motion of the disc was observed in the direction of pole piece no. 5 - indicates the smallest air gap between this pole piece and the levitated disc. Also, the 2nd sensor first returns information about pulling up the disc, but the 4th sensor shows the position change as the last one – this may be a hint that the surfaces of pole pieces no. 1 and 2 are parallel. Pole pieces no. 3 and 4 are less protruded compared to 5. Pole pieces no. 5 and 6 are acting on the disc faster than 1 and 2, causing the disc plane to skew and its slight decline in relation to the reference plane of the pole piece no. 1 and 2. Figures 8.4-8.8 present all scenarios analyzed. Individual experiments were analyzed as above and evaluated on the basis of the values of the calculated state variables (Table 8.4). The collected information was used to propose an automatic method to judge the quality of the 6pAAMB prototype manufacturing and assembly process.

8.2.5. Detection algorithm for actuator assembly faults

A vertical position of the electromagnetic actuator in the test system is used to identify the axial electromagnetic force and the heights of particular pole pieces, but the 6pAAMB is intended to operate horizontally, complementing the radial bearing. As a result of this research, the automatic algorithm to detect the surface inequality of 6AAMB was proposed. The algorithm, based on measurements of the position of the disc from four sensors, current and control signal, using the plane equation, calculates the height of the pole pieces. In the case of 4 independent position measurements, it was possible to calculate the equation of the disc plane together with the angles between the plane and the axis X,Y. Assume that $P_i = [x_i, y_i, z_i]$, where i=1÷4, denote 4 points, where the z_i component is the sensor measurement i^{th}.

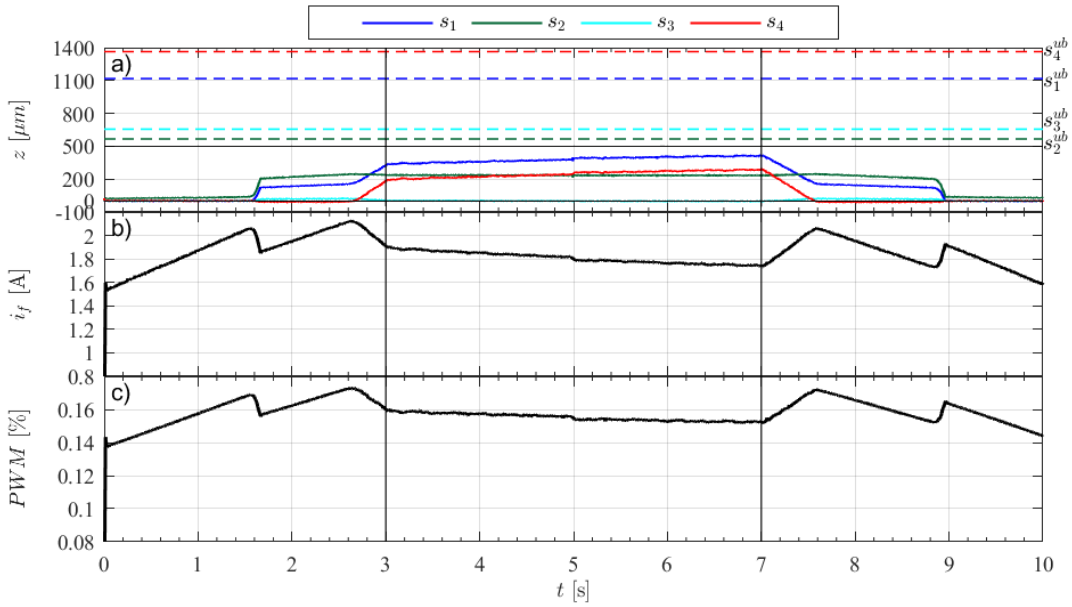

Fig. 8.4. Waveforms of: a.) the position signals, b.) filtered current, c.) filtered control signal duty cycle for closed loop experiment with PID regulator, feedback from the 1st sensor and the desired gap set at 500μm.

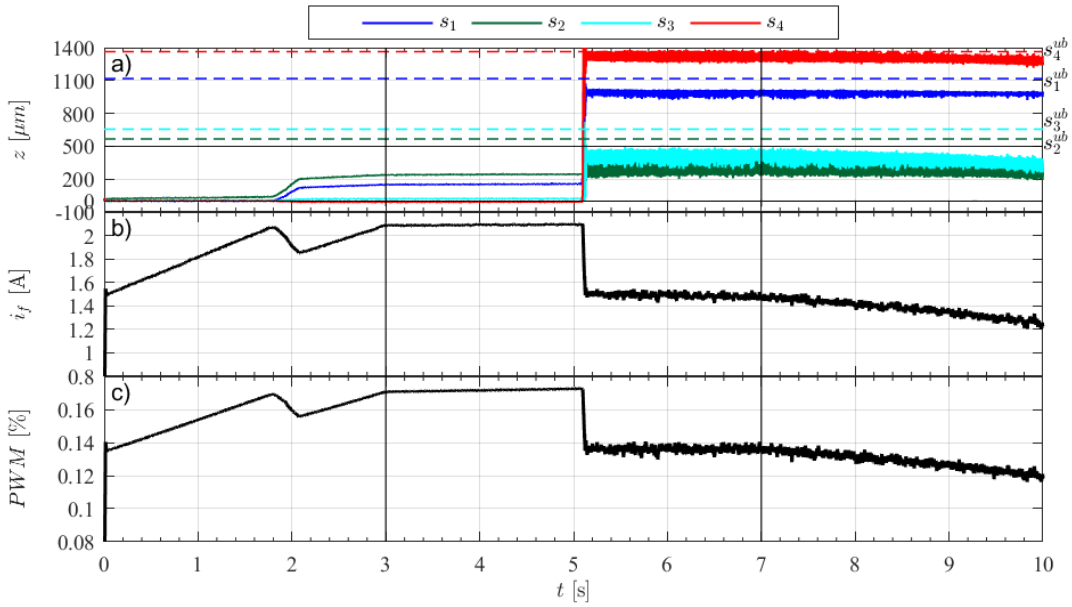

Fig. 8.5. Waveforms of: a.) the position signals, b.) filtered current, c.) filtered control signal duty cycle for closed loop experiment with PID regulator, feedback from the 2nd sensor and the desired gap set at 500 μm.

Let us introduce the following points: P_x = [1,0,0], P_y = [0,1,0] and P_0 = [0,0,0]. The general form of the equation for a plane in $\mathbb{R}^3$ is the following:

$$Ax + By + Cz + D = 0 \tag{8.4}$$

where A,B,C,D are constants and at least one of the coefficients A,B,C is not zero. A plane has a vector $\bar{N} = [A, B, C]$, which is perpendicular to a plane.

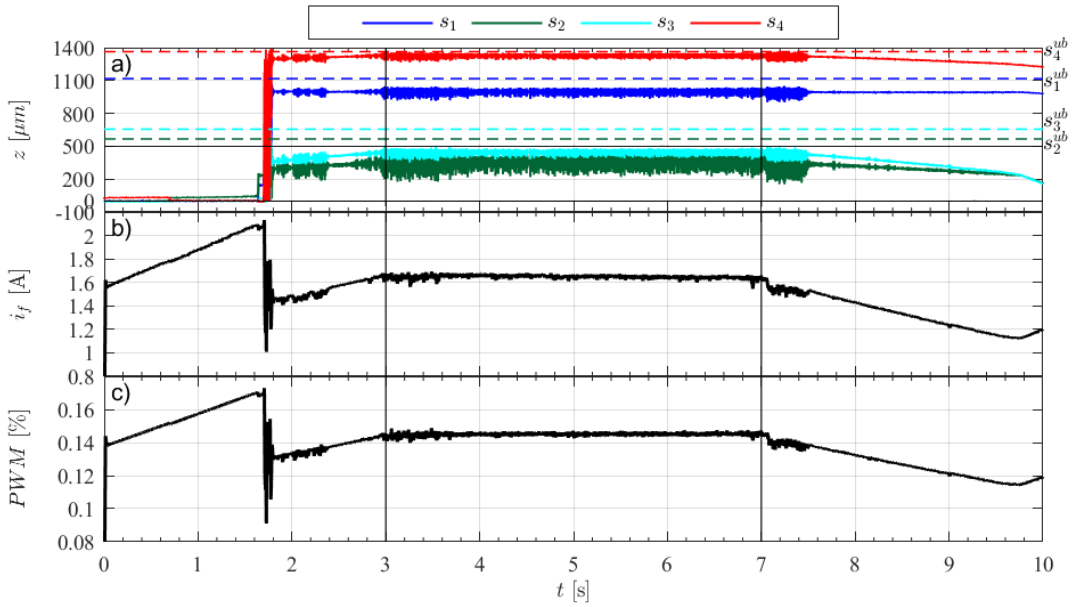

Fig. 8.6. Waveforms of: a.) the position signals, b.) filtered current, c.) filtered control signal duty cycle for closed loop experiment with PID regulator, feedback from the 3[rd] sensor and the desired gap set at 500 μm.

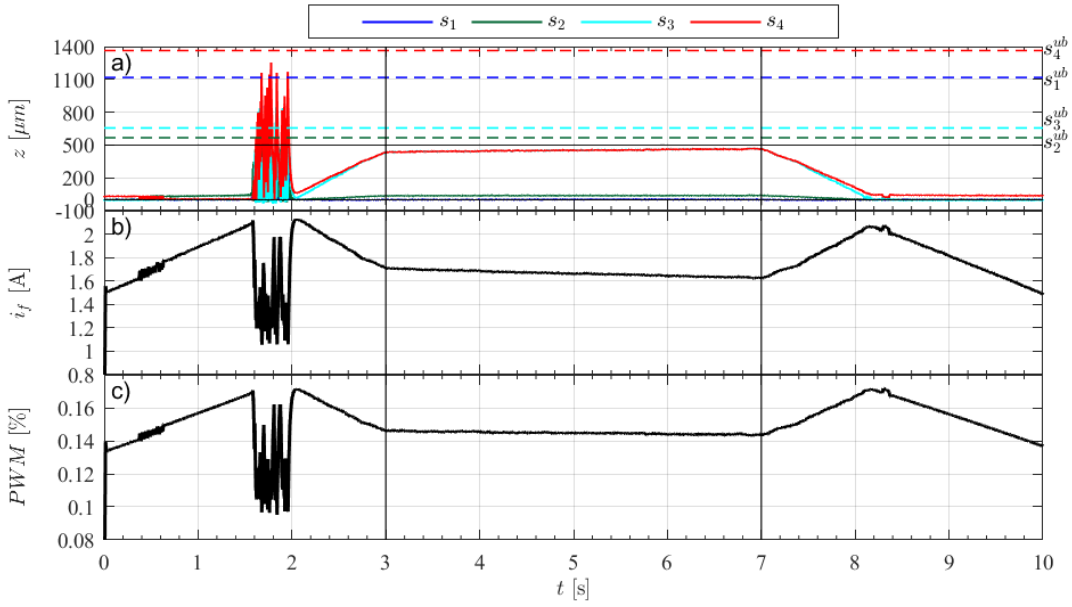

Fig. 8.7. Waveforms of: a.) the position signals, b.) filtered current, c.) filtered control signal duty cycle for closed loop experiment with PID regulator, feedback from the 4[th] sensor and the desired gap set at 500 μm.

The angles α,β between the disc plane and the axis, respectively, X,Y can be calculated as follows:

$$\alpha = \left| \frac{\pi}{2} - \arccos\left(\frac{(\bar{P}_x - \bar{P}_0)\bar{N}}{\|\bar{P}_x - \bar{P}_0\|\|\bar{N}\|} \right) \right| \tag{8.5}$$

$$\beta = \left| \frac{\pi}{2} - \arccos\left(\frac{(\bar{P}_y - \bar{P}_0)\bar{N}}{\|\bar{P}_y - \bar{P}_0\|\|\bar{N}\|} \right) \right| \tag{8.6}$$

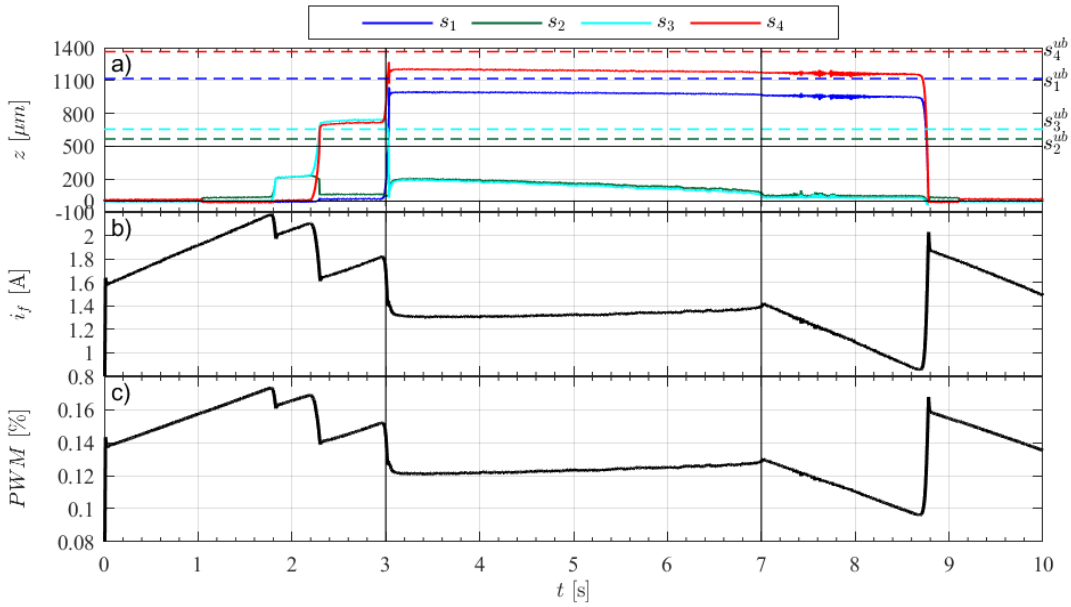

Fig. 8.8. Waveforms of: a.) the position signals, b.) filtered current, c.) filtered control signal duty cycle for closed loop experiment with PID regulator, feedback from the signal fusion and the desired gap set at 500 μm.

Table 8.4. Steady state position, control and current values from experiments with different reference source.

sensor	gap[μm]	z[μm]				PWM[%]	i_f[A]
		1	2	3	4		
1	500	380.7	235.7	1.1	247.3	0.1552	1.8093
2	500	985.1	320.8	415.6	1311.4	0.1360	1.4896
3	500	994.1	348.0	442.3	1327.1	0.1448	1.6454
4	500	1.8	37.6	451.7	1327.1	0.1448	1.6648
fusion	500	981.3	156.2	143.8	1190.4	0.1236	1.3318
fusion	600	962.4	291.5	363.5	1263.8	0.1285	1.4035
fusion	700	1009.3	286.6	340.3	1303.5	0.1333	1.4598
fusion	800	1008.8	321.8	406.8	1333.6	0.1420	1.5818
fusion	1000	1017.5	382.4	493.2	1365.4	0.1621	1.9168

The algorithm (Fig. 8.9) returns a logical table, where the rows correspond to the stabilization levels according to the selected resolution and the columns indicate the individual pole pieces. If there is a value of 0 in a given cell, it means that the disc did not stabilize at the given level under the pole piece. Eight gap intervals were adopted, that is, 0, 200, 300, 400, 500, 600, 800 and 800+. A lower number gave poorer precision, but increasing the measuring intervals to 16 did not improve the resolution. The number of intervals is chosen automatically. The final table contains values 0 and 1, but in previous steps, one can read how many times the disc occupied a position in a given spatial location. Additionally, from the current and voltage measurement, a fictitious current plane is calculated in the final actuator fault assessment by introducing a current correction. It is important because of the hazard that the actuator coils' bobbins may protrude above the pole piece surface, possibly confusing the bobbin's protrusion with the pole piece one. For a valid current correction, it is necessary to assume identical coils. Although

they were manually wounded, due to the small number of turns, the resistance measurement showed a negligible difference between them. Thus, measurement of the current allows one to reject the influence of the bobbin or nonmetallic element on the diagnosed actuator active surface.

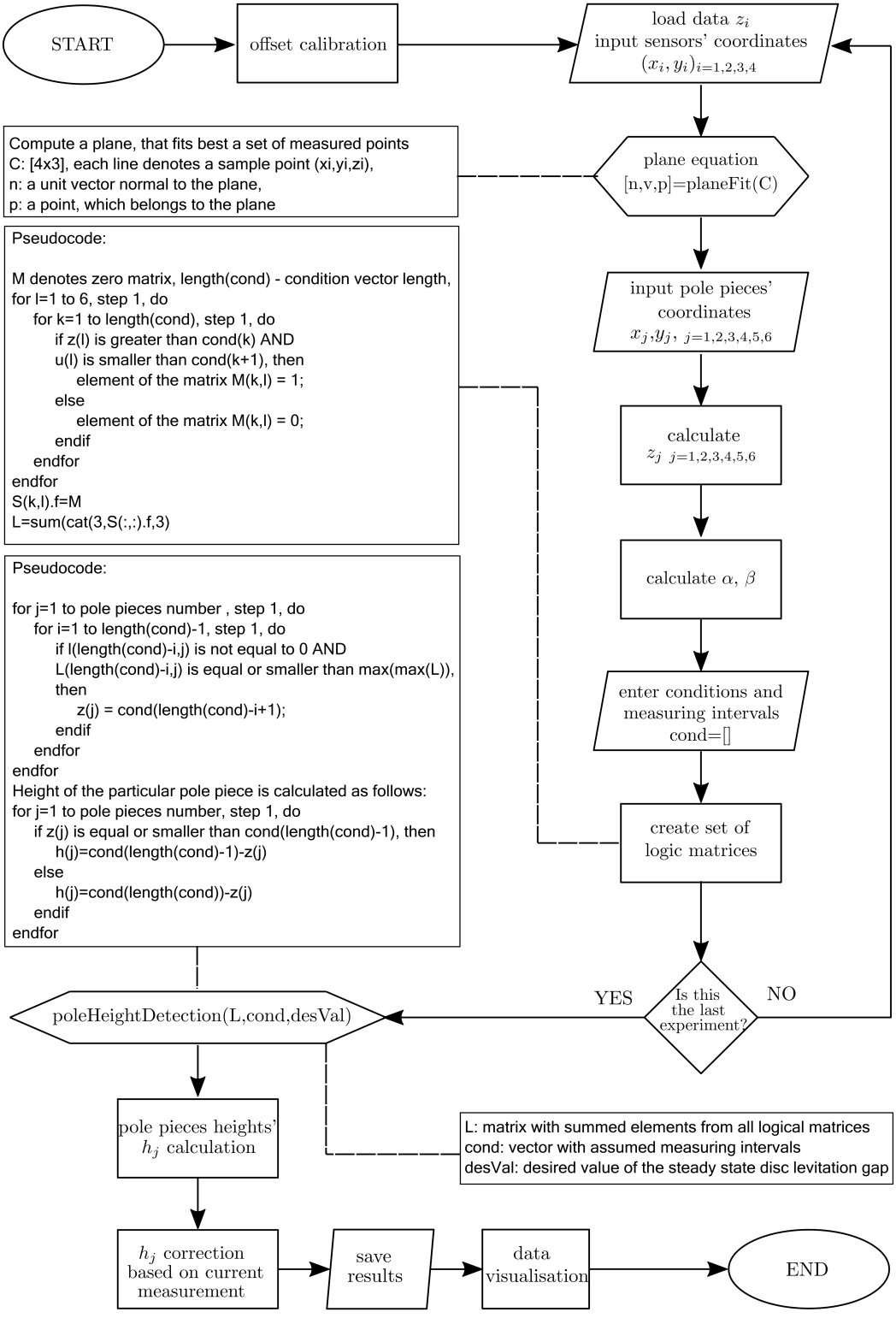

Fig. 8.9. Detection algorithm for actuator assembly faults on the example of the 6pAAMB.

To verify obtained results the coordinate measuring machine (CMM) was used. Measurements were made courtesy of Halina Nieciąg, BEng, Ph.D. Table 8.5 compares the results obtained from the algorithm and CMM[2], which is a reference point to assess the performance of the proposed algorithm. Figure 8.10 visualizes the heights of the measured pole pieces and shows the utilized CMM. The algorithm detection result confirmed the usefulness of the proposed solution, which may be developed towards sensorless fault detection procedure.

Table 8.5. Piece poles height results from CMM and the proposed algorithm.

No.	h^{CMM}[mm]	$\Delta h^{CMM}[\mu m]$	$\Delta h^{ALG}[\mu m]$	$\Delta h^{CMM} - \Delta h^{ALG}[\mu m]$
1	6.089	89	60	29
2	6.012	12	0	12
3	6.134	134	100	34
4	6.122	122	100	22
5	6.371	371	350	21
6	6.028	28	50	22

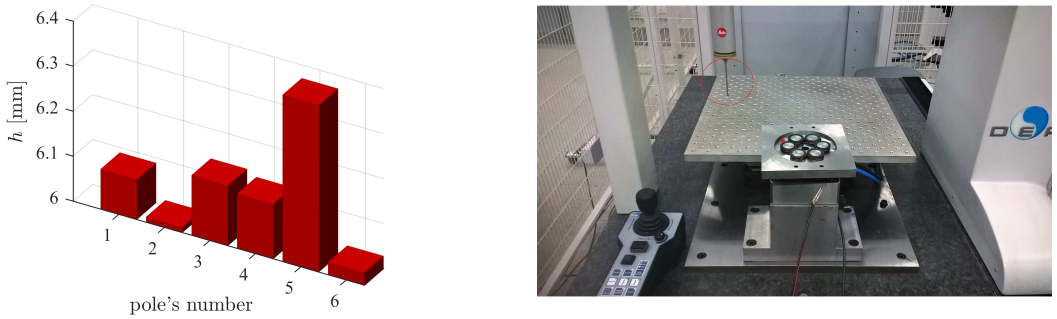

(a) Pole pieces measurement visualization.

(b) DEA Global Silver Performance device.

Fig. 8.10. Pole pieces height measurement by using coordinate measuring machine.

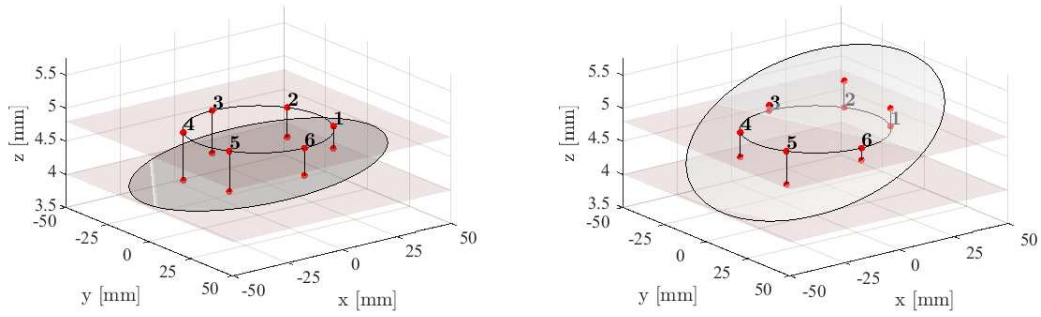

(a) Feedback from sensor 1.

(b) Feedback from sensor 2.

Fig. 8.11. Inclined disc plane during its pull-up to 500 μm level with two reference sensors.

[2]During CMM measurements, the reference plane was the upper surface of the 6pAAMB stator yoke.

8.2.6. Quality control with laser profiler

The surface of the 6pAAMB pole pieces can be visualized with a laser profiler. To carry out the measurement, it was necessary to assemble the frame and linear guide on which the LJ-V7200 laser profiler head was mounted. Due to the laser beam limitation, the measurement was made twice, for each half of the actuator and then profiles were joined. With respect to the reference plane, the height of the pole pieces was determined. The measurement involved the next iteration of the 6pAAMB prototype with rewounded coils. A hydraulic press with a maximum pressure of 600 kN was used to level the surface of the 6pAAMB pole pieces, coils and bobbins. Despite that, there is still a noticeable difference in the height of individual pole pieces, i.e. starting with the first one, respectively, 6.248, 6.242, 6.133, 5.988, 5.994, 6.145. The use of the laser profiler required additional equipment, data postprocessing in the form of image files and significant financial expense. However, it serves as a desirable tool for verifying the quality control of mechanical components, especially in case of a larger-scale production.

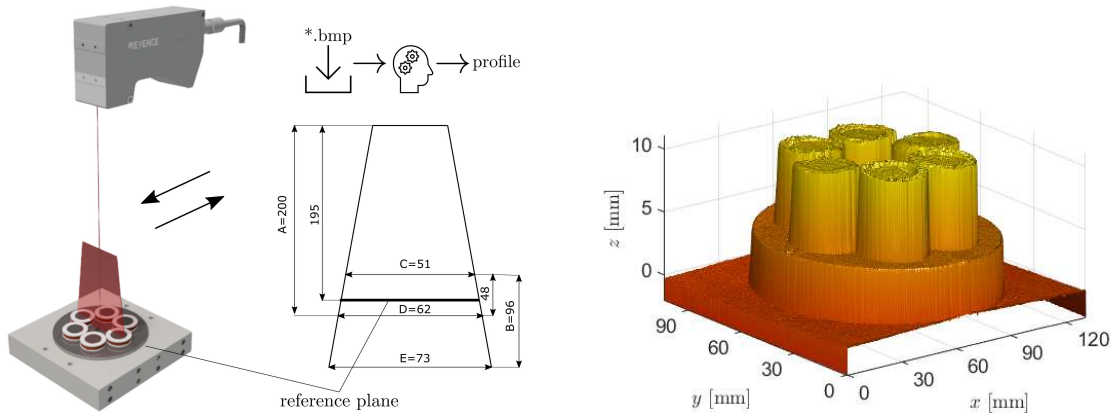

(a) Measurement scheme with LJ-V7200 laser profiler.

(b) The 6pAAMB stator surface scan.

Fig. 8.12. Surface roughness and quality check of mounting the pole pieces in the 6pAAMB stator yoke.

Summary of results

The research described above aimed to identify and recognize mechanical assembly inaccuracies in axial active magnetic bearings with multiple poles. A tool has been developed to detect defects in the assembly or operation of axial machines in situ. The open-ended procedure for semiautomatic identification of the axial actuator has been proposed. This chapter discussed 6pAAMB applied as a measurement system for its quality assessment and indicates the potential of AMS to self-monitoring or diagnostic systems.

Chapter 9

Axial active magnetic bearing in rotor system

Introducing an interdisciplinary approach to the design of active magnetic bearings, the concept of a slim-type AAMB with six cylindrical poles was tested and adapted to the vertical rotor-shaft configuration. During this process, mechanical engineering tools were used to support the design of the rotor shaft. The rotor deflection was studied with the support of modal analysis by using COMSOL Multiphysics. This chapter describes several variants of laboratory test rigs of the vertical axis shaft supported by two active magnetic bearings, the axial active magnetic bearing alone or in combination with radial passive magnetic bearings.

9.1. Setup of active magnetic bearings for vertical long shaft

This section presents the new laboratory test rig of the vertical axis shaft supported by two active magnetic bearings. Behind the motivation of setting up this system is control of the rotor-shaft vibration modes, while the rotational speed varies and the unbalanced mass on the whirling disc is introduced to the system. The proposed numerical model aims to simulate real operating conditions of rotating machinery with applied external load, with variable structure caused by change of material properties of the rotor-shaft assembly or due to a fault of some elements coupled with the rotor. Radial and axial AMB properties were selected to achieve good operating conditions. The individual stages of the design process were considered with reference to the synergy of mechanical and electrical engineering.

9.1.1. Selected discussion on radial and axial active magnetic bearing prototyping

A. Parallel design process

Nowadays, many inventions are designed to improve a manufacturing process. Many of them were developed by trial and error, often without using computer simulations. It produces failures that can be costly. Equations to determine the load, stresses and impact of selected physical values in a considering system were developed by science, mainly mathematics [24], [109]. To deal with often extensive calculations, it is necessary to use a computer to assemble and solve a complex set of equations that describe

an object. The COMSOL Multiphysics software allows to expose mechanical and electrical engineering aspects in the AMB design process, by FEM [29]. Complex simulations are a key part of the design process for almost all types of systems. Based on their results, a virtual prototype of a designed object is created and optimized. Some synergies of science will lead to improving the efficiency of the design process by reducing the number of real prototypes and destructive tests.

From an idea to a prototype, there are some steps that are complex in execution. To minimize time and cost, the AMB system is designed by introducing an interdisciplinary course of proceeding. The scheme (Fig. 9.1) contains its steps. A user may start from the analysis of the system specifications according to a specified application. In a given case, a modal analysis is applied to a flexible shaft. The deflection of the shaft and the distribution of force in the system will be of key importance for further procedures [110]. Next, integrated calculations are performed referring to the mechanical, electrotechnical, material and control system engineering of the designed machine. The mechanical part includes the geometry of AMB, often based on analytical modeling [24] and production technology (see Chapter 8). Particularly desirable are the accuracy of the manufacturing and the quality of the assembly of the system structure. Additionally, the air gap between the stator pole pieces and the rotor surface significantly influences the engineering fit and shape tolerance of AMB. The electrotechnical part consists of a project of a magnetic and electric circuit with an electromagnetic force distribution. Control theory is responsible for algorithm implementation. Material selection remains in strict relation to previous ones. After the first iteration of the described approach, the input parameters are verified and potentially modified. The second iteration begins with rapid prototyping in which a virtual model is developed. The model is subsequently subjected to parametric optimization according to the design procedures mentioned. As a result, a prototype is manufactured and assembled. Subsequently, identification of the system is carried out. The first experiments contain valuable knowledge, which is the necessary feedback to improve the future product.

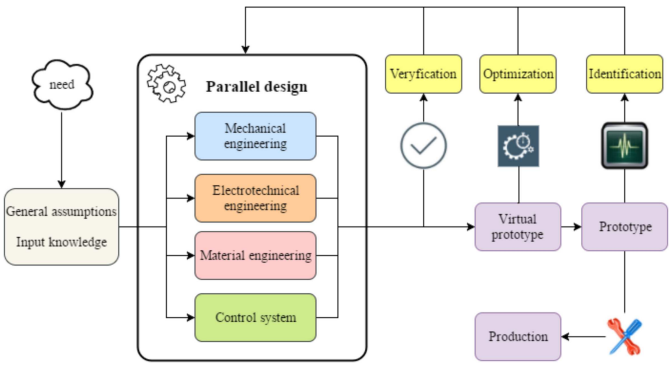

Fig. 9.1. Scheme of adopted approach for interdisciplinary synergistic design (based on [29].

B. The role of the supported software

The experience from 2D simulation of a levitated sphere, radial magnetic bearing with three and four C-shaped electromagnets, including the equations of motion dynamics and controller equation, has

indicated that the complex and interdisciplinary approach is feasible [108]. Today, due to the increasing computer computational power and extended functionality of software tools, models may be developed with more complexity and better matching of real devices. Three models of the system components were designed: shaft with rotor, radial and axial AMBs. The 3D models allow one to use geometry as prototyped and further manufactured. Therefore, it is possible to model aspects used during assembly (e.g. holes and irregular curved surfaces in a stator to achieve correct magnetic flux flow; holes in rotors for unbalance analysis). On the other hand, there is a set of limitations for software and solvers. The 3D analysis requires a lot of memory and processing power to solve the model. Especially in the case of active levitation systems, the problem is directly connected with levitation phenomena - the air gap is relatively small with respect to the system dimensions. For the considered models, the COMSOL Multiphysics 5.6 software was running on Windows 10, hosted by 36GB RAM and Intel i7 975/3.33GHz workstation.

C. Discussion on time domain modelling

The designed models are available for time domain modeling, but this task has not yet been solved. This is due to the source of the control signal. The models developed assumed that the electromagnetic actuator is driven by current signals. From the hardware point of view, it means that the driven current source is used and when connected, the time constant of the rising current edge can be neglected. Another approach is to apply electrical circuits and extend the modeling to the voltage-driven case. Today, the PWM technique is commonly used to drive a coil. In such a case, the model requires a solver with a time-stepping adjusted to the PWM signal frequency. Moreover, the electrical circuit needs to be modeled (voltage-driven case) and the smoothing of square wave signal with variable duty cycle must be applied to guarantee solver convergence. Please note that the 2D model in axis-symmetry mode describing the soft iron core 9mm×6mm with copper coil 3mm×6mm, soft iron armature 12 mm × 5 mm with air gap 500 μm located at air region 20 mm × 20 mm with 1781 DoF was solved for the current step (0 to 1 A) and simulation time of 100 s in 53 minutes and 32 seconds. Therefore, due to the huge computational effort, modeling the AMBs dynamical aspects requires running solvers at specialized computing centers.

D. Radial active magnetic bearing

Although the PhD dissertation focuses on the topic of axial active magnetic suspension, the configuration of the active radial magnetic bearing used in the vertical rotor system should be briefly presented. Radial AMB was constructed [111], [112] to eliminate shaft vibrations in the x-y plane. The stator contains an eight-pole magnetic bearing actuator with four symmetrically placed electromagnets with a horseshoe shape. In technical applications, two electromagnets counteract, which are operated in the area of the radial AMB. Figure 9.2 shows the electromagnetic force of the single upper electromagnet generated by the current I=0.5 A as the function of rotor position during vertical (Fig. 9.2b) and horizontal (Fig. 9.2c) movement of the rotor. To provide the proper position of the shaft in one axis, two

identical electromagnets exert an attraction force in the opposite direction. The prototype of AMB has already been manufactured and is ready to be assembled on the laboratory test rig [37].

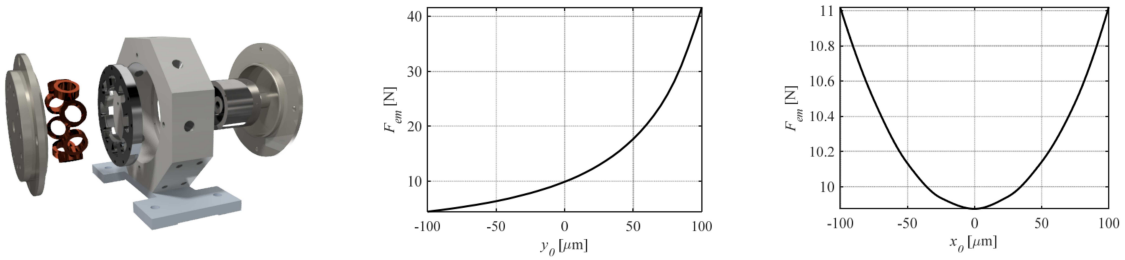

(a) (b) (c)

Fig. 9.2. The radial AMB and its electromagnetic force of the single upper electromagnet versus rotor's position.

E. Impact of the rotor's skew angle

This issue has been omitted from the first AMB solutions [113] or briefly described without proper analysis combined with the force distribution [114], [115]. Let us assume a lack of parallelism between the surface of the rotor and the plane of the electromagnet pole pieces so that the main axis of the rotor is inclined by an angle with respect to the radial AMB symmetry axis. The position of this rotor in a cross-sectional area of the radial AMB results in a variable air gap, which causes different values of the electromagnetic force acting on the specified rotor surface. If one consider a flexible shaft, the line of the rotor center will not be straight. In that case, the concentricity between the rotor and the radial AMB is not obtained (Fig. 9.3a). The modal analysis of the shaft is recommended. The value of the air gap must be chosen so that there is sufficient reserve of a displacement caused by vibrations. The sum of displacements of these vibrations and force changes cannot lead to mechanical contact between the rotor surface and the pole pieces of the electromagnets. This problem will be solved by ensuring the right value of the radial AMB stiffness.

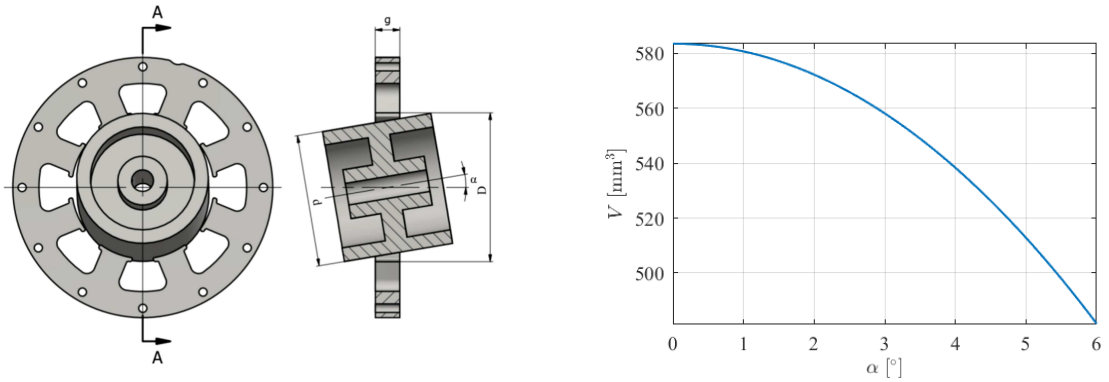

(a) Lack of concentricity between rotor and stator.

(b) The air gap volume versus the rotor's skew angle.

Fig. 9.3. Consequence of a skewed rotor surface with respect to the radial AMB stator.

$$V = \pi \left(\frac{D}{2}\right)^2 g - \left[\left(\frac{g}{\cos\alpha} - d\tan\alpha\right)\pi\left(\frac{d}{2}\right)^2 + 2\pi\tan\alpha\left(\frac{d}{2}\right)^3\right] \tag{9.1}$$

Bearing capacity is a very important parameter that should be calculated at the beginning of the design process [116]. It depends on the maximum force generated by the electromagnet and the cross-sectional area of the pole piece of the electromagnet. The maximal force varies from saturation induction, which is one of the properties of magnetic material and depends also on the proposed electromagnet core geometry. In this case, the direct coupling between mechanical, electrotechnical and material engineering in a design process is shown. The variable angle of inclination of the rotor in the AMB space causes a variable air gap volume (Fig. 9.3b), resulting in different values of electromagnetic force acting on the surface of the rotor. From this point of view, proper analysis of the motion of the rotor shaft and the electromagnetic field distribution in the AMB actuator is necessary to propose the control algorithm [117], [109].

9.1.2. Setup configuration

The designed setup consists of an aluminum frame from Bosch Rexroth profiles 40 x 40 mm, an asynchronous motor MS561-2 (90 W), a long flexible rotor shaft assembly, load, clutch and magnetic suspension system that includes axial and radial AMB. The shaft is made of C45 carbon steel and has a length of 800 mm and a diameter equal 8 mm. Mechanical excitation is generated by the asynchronous motor and transmitted through a simple clutch to the driven shaft. The cylindrical rotor, disc and load are mounted on the length of the shaft. The first two act as armatures in magnetic suspension systems. The measurement system consists of three position sensors applied to the axial magnetic bearing to obtain a fully observable disc motion plane in the axial bearing space. The other two position sensors measure the air gap in the x-y plane of the radial AMB. Figure 9.4 presents the setup of the designed research. Selected mechanical parts, such as the rotor, shaft, bearing housing and disc, were manufactured in the AGH Department of Manufacturing Systems with the desired quality and tolerance up to 10 μm. The critical assembly issue is the horizontal and vertical alignment of all components. The laboratory test rig extends the previously realized research test rig [117].

9.1.3. Rotor eigenvalues

From the control point of view, it is an interesting task to keep the rotor levitating at variable speed [109], [118]–[120]. Therefore, an initial study of the rotor configuration and dynamics is provided. The numerical model of the rotor was developed in COMSOL Multiphysics software. Some initial bending modes were calculated and the rotor deflection is presented in Fig. 9.5 in relation to the values listed in Table 9.1. One can find that the configuration is well suited for identification and control algorithms due to relatively low eigenfrequencies. Therefore, the typical configuration of a real-time environment based on MATLAB/Simulink and data acquisition board, as well as embedded PAC architecture, will

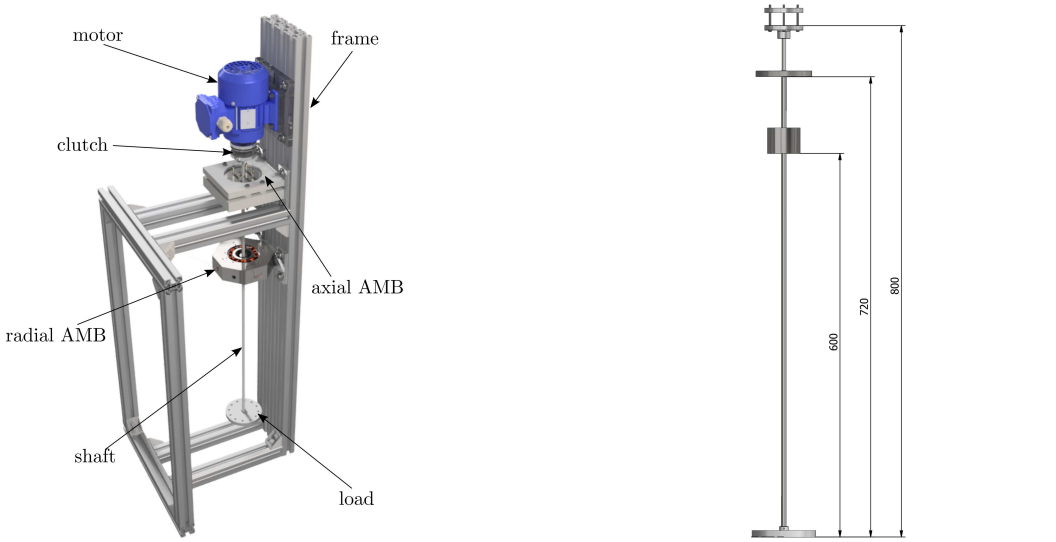

(a) Model of the proposed magnetic suspension set-up.

(b) Geometrical dimensions of the rotor shaft assembly.

Fig. 9.4. Designed test rig of the vertical axis shaft supported by the magnetic suspension system.

satisfy the real-time control requirement. In this case, the model-based design of the control system may be adopted.

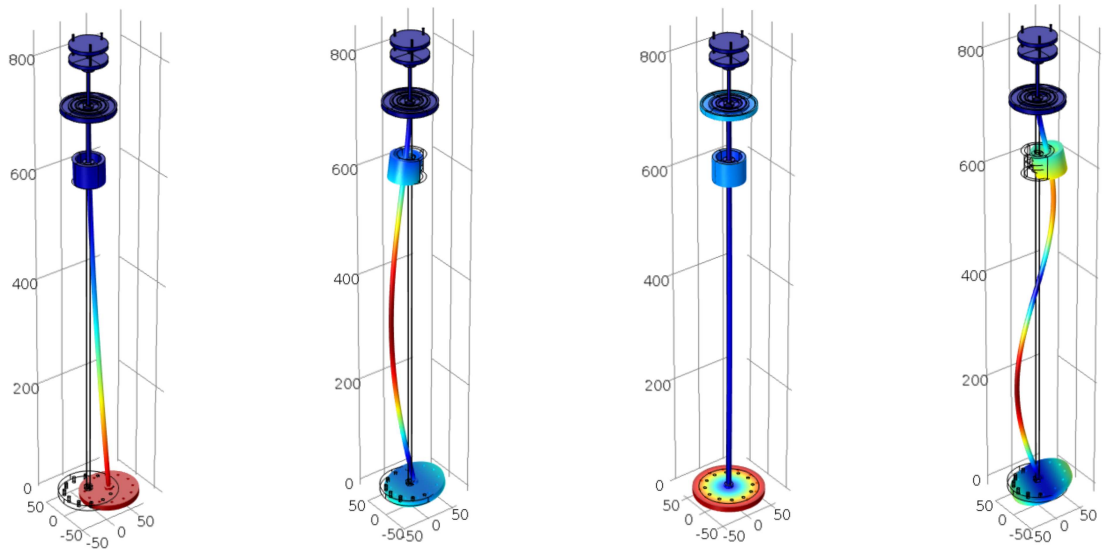

(a) (b) (c) (d)

Fig. 9.5. Eigen modes of the rotating shaft – 2nd(a), 4th(b), 5th(c), 7th(d).

Table 9.1. Eigenfrequencies of the flexible shaft.

number of eigenfrequency	1	2	3	4	5	6	7
f[Hz]	5.96	5.98	49.42	49.57	65.43	116.50	116.97

Programmable Automation Controller

To perform diagnostic and control tasks, the OPTISTER company developed the Programmable Automation Controller [121] according to the AGH license. This device was successfully applied to control the active magnetic radial bearing [108]. The laboratory test rig consists of a HITACHI inverter to control the AC drive. The inverter is controlled by the analog output. The axial magnetic bearing requires two control signals to steer the upper and lower electromagnets (at this stage, the coils of the actuators remained connected in series). The radial magnetic bearing uses four control signals to steer the heteropolar configuration independently. Rotor displacement is measured by proximity sensors. The PAC controller operates in two configurations:

1. as front-end hardware, PAC operates as a signal scaling and power actuator device; the control algorithm runs on Windows platform supported by MATLAB/Simulink in real-time mode, and the installed RTDAC board handles the signal exchange between the PC and PAC,
2. as an embedded controller into the PAC main module to process signals directly via the controller.

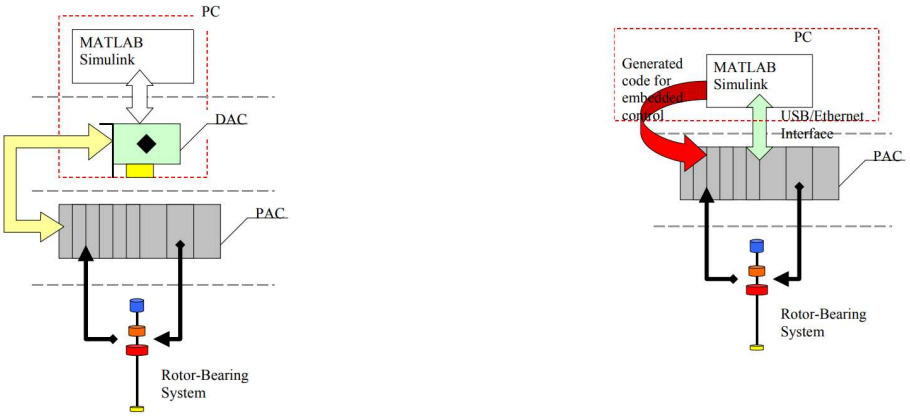

Fig. 9.6. Two variants of the rapid prototyping applied with PAC: (a) in a frontend mode; (b) in an embedded mode.

In the first configuration, PAC performs all the scaling and initial processing of the analog signal. The power modules are used to supply magnetic bearings. The signals are exchanged by the digital-to-analog (DAC) board and converted in analog-to-digital and digital-to-analog ways by the DAC board and MATLAB/Simulink device drivers. This configuration provides an opportunity for rapid prototyping of the identification and control task. However, it has one disadvantage as a result of the application of the DAC board with multiplexed A/D. In this configuration, the target application runs on a PC with real-time performance limited by the Windows and Simulink Real-Time Desktop kernel. In the second configuration, the designed signal processing procedure can be developed manually in the form of S-function or C code and embedded in the PAC software. The real-time control algorithm is carried out directly by PAC with full access to its resources, such as parallel measurements performed by the A/C module or parallel signal generation by the D/A module.

9.2. Reconfigurable set-up of six pole axial active magnetic bearing

The section core is the identification and experimental verification of the novel design of active axial magnetic bearings with six cylidrical poles (see Chapter 6). The aim of this investigation was to add axial AMB to a rotor-shaft assembly and potentially replace radial AMB with a passive configuration based on PMs. One can notice that the developed test rig is universal for research purposes and can be configured with different locations and the presence of components to emulate different types of machinery. For the considered test rig (Fig. 9.7a) three scenarios were adopted. Firstly, a single axial AMB arrangement with a long shaft, then supported, respectively, by one and two passive radial magnetic bearings. For the first two cases, the rotor consists of a disc on a shaft and a measuring surface in a form of mechanical bearing (Fig. 9.7b). Five proximity sensors were used, three for a disc plane (Fig. 8.1c) and the other two to measure the position x-y of the rotor shaft.

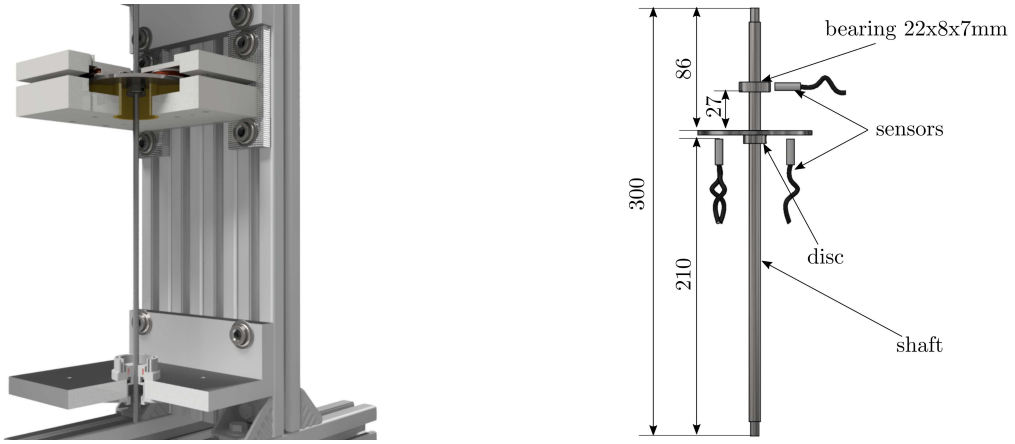

(a) The 3D model of the 6pAAMB reconfigurable setup.

(b) Rotor-shaft assembly dimensions.

Fig. 9.7. The 6pAAMB test rig with a disc mounted on a long shaft.

The 6pAAMB prototype was supplied by the 12 V 6 A H-bridge to investigate the actuator time constant and to lift the rotor-shaft assembly. The real-time experiment was performed with the support of MATLAB/Simulink running at 1 kHz. In the designed control system, RT-DAC4/PCI (www.inteco.pl) was used. This board contains 4 output PWM channels. Counters of the base PWM period may work in the 8 or 12 bit mode. The default input frequency of the PWM channel is equal to 20 MHz. The given frequency is divided by the prescaler to obtain the PWM base period.

9.2.1. Axial active magnetic suspension of rotor-shaft assembly

The first configuration variant is the rotor shaft (Fig. 9.7b) levitated by the 6pAAMB. The actuator used during the experiments was a voltage-controlled device, which means that the input is a voltage and the output parameters are controlled by the input voltage. The measurement was recorded with Rigol DS1104Z Plus 100 MHz 1 GSa/s digital oscilloscope. The LCR meter was used to examine the

electrical parameters of the electromagnets connected in series and individually as a function of the signal frequency (see Table 9.2). It is possible to estimate the differences in electromagnet performance and introduce potential correction factors. In the desired operating frequency range of the actuator, the maximum differences in R and L between particular electromagnets are less than 5%. This is a satisfactory result, considering the manual winding of the coils on 3D printed bobbins. In the course of parameter identification, the time constants of the electromagnet's current increasing and falling edges were determined (Fig. 9.8). They are less than 1 ms, which allows for model simplification by introducing direct force control due to the practically instantaneous current response in a single sampling period.

Table 9.2. LCR measurement versus frequency for the 6pAAMB 1st prototype with disc.

f[kHz]	EM	L[mH]	R[Ω]	C[mF]	Z[Ω]	ϕ[°]	Q[-]
0.1	all	1.408	3.309	1.793	3.426	15.0	0.265
	1	0.453	1.088	5.564	1.124	14.7	0.261
	2	0.434	1.076	5.820	1.110	14.3	0.253
	3	0.437	1.088	5.790	1.119	14.1	0.250
0.12	all	1.392	3.324	1.124	3.487	17.5	0.315
	1	0.447	1.094	3.890	1.145	17.2	0.309
	2	0.428	1.085	4.060	1.130	16.6	0.300
	3	0.432	1.094	4.030	1.142	16.6	0.299
1	all	1.179	4.534	$2{,}140 \times 10^{-2}$	8.686	58.5	1.630
	1	0.379	1.475	$6{,}680 \times 10^{-2}$	2.803	58.2	1.610
	2	0.362	1.456	$6{,}990 \times 10^{-2}$	2.700	57.4	1.560
	3	0.369	1.463	$6{,}870 \times 10^{-2}$	2.736	57.7	1.580
10	all	0.789	20.220	$3{,}200 \times 10^{-4}$	53.470	67.8	2.450
	1	0.256	6.429	$9{,}900 \times 10^{-4}$	17.309	68.2	2.510
	2	0.244	6.172	$1{,}040 \times 10^{-3}$	16.501	68.1	2.480
	3	0.248	6.301	$1{,}020 \times 10^{-3}$	16.785	68.0	2.480
100	all	0.418	118.880	$6{,}050 \times 10^{-6}$	287.300	66.2	2.270
	1	0.138	38.100	$18{,}300 \times 10^{-6}$	94.810	66.3	2.280
	2	0.132	36.340	$19{,}200 \times 10^{-5}$	90.430	67.0	2.350
	3	0.134	36.470	$18{,}900 \times 10^{-5}$	91.700	66.5	2.300

Cross coupling analysis between the 6pAAMB electromagnets

In the described system, it was necessary to investigate the possibility of cross-couplings between individual electromagnets. For the purpose of this analysis, a set of experiments was proposed to help determine the presence or absence of such interactions. The experiments were carried out according to 4 scenarios:

1. disc's position fixed on the reference plane and the 6pAAMB electromagnets driven by:
   (a) square wave voltage signal with 5 s period, 3.5 V amplitude and 50% duty cycle,
   (b) sine wave signal with 3.5 V amplitude, 1 V offset, 1 Hz frequency and zero phase,
   (c) trapezoidal signal: ramp to 5th s, 5 V constant value to 10th s and ramp to 15th s.

2. disc with zero air gap adheres to the actuator plane; the 6pAAMB electromagnets driven as in 1,
3. disc with trapezoidal excitation; observation of the minimum conditions necessary to lift the rotor,
4. disc attracted to the actuator plane with subsequent switching off of the electromagnets; study of the rotor's motion during the fall.

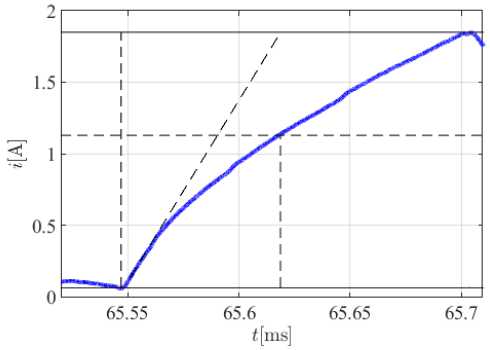

(a) Current rising edge; T_i^{up}=71.7 μs.

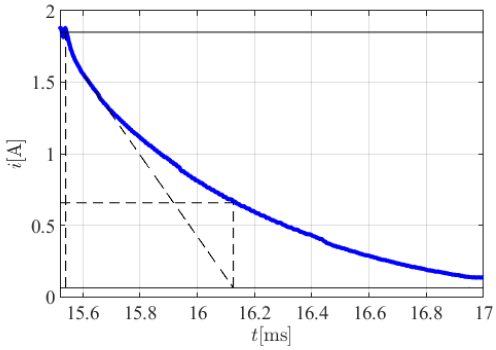

(b) Current falling edge; T_i^{dn}=585.5 μs.

Fig. 9.8. Time constant of the 6pAAMB first electromagnet with disc presence (graphical method).

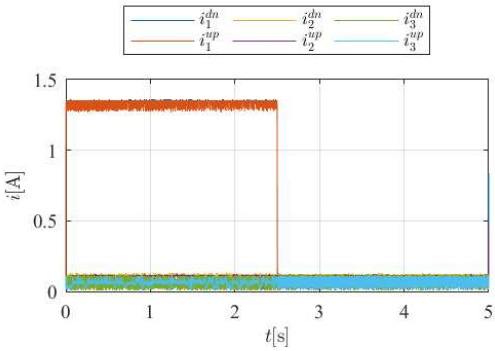

(a) Current from 1st EM driven by square wave signal.

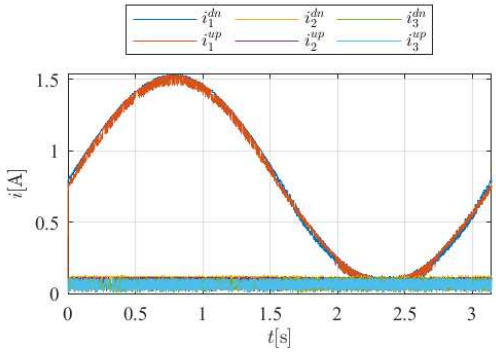

(b) Current from 1st EM driven by sinusoidal signal.

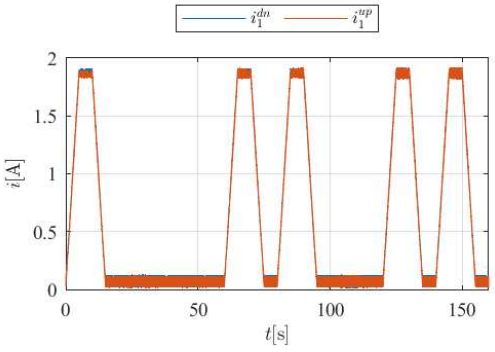

(c) Current in 1st EM for 1.c and 2.c experiment.

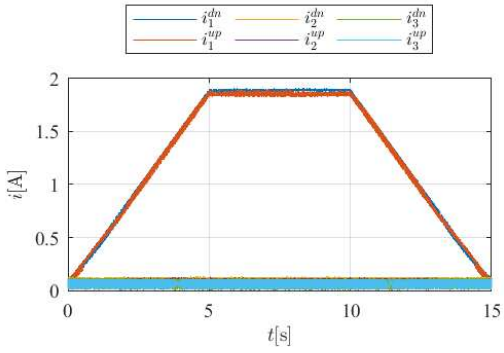

(d) Current from 1st EM driven by trapezoidal signal.

Fig. 9.9. Comparison between 1st and 2nd experiment in the 6pAAMB cross coupling analysis.

Experiments 1-3 were carried out for the following sequence of electromagnet control: 1, 2, 3, 1+2, 1+3, 2+3, 1+2+3. Experiment 4 e.g. 123,12,-,123,13,-,123,23,-.

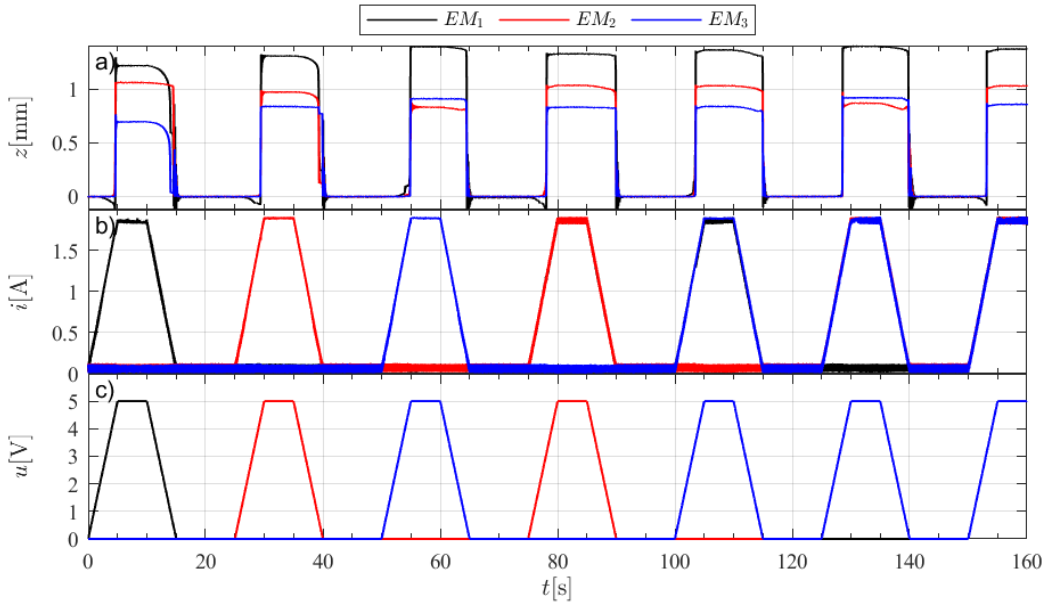

Fig. 9.10. Waveforms of: a.) the position signals, b.) current, c.) control signal for open loop experiment with trapezoidal excitation according to test scenario no. 3.

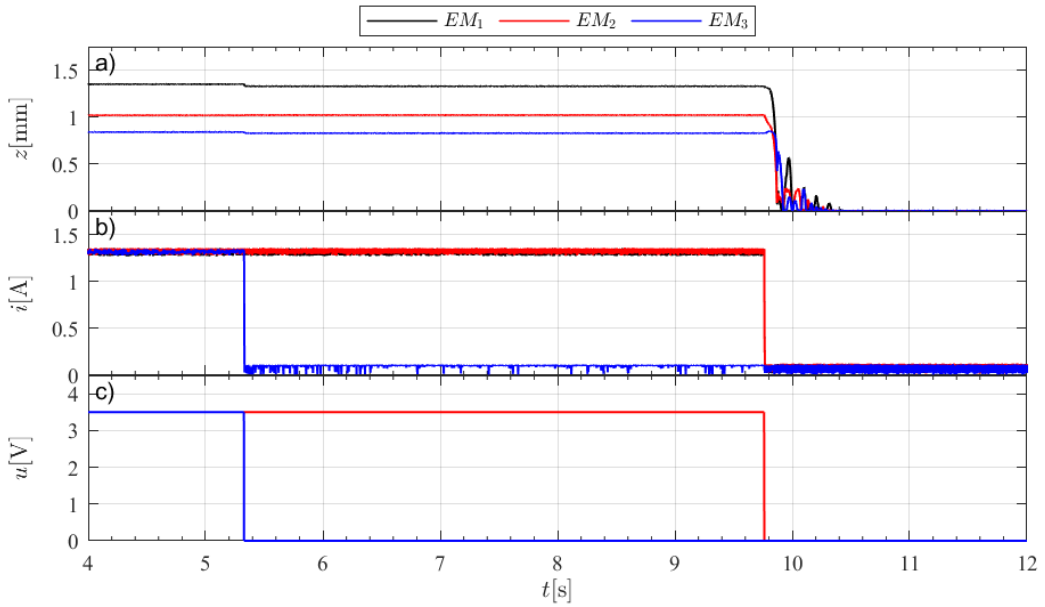

Fig. 9.11. Waveforms of: a.) the position signals, b.) current, c.) control signal for open loop experiment with with switching off individual electromagnets according to test scenario no. 4.

Analysis of the waveforms (see Figs. 9.10, 9.11) allow us to draw conclusions regarding not only cross-couplings, the influence of which in the tested configuration can be neglected, but also the current minimum value necessary to lift the disc, as well as the dynamics of both lifting and falling of the disc.

A deeper analysis of the disc position measured by individual sensors and the current waveforms can be helpful in determining possible differences in the performance of the coils or the chaotic movement of the armature in a given system after assembly. Experimental studies presenting potential cross-couplings were not accompanied by motion diagrams in the x-y plane. These tests did not require analysis of lateral motion, however, it is worth mentioning that the position x-y of the disc in a closed-loop system was not statistically repeatable and that the disc had touched the edge of the housing multiple times.

Table 9.3. The mass of the rotor components in the 1st 6pAAMB test rig.

Element	load handle	bearing	shaft	disc
m[g]	14.70	11.50	110.30	116.50

Due to this observation, a radial passive magnetic bearing (see Fig. 9.12) consisting of eight cylindrical magnets arranged around the periphery in the stationary and rotating parts of the system (Fig. 9.7) was added to the test stand (Fig. 9.7). The RPMB rotor was fixed 30 mm from the bottom plane of the shaft. The purpose of the radial bearing was to increase the stiffness and damping in the x-y plane while ensuring the repeatability of the bearing operating points. Metal spheres of constant diameter 56 mm and variable mass, 103.10 g, 61.40 g and 28.80 g, were attached to the lower part of the shaft. The sphere simulates a static load while helping to center the rotor during levitation. Table 9.4 shows the measured state variables for three different spheres and for seven set points of levitation. Figure 9.14 shows a selected experiment for a levitation level of 500 μm and the 3rd sphere. The disc stabilizes in the z axis and occupies repeatable positions in the x-y space with an accuracy less than 0.075 mm (average of 10 experiments). It can be seen that the current of the 3rd electromagnet is much greater than that of the other. This is due to the nonuniform magnetic field of RPMB and no concentricity with the axial actuator during assembly. RPMB introduces a distributed component of the axial force, which must be identified. Figure 9.13 shows the position of the disc in the x-y plane as a function of its axial air gap z. Taking into account the accuracy and repeatability of these results, a linear trend of change is visible.

(a) (b)

Fig. 9.12. Radial passive magnetic bearing prototype: (a) various 3D printed configurations, differing in the size of magnets and radial clearance; (b) an isometric illustrative model.

Table 9.4. State variables of 6pAAMB with cylindrical poles supported by RPMB (see Fig. 9.12).

m_i	$z[\mu\text{m}]$				$x[\mu\text{m}]$	$y[\mu\text{m}]$	$i[\text{A}]$		
	des	1	2	3			1	2	3
1		320.36	266.68	322.69	736.02	749.25	0.649	0.784	0.890
2	300	289.30	282.68	296.91	809.21	763.61	0.591	0.650	0.838
3		294.82	285.14	272.27	856.30	820.42	0.519	0.547	0.778
1		370.66	327.87	372.49	776.84	754.76	0.593	0.694	0.842
2	350	346.04	342.50	351.82	836.02	788.36	0.527	0.568	0.797
3		347.12	338.82	326.96	876.63	841.65	0.467	0.481	0.730
1		420.10	384.96	420.08	805.62	771.32	0.535	0.619	0.812
2	400	401.07	400.00	405.00	859.33	810.63	0.478	0.499	0.757
3		398.69	390.33	377.06	899.95	849.00	0.425	0.422	0.701
1		473.36	438.23	472.10	824.28	790.24	0.476	0.540	0.780
2	450	457.52	456.80	459.00	873.91	826.40	0.430	0.429	0.716
3		450.61	441.49	427.12	892.67	846.67	0.385	0.364	0.677
1		541.54	488.97	533.39	828.45	831.94	0.403	0.461	0.735
2	500	514.35	514.41	514.49	889.65	847.47	0.373	0.350	0.674
3		502.44	493.60	480.00	913.66	868.02	0.338	0.300	0.642
1		590.21	541.87	571.16	859.68	852.32	0.349	0.369	0.700
2	550	574.26	570.86	552.44	924.29	880.65	0.308	0.263	0.641
3		555.51	545.10	523.46	937.99	901.60	0.286	0.234	0.614
1		641.28	574.88	575.76	896.82	868.34	0.296	0.296	0.662
2	600	609.07	615.81	608.31	967.01	901.99	0.275	0.220	0.596
3		611.18	591.72	555.11	951.07	914.14	0.233	0.176	0.555

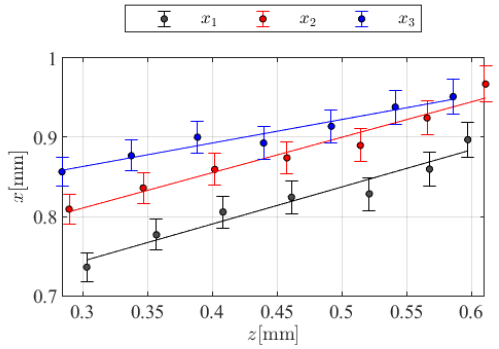

(a) Position x versus axial position.

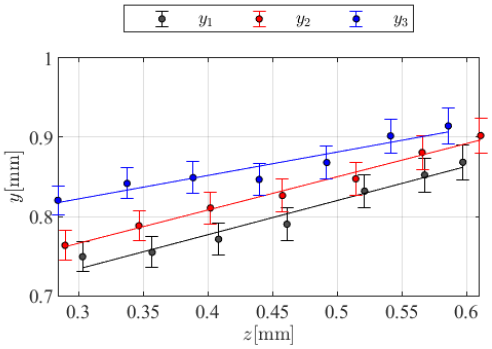

(b) Position y versus axial position.

Fig. 9.13. Average steady state values of planar disc position with the linear trend.

The developed 3D models of the axial and radial AMBs were helpful in analyzing the magnetic field distribution, the electromagnetic force values with respect to the coil current and the position of the rotor. Moreover, the analysis of possible shaft deflection provides feedback for the design and control of AMBs. The shaft-rotor deflection can be included in the electromagnetic field calculation. The models and simulation results serve as the basis for mathematical modeling of such a system.

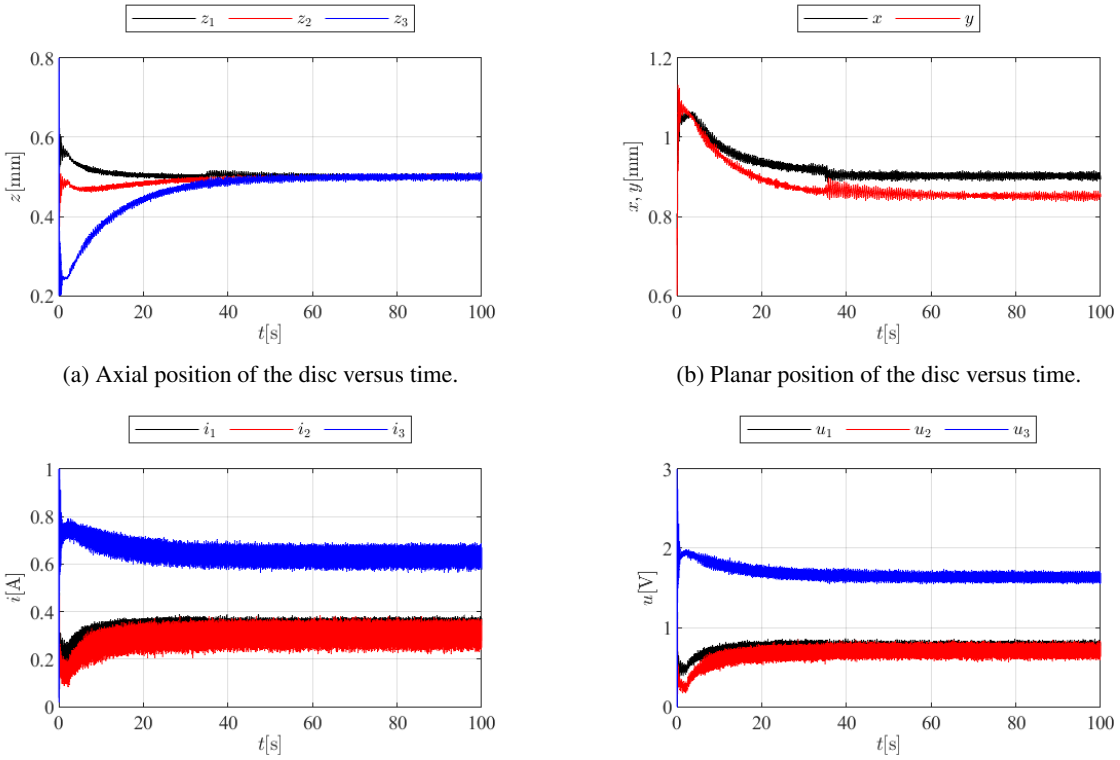

(a) Axial position of the disc versus time.

(b) Planar position of the disc versus time.

(c) Currents of the 6pAAMB versus time.

(d) Control signals of the 6pAAMB versus time.

Fig. 9.14. Disc levitation with 500 μm desired air gap, for the 3rd sphere with mass equal to 28.80 g and a single radial passive magnetic bearing.

Summary of results

This chapter followed on from preliminary research on a reconfigurable magnetic bearing system for flexible shaft machines. The author at that time visited Kumamoto University in Japan, where he saw the ultracentrifuge apparatus for mega-gravity materials science [122], which required the application of magnetic bearings due to the high-speed rotor with uneven radial weight distribution. This was another inspiration for research on AAMB configurations with a few controllable force vectors in the vertical rotor system. Modeling AMS with hybrid actuators or a combination of active and passive bearings is a nontrivial task that requires the identification of mutual interactions between individual elements. It is recommended to extend the 3D modeling to the time domain. In future research, developed models should be enhanced with a deformed mesh to consider shaft-rotor deflection in bearing regions.

Chapter 10

Analytical modeling and experimental validation of six pole axial magnetic bearing

The chapter presents an analytical model of a novel design of the six-pole axial magnetic bearing, which was developed to provide the 3D axial magnetic induction distribution. The model utilizes the magnetic vector potential formulation and Schwarz–Christoffel mapping. The research covers in-depth deliberations on the end effect influence and the conjugate complex permeance function. The numerical model and simulations were provided in the 3D mode with support of COMSOL Multiphysics software. The six pole axial active magnetic bearing was experimentally investigated. Identification of the magnetic field distribution was carried out with a single axis magnetic induction sensor using a custom automatic field scanner. The high convergence of the modeling results and the experimental research was demonstrated. The main advantage of the proposed analytical method is the significantly shorter computation time compared to the numerical one, which is useful from the modeling and controller study point of view. The configuration, modeling, simulation and experimental investigation results are well illustrated for a better overview.

10.1. Review of mathematical modeling methods

In most cases, AMBs are designed based on FEM modeling (see Chapter 7, [40]). Especially in AAMBs, a 3D FEM model requires substantial computational resources. Extending the model with control theory aspects causes a further increase in time consumption, but allows to study the embedded controller in the whole complex model [108]. The key point is to well express nonlinear functions, which describe physical phenomena and geometrical dependencies of the applied design. The continuity and differentiation of the proposed functions is highly demanded. Nevertheless, the analytical results of the magnetic field should be extensively verified with FEM and experimental investigation.

Currently, solutions of AAMBs, which meet the specified application requirements, are the subject of research. The emphasis is on self-bearing drives with the function of axial active suspension [25]. For example, the already mentioned conical AMB with a claw structure [22], which is suitable for use in a limited radial space or actuators based on an axial Halbach array [123] are among the desired configurations. To efficiently model such custom configurations of AAMBs, numerous analytical methods are used during the initial design stage. The paper [24] provides a new graphical approach to the shape

design of the AMB stator using the Bèzier functions. AFPMM slotless configuration is presented in [31]. By imposing suitable boundary conditions, a new method is introduced for the influence of slotting in linear electric machines [124]. In [32] an optimization of PMs design was systematized. The analysis of a pole transition over slots was carried out in [125] while an improved analytical model based on a subdomain technique was presented in [126]. The subdomain model of the PMs-biased homopolar radial magnetic bearing may be found in [35].

The key issue in the AAMB actuator is the distribution of the magnetic field in a bearing space. The chapter presents a comprehensive approach to modeling 6pAAMB (see Chapter 6; refer to Tab. 6.2 for model parameters). The feasibility of the proposed analytical model is verified by 3D FEM and validated by the experimental data. The model introduces the complex permeance function expanded by a radial variation of the magnetic field due to the end effect and applies it to the armature reaction filed from an actuator to obtain a 3D magnetic field distribution in the 6pAAMB air gap.

10.2. Analytical modeling of the six pole axial magnetic bearing

10.2.1. Armature reaction field

A current density distribution in armature coils can be written using the Fourier series [127]. It is possible to express the equivalent current density with the use of various functions, which can facilitate the following symbolic calculations. The chosen function (10.1) defined for $u \in [-\pi r, \pi r]$ is given in Fig. 10.1. It is assumed that the current is uniformly distributed so that the total current that crosses any segment of width Δu along the u direction is $J(u)\Delta u$. The line current density is provided by Ampere's circuital law.

$$J(u) = \begin{cases} \frac{N \cdot i}{w_c} \ , & for\ u \in (\frac{w_p}{2}, \frac{w_p}{2} + w_c) \\ 0 \quad , & for\ other\ \ u \end{cases} \tag{10.1}$$

where N is the number of turns in each coil, w_p, w_c α_c denote the pole arc segment, the coil side arc segment and its span angle, u refers to the circumferential coordinate, l and l' denote the total air gap length of the 6pAAMB and the distance from the rotor to the current sheet plane.
Current density Fourier series expansion up to the N_h^{th} harmonic for variant b.) in Fig. 10.1 is in the following form:

$$J(u) = \sum_{n=1}^{N_h} \frac{4Ni}{n\pi w_c} \cdot \sin\frac{Kw_c}{2} \cdot \sin\frac{K(w_c + w_p)}{2} \cdot \sin(Ku) = J_n \sin(Ku), \tag{10.2}$$

where n denotes the harmonic number and $K = \dfrac{n}{r}$.

Variant b.) from Fig. 10.1 enables setting a current for each coil, thus proposing any coil connection. The current sheet method is commonly used in various analytical models of electrical machines [99], but this approach does not take into account dependencies between particular coils and the calculated path of the magnetic field differs from the real one due to the slotting effect, which is not included in an adopted slotless configuration at this stage of modeling. By combination of numerical and analytical tools, coefficients that correct for the magnetic field density distribution may be proposed [128].

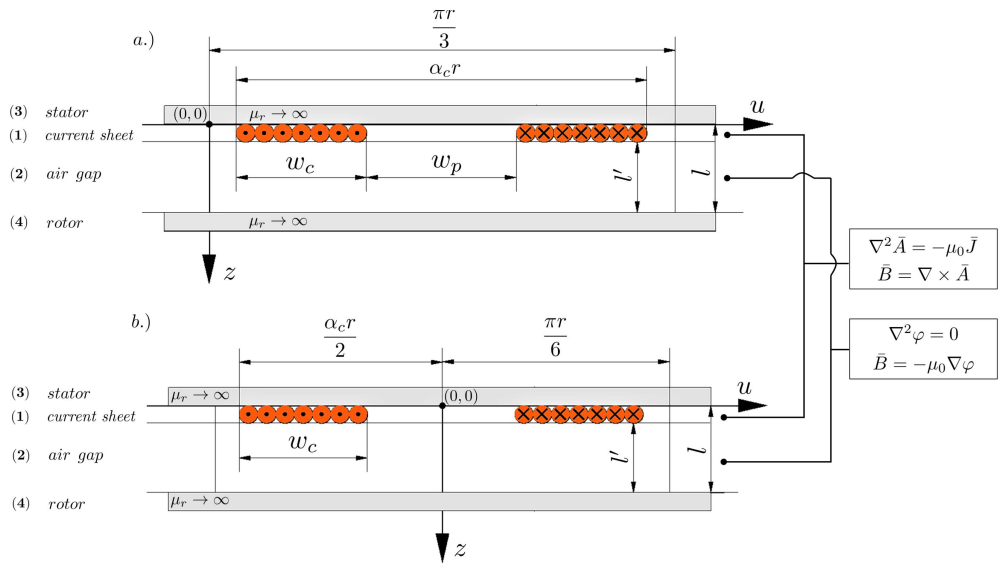

Fig. 10.1. Equivalent current sheet model: a.) a pair of coils as an even function, b.) single coil as an odd function.

Several equivalent current sheet models were developed, including six separately modeled coils, three pairs of adjacent coils or a single function, which covers all the winding. The vector and scalar magnetic potential in the region (**1**) and (**2**) (Fig. 10.1) are described by general formulae given by the following Maxwell's equations in quasi-static form:

$$\nabla \times \bar{H} = \bar{J} \tag{10.3a}$$

$$\nabla \cdot \bar{B} = 0 \tag{10.3b}$$

The Laplace and Poisson equations can be derived from (10.3a) and (10.3b), as follows:

$$\nabla^2 \bar{A} = -\mu_0 \bar{J} \qquad \text{region (1)} \tag{10.4a}$$

$$\nabla^2 \varphi = 0 \qquad \text{region (2)} \tag{10.4b}$$

Solving both the Laplace and Poisson equations, it is possible to express the magnetic flux density distribution in particular regions:

$$\bar{B} = \nabla \times \bar{A} \qquad \text{region (1)} \tag{10.5a}$$

$$\bar{B} = -\mu_0 \nabla \varphi \qquad \text{region (2)} \tag{10.5b}$$

The general solutions[1] of (10.4a) and (10.4b) can be found using the separation of variables, also known as the Fourier method [34], [129]:

$$A^{(1)}(u,z) = \sum_{n=1,3,5...}^{N_h} (C_{11}e^{Kz} + C_{12}e^{-Kz})\sin(Ku) + \sum_{n=1,3,5...}^{N_h} (C_{21}e^{Kz} + C_{22}e^{-Kz})\cos(Ku) + \sum_{n=1,3,5...}^{N_h} \mu_0 \frac{1}{K^2} J_n \sin(Ku) \tag{10.6}$$

$$\varphi^{(2)}(u,z) = \sum_{n=1,3,5...}^{N_h} (C_{31}e^{Kz} + C_{32}e^{-Kz})\sin(Ku) + \sum_{n=1,3,5...}^{N_h} (C_{41}e^{Kz} + C_{42}e^{-Kz})\cos(Ku) \tag{10.7}$$

which, due to the selected current density Fourier series expansion (10.2), are simplified:

$$A_j^{(1)}(u,z) = \sum_{n=1,3,5...}^{N_h} (C_1 e^{Kz} + C_2 e^{-Kz} + \mu_0 \frac{1}{K^2} J_n) \sin\left(Ku - \frac{1}{3}n\pi(j-1)\right) \tag{10.8}$$

$$\varphi^{(2)}(u,z) = \sum_{n=1,3,5...}^{N_h} (C_3 e^{Kz} + C_4 e^{-Kz})\sin(Ku) \tag{10.9}$$

where C_1, C_2, C_3, C_4, which depend on z and n, are obtained from the boundary conditions (10.11), as a solution to a set of equations that describes regions (**1**) and (**2**) and j stands for a coil's number. It was assumed that the stator and rotor iron cores are infinitely permeable, which makes the tangential component of the magnetic field intensity negligible. The total magnetic potential vector is a sum produced from each coil (10.10):

$$A^{(1)}(u,z) = \sum_{j=1}^{6} A_j^{(1)}(u,z) \tag{10.10}$$

$$\begin{cases} H_z^{(1)}(u,z) \Big|_{z=l-l'} = H_z^{(2)}(u,z)\Big|_{z=l-l'} \\ H_u^{(1)}(u,z) \Big|_{z=0} = 0 \\ H_u^{(2)}(u,z) \Big|_{z=l} = 0 \\ H_u^{(2)}(u,z) \Big|_{z=l-l'} - H_u^{(1)}(u,z)\Big|_{z=l-l'} = -J(u) \end{cases} \tag{10.11}$$

[1] Refer to Tab. 6.2 for model parameters and the adopted coordinate system of 6pAAMB.

where $l-l' \to 0$, but to facilitate calculations the value was set to 10^{-4}m. The flux densities are calculated from:

$$\begin{cases} B_z^{(1)}(u,z) & = \frac{\partial A^{(1)}(u,z)}{\partial u} \\ B_u^{(1)}(u,z) & = \frac{\partial A^{(1)}(u,z)}{\partial z} \\ H_z^{(2)}(u,z) & = -\frac{\partial \varphi^{(2)}(u,z)}{\partial z} \\ H_u^{(2)}(u,z) & = -\frac{\partial \varphi^{(2)}(u,z)}{\partial u} \end{cases} \tag{10.12}$$

10.2.2. Effect of slotting

Slotting influence on the magnetic flux distribution in the air gap can be implemented analytically in a few ways. The Carter coefficient may consider the flux variation per pole, but is not accurate enough for the slotted axial geometry and does not include the imaginary part of the permeance function. The more precise analysis is magnetic equivalent circuit (MEC) [130], the accuracy of which greatly depends on the used discretization level. Furthermore, air gap reluctance paths, when consider rotating rotor, are time-dependent, thus need to be properly modeled to find a compromise between the accuracy of the result and the complexity of the calculations. The subdomain modeling technique considers the interdependence of different slots, but often the model preparation and computation consume more time compared to other techniques. In case of 6pAAMB, a complex Schwarz-Christoffel transformation (SC) was incorporated to account for a slotting effect to obtain the relative permeance function (10.13).

$$\lambda_{sc}(u,z) = \lambda_z(u,z) + j\lambda_u(u,z) \tag{10.13}$$

$$\begin{cases} a & = \frac{1}{b} \\ b & = \left(\frac{w_{so}}{2l} + \sqrt{\left(\frac{w_{so}}{2l}\right)^2 + 1} \right)^2 \\ Z & = j\frac{l}{\pi}\left(\ln\left|\frac{1+p}{1-p}\right| - \ln\left|\frac{b+p}{b-p}\right| - \frac{2\cdot(b-1)}{\sqrt{b}} \arctan\frac{p}{\sqrt{b}} \right) + l + ju_2 \\ p^2 & = \frac{w-b}{w-a} \end{cases} \tag{10.14}$$

In order to account for a slotting effect, the conformal mapping technique (based on SC) was introduced by Žarko et al. in [32], where the equations of this transformation are described in detail. Axial geometry requires several operations between complex Z-plane, W-plane and smooth surface T-plane (Fig. 10.2). The key coefficients and equations are presented in (10.14). The value of the argument w cannot be calculated explicitly due to the nonlinearity of the function Z. To solve this problem, the nonlinear least-squares solver with an optimization algorithm based on the Levenberg-Marquardt method was used as a built-in MATLAB function *lsqnonlin* (10.15).

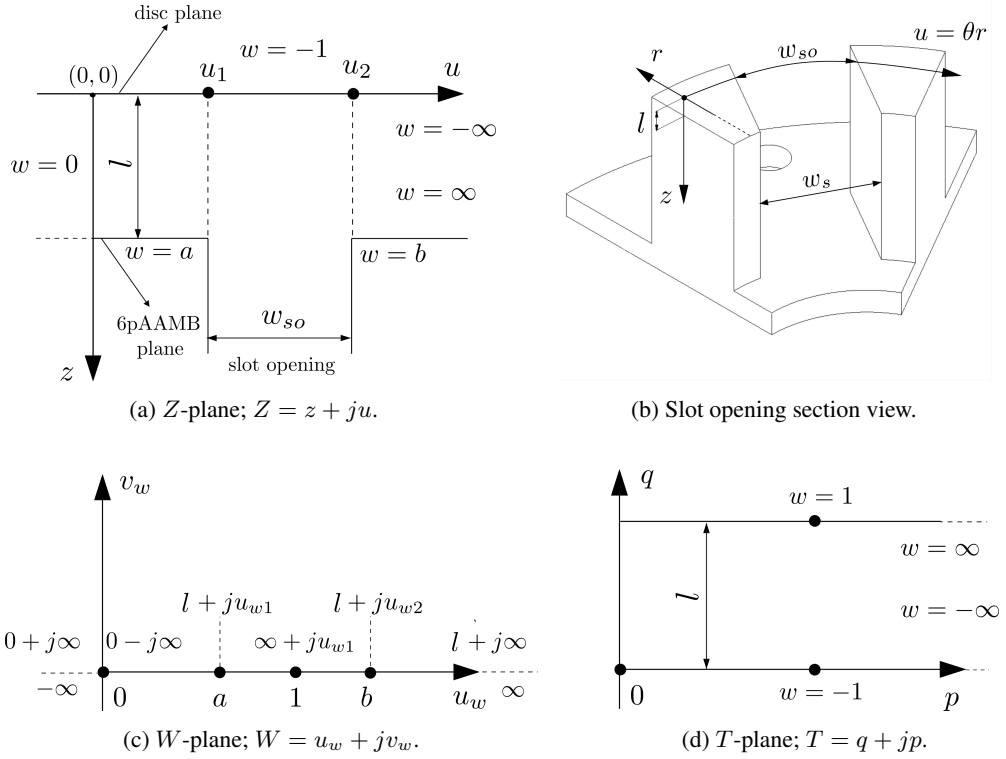

(a) Z-plane; $Z = z + ju$.

(b) Slot opening section view.

(c) W-plane; $W = u_w + jv_w$.

(d) T-plane; $T = q + jp$.

Fig. 10.2. Conformal mapping of the 6pAAMB slot opening, by using complex SC transformation.

$$\min_{w\in\mathbf{C}} f(w) = \sum_{i=1} (Z - Z_m)^2 \tag{10.15}$$

where Z denotes the nonlinear function dependent on w and calculated with its current iteration. The complex permeance function will be calculated along a given path Z_m (10.16).

$$Z_m = z_m + ju_m \quad \text{defined for} \quad \begin{cases} z_m \in [0, l] \\ u_m \in [0, 2\pi r] \end{cases} \tag{10.16}$$

The outcome of the nonlinear least-squares problem approximation enables to calculate the complex relative permeance function. The slotless magnetic field distribution in the air gap multiplied by the conjugated permeance results in the 6pAAMB total air gap magnetic field distribution (10.18)-(10.20):

$$\lambda^*_{sc}(u,z) = \frac{\partial T}{\partial W} \cdot \frac{\partial W}{\partial Z} = \left[\frac{w-1}{\sqrt{w-a}\cdot\sqrt{w-b}}\right]^* \tag{10.17}$$

$$B^t(u,z) = B(u,z)\lambda^*_{sc}(u,z) \tag{10.18}$$

$$B^t_z(u,z) = B_z(u,z)\lambda_z(u,z) + B_u(u,z)\lambda_u(u,z) \tag{10.19}$$

$$B^t_u(u,z) = B_u(u,z)\lambda_z(u,z) - B_z(u,z)\lambda_u(u,z) \tag{10.20}$$

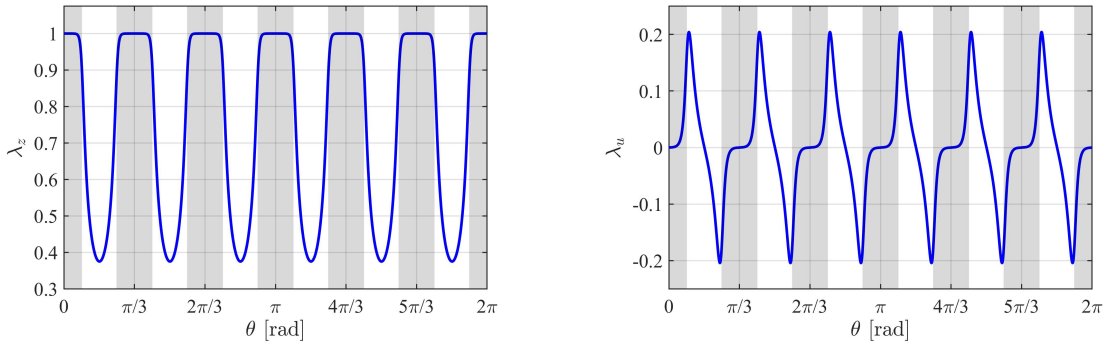

(a) Real part.

(b) Imaginary part.

Fig. 10.3. Complex relative permeance λ_{sc} in the middle of the air gap of 6pAAMB for the average radius.

where $B_z(u,z)$, $B_u(u,z)$ are the axial and tangential components of the flux density in the slotless air gap and $\lambda_z(u,z)$, $\lambda_u(u,z)$ are the real and imaginary parts of the complex relative air gap permeance. It is important to note that, for example, the axial component of the flux density in the slotted air gap (10.19) is a function of the axial and tangential components of the flux density in the slotless air gap. Figure 10.3 presents a real and imaginary part of the complex relative permeance, where the gray bars indicate the position of the pole pieces; thus, a decrease in the real part outside the pole pieces, as well as a value of the imaginary part above their surface, which tends to zero, can be observed.

10.2.3. End effect analysis

In electrical machines with axial flux, the variation of the flux density along the radial component r in the air gap has an impact on the electromagnetic force and a possible location of sensors, so it is important to model the end effect [131] of 6pAAMB accurately.

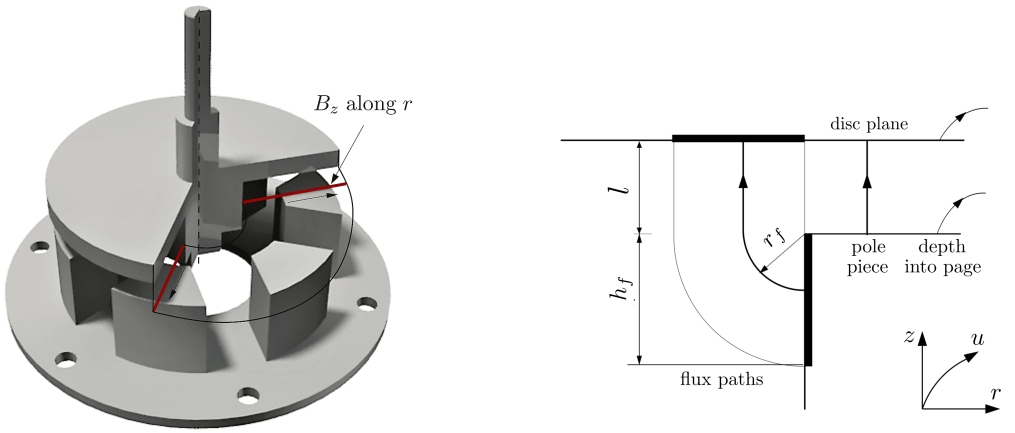

(a) Flux measurement path in the radial direction.

(b) Path of the fringing flux for a single pole piece.

Fig. 10.4. End effect consideration in 6pAAMB.

This issue is particularly relevant not only for designing a favorable magnetic circuit, but also for determining the influence of transverse flux in the active space of the actuator on the levitating object with given parameters. A thorough analysis of the end effect allows to obtain a complete spatial distribution of the magnetic field in 6pAAMB. This is crucial for the description of potential cross-couplings in the actuator or the optimal stator geometry design.

The magnetic field distribution along the radial direction is described by the end function F_{end} by analyzing the inner and outer fringing flux path. The end fringing coefficient F_e, which is a ratio between the flux from the main magnetic circuit and the total one, was calculated using several methods, i.e.:

- 1D MEC analysis [59],
- a total permeance of a given surface (2D),
- conformal mapping (SC),
- 3D FEM analysis.

The permeance of the 1D MEC method, shown in Fig. 10.4b, is expressed as:

$$P_{main} = \frac{\mu_0}{g}, \tag{10.21}$$

$$P_f(r) = \begin{cases} \frac{\mu_0}{\frac{\pi}{2}(R_i - r) + l} \; for \; r \in (R_i - h_f, R_i), \\ \\ \frac{\mu_0}{\frac{\pi}{2}(r - R_o) + l} \; for \; r \in (R_o, R_o + h_f), \end{cases} \tag{10.22}$$

where h_f denotes an arbitrary distance at which the fringing effect begins. The end function from 1D MEC is as follows:

$$F_{end}^{MEC}(r) = \begin{cases} \frac{l}{\frac{\pi}{2}(R_i - r) + l} \; for \; r \in (R_i - h_f, R_i) \\ \\ 1 \qquad\qquad for \; r \in (R_i, R_o) \\ \\ \frac{l}{\frac{\pi}{2}(r - R_o) + l} \; for \; r \in (R_o, R_o + h_f) \end{cases} \tag{10.23}$$

A total permeance of the pole piece based on 2D approach requires calculating its area and surface integration over the variable flux path, using, e.g., Green's theorem. This approach does not provide the end effect function distribution along the radial direction. Another approach, so far not noticed in the literature, is the use of SC for the description of the end function in electric motors and actuators. In 6pAAMB the SC method was adapted to opposite pole pieces. The distance between them corresponds to the slot opening (Fig. 10.5a) and it was assumed that the radial length of the pole piece is its width. The applied transformation in the form of the real part lambda function (Fig. 10.5b) is approximately consistent with the performed measurement along the radius of the pole piece. The discrepancy occurs when the magnetic induction drops beyond the pole piece. To achieve even more matched results, the function is squared (10.24) or the slot opening in the end effect can be increased.

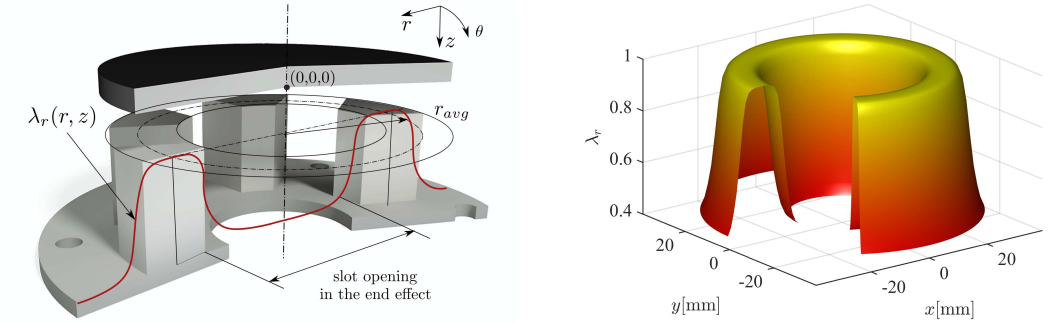

(a) Scheme of SC in the end effect description.

(b) The 3D end function obtained from SC.

Fig. 10.5. The 6pAAMB end effect analysis based on the conformal mapping (SC).

$$F_{end}^{SC}(r,z) = \mathrm{Re}(\lambda_{end}^{*}(r,z))^2 = \lambda_r(r,z)^2 \tag{10.24}$$

$$\lambda_z(r,\theta,z) = \lambda_z(\theta,z)F_{end}^{SC}(r,z) \tag{10.25}$$

$$\lambda_\theta(r,\theta,z) = \lambda_\theta(\theta,z)F_{end}^{SC}(r,z) \tag{10.26}$$

where $\lambda_{end}(r,z)$ denotes complex relative permeance of the slot geometry depicted in Fig. 10.5a. Taking into account the radial variation in the real and imaginary parts of the complex relative air gap permeance (10.25), (10.26), the 3D function is obtained (Fig. 10.6). With its help, it is possible to describe the influence of a pole pieces with the adopted geometry on the magnetic field distribution in the 3D space.

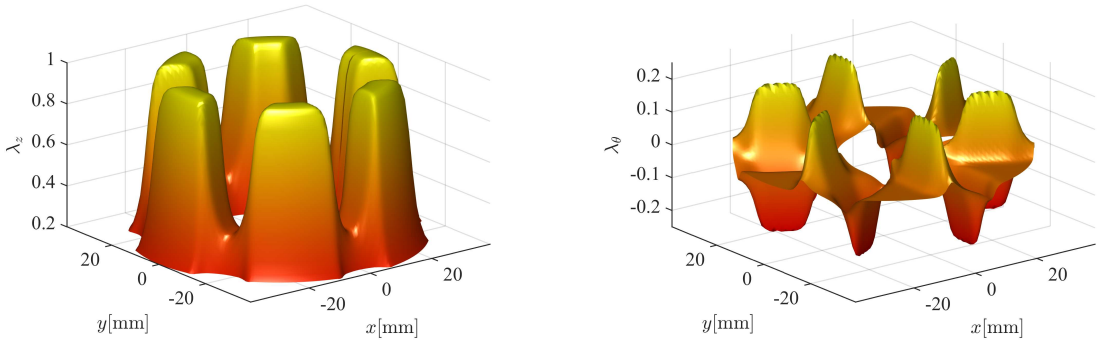

(a) Real part.

(b) Imaginary part.

Fig. 10.6. Complex 3D relative permeance in the middle of the 6pAAMB air gap.

10.3. Numerical model

The numerical simulation of 6pAAMB was prepared (Fig. 10.7) in COMSOL Multiphysics to demonstrate the accuracy of the analytical model. The mesh consists of 135183 tetrahedral elements and is solved for 844128 DoF. The model uses a stationary magnetic field (*mf*) module with six separately modeled coils. The stationary simulation takes about 3 minutes. All computations were performed on a PC with Intel(R) Core(TM) i7 CPU 975 processor with 4 cores.

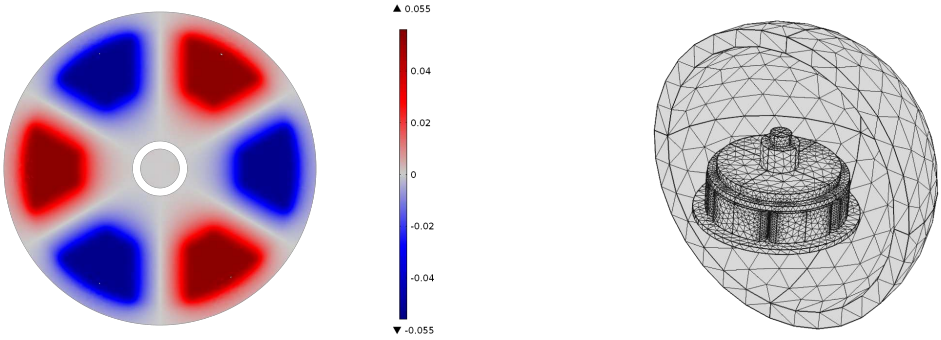

(a) Axial component of the magnetic field in 2D plane.

(b) 3D mesh of the 6pAAMB model domains.

Fig. 10.7. 3D numerical model of 6pAAMB.

Table 10.1. Mesh size versus mesh quality comparison.

mesh refinement	n_t	$\bar{q}$
normal	77942	0.6403
fine	184172	0.6902
finer	510457	0.7101
extra fine	1507779	0.7295

Table 10.2. Comparison of the numerical simulation parameters for different total air gap length l.

l [mm]	t [s]	$\bar{q}$	DoF	RAM [GB]	n_t
3	173	0.6602	844128	3.49	135183
2.5	177	0.6608	846952	3.50	135629
2	180	0.6808	848876	3.57	135931
1.5	190	0.6633	922844	3.68	147620
1	269	0.6731	1174018	3.80	187252
0.5	578	0.6676	2684342	4.69	425621

Table 10.1 compares the size of the mesh with its quality of its average element $\bar{q}$, i.e., a dimensionless quantity between 0 and 1, which reflects a degenerated and perfectly regular element in the chosen quality measure, respectively. The shape regularity of the mesh elements may be evaluated by a mesh element quality factor, which indicates inverted mesh elements and high condition numbers for

Jacobians. This causes solver convergence problems. The COMSOL Multiphysics modeling involves taking into account limitations such as an influence of mesh parameter selection on the numerical output accuracy, the hardware and RAM required to complete computation (DoF solved for), the necessary effort to prepare and properly validate a model or discretization of shape functions, i.e. equations within each element. A more accurate solution may be obtained by increasing the discretization, but without changing the number of mesh elements, it will require more computational time and resources, therefore, it is recommended to study mesh refinement.

Table 10.2 shows the numerical output, which is strongly dependent on the mesh parameters, e.g. the number of tetrahedral elements n_t and the average quality of the mesh element $\bar{q}$, which together with mesh resolution are important aspects of proper validation of a model. Variation in the geometry of the model, e.g. a variable air gap length may lead to inaccurate results.

In the case of 6pAAMB numerical simulation, particular attention was paid to the air gap region of which the mesh was refined separately. Table 10.2 shows the simulation parameters for different set values of air gap l. It can be noticed that with the l reduction, for the adopted mesh size, the simulation is more resource-consuming in terms of time and computational power. This introduces potentially serious limitations when simulating 6pAAMB operation under conditions of disc eccentricity or introducing a preset coil control current in a time-dependent simulation. The 3D finite element analysis may return reliable results, but even then, e.g. in the case of a winding with complex geometry, a difference between measurement and simulation can be observed (Fig. 10.12b).

10.4. Experimental setup

The proposed test setup (Fig. 10.8) was assembled to measure the magnetic induction distribution. The system uses the JK42HS40-0504 stepper motor with 200 default steps per revolution with the DRV8825 45 V / 2.2 A motor driver. The nominal motor torque equaled 0.43 Nm. Induction was measured using the magnetic field meter[2] equipped with a hall sensor. 6pAAMB was attached to the motor axis using printed hyphens. A printed spacer, which allowed for smooth 6pAAMB rotation over the magnetic field sensor, was adjacent to the plane of the stator. The measurement was recorded during a single revolution. The distance between the stator and disc planes was burdened with measurement uncertainty due to the accuracy of the 3D printed elements, the attraction forces of the electromagnets and the fillet radius of the part of the disc adjacent to the spacer. During the experiment, all electromagnets were supplied with the same current in three scenarios: 1.00, 1.66 and 2.00 A. The magnetic induction measurements were made on several radii (Fig. 10.9a), that is, 16.5, 18.5, 22.5, 26.5, 28.5, 30.5 and 32.5 mm. The sample period was equal to 1 ms.

To verify and compare different methods of the end effect analysis, the magnetic induction was measured along the radius of 6pAAMB in the midspan of the air gap (Fig. 10.4a). The probe was moved

[2]TEL-Atomic Inc., Smart Magnetic Sensor, model SMS 102

by half a screw pitch (0.8 mm) every 0.5 s, from 14 mm to 40 mm. A hall sensor was located approximately 1.5 mm from the edge of the probe. The measurement may be affected by an error resulting from:

- the measurement of the probe thickness (caliper accuracy 0.02 mm),
- the manual rotation of the screw that allows the probe radial movement,
- the digital magnetic field meter accuracy (0.5%),
- the hall sensor location estimation in the probe,

which resulted in the assumption of a magnetic induction measurement error of 1.5% and a shift on the radius up to 0.5 mm (Fig. 10.12a). The experimental investigation of 6pAAMB is summarized and discussed in the next section.

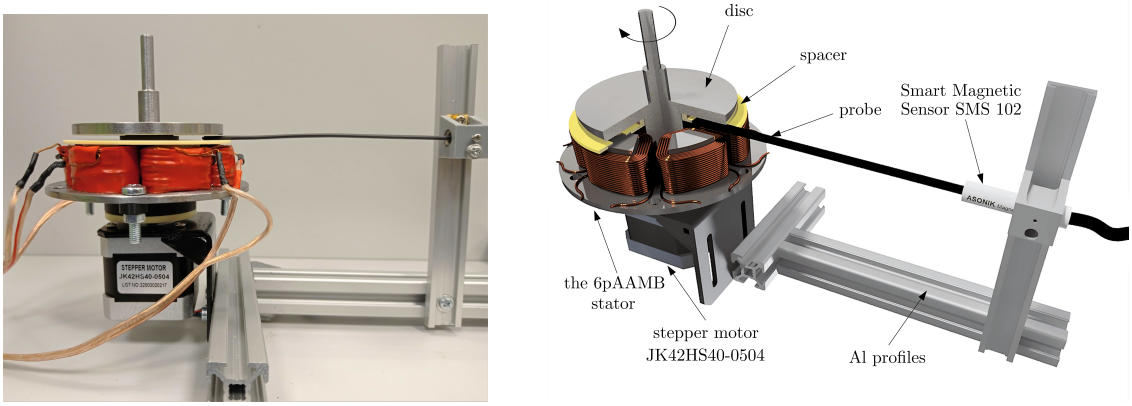

(a) Assembled laboratory test stand.

(b) The 3D model - isometric view.

Fig. 10.8. The setup to measure the magnetic filed distribution around the 6pAAMB stator circumference.

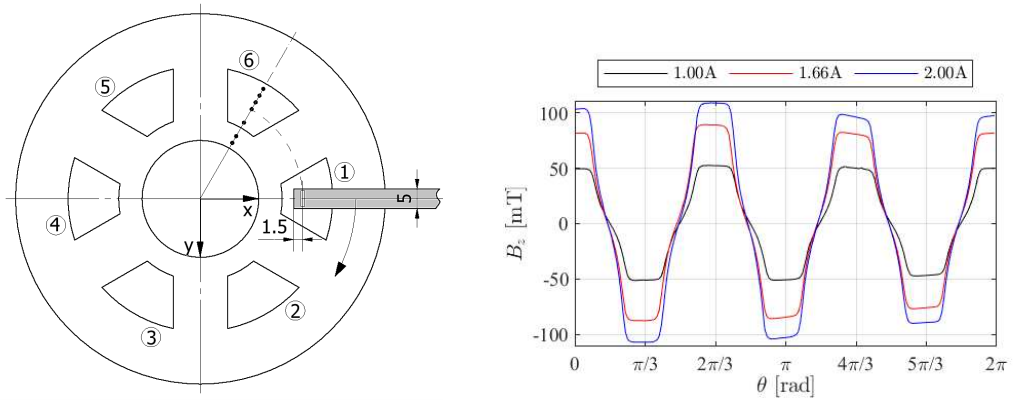

(a) Diagram presenting measurement procedure.

(b) The magnetic field distribution for r=28.5mm.

Fig. 10.9. The magnetic field measurement on the 6pAAMB stator circumference.

10.5. Results and discussion

The experimental data were compared with the results of analytical and numerical calculations. RMSE with regard to experimental data for the 2D analytical model slightly deviated from the 3D numerical one with an average of 0.57 mT (Tab. 10.3). The differences were mainly visible in the extreme radii near the edge of the pole piece or beyond, where the measurement was carried out.

Table 10.3. Comparison of RMSE [mT] between simulation and experimental results for several radii.

RMS	i[A]	r[mm]						
		16.5	18.5	22.5	26.5	28.5	30.5	32.5
EXP-2D	1.00	2.6	3.3	2.2	2.9	2.7	3.0	2.7
	1.66	3.7	5.1	3.6	5.1	4.8	8.2	6.6
	2.00	4.2	6.7	4.7	10.0	8.5	9.1	6.9
EXP-3D	1.00	3.2	3.2	2.9	2.8	2.8	3.0	4.1
	1.66	4.1	5.2	5.0	5.0	5.0	7.7	8.4
	2.00	4.3	6.2	5.6	9.5	7.9	8.5	8.8

Table 10.4. Comparison of the maximum magnetic induction between simulation and experiment for several radii.

B_{max}[mT]	i[A]	r[mm]						
		16.5	18.5	22.5	26.5	28.5	30.5	32.5
EXP	1.00	10.6	19.3	50.8	52.8	52.5	51.7	51.6
	1.66	17.3	31.5	85.6	88.5	89.3	91.1	86.2
	2.00	21.1	38.2	103.9	107.7	108.9	107.7	105.1
2D	1.00	11.1	16.9	49.5	52.5	52.1	52.5	49.4
	1.66	18.4	28.0	82.1	87.2	86.5	87.1	82.1
	2.00	22.2	33.8	98.9	105.0	104.2	104.9	98.9
3D	1.00	12.6	22.5	51.8	52.7	52.5	52.6	53.4
	1.66	20.9	37.5	85.7	86.2	86.6	86.3	86.7
	2.00	25.2	45.2	103.3	103.9	104.4	104.0	104.4

Figure 10.10 shows the magnetic field distribution of 6pAAMB in 2D and 3D. Measurements were carried out for seven radii values. Due to the type of utilized probe, no end effect measurements were performed on the outer side of the stator. The range of results compared to the 2D and 3D models was marked with a transparent cylinder (Fig. 10.10c, Fig. 10.10e). The 2D charts show not only the magnetic induction maximum values on the surface of the pole piece, but also illustrate the trend of the magnetic distribution outside the pole pieces. The analytical model has a slightly flattened transition of the magnetic field distribution through the abscissa, however, the transition point is not shifted and coincides with the experiment and the 3D FEM. Table 10.4 presents the maximum magnetic induction values from experimental data, analytical model and numerical simulation. One can observe the convergence of the results, especially on the radii corresponding to the center of the pole piece.

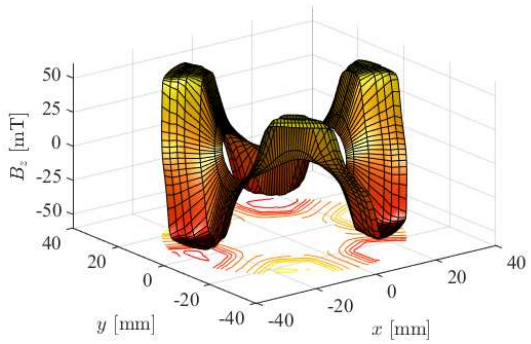

(a) Experimental results (surface).

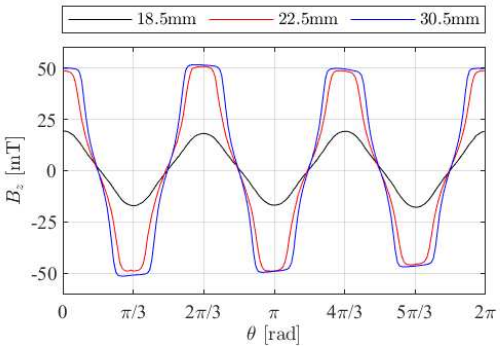

(b) Experimental results for different radii.

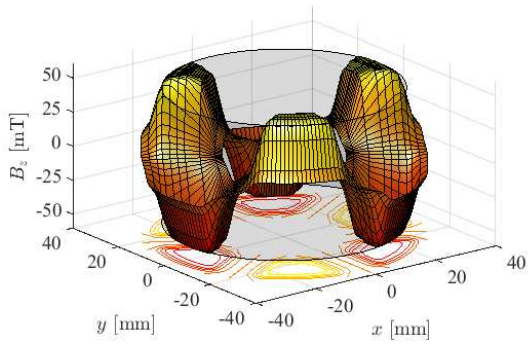

(c) 2D analytical results (surface).

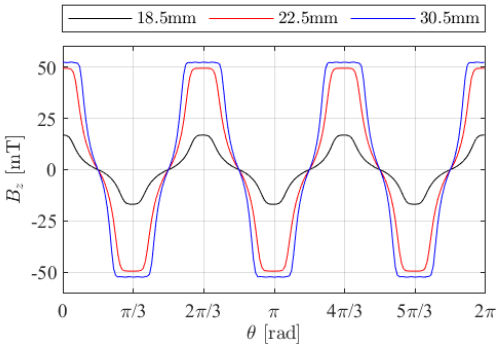

(d) 2D analytical results for different radii.

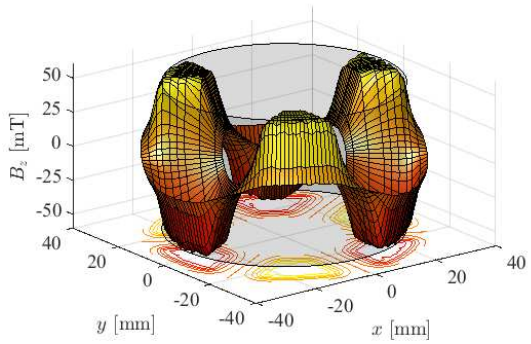

(e) 3D FEM results (surface).

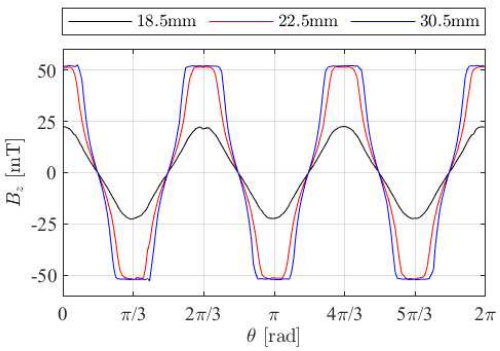

(f) 3D FEM results for different radii.

Fig. 10.10. The axial component of the magnetic field distribution in the middle of the 6pAAMB air gap.

Figure 10.11 shows the absolute error plots. The gray rectangular boxes indicate the areas of the pole pieces. Within them, the differences between individual errors remain constant (Fig. 10.11b, Fig. 10.11c) and decrease as the radius is close to the center of the pole piece (Fig. 10.11d). The relative error of the magnetic induction waveform (Tab. 10.5) for the radius of 28.5 mm and the current 1 A equals 0.5% and 0.1% for the analytical and numerical model, respectively. With an increasing current, the error increases as well, but remains within the model utility limit. The end effect is more accurately reflected in the analytical model.

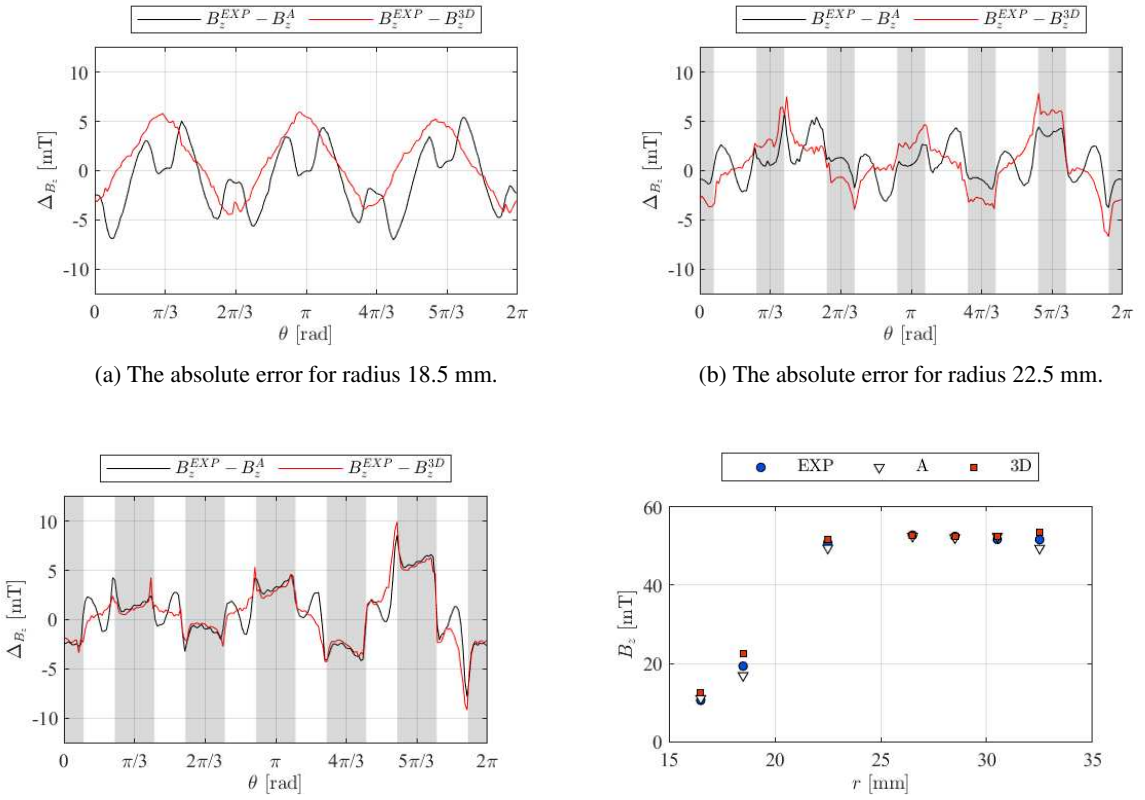

(a) The absolute error for radius 18.5 mm.

(b) The absolute error for radius 22.5 mm.

(c) The absolute error for radius 30.5 mm.

(d) The maximum magnetic field in relation to the radius.

Fig. 10.11. The absolute error of the magnetic field distribution in relation to the experiment.

Table 10.5. Comparison of the relative error δ_B between simulation and experimental results for different radii.

$\lvert\delta_B\rvert$[%]	i[A]	r[mm]						
		16.5	18.5	22.5	26.5	28.5	30.5	32.5
2D	1.00	4.8	12.5	2.6	0.5	0.6	1.5	4.3
	1.66	6.5	11.0	4.1	1.5	3.1	4.4	4.8
	2.00	5.2	11.7	4.8	2.5	4.3	2.6	5.9
3D	1.00	19.4	16.6	1.9	0.1	0.1	1.7	3.5
	1.66	21.0	19.1	0.1	2.6	3.0	5.2	0.5
	2.00	19.5	18.1	0.6	3.5	4.1	3.5	0.6

Table 10.6 and Figure 10.12 present several methods utilized in calculating the end effect. The experiment stands for the reference of this comparison with quality factors, as follows: mean square error MSE, the end fringing coefficient F_e, a mean value of the end function $\overline{F}_{end}$ for a given radial range and the relative errors $|\delta_e|$, $|\delta_{end}|$. The approach of calculating the permeance of a particular surface, using Green's function, returns only F_e. The MEC 1D analysis does not take into account the flux reduction at the pole piece edges. According to the Table 10.6, the measurement end effect function is best approximated by the adapted approach of SC discussed in the *End effect analysis* subsection.

Table 10.6. Comparison of different end effect calculation methods.

method	F_e [-]	MSE [-]	$\lvert\delta_e\rvert$ [%]	$\overline{F}_{end}$ [-]	$\lvert\delta_{end}\rvert$ [%]
EXP	0.782	-	-	0.693	-
MEC	0.765	0.0144	2.222	0.779	12.410
SC	0.801	0.0043	2.372	0.713	2.870
2D	0.735	-	6.395	-	-
3D	0.710	0.0050	10.141	0.744	7.420

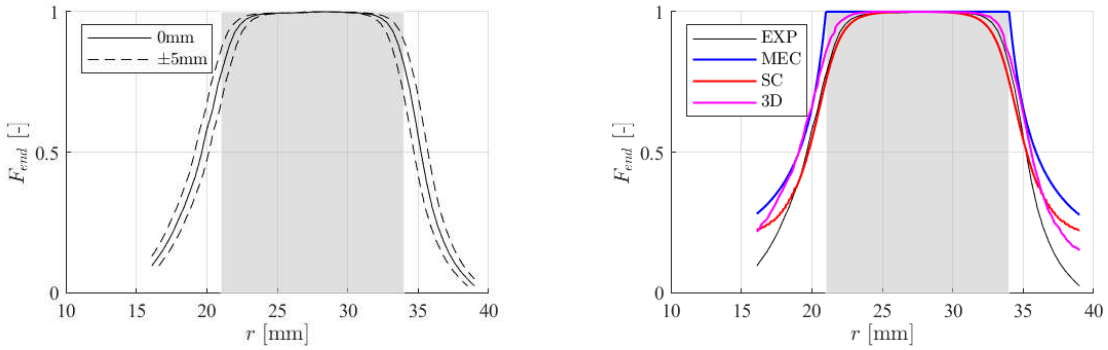

(a) Expected measurement accuracy.

(b) Different modeling approaches.

Fig. 10.12. The end effect function with respect to the radial dimension.

Figure 10.13 shows the distribution of the magnetic field of the analytical model with a different number of harmonics N_h and requested samples N_{div}. Detailed data of this analysis is presented in Table 10.7, which provides the CPU time and RMS between the experimental and analytical results. It can be noticed that, e.g. the fourth simulation output is acceptably close to the first one, with almost 9 times less computational time.

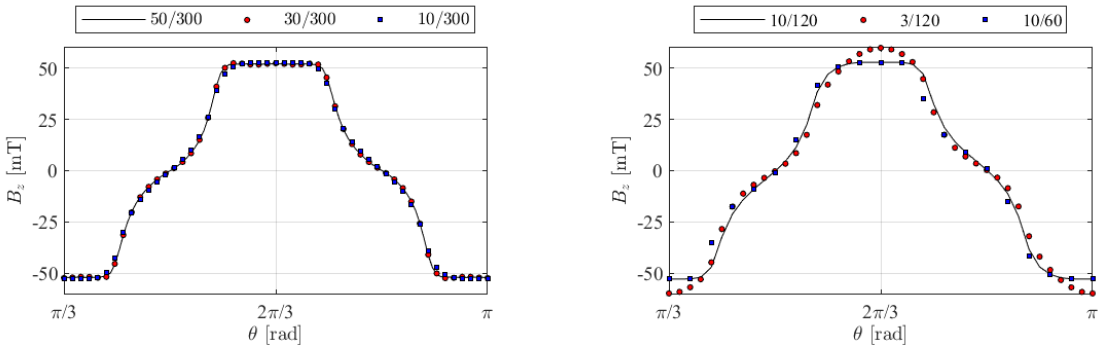

(a) Result of simulations 1÷3.

(b) Result of simulations 4÷6.

Fig. 10.13. The magnetic field distribution of the analytical model for various N_h/N_{div} scenarios.

Table 10.7. Computing resources of the analytical model for various number of harmonics N_h and samples N_{div}.

sim	N_h	N_{div}	t_{CPU}[s]	RMS[mT]
1	50	300	27.8	3.0
2	30	300	16.6	3.3
3	10	300	8.5	3.5
4	10	120	3.1	4.4
5	3	120	2.0	7.0
6	10	60	1.6	6.9

Summary of results

The validated analytical model of the 6pAAMB design, which is effective in terms of computational resources, is the outcome of this chapter. The model is highly convergent with experimental measurement and numerical simulation. In general, it is an extremely useful tool for studying the magnetic field of axial flux machines with a slotted air gap. The mathematical model provides explicit formulae, which are a valuable insight into the magnetic field distribution in the 6pAAMB air gap. To calculate the end effect accurately, the variation of the air gap flux density along the radial direction was calculated using the end function based on the conformal mapping technique, which is a new approach, yielding a result that differed from the experiment with a relative error of less than 3%. The 3D magnetic field distribution in the air gap was calculated rapidly and accurately considering the slotting effect and the end effect without using 3D FEM. The particular parts of the mathematical model comprised separate steps of the design process, enabling the optimization of each stage in line with the individual requirements of a design actuator.

To summarize, the distinguishing features of the proposed model are high convergence with the experiment, fast computing time and the 3D permeance function designed to optimize a slot geometry or select a proper sensing element location for identification and/or control feedback purposes. However, the model does not take into account slot interdependencies and mutual inductance of adjacent coils.

The contribution of the presented chapter serves as a basis for further research, which should focus on a global dynamic model of the levitating disc with 6-DoF and a description of the magnetic induction function $B = f(i, \theta, r, z, \alpha, \beta)$ necessary to control the disc under eccentric conditions. In the following chapters, the reader can appreciate the developed model, which is a useful tool in the process of interdisciplinary design of axial actuators at the stage of construction, identification and optimization.

Chapter 11

Radial passive magnetic bearing in configuration with axial active magnetic suspension

The reliable implementation of passive magnetic bearings depends on the comprehensive design process and the analysis of the magnetic field. Rotating machines require radial bearings to support the rotor. Passive magnetic suspensions are desired when used for industrial applications, such as centrifuges or flywheels, because they do not require any electromagnetic coil supply and can be used in applications that demand low-stiffness capabilities. This chapter presents the configuration of cylindrical magnets that act as a passive radial bearing that supports the lateral stabilization of the levitating rotor in the active axial suspension system with the six-pole actuator. Several experiments showing the properties of the proposed solution are presented. Finally, a proprietary magnetic coupling is used to accelerate the rotor to a speed of 4000 rpm without contact, observing its operation under the given conditions.

11.1. Overview on passive magnetic bearings

Passive magnetic bearings are capable of providing contactless support of an object by attractive or repulsive permanent magnetic forces. Stabilization in a given direction, i.e. radial, axial or tilt depends on a proposed configuration. It is known from Earnshaw's theorem that it is not possible to obtain a stable position in all degrees of freedom only by passive magnetic levitation [132]. In [133] a comprehensive overview of passive magnetic bearing (PMB) configurations is provided. Currently, numerous studies are aimed at obtaining useful PMs structures and configurations in a wide range of their applications supporting the AMB system for rotating machines [134]. Companies specializing in proposing proprietary PMB solutions that meet the expectations of demanding customers and applications for higher reliability and lower power consumption are established [135], [136]. Still the problems to be faced are the inaccuracy of PMs caused by its manufacturing tolerance, the difficulty in the availability of non-standard PM shapes, the interaction with the other ferromagnetic elements of a system as well as problems with the assembly, possible machining and balancing of a PMB rotational part.

Among the most interesting solutions, one can find a conical passive magnetic bearing with constant stiffness [95] with the highest force identified as a function of the tilt angles of the stator and rotor rings. In [137] a PMB was presented with the ability to take radial and axial loads in both directions by

using permanent magnets with axial magnetization. The key in PMB design is to determine the required force characteristics. The known risk of PMBs is due to the relatively low stiffness of the unit compared to rolling bearings. Numerical modeling [138] and analytical calculations [139] are commonly used to describe magnetostatic interactions and forces between PMs of various shapes utilized in magnetic actuators or sensors. The capabilities and potential of PMB have been proved in innovative optimal configurations implemented in diverse applications, to name a few, a magnetically suspended drive with two-axis active position regulation and a bearingless motor for possible flywheel applications [140], a novel structure for PMs-biased radial hybrid magnetic bearing with B_x and B_y magnetic fields independent of each other [17], PMB for a vertical axis wind turbine toward zero friction losses with improved stiffness [141]. An interesting use of passive suspension applicable to water propellers was presented in [142], with a mathematical model that evaluates the value and direction of the magnetic force. Examination of PMB with Halbach array with its stability issues was covered in [143]. Experimental and numerical research was carried out, resulting in satisfactory convergence. Halbach array may be used in axial magnetic coupling [144], where a detailed 3D analytical model is presented. The solution to the 2D problem is incorporated into a 3D magnetic charge sheet model, enabling for accurate torque computation.

11.2. Radial passive bearing design

A model of a PMB housing was prepared (3D printed with Zortrax M200). The cylindrical magnets MW10x5 were selected for the stationary part (Fig. 11.1a) and the ring magnets MP10x6x4 for the rotor. Ring magnets (Fig. 11.1b) are arranged in the same direction and the magnetic field of each magnet affects the moving part of the rotor, bringing it to the equilibrium position. Ring magnets are mounted on the rotor axis together with a height adjustable spacer flange.

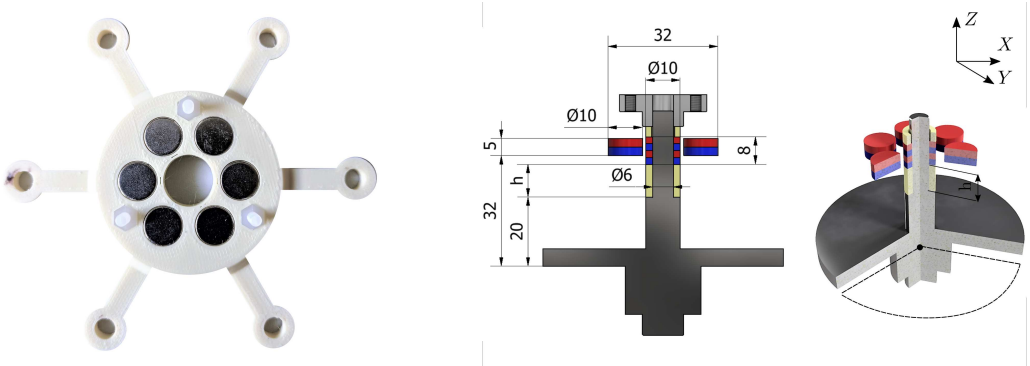

(a) (b)

Fig. 11.1. Passive radial magnetic bearing design: a.) outer stationary part, b.) dimensions and position of the magnets relative to the rotor measuring plane.

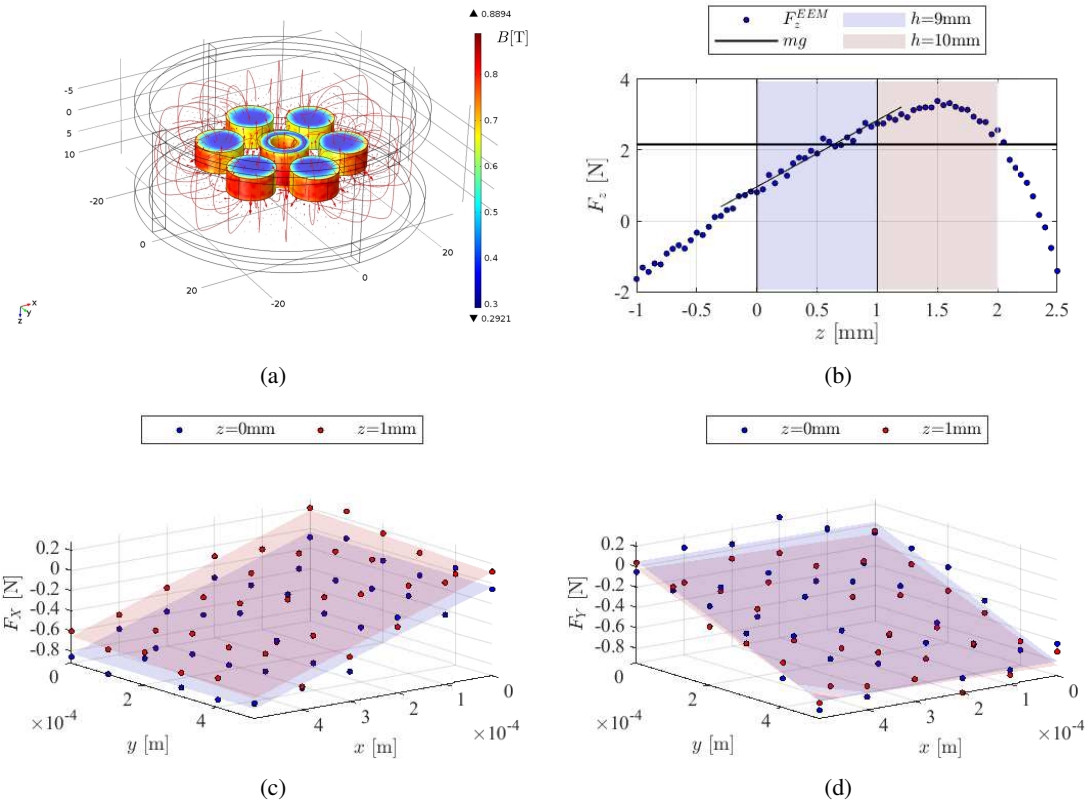

Fig. 11.2. Numerical analysis of the proposed PMB configuration with individual force components characteristics.

The numerical model of the proposed PMB configuration was developed in COMSOL Multiphysics (Fig. 11.2a). PMs were modeled using the constitutive relation with the assumed[1] remanent flux density B_r = 1.2 T in the axial direction. The physics-controlled mesh consists of extra fine elements. A complete model was solved for 565466 DoF. Finalized geometry has 23 domains, 111 boundaries, 184 edges and 104 vertices.

The model confirms the stabilizing effect of the magnetic interactions between the magnets. Figure 11.2b shows the axial force versus its axial displacement. The characteristic is non-linear and depends on the mutual arrangement of the PMB movable part with respect to the fixed one. For z=0 mm the corresponding distance h_1 is 9 mm. For the 1 mm levitation range, the force is linear, balancing the rotor gravity for about 0.7 mm (light blue). However, with the distance h_4, which is 10 mm (light red), the force characteristic is no longer a monotonic function. By optimizing the arrangement of the magnets, an approximately linear or even constant force trend may be obtained. Figures 11.2c-11.2d provide lateral forces versus the position of the rotor in the xy plane. The linear trend of the lateral forces was indicated (see Tab. 11.1) as well as a linear dependence on the axial position of the rotor. At the desired PMB operating point for 0.5 mm axial gap, the lateral forces may be smaller by an order of magnitude compared to the axial component (Fig. 11.3a), thus confirming its low stiffness. With an axial gap of 0.5 mm and the rotor displaced by the same radial clearance in the $x - y$ plane, the ratio of the lateral to axial force

[1]Parameter specified on the manufacturer's website *www.magnesy.pl*

is approximately 37.5% (Fig. 11.3b) and forms symmetric linear planes around the y and x axes, respectively, for F_x and F_y. The radial force relative to the axial force according to the above comparison is approximately 44%. With an accuracy of 92%, the results of the numerical simulation are approximated by the equation of an elliptical cone (11.2)[2](Fig. 11.3c). With a smaller displacement of the rotor in both axes, one can obtain comparable characteristics. In the second part of the investigation, the experiment with free vibrations will indicate the difference in the damping of lateral motion in individual directions.

$$F = p_{00} + p_{10}x + p_{01}y \tag{11.1}$$

$$\frac{F_r}{F_z} = \sqrt{\frac{x^2}{a^2} + \frac{y^2}{b^2}} \tag{11.2}$$

Table 11.1. Approximated PMB lateral forces (11.1) for different levitation levels (coefficients for x, y in [m]).

F[N]	z[mm]	p_{00}	p_{10}	p_{01}	R^2[%]
F_x	0	-0.0352	-1581	0.8695	92.89
	1	0.1819	-1670	-144.8	91.69
F_y	0	0.0279	46.74	-1664	91.12
	1	-0.0930	139	-1500	90.36

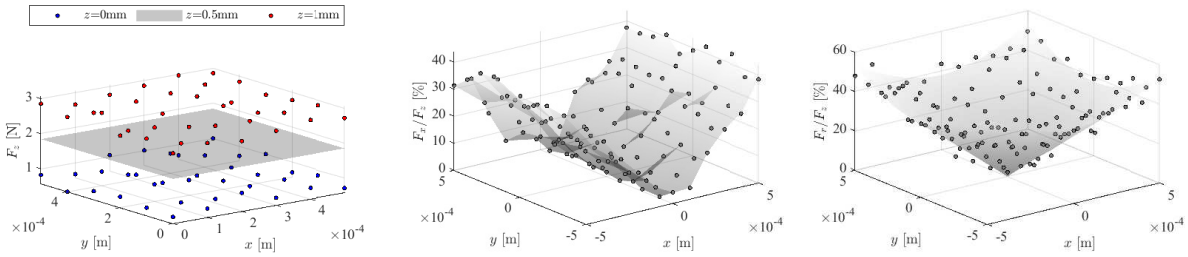

(a) (b) (c)

Fig. 11.3. Numerical analysis of the proposed PMB configuration with individual components force characteristics.

11.3. Experimental investigation

Among the many technological problems posed by the design of a passive radial bearing, an important issue is the identification of the force characteristics and dynamics of PMB in a magnetic suspension system. Due to the interactions between the active axial and passive radial bearings, obtaining the favorable parameters of the system requires an interdisciplinary approach. The use of an axial actuator with several force components to control the tilt and axial position of the rotor will allow the unique identification of the PMB parameters in a closed-loop system during levitation mode.

[2]A plane section of an elliptic cone is in a form of ellipse; for this case a=1.3341 $\times$ 10^{-5}, b=1.3211 $\times$ 10^{-5} for x, y in [m].

In the investigation, a stand with 6pAAMB was used, the interdisciplinary analysis of which is the main subject of this doctoral dissertation. The test stand enables axial levitation of the rotor and is equipped with a set of distance sensors. Thus, it allows testing of PMB using a proposed set of experiments. The stand consists of a housing (Fig. 11.4a) and five proximity sensors[3]. The 220 g levitating rotor is stabilized on the z axis by 6pAAMB, while RPMB is responsible for centering in the x-y plane. An aluminum hub with a magnetic clutch is mounted to the rotor axis, which is used for the noncontact transmission of rotary motion from the BLDC motor drive (Tarot 6S 380KV). Another difficulty in PMB design is maintaining the concentricity of the planes during assembly (see Fig. 11.4b). Correct alignment of the structure with the assumed inaccuracies of the elements poses a significant challenge in the subsequent identification process. Figure 11.4c indicates the distance h, which was selected experimentally. Its height influences the dynamic properties of the RPMB and the net axial force component.

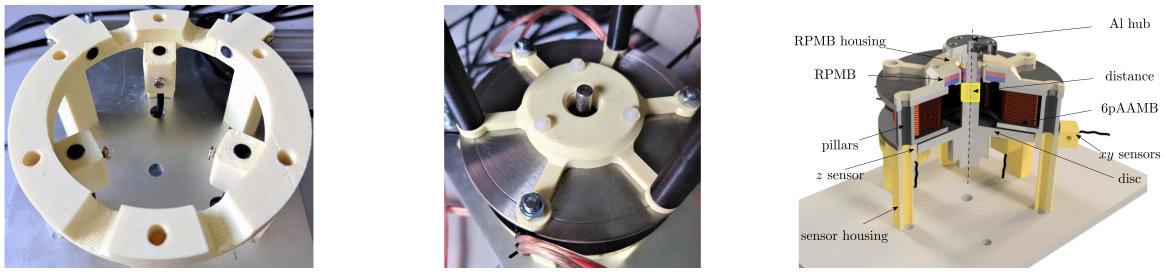

(a) (b) (c)

Fig. 11.4. Test stand with RPMB: a.) housing with sensors, b.) RPMB assembly, c.) isomteric cross-section.

Experiments were prepared for four different heights of the distance (Table 11.2). In the following, the results for h equal to 9 mm are discussed mainly due to the best performance in the tested configuration[4]. The parameters of the local PID controllers did not change during all the experiments.

Table 11.2. Tested spacer flange heights.

h	h_1	h_2	h_3	h_4
[mm]	9.00	9.25	9.75	10.00

To observe the RPMB parameters in the AMS system, four scenarios were designed as follows:

1. raising and lowering the rotor from 0 mm to 1 mm (2.7 mm to 1.7 mm axial gap); t=100 s,
2. rising the rotor from 0 mm to 0.3 mm, then a step change to 0.8 mm; t=30 s,
3. free vibrations after raising the rotor to 0.5 mm (2.2 mm axial gap),
4. raising the rotor to 0.5 mm (2.2 mm axial gap) and gradually accelerates to 4000 rpm.

Figure 11.5 presents changes in the state variables during raising and lowering the rotor. One can notice a change in the position of the rotor in all axes and a change in currents and control signals as a function of time. Applying a ramp control signal to the rotor causes a linear motion along each axis of

[3]Refer to subsection 12.2 for the exact sensor locations and the test stand parameters
[4]Refer to section 9.2 for hardware details; see section 12.7 for PID regulator details; settings K_p= -500, K_i= -20, K_d= -20.

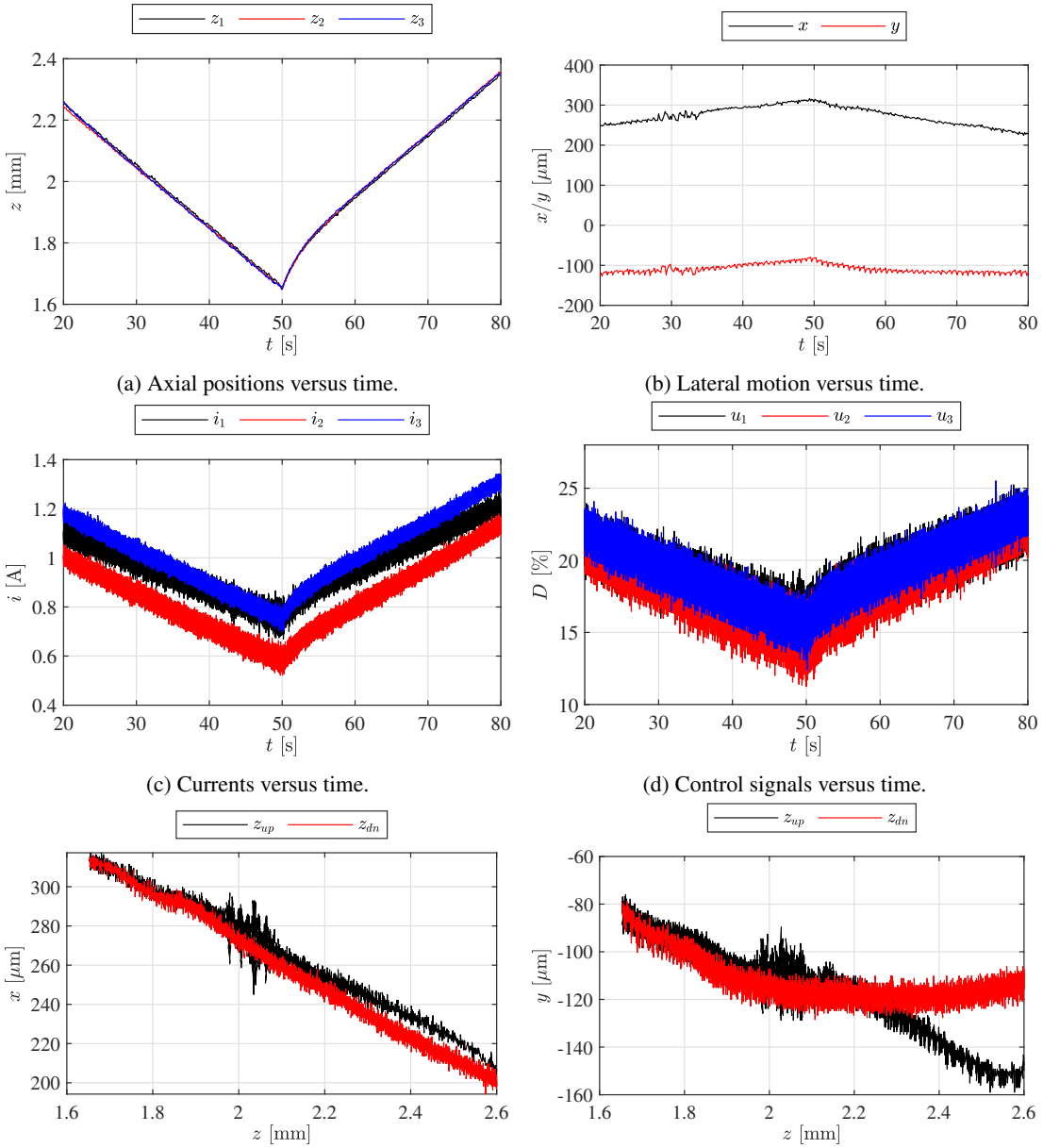

(a) Axial positions versus time.

(b) Lateral motion versus time.

(c) Currents versus time.

(d) Control signals versus time.

(e) Lateral displacement x versus axial motion.

(f) Lateral displacement y versus axial motion.

Fig. 11.5. Experiment according to 1st scenario for h_1=9 mm.

the rotor during its lifting. In the initial phase of rotor descent, the nonlinearity of the axial motion can be noticed. The movement along the y axis is described by a higher-order function, while along the x axis the rotor moves linearly. These effects are caused by RPMB, the design of which introduces stiffness that is dependent on the lateral position of the rotor with respect to the configuration of the PMs external structure.

The experiment in Fig. 11.6 shows a step change in currents and the axial position of the levitating rotor as a result of applying a step change in the control voltage. The experimentally selected PID controller settings guaranteed aperiodic changes in currents and axial position of the rotor with only 6pAAMB. RPMB introduces an additional component of the axial force, which was not taken into

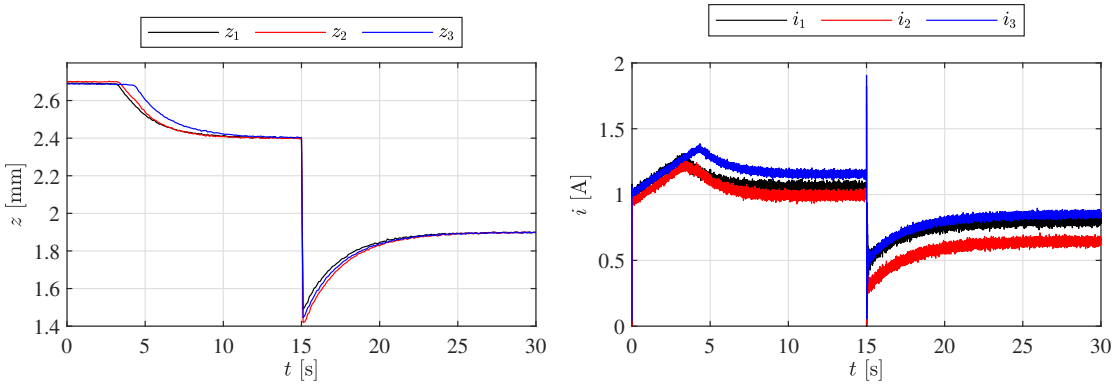

(a) Axial position versus time.

(b) Currents versus time.

Fig. 11.6. Experiment according to 2nd scenario for h_1=9 mm.

account by the originally tuned regulator, hence the visible overshoot and a significant decrease in the current values, that is, respectively 21.7%, 32.8%, 26.0% and 14.6%, 15.8%, 13.1% for the variant with and without RPMB for currents i_1,i_2,i_3.

Table 11.3. Approximation of free vibrations with (11.3) according to the 3rd experiment scenario.

h[mm]	parameter	1-x	1-y	2-x	2-y	3-x	3-y	4-x	4-y
9.00	A	-0.13	-0.13	-	-	0.11	0.13	0.09	-
	δ	1.04	1.11	-	-	0.94	1.11	1.28	-
	ω	42.31	43.23	-	-	42.61	42.97	42.08	-
	ϕ	0.05	0.16	-	-	0.36	0.57	0.42	-
9.25	A	-0.25	0.21	-0.10	0.32	0.17	0.18	-0.36	0.20
	δ	1.70	0.58	2.21	1.36	1.76	0.52	1.89	0.55
	ω	41.90	42.44	40.75	41.93	41.41	42.46	41.13	41.20
	ϕ	-0.18	-1.99	-0.09	-0.68	0.03	0.11	-0.05	-1.12

$$x(t) = A \cdot e^{-\delta \cdot t} \cdot sin(\omega t + \phi) \tag{11.3}$$

where A, δ, ω and ϕ are the amplitude, damping coefficient, vibration frequency and phase shift, respectively. Along with the change in the position of the 2xMP10x6x4 magnets in relation to the stationary part with MW10x5 magnets, the dynamic parameters of the bearing change. With increasing height h, the frequency of vibrations ω decreases slightly, the amplitude A increases, the damping coefficient δ increases in both axes, together with its difference between the individual axes.

The experiment depicted in Fig. 11.7 and tabulated in Tab.11.3 presents the results of the approximation of the free rotor vibrations during its levitation at 2.2 mm axial gap. The rotor was unbalanced with a gentle hammer blow at four different points on the aluminum hub. The vibrations on the x and y axes were approximated, finding a minimum of an unconstrained function (11.3) with a given starting point. The convergence of the match with the raw data exceeded 92.5% in each case. The results

confirmed differences in the stiffness of the individual axes (x,y) and a possible lack of RPMB alignment with respect to the active levitation plane. The frequency of damped vibrations according to the approximation is approximately 42.60 Hz and 41.65 Hz for distances h_1 and h_2, respectively. The above observations show the influence of the RPMB assembly and the level of levitation on the dynamics of rotor motion.

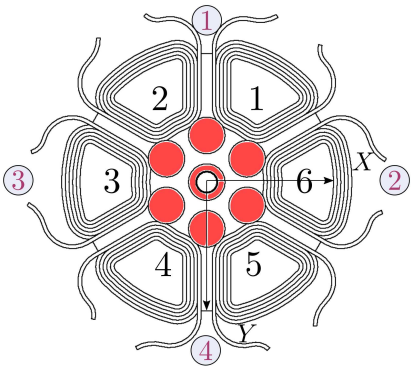

(a) RPMB orientation in adopted coordinate system.

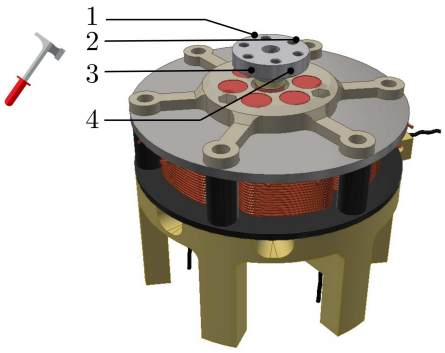

(b) Point excitations of rotor free vibrations.

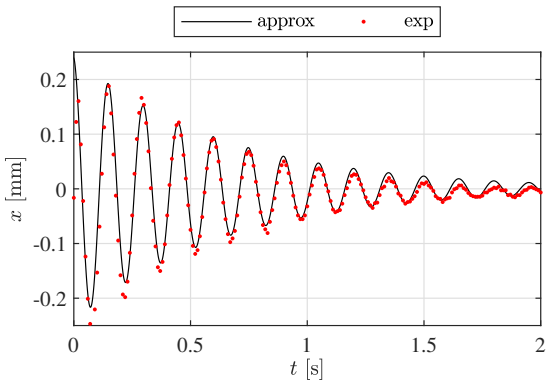

(c) Free vibrations in x axis for 1st excitation point.

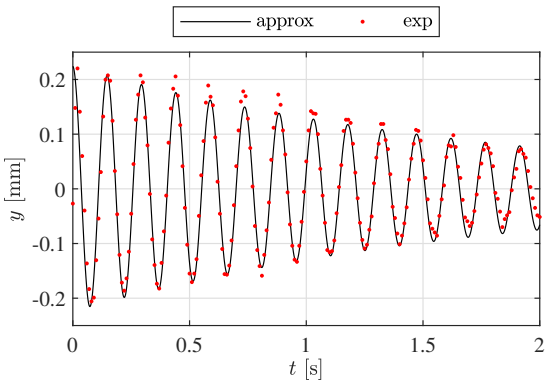

(d) Free vibrations in y axis for 1st excitation point.

Fig. 11.7. Experiment according to 3rd scenario.

The last experiment in the 4th scenario describes the rotation of the rotor with all its degrees of freedom released. For this purpose, a magnetic coupling (Fig. 11.8b) was designed and manufactured using 3D printing and two BLDC motors. The outer rotor of the second motor is attached to the first motor as the outer part of the magnetic coupling. The inner part of the coupling is filled with the same number of magnets as the motor rotor, providing a 1:1 gear ratio. The design of the magnetic coupling was carried out with the support of numerical analyses, verified by trial and error on a real stand. The third iteration of the inner rotor allowed rotational motion to be obtained within the housing geometry and power supply limitations. The main emphasis of the doctoral dissertation is the design, implementation and identification of 6pAAMB, hence the details of the construction and operation of the magnetic coupling will be developed in the author's further research. Figures 11.8d-11.8e show the axial rotor motion and the corresponding current graphs. The axial force components of PMs cause the rotor to oscillate axially, with the waveforms in the z axis and currents approximated by an offset sine wave (Tab. 11.4). To

ensure a stable axial position, an opposite actuator should be added in differential mode (see Chapter 2). The experiment lasted 180s; during the first 80 s the rotor accelerated to 4000 rpm, going through several eigenmodes. The experiment showed that RPMB, with the proper identification of the system, can support axial and radial stabilization; however, it requires the support of an active suspension in the radial direction in situations of variable dynamics and increased loads. The rotation speed was measured with a noncontact magnetic encoder RM08[5] mounted above the drive motor axis. Figure 11.8f shows the orbit of radial displacements of the rotor during a single revolution. In each rotation, the trend of varying stiffness is observed in each axis. Due to the unknown interactions from the magnetic coupling, this trend is unique in each rotation. Figures 11.8g-11.8h show the lateral motion of the rotor. As a result of an insufficient sampling frequency, the obtained data required filtration. Signal filtering was designed using a low-pass Butterworth filter of 4$^{\text{th}}$ order with cutoff frequency 0.35[6]. Then, zero-phase digital filtering was performed by processing the input data in both directions to ensure zero-phase distortion. The final data were approximated using the nonlinear least squares method with given constraints using the sum of eight sines (11.4). Table 11.5 contains the fit results along with the frequencies of the lateral motion in x and y axes for the first two components of the sum of sines. The optimization algorithm was unable to fit the lateral motion using a Fourier series, indicating that periodic motion should not be considered simply harmonic. The components of the rotor frequency from Tab. 11.5 are related to the frequency of rotation and the frequency of free vibrations from the experiment according to 3$^{\text{rd}}$ scenario (Fig. 11.7). In the future, sufficient sampling and signal processing should be ensured to continue studies with the rotating and levitating rotor.

$$f(t) = A_1 \sin(\omega_1 t + \phi_1) + A_2 \sin(\omega_2 t + \phi_2) \tag{11.4}$$

Table 11.4. Approximation of the rotor axial displacements and currents during its rotation with 4000 rpm.

z	parameters				i	parameters				R_z^2[%]	R_i^2[%]
	A_1	A_2	ω	ϕ		A_1	A_2	ω	ϕ		
z_1	0.501	0.121	414.7	-0.095	i_1	0.894	0.918	414.6	-3.085	98.76	98.63
z_2	0.501	0.062	414.7	-2.117	i_2	0.781	0.655	414.8	0.651	98.54	98.99
z_3	0.500	0.078	414.5	2.085	i_3	0.998	0.403	414.5	-1.142	98.91	99.29

Table 11.5. Approximation of the rotor lateral displacement during its rotation with 4000 rpm.

$f(t)$	parameters						R^2[%]	$RMSE$
	A_1	ω_1	ϕ_1	A_2	ω_2	ϕ_2		
$x(t)$	11.16	414.80	2.79	3.29	41.60	-2.569	92.57	2.36
$y(t)$	23.40	414.70	1.08	5.83	42.68	2.68	97.82	2.57

[5] *https://www.rls.si/eng/rm08-super-small-non-contact-rotary-encoder*

[6] For digital filters, the cutoff frequency lies between 0 and 1, where 1 corresponds to the Nyquist rate-half the sample rate.

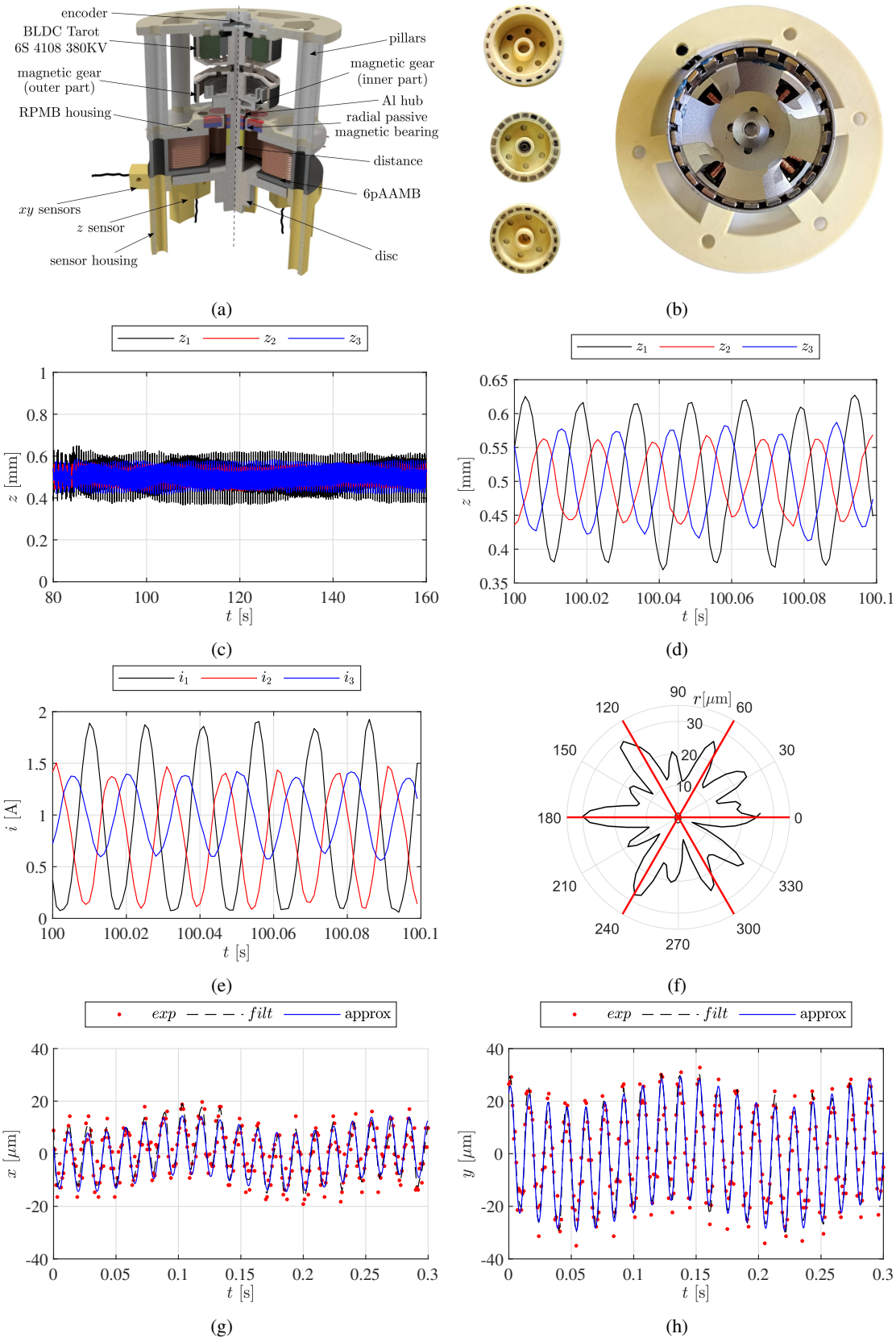

Fig. 11.8. Experiment according to 4$^{\text{th}}$ scenario with the free rotor rotated at 4000 rpm: a.) prototype research system, b.) proprietary magnetic coupling. c-d.) axial displacement, e.) currents, f.) the orbit of the lateral motion of the rotor in a single revolution, g-h.) lateral displacement x, y.

Summary of results

The developed RPMB prototype fulfills its task of supporting the stabilization of the rotor in the x-y plane to some extent, both during levitation and rotation. The assembly, preliminary tests and experiments provided a number of conclusions for the potential application of the proposed rotor configuration.

1. The RPMB design can be extensively modified and miniaturized due to its simplicity. The range of possible displacement in the z axis should be identified for the given structure.
2. Before adapting the RPMB solution to a specific application, it is necessary to provide a comprehensive analysis of the magnetic field distribution in the 3D space. All housing and rotor parts must be considered.
3. A passive magnetic bearing, depending on the position of the rotating part in relation to the stationary part, may generate a negative or positive axial electromagnetic force component.
4. The location of the magnets of the rotating and stationary parts relative to each other plays a key role in orienting the axial electromagnetic force component and the dynamic properties of the 6pAAMB. From the presented experiments, one can choose the appropriate RPMB configuration. The described experimental scenarios are used to determine the impact of RPMB on the AMS system and, consequently, to propose integrated force and dynamic characteristics.

In addition, a prototype of the noncontact magnetic gear was developed. The author would like to devote more attention to this issue in the future. Due to the complex identification issues of the system described above, in the next chapter the reader will get acquainted with the proposal of an interdisciplinary course of identifying the 6pAAMB parameters. This will be a reference point for expanding the AMS system with new actuators cooperating with 6pAAMB.

Chapter 12

Interdisciplinary identification of six pole axial active magnetic bearing prototype

This elaboration presents a comprehensive approach to identify the parameters of the novel six-pole axial active magnetic bearing actuator with current-driven electromagnets. The developed actuator is devoted to compensate for the tilt motion of disc-type machines by suppressing lateral vibrations with three actively controlled force vectors. This research emphasizes the interdisciplinary identification of magnetic bearing parameters using various measurement methods. In particular, the impact of inaccuracy inspired by the imperfections of the real prototype was investigated. Furthermore, a chaotic motion of the disc was observed in the plane perpendicular to its levitation direction. The coil parameters were measured with a precise indication of the differences. The thermal reliability of the bearing was tested with an increase in current and weight load up to twice the nominal operational temperature. The study extends the crucial aspect of measuring and calculating the electromagnetic force through four methods with decent convergence between them. In general, the proposed mechatronic actuator is capable of increasing the stability range of rigid or flexible rotors and is characterized by favorable dynamic properties, which was demonstrated in the shaker test with external harmonic excitation. A complete description of the actuator with uncertainties in the parameters was obtained by accessible in situ identification.

12.1. Introduction

The design of an axial actuator with a few pole pieces and associated with them electromagnets requires the development of numerical and analytical models supporting the virtual prototyping process. Previous chapters as well as articles [40], [41] present various approaches to modeling the original concept of the 6pAAMB actuator. It is desirable that the model should be able to take into account the difference in parameters between individual electromagnets. Often the system parameters can be estimated only experimentally. The key point of this study is the interdisciplinary identification of the original actuator design for its reliability of operation, taking into account the uncertainty of the parameters. The eccentricity of the armature and the tilting motion are fundamental problems of disc-type machines [145], [146], therefore, 6pAAMB by using separate control of the three components of the electromagnetic force is capable of compensating disc vibrations. Three force components resulting from three electromagnets entail new challenges in the field of identification because it is necessary to precisely

determine the dynamics and force values of each electromagnet as well as to examine the differences and potential couplings between them, which may affect the regulator synthesis. The question then may be asked, what could be the cause of possible differences between the operation of the 6pAAMB electromagnets? In disc-type machines, failure may occur due to incorrect assembly [106], differences between coils with parameter dispersion [147], magnetic circuit design with flux leakage [148] or electromagnetic noise [149]. During rapid prototyping, the 6pAAMB coils were manually wounded, resulting in different electrical parameters, which perfectly simulates the effect of the defects mentioned above. The novel creativity of the identification study is contained in the comprehensive testing of various actuator parameters performed in situ, often in several complementary ways, to achieve effective control. In particular, the electromagnetic force was extensively identified in four different ways, converging within a satisfactory operational range. The reader, following the identification description, selecting a convenient method from those described, and using easily replicated stand modifications, is able to obtain a complete characterization of the actuator.

12.2. Axial active magnetic bearing test stand

The prepared stand consists of the 6pAAMB stator with polished steel disc and 3D printed pillars. The plane of the stator pole pieces is separated from the disc by a 1 mm thick black spacer. Proximity sensors are placed in the pastel casing. Figure 12.1a shows a cross-sectional view of the CAD model with the adopted coordinate system. Its origin is located in the stator pole piece plane at its center of symmetry. Three independent hardware current drivers provide the required power supply for each electromagnet. The driver's core is the LMD18245 full-bridge power amplifier, which incorporates the necessary circuit blocks to control the electromagnet's current via a fixed off-time chopper technique with internal current feedback. Therefore, the 6pAAMB is steered by the requested current values in every electromagnet. Levitation is accomplished by the stator with three electromagnets that produce upward attraction forces. In the laboratory test rig (Fig. 12.1b) 5 Keyence proximity sensors measure the axial and planar displacement of the disc and relay this to the RT-DAC4/PC control board, where this information is processed to drive the electromagnets. Proximity sensors measuring the axial position and tilt angles are installed at the bottom of the disc to prevent magnetic field interactions. The exact locations of the sensors are shown in Fig. 12.1c and Tab. 12.1, where the inertial parameters of the disc are also listed.

Table 12.1. 6pAAMB inertial parameters (left) and coordinates of sensors location (right).

Symbol	Quantity	Value
l	total air gap	2.7mm
m_d	disc mass	252.60g
I_{xx}	transverse moment	98950gmm^2
I_{yy}		
I_{zz}	axial moment	129934gmm^2

sensor	x [mm]	y [mm]
1	0	-30
2	$-30\cos\frac{\pi}{6}$	$30\sin\frac{\pi}{6}$
3	$30\cos\frac{\pi}{6}$	$30\sin\frac{\pi}{6}$
4	$35.7\sin\frac{\pi}{4}$	$-35.7\cos\frac{\pi}{4}$
5	$-35.7\sin\frac{\pi}{4}$	$-35.7\cos\frac{\pi}{4}$

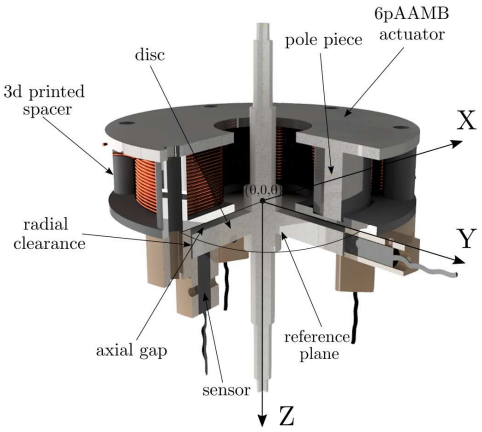

(a) Three-quarter 6pAAMB CAD model view.

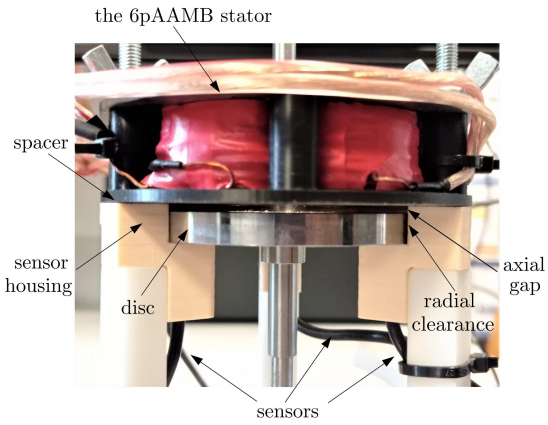

(b) Assembled test stand for the disc levitation.

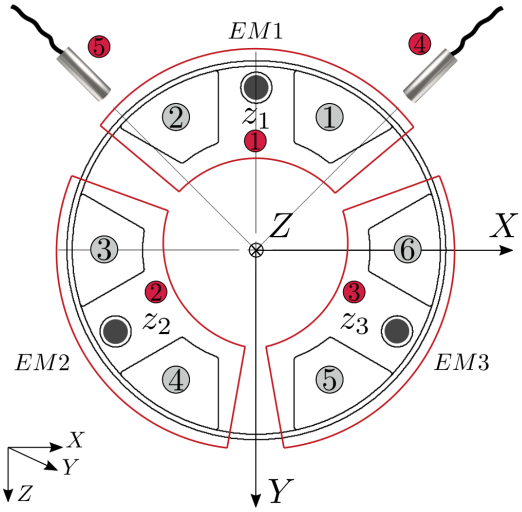

(c) Sensor's position in the 6pAAMB system.

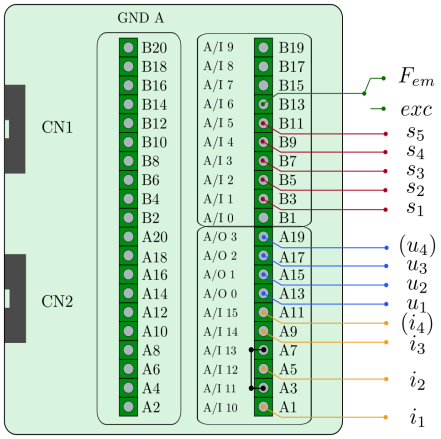

(d) Wiring board of the 6pAAMB test stand.

Fig. 12.1. Axial active magnetic bearing test stand; model (a), built and assembled prototype (b), top view with position of sensors (c), list of measurement and control signals (d).

12.3. Discussion of disc eccentricity

In rotating machines, especially in the AFPMM motors and magnetic bearings, an eccentricity is a misalignment condition of a stator or a rotor axis (Fig. 12.2a), thus static and dynamic eccentricity can be distinguished, respectively. In the case of 6pAAMB, when the disc axis is deflected from the axial magnetic bearing stator, it causes a nonuniform air gap (Fig. 12.2b). By default, the length of the air gap l is constant along the angular coordinate θ. During disc levitation before steady state, the air gap dynamically varies around the stator circumference. Taking into account the influence of eccentricity in the axial actuator, it is crucial to ensure its healthy operating mode and avoid critical load conditions. In [99] an approach to model a double rotor AFPMM with SE is shown. Figure 12.2d presents the tilted disc levitation at three different desired axial positions. The experiment exposes the main feature of the

proposed design, which is the ability to control the current (Fig. 12.2f) in each electromagnet, thus setting the desired position of the disc in a bearing space. The experiment in Fig. 12.2) was carried out 10 times at a given disc inclination, i.e., (z_1 = 2.1 mm, z_2 = 2.0 mm, z_3 = 2.2 mm) and the final position of the disc in the x-y plane is statistically repeatable with its determined mean and standard deviation values of x 287.5; 17.7 μm and y 473.6; 4.7 μm, respectively. The measured resolution of the 12-bit ADC in the given range is equal to 2 μm.

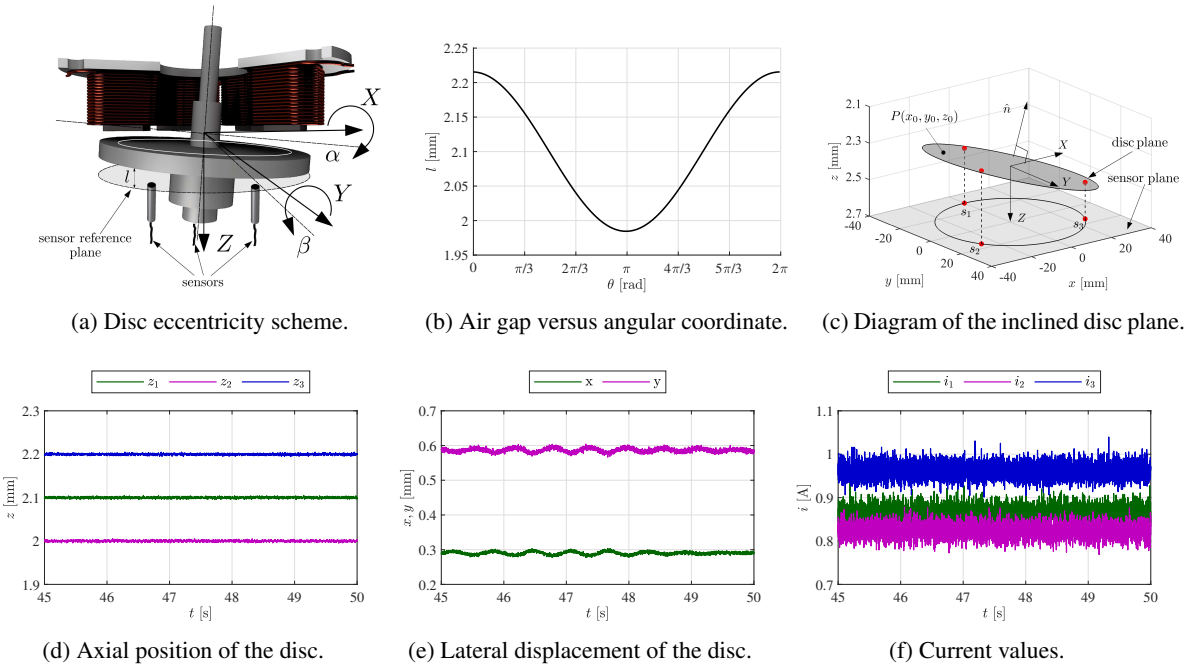

(a) Disc eccentricity scheme. (b) Air gap versus angular coordinate. (c) Diagram of the inclined disc plane.

(d) Axial position of the disc. (e) Lateral displacement of the disc. (f) Current values.

Fig. 12.2. Eccentric condition of the levitated disc tilted with respect to x-y plane and with lateral chaotic motion.

The 6pAAMB design has the potential to suppress lateral vibrations with three controlled force vectors and may improve the stability of the rotor for nonlinear AMBs with variable stiffness [150] with respect to the controllable dynamics of the magnetic suspension [46]. It is even possible to operate under near-resonance conditions with periodic or chaotic rotor motion [151]. Figure 12.2e demonstrates a chaotic lateral motion of the disc, which may cause nonlinear vibrations [152] and stability problems, so it must be included in the control strategy. With reference to Chapter 10, the disc plane that best fits a set of sample noncollinear points is computed by solving a system of plane equations in a general form:

$$Ax + By + Cz + D = 0 \tag{12.1}$$

The input to the function is a 3 $\times$ 3 coordinate matrix, where each line corresponds to a sample point (x_i, y_i, z_i). The output is a unit vector $\hat{n}$ normal to the plane and a point P that belongs to this plane (Fig. 12.2c). Based on this output, the coefficients of a plane equation and the tilt angles about the x and y axes are calculated. The variable air gap l^* is expressed by the following equation:

$$l^*(r,\theta) = h_d \cdot (1 - \frac{1}{\cos(\alpha)\cos(\beta)}) + l_{max} - \frac{A \cdot rcos(\theta) - B \cdot rcos(\theta) - D}{C} \tag{12.2}$$

where h_d denotes the height of the disc, α and β are the angles between the plane and the x, y axes; l_{max} is the total length of the air gap. The calculated air gap (12.1) may be directly substituted for the symbolic magnetic field equation, which, to the author's knowledge, is a new approach in the SE analytical modeling, where the air gap may be described as a function of the circumferential component θ and directly implemented in the boundary conditions (10.11).

12.4. Measurement of six pole axial active magnetic bearing parameters

Technical methods and direct measurements of the electromagnetic actuator circuit often provide the first cognitive step toward a complete system modeling. They often contribute to the identification of a specific task and determine further modeling steps. The initial experiments of electromagnetic actuators include measurements of resistance, inductance, magnetic induction, and time constants, which will determine an appropriate hardware application and the selection of a valid step in a model computation. The key motivation of this chapter focuses on the estimation of differences between the 6pAAMB electromagnets, which results from the above-mentioned manual coil winding and assembly inaccuracies representing the defective system affecting a compatible actuator operation for identical electromagnet input settings.

12.4.1. Resistance and inductance measurement

Results from the GW Instek LCR-821 measurement unit illustrate the variation of the electromagnet parameters due to the variable signal frequency. The lowest frequency (12 Hz) resistance was compared to the DM3058E RIGOL digital multimeter measurement with relative error less than 1% (Tab. 12.2). The measurements (Tab. 12.3) highlight the changes in the RL (resistance and inductance) parameters versus the control signal frequency. Measurements were carried out in the serial RL mode, in the absence of the disc. It will be important to take into account these changes in future research aimed at extending the actuator's operation with a dynamic input for a wide frequency range.

Table 12.2. Measured resistance comparison.

EM	1	2	3
$R_{DM3058E}[\Omega]$	1.048	1.069	1.039
$R_{LCR}[\Omega]$	1.043	1.059	1.033
$\delta_R[\%]$	0.48	0.94	0.58

12.4.2. Magnetic induction measurement

The axial magnetic field of a single electromagnet was investigated. Only the first pole piece for the averaged radius was considered. Measurements were carried out for three cases of the air gap between the disc and the stator surface, that is, l_1 = 2.2 mm, l_2 = 3.2 mm, and l_3 without the disc. Some configurations

Table 12.3. RL measurement of the 6pAAMB electromagnets.

$f[kHz]$	EM 1		EM 2		EM 3	
	$R_1[\Omega]$	$L_1[mH]$	$R_2[\Omega]$	$L_2[mH]$	$R_3[\Omega]$	$L_3[mH]$
0.012	1.04	3.20	1.06	3.24	1.03	3.05
0.1	1.35	2.94	1.36	2.97	1.32	2.79
0.25	2.11	2.57	2.13	2.62	2.04	2.45
0.5	3.41	2.22	3.43	2.26	3.26	2.13
0.75	4.63	2.00	4.67	2.04	4.41	1.91
1	5.79	1.84	5.85	1.89	5.50	1.77
3	13.22	1.30	13.46	1.34	12.56	1.25
5	18.91	1.09	19.26	1.12	17.99	1.06

of the electromagnet power supply were examined, that is, 1, 2, 3, 1+2, 1+3, 2+3, 1+2+3. The results are presented in Fig. 12.3). The induction was measured using the magnetic field meter[1]equipped with a hall sensor.

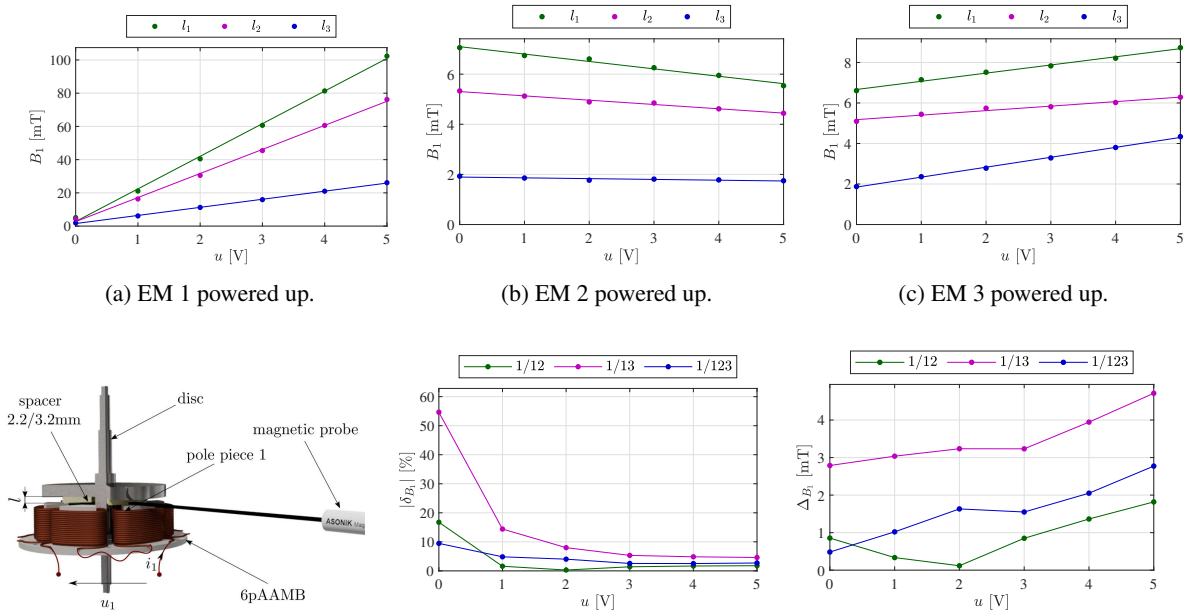

(a) EM 1 powered up.

(b) EM 2 powered up.

(c) EM 3 powered up.

(d) Magnetic field B_1 measurement.

(e) Magnetic field relative error.

(f) Magnetic field absolute error.

Fig. 12.3. Axial magnetic field measured for the first pole piece of 6pAAMB versus the applied voltage for different electromagnets power supply configurations.

One may observe the leakage magnetic field for electromagnets 2 and 3, which constitute more than 10% of the closed field in the first electromagnet magnetic circuit. Figures 12.3e-12.3f show the error between the selected power supply configurations: 1-1+2, 1-1+3, 1-1+2+3. In the desired case of supplying all three electromagnets, the relative error is less than 4% and remains at this level from the 2 V starting point. Demonstrated differences clearly indicate the distinction in the electromagnets' performance, which cannot be ignored in further modeling.

[1]TEL-Atomic Inc., Smart Magnetic Sensor, model SMS 102

12.4.3. Time constant identification

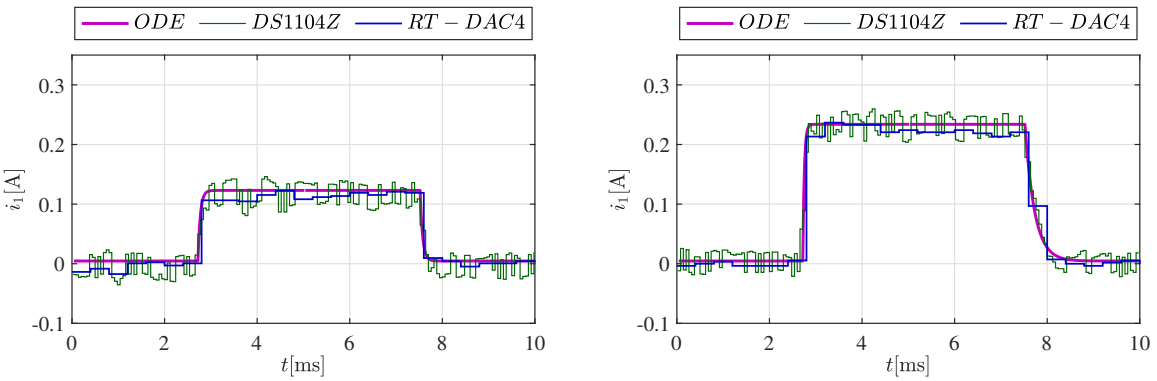

(a) Experiment 1; scn 1; EM 1.

(b) Experiment 1; scn 2; EM 1.

Fig. 12.4. The current response with a rising and falling edge for the fixed rotor position and the square excitation.

Table 12.4. Time constant of the 6pAAMB actuator; experimental data approximated by the 1st order model.

	experiment 1				experiment 2				experiment 3			
distance	scn 1		scn 2		scn 1		scn 2		scn 1		scn 2	
900[μm]												
500[μm]												
100[μm]												
$T_i[\mu s]$	↑	↓	↑	↓	↓	↑	↑	↓	↓	↑	↓	↑
EM 1	51	53	31	207	40	36	56	58	61	33	224	38
EM 2	63	65	35	169	87	28	43	54	59	40	238	42
EM 3	30	77	38	168	82	37	59	65	50	18	145	28

Finally, a comprehensive measurement of the time constant was performed using the DS1104Z RIGOL oscilloscope during square control signal excitation with a sampling frequency of 1 kHz. A waveform capture time was set to 20 ms with a maximum sampling rate of 125 MS/s. To analyze the results collected, an ordinary linear differential equation (ODE) describing the current change was used, which allowed the recorded waveform approximation with the mean square error less than 5% (Fig. 12.4). The obtained current time constants for the rising and falling edge in several scenarios are presented in Table 12.4. For a cognitive comparison of disc inertia, Table 12.5 shows its rising and falling time in the maximum air gap range. The dynamics of the disc position can be approximated by the higher-order system response (Fig. 12.5).

The calculated current time constants are 5 to 30 times smaller than the 1 ms sampling period, which confirms a satisfactory system time response and allows the current equation to be skipped in a further modeling process for the 6pAAMB hardware control system.

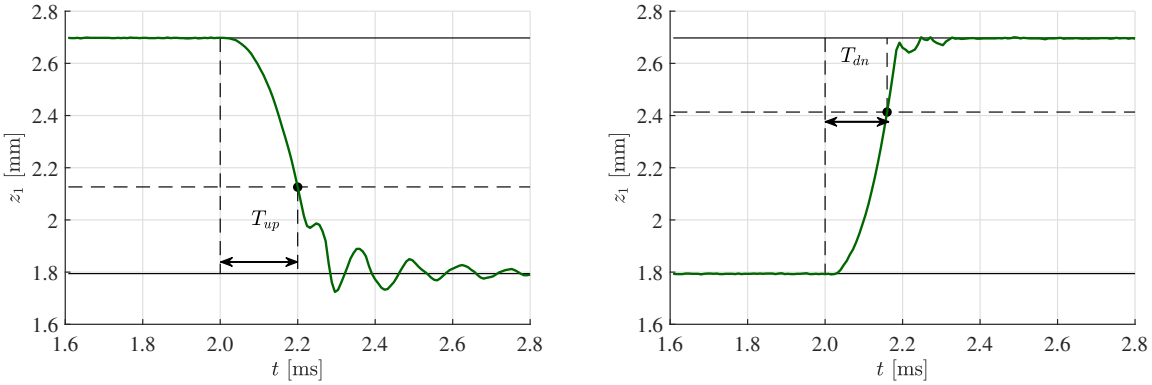

(a) Rising from 0 to 900 μm; EM 1.

(b) Falling from 900 to 0 μm; EM 1.

Fig. 12.5. The position of the rising and falling disc excited by the square voltage.

Table 12.5. Time constant of the disc's position from zero to the given distance.

distance	$400[\mu m]$		$900[\mu m]$	
$T_z[ms]$	$\uparrow$	$\downarrow$	$\uparrow$	$\downarrow$
EM 1	8.0	6.5	12.5	9.5
EM 2	9.25	8.5	14.5	12.0
EM 3	8.0	7.0	10.0	10.0

12.5. Thermal identification

The simulation of the temperature distribution is a crucial part of the electrical device design process. When the nominal parameters of an actuator are increased to their limits, it is important to test the operating mode of a device under critical conditions. Numerical FEM methods are often used in thermal design. In [153] thermal FEM modeling of hybrid magnetic bearing was used. On the basis of the 3D model, the maximal value of the excitation current can be obtained in the actuator windings.

Thermal tests of the 6pAAMB actuator with and without load were carried out in several control scenarios. The load was a mass of 206.35 g attached to a levitating disc. Temperature was measured by the Optris PI 400i thermal camera through infrared imaging (Fig. 12.7a). The identification of the change in coil resistance as a function of temperature (Fig. 12.6a) was carried out with the 20-TOM sheathed thermocouple series, which is characterized by high resistance to vibration and high flexibility with diameters below 3 mm. The thermocouple was placed under the outer insulation of the first electromagnet, between its two coils. Taking into account the thermal phenomena in an electromagnetic actuator modeling, especially in a magnetic bearing, a temperature variation forces different current and control values, which entails a change in the dynamic properties of an armature. As a result of the experiments, the heat capacity ϵ and the generalized thermal conductivity λ were numerically optimized for the solution of the 1D differential Joule heating equation. The verification of the 10-hour actuator heating experiment (Fig. 12.6b) through various control scenarios is shown in Figures 12.6c-12.6d.

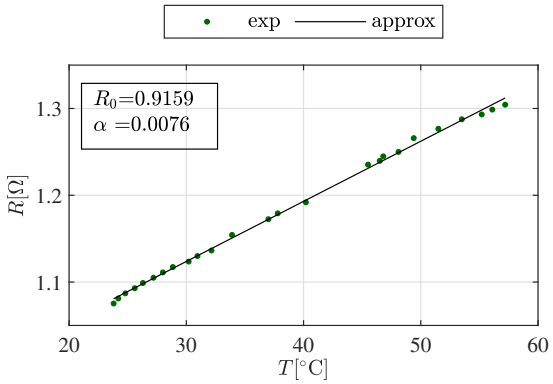

(a) Resistance of the electromagnet versus temperature.

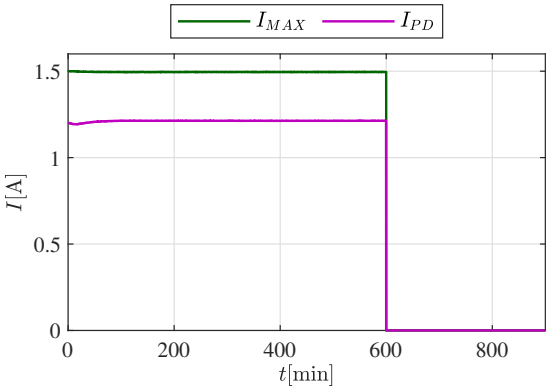

(b) Current in time for maximal and PD control.

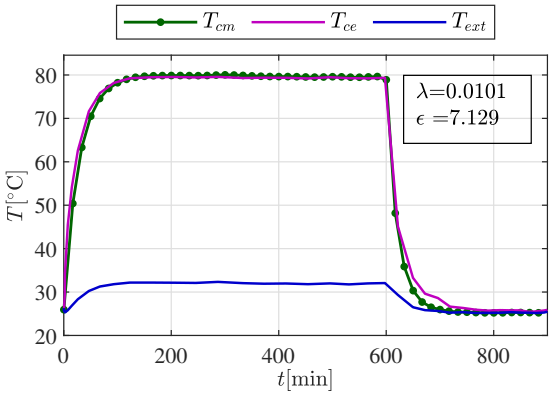

(c) Thermal model for maximal control; I=1.48 A.

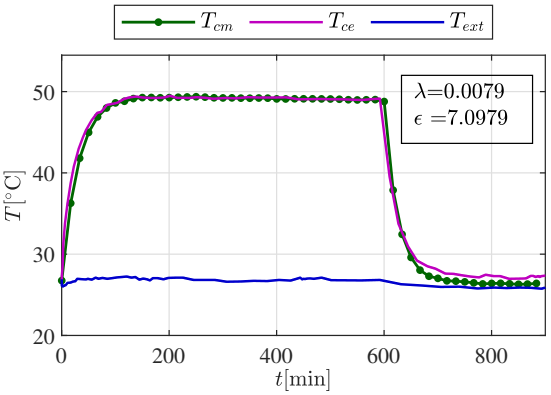

(d) Verification for PD control without load; I=0.90 A.

Fig. 12.6. The coil thermal identification; temperature: T_{cm}- modeled coil, T_{ce}- experiment, T_{ext}- ambient.

Table 12.6. Summary of the measured parameters values of the 1D thermal model for various control scenarios.

parameters		MAX +load	PID +load	PD +load	PD
$T_{max}[^\circ C]$		79.35	64.05	64.08	49.14
I_{max} [A]		1.48	1.21	1.19	0.90
λ [-]		0.0101	0.0079	0.0079	0.0079
ϵ [JK^{-1}]		7.1290	7.0979	7.0979	7.0979
T_{up}[min]		128.5	131.9	138.5	140.7
T_{dn}[min]		127.5	123.4	152.5	135.2
$\Delta z[\mu\mathrm{m}]$	1	-	500	501	465
	2		500	517	455
	3		500	508	447

One may observe that due to the disc attracted to the actuator spacer surface, a change in heat distribution occurs, which is reflected in different thermal parameters (Tab. 12.6). The presented experimental results allow one to capture the heating curves versus time. After taking into account the optimized coefficients of the 1D thermal equation, the transient heating model is developed. It can be used to determine the power losses and temperature distribution of 6pAAMB in steady state conditions, as well as during the transition between operational points due to time-varying state variables.

$$\begin{cases} d\Delta Q_{in} = Ri^2 dt \\ d\Delta Q_{out} = \kappa(\Delta T + T_0 - T_{ext})dt \\ \Delta Q = \Delta Q_{in} - \Delta Q_{out} \\ \Delta T = \dfrac{\Delta Q}{\epsilon} \end{cases} \tag{12.3}$$

where R - electromagnet resistance [Ω], i - electromagnet current [A], Q - heat [J], κ - thermal conductivity [WK^{-1}], λ - generalized thermal conductivity [-], ϵ - heat capacity [JK^{-1}], T_0 - initial electromagnet temperature [$^{\circ}C$], T_{ext} - ambient temperature [$^{\circ}C$], ΔT - temperature change [$^{\circ}C$].

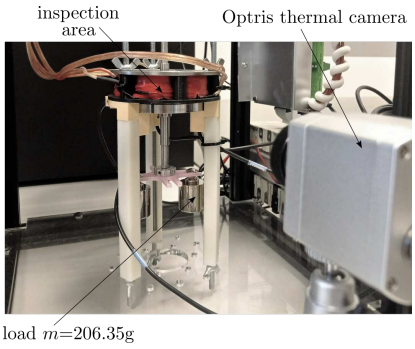

(a) Thermal measurement test rig.

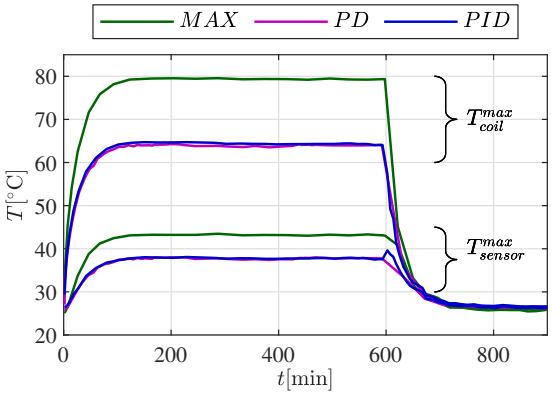

(b) Coil and sensor temperature for various control.

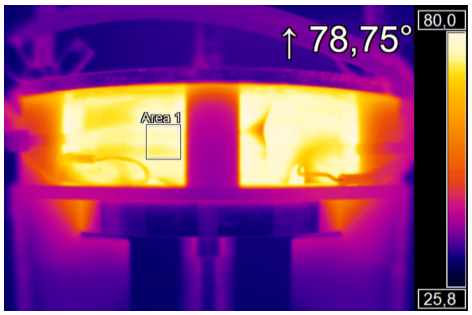

(c) Front view; 10^{th}hour; maximal control; I=1.48 A.

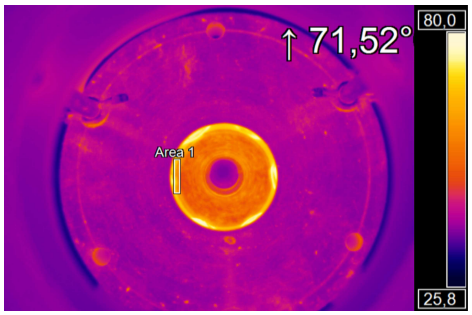

(d) Top view; 10^{th}hour; maximal control; I=1.48 A.

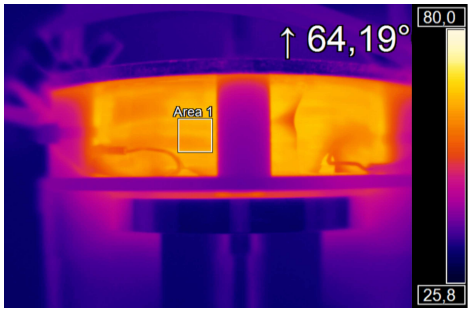

(e) Front view; 10^{th}hour; PD control; I=1.19 A.

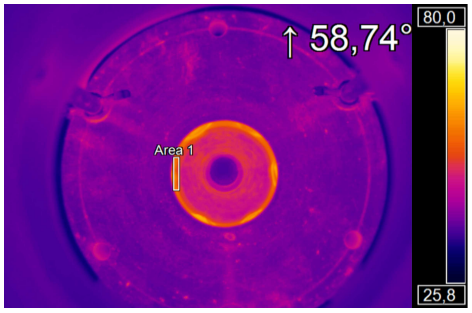

(f) Top view; 10^{th}hour; PD control; I=1.19 A.

Fig. 12.7. The 6pAAMB thermal distribution.

For an electromagnet's cooper coil, its resistance versus temperature can be represented by the linear dependence $R(T) = R_0(1+\alpha\Delta T)$, where R_0 was identified as 0.9159 Ω and α, which denotes the thermal expansion coefficient, equals 0.0076 K^{-1}. Taking into account (12.3), the 1D thermal equation for the 6pAAMB electromagnet can be applied in the following form:

$$\frac{d\Delta T}{dt} = \frac{R_0(1+\alpha\Delta T)i(t)^2}{\epsilon} - \lambda(\Delta T + T_0 - T_{ext}) \tag{12.4}$$

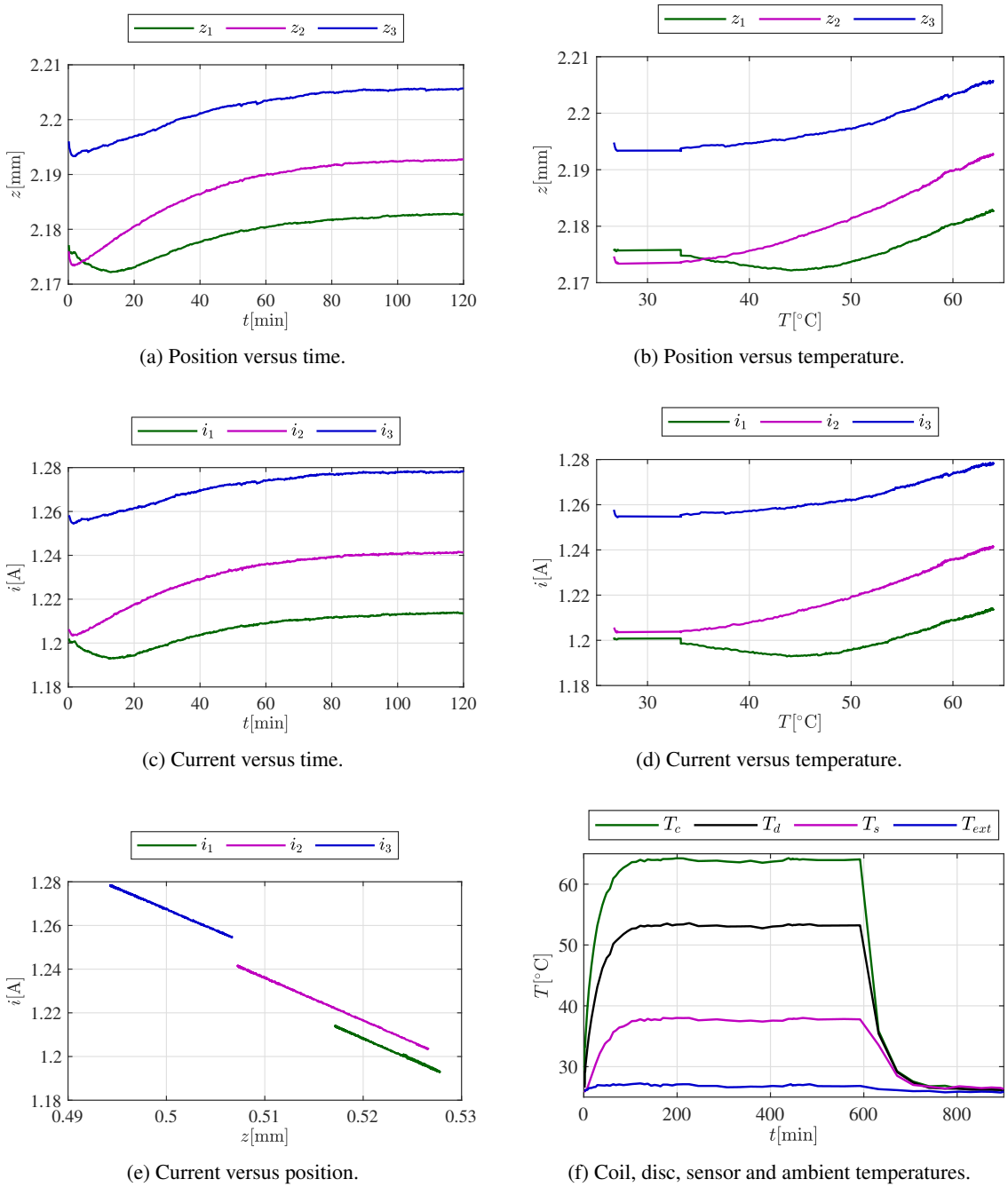

(a) Position versus time.

(b) Position versus temperature.

(c) Current versus time.

(d) Current versus temperature.

(e) Current versus position.

(f) Coil, disc, sensor and ambient temperatures.

Fig. 12.8. Temperature influence on the current and position during the PD control of the disc in 6pAAMB.

When recording the heating of 6pAAMB, the thermal camera was placed at the front and at the top of the test rig. In the case of the maximal control, the thermal distribution around the disc differs not only in the measured values but also in the trend itself because of the lack of air gap. When designing electrical machines, the influence of temperature on the sensors in the actuator space should be carefully investigated to eliminate measurement disturbances and choose a proper sensor location. The proximity sensors[2]maintain a linear characteristic throughout the measured temperature range (Fig. 12.7b).

Figure 12.8 shows the variables of state that vary over time as the temperature increases. The temperature stabilizes in 2 hours. The actuator was designed to predict possible thermal loads, as evidenced by a slight change in the position of the disc and the electromagnet currents of 0.8 and 2.5%, respectively. The change in current as a function of disc position is linear (Fig. 12.8e). The observed temperature dependence may constitute an additional state equation in the extended 6pAAMB model (refer to Chapter 3), allowing a robust controller design during actuator exposure to boundary thermal conditions.

Thermal consideration is strictly necessary for the optimal design of the actuator and allows rapid assessment of its thermal stability. Based on experimental and simulation of thermal processes in a transient real operating mode, geometric optimization can be performed to improve the cooling conditions of the device together with the miniaturization of the actuator and the choice of the applicable sensitive thermal material.

12.6. Force identification

Determining the force characteristics of an electromagnetic actuator is a key step toward system identification and its further controller synthesis. The electromagnetic force generated by 6pAAMB is as follows:

$$F_{em} = \frac{1}{2}\left(k_{L1}\frac{dL_1(z_1)}{dz_1}i_1^2 + k_{L2}\frac{dL_2(z_2)}{dz_2}i_2^2 + k_{L3}\frac{dL_3(z_3)}{dz_3}i_3^2\right) \tag{12.5}$$

where $L_i(z_i)$, k_{Li}, $i \in \{1,2,3\}$ denote respectively the inductance of three electromagnets and their ratio in the generated force. The relationship between inductance and armature position is a decreasing function (12.6), which, by derivative over position (12.7) determines the electromagnetic force.

$$\begin{cases} L_I(z) & = L_0 + ae^{-bz} \\ L_{II}(z) & = L_0 + \frac{2mg}{c^2z+cd} \end{cases} \tag{12.6}$$

$$\begin{cases} L_I'(z) & = -bae^{-bz} \\ L_{II}'(z) & = \frac{2mg}{(cz+d)^2} \end{cases} \tag{12.7}$$

[2]Inductive Gauging Sensor EX-200 series; Sensor head EX-305;

Electromagnet inductance identification may be conducted using:

1. the voltage drop measurement at the electromagnet terminals, the current that flows through the coil wire and the position of the disc in the open loop system,
2. the measurement of the position, coil current and control signal at the equilibrium point, when the system operates in the closed-loop mode, e.g. with the PD regulator.

The second method, that is, indirect identification, was chosen. Inductance values measured with the RLC meter were used to describe the coefficients of influence of the individual electromagnets on the total electromagnetic force. The inductance as a function of the position may be approximated by exponential or rational functions (12.6), which are presented in (Tab. 12.7, 12.8).

Table 12.7. Derivative of inductance approximation using exponential and rational functions.

Coeff	EM 1	EM 2	EM 3
a	24.096	30.131	17.742
b	-621.300	-713.380	-520.020
c	271.050	304.530	239.570
d	0.305	0.223	0.412

Table 12.8. Goodness of fit comparison for approximated inductance with respect to position.

	$L'(z)$	EM 1	EM 2	EM 3
$\lvert\delta\rvert$[%]	I	-0.102	-0.119	-0.101
	II	0.020	0.072	-0.035
$RMSE[\frac{H}{m}]$	I	0.099	0.110	0.090
	II	0.011	0.052	0.027

Figure 12.9 provides the derivative of the inductance versus position for the three electromagnets. Steady-state measurement of the levitated disc was carried out 20 times to check the repeatability of 6pAAMB. Results are shown in Table 12.9.

The differences between particular displacements and coil currents in the active z axis of the system are less than 1% compared to their mean values, while the variation in the x-y plane reaches up to 5% in standard deviation with the highest amplitude of change up to 20% of the signal. It is caused by the inability to maintain a fixed starting point for the disc levitation and confirms a chaotic motion in the uncontrolled actuator plane.

Table 12.9. Statistical data of the measured 6pAAMB equilibrium points.

	i[mA]			z[μm]			x[μm]	y[μm]
EM	1	2	3	1	2	3		
σ	2.1	2.3	2.8	1.0	1.2	1.4	24.3	34.1
Δ	7.9	8.3	10.6	3.9	4.2	5.2	72.6	189.2

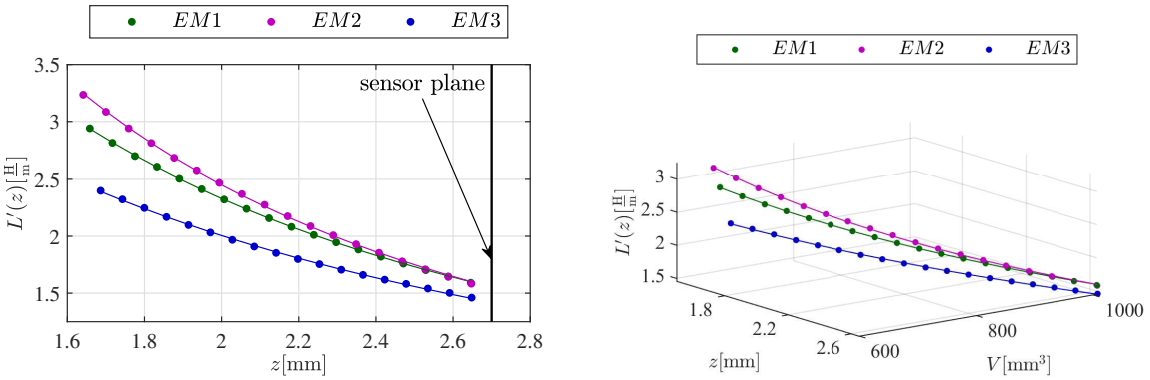

(a) Derivative of inductance versus position.

(b) Derivative of inductance versus position, gap volume.

Fig. 12.9. The electromagnetic force indirect identification via levitation steady states with PD regulator.

In order to comprehensively compare and visualize the various methods aimed at measuring and identifying the electromagnetic force of 6pAAMB, four were selected and presented, i.e., indirect identification by steady-state rotor levitation, direct measurement with the uniaxial strain gauge sensor, the quasi-3D analytical model based on Maxwell's equations (see Chapter 10) and 3D numerical simulation in the COMSOL Multiphysics calculation package. Figure 12.11 presents the resulting forces as a function of current and position with their relative error.

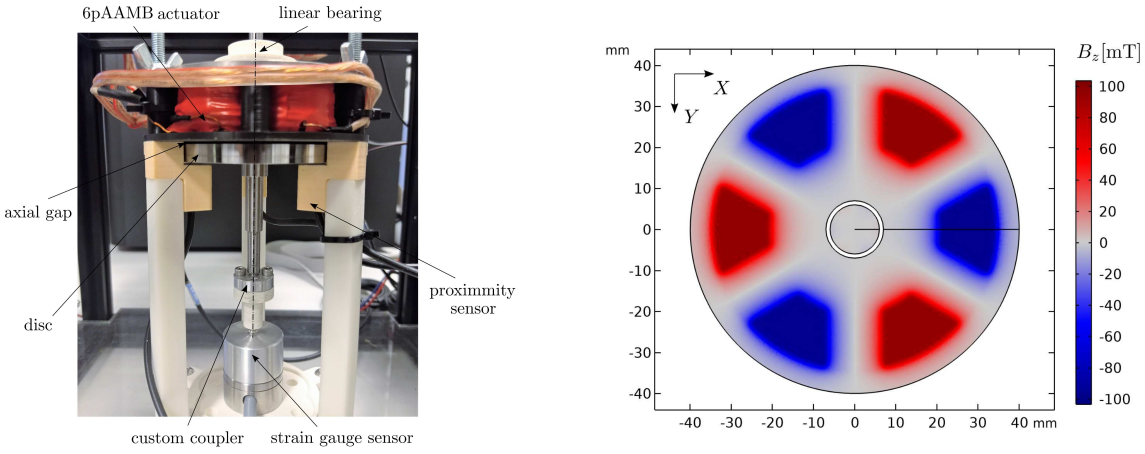

(a) Test stand for measuring the 6pAAMB force.

(b) Axial magnetic field in the air gap midspan.

Fig. 12.10. Verification of the electromagnetic force using an uniaxial force sensor and the 3D simulation.

Developed in [41] the analytical magnetic bearing model provides the axial magnetic induction distribution in 3D, which allows obtaining the electromagnetic force. The model utilizes magnetic vector potential formulation and SC mapping with the end effect influence and the conjugate complex permeance function. The main advantage of the proposed solution is a significantly shorter computation time compared to the numerical one that is useful from the modeling and controller study point of view.

$$\begin{cases} R^i_{avg} & = R_i + \frac{R_o - R_i}{n_s}, i \in 1, 2, ..., n_s \\ t_{slice} & = \frac{R_o - R_i}{n_s} \end{cases} \tag{12.8}$$

where n_s denotes the number of 6pAAMB slices in the radial direction with each slice's i radius R^i_{avg} and width t_{slice}.

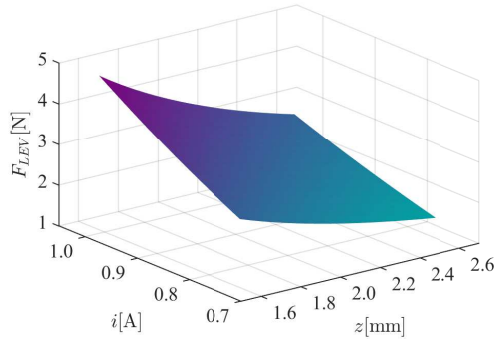

(a) Force from levitation experiment.

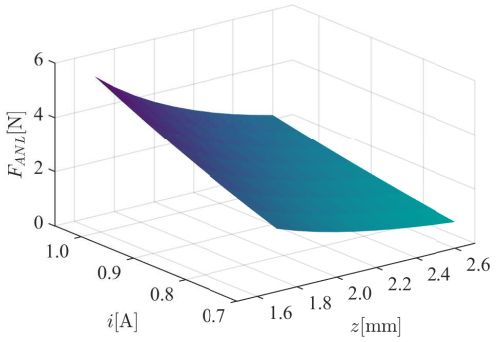

(b) Force from quasi-3D analytical model.

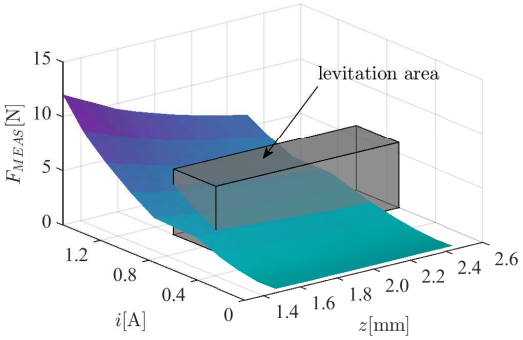

(c) Force from an uniaxial sensor measurement.

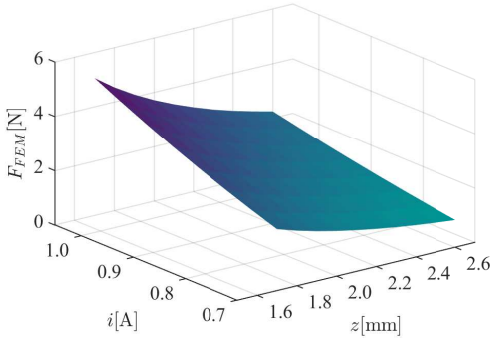

(d) Force from 3D numerical simulation.

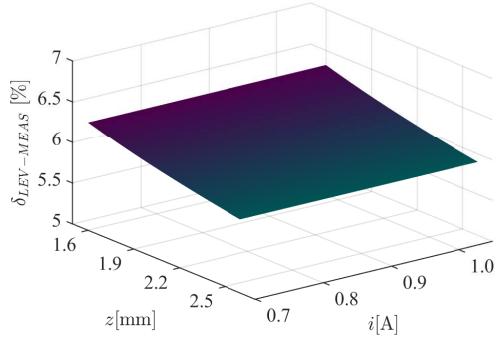

(e) Relative error between experiment and measurement.

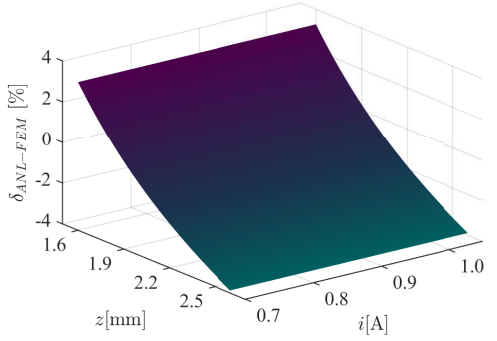

(f) Relative error in analytical and numerical model.

Fig. 12.11. The 6pAAMB electromagnetic force obtained from various methods.

The total force is obtained by superposition over all slices:

$$F_{em} = \sum_{i=1}^{n_s} \frac{t_{slice} \pi R_{avg}^i}{\mu_0} \left(\sum_{n=1}^{N_{div}} \frac{1}{N_{div}} \left(B_z^2 - B_u^2 \right) \right) \tag{12.9}$$

where B_z, B_u are axial and tangential magnetic flux components, respectively, with N_{div} state as the number of calculated points around the 6pAAMB perimeter.

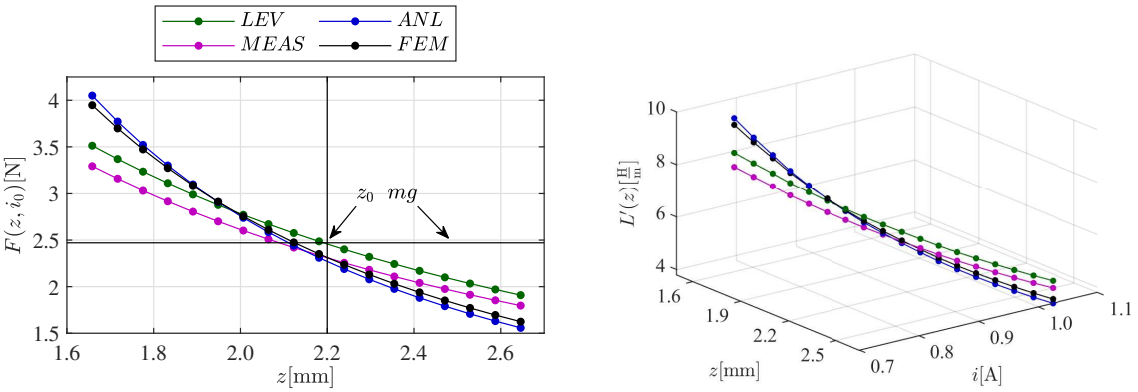

(a) Force versus position for the nominal current in z_0.

(b) Derivative of inductance versus position and current.

Fig. 12.12. Comparison of the electromagnetic force at a given operating point and the inductance obtained from various methods.

The numerical simulation of 6pAAMB was prepared (Fig. 12.10b) in COMSOL Multiphysics software to verify the experimental results and demonstrate the precision of the analytical method, which can be successfully used for further regulator synthesis. The fine simulation mesh consists of 228414 tetrahedral elements and is solved for 844128 DoFs. The model uses a stationary magnetic field (*mf*) module with separately modeled six coils and a parametric sweep procedure. The single stationary simulation takes about 3 minutes. All calculations were performed on a PC with an Intel (R) Core (TM) i7 CPU 975 processor with 4 cores.

The proposed test stand (Fig. 12.10a) was assembled to directly measure the electromagnetic force. The force transducer and the measuring system allow us to measure the axial force up to 40 N. The stand is able to obtain a much wider measurement range compared to the levitation area (Fig. 12.11c). The measurement may be affected by an error due to an uncertainty resulting from:

- a friction due to the linear bearing mounted on the upper part of the disc-rotor axis, which allows maintaining the axial movement of the disc during the measurement procedure,
- the manual rotation of the custom coupler enabling the disc axial movement,
- a misalignment of the sensor and actuator due to an incorrect assembly,
- the accuracy of sensor calibration and disturbances transmitted by the RT-DAC4/PCI board.

Figure 12.11e confirms that as a result of the factors mentioned above, the direct force measurement is burdened with an approximately constant error with the mean value 6.09% and standard deviation 0.12.

Figure 12.11f shows the relative error between the analytical model used and the numerical simulation in the range of -3.9% and 3.3%, which is a satisfactory result taking into account the nontrivial geometry of 6pAAMB and a decrease in computing resources and time compared to the 3D numerical model.

The differences between the experimental and simulation methods result from the fact that the latter did not introduce any imperfections in the 6pAAMB model. Figure 12.12 compiles the force diagrams with the operating point current in z_0 = 2.2 mm for each method. Table 13.3 shows a comparison of the selected approximation functions used to describe the force characteristics. It can be seen that the classical formula $\left(k\frac{i^2}{z^2}\right)$ fits well with the analytical and numerical model, but cannot take into account the defects of the model in the case of levitation and force measurement. However, extending this formula with current and position derivatives (12.10) returns the acceptable accuracy of the approximation.

Table 12.10. Comparison of various functions describing the 6pAAMB electromagnetic force.

F_{em}	Coeff/Fit	LEV	$MEAS$	ANL	FEM
$\frac{1}{2}\frac{mg}{(az+b)^2}i^2$	a	274.30	285.00	438.90	405.80
	b	0.30530	0.32380	-0.01996	0.04409
	R^2	1	0.9995	1	1
	$RMSE$	0.0050	0.0701	0.0014	0.0010
$k\frac{i^2}{z^2}$	k	1.3421×10^{-5}	1.0491×10^{-5}	1.3441×10^{-5}	1.3481×10^{-5}
	R^2	0.8561	0.9584	0.9997	0.9986
	$RMSE$	0.2567	0.0622	0.0153	0.0339
F_z^*(12.10)	k_1	2.3671×10^{-5}	2.0611×10^{-5}	1.3441×10^{-5}	1.3481×10^{-5}
	k_2	1.2121×10^{-7}	-3.9341×10^{-7}	-1.4621×10^{-7}	3.2621×10^{-7}
	k_3	9.7581×10^{-9}	7.2551×10^{-9}	-3.2041×10^{-10}	7.1211×10^{-10}
	R^2	0.9993	0.9984	0.9999	0.9993
	$RMSE$	0.0182	0.0750	0.0108	0.02385

$$F_z^* = k_1\frac{i^2}{z^2} + k_2\frac{2i}{z^2} + k_3\frac{-2i^2}{z^3} \tag{12.10}$$

12.7. Six pole axial active magnetic bearing single-axis model

The differential equations that describe the 6pAAMB system can be derived based on the Lagrange formula. The kinetic energy is related to the motion of the disc and the magnetic field of the electromagnets, whereas the potential energy depends on the position of the disc. The following discussion assumes a linear operating range of the actuator due to the absence of core saturation in the given range of current carrying capacity. The Lagrange function (12.11), which is the difference between the kinetic and potential energy, is given in the following form:

$$L = \sum_{i=1}^{3}\frac{1}{2}k_{L_i}\left(m\dot{z_i}^2 + L_i(z_i)\dot{q_i}^2 + \int_0^t R_i\dot{q_i}^2dt + mgz_i + qu_i\right) \tag{12.11}$$

where m - disc mass, g - gravitational acceleration, q_i - electric charge flows through the i^{th} electromagnet, z_i - disc distance from the actuator, R_i, $L_i(z_i)$, $\dot{q}_i$, u_i denote the i^{th} electromagnet's resistance, inductance, current and control respectively with $i \in [1, 2, 3]$. The functions $z_i(t)$ and $q_i(t)$ satisfy the following system of differential equations:

$$\begin{cases} \dfrac{d}{dt}\dfrac{dL}{d\dot{z}_i} = \dfrac{dL}{dz_i} \\ \\ \dfrac{d}{dt}\dfrac{dL}{d\dot{q}_i} = \dfrac{dL}{dq_i} \end{cases} \tag{12.12}$$

Substituting (12.11) into (12.12) one can get the 6pAAMB model equations:

$$\begin{cases} \dfrac{dz_i}{dt} = v_i \\ \\ \dfrac{d^2 z_i}{dt^2} = \dfrac{kL_i}{2m}\dfrac{dL_i}{dz_i} i_i^2 + g \\ \\ \dfrac{di_i}{dt} = \dfrac{1}{L_i(z_i)}\left(-\dfrac{dL_i}{dz_i}\dfrac{dz_i}{dt} i_i - R_i i_i + u_i\right) \end{cases} \tag{12.13}$$

In the conducted research, the 6pAAMB system was equipped with a hardware current controller based on a chopping technique. When controlling the system with MATLAB/Simulink operating in real-time mode on RT-DAC4/PCI board with a sampling frequency of 1 kHz, it was possible to neglect actuator dynamics with the internal current controller and consider the magnetic levitation system as a current-driven one. The measured time constants of the actuator are 4 to 50 times lower than the sampling period during the disc position, varying in the full levitation range. Therefore, a single axial model of 6pAAMB was proposed (Fig. 12.13), choosing as a reference the current of the first electromagnet i_1 and the position measured in its levitation space z. Finally, 6pAAMB can be described by the set of following differential equations:

$$\begin{cases} v = \dot{z} \\ \dot{v} = g - \dfrac{1}{2m}\left(k_{L1}\dfrac{dL_1(z)}{dz} i_1^2 \quad + k_{L2}\dfrac{dL_2(z)}{dz}(i_1 + \Delta i_2)^2 \right. \\ \qquad\qquad\qquad\qquad \left. + k_{L3}\dfrac{dL_3(z)}{dz}(i_1 + \Delta i_3)^2\right) \end{cases} \tag{12.14}$$

where: z - the disc axial distance to the actuator ($z \in (0, z_{max}), z > 0$), v - the disc axial velocity, i_1 - the current of 1st electromagnet, $\Delta i_{2,3} = i_1 - i_{2,3}$ - the added current correction value for 2nd and 3rd electromagnets.

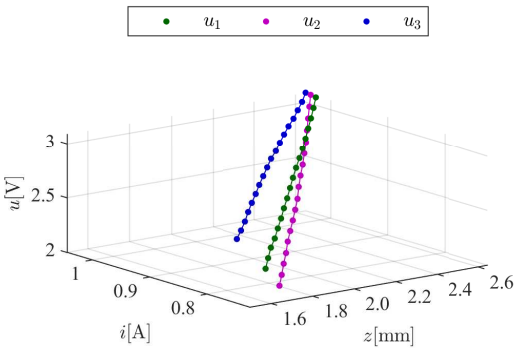

(a) Control signal versus position and current.

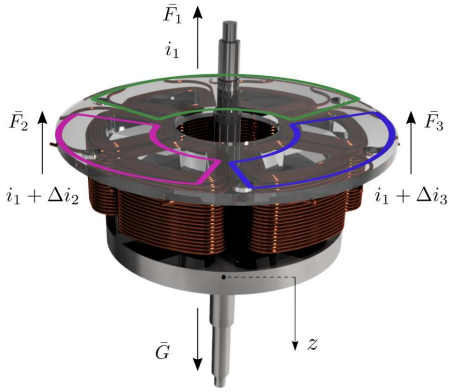

(b) The 6pAAMB single axial diagram.

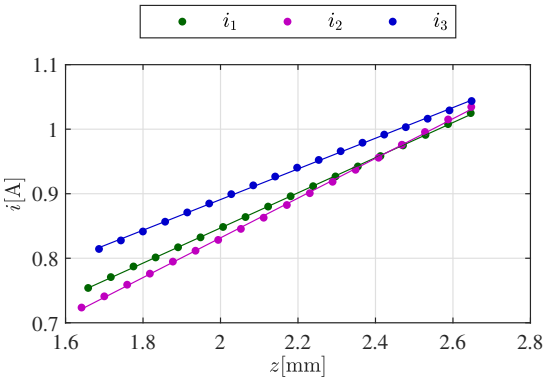

(c) Current versus position.

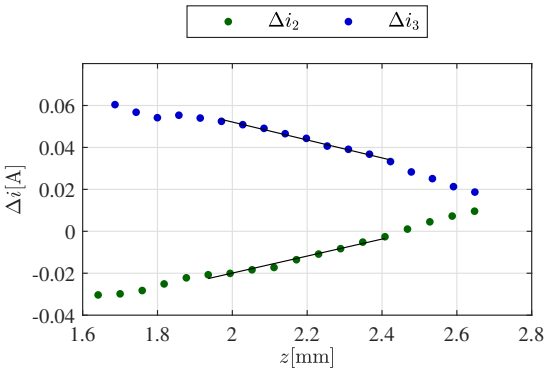

(d) Current correction versus position.

Fig. 12.13. The 6pAAMB identification characteristics towards the single axis model.

12.7.1. Linear model

The considered system is limited by the parameter values given in Tab. 12.11. To linearize the system given in (12.14), the requested position z_0 is defined. Then, the desired steady-state coil current i_{10} is calculated to be used together with a state feedback controller at the stabilization point.

$$i_{10} = \sqrt{k_{L1} \frac{2mg}{L_1(z_0)}} \tag{12.15}$$

To provide a simple tunability of the stiffness and damping, the state feedback controller is proposed:

$$i_1(t) = -K_p z(t) - K_d v(t) \tag{12.16}$$

Knowing that there are two control coefficients available, the dynamic properties of the control feedback loop can be configured as desired. Analyzing the characteristic equation of a closed-loop system of the form (12.17) one may notice that the distribution of eigenvalues depends on the selection of controller

parameters for the particular operating point.

$$\dot{z} = \begin{bmatrix} 0 & 1 \\ \alpha - \beta K_p & -\beta K_d \end{bmatrix} z \tag{12.17}$$

Table 12.11. Parameters limitations of the single axis 6pAAMB model.

Parameter	z_{min}	z_{max}	v_{min}	v_{max}	i_{max}	u_{max}	g	m
Value	0m	2.7e^{-3}m	0m/s	50m/s	2A	4.5V	9.81m/s^2	0.2526kg

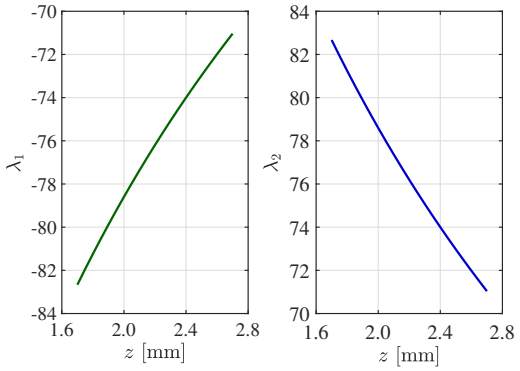

(a) Eigenvalues distribution.

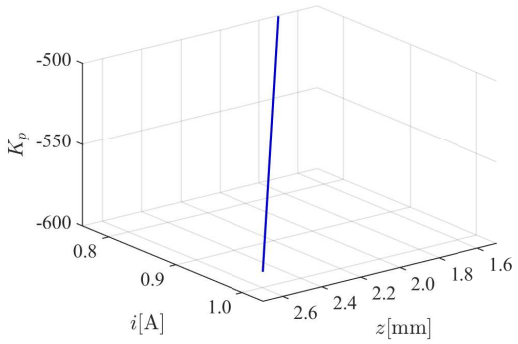

(b) Controller parameter K_p versus position and current.

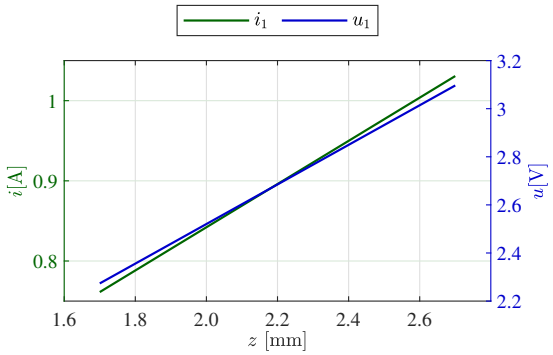

(c) Current and voltage versus position.

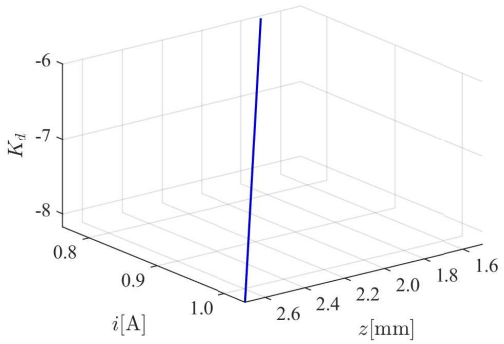

(d) Controller parameter K_d versus position and current.

Fig. 12.14. Eigenvalues, state variables and controller parameters of the 6pAAMB single axis model.

The number and type of the system eigenvalues depend on the determinant of the closed-loop system characteristic equation. The permissible values of K_p and K_d are limited by the asymptotic stability criterion of the closed-loop system. The asymptotic stability condition $Re(\lambda_i) < 0, i = 1, 2$ is satisfied for $-\beta K_d < 0$, hence $K_d < 0$. Feedback parameters should be determined so that the damping and elastic coefficients of the closed system are given in advance. It can be seen that the linear system is observable and controllable. The eigenvalues λ_1 and λ_2 depending on the operating point are presented in (Fig. 12.14a). To satisfy a stable operation, the control law is given by equation (12.16).

It can be observed that the linearized 6pAAMB system under state feedback control corresponds to the ideal mechanical equivalent with a programmable form of elasticity and damping coefficients ([46]). The configurable dynamics means that the controller parameters are calculated on the basis of the requested eigenvalue distribution. An example of aperiodic damping is presented in Tab. 12.12.

Table 12.12. Controller parameters for the aperiodic property ($\lambda_1 = \lambda_2$) set for all steady-state points.

z_0[mm]	i_{10}[A]	K_p	K_d	$\lambda_{1,2}$
1.7	0.761	500.33	-6.03	-82.67
2.0	0.842	-524.97	-6.68	-78.60
2.2	0.896	-541.34	-7.10	-76.19
2.4	0.950	-557.69	-7.53	-74.00
2.7	1.031	-582.17	-8.18	-71.04

12.7.2. Model verification

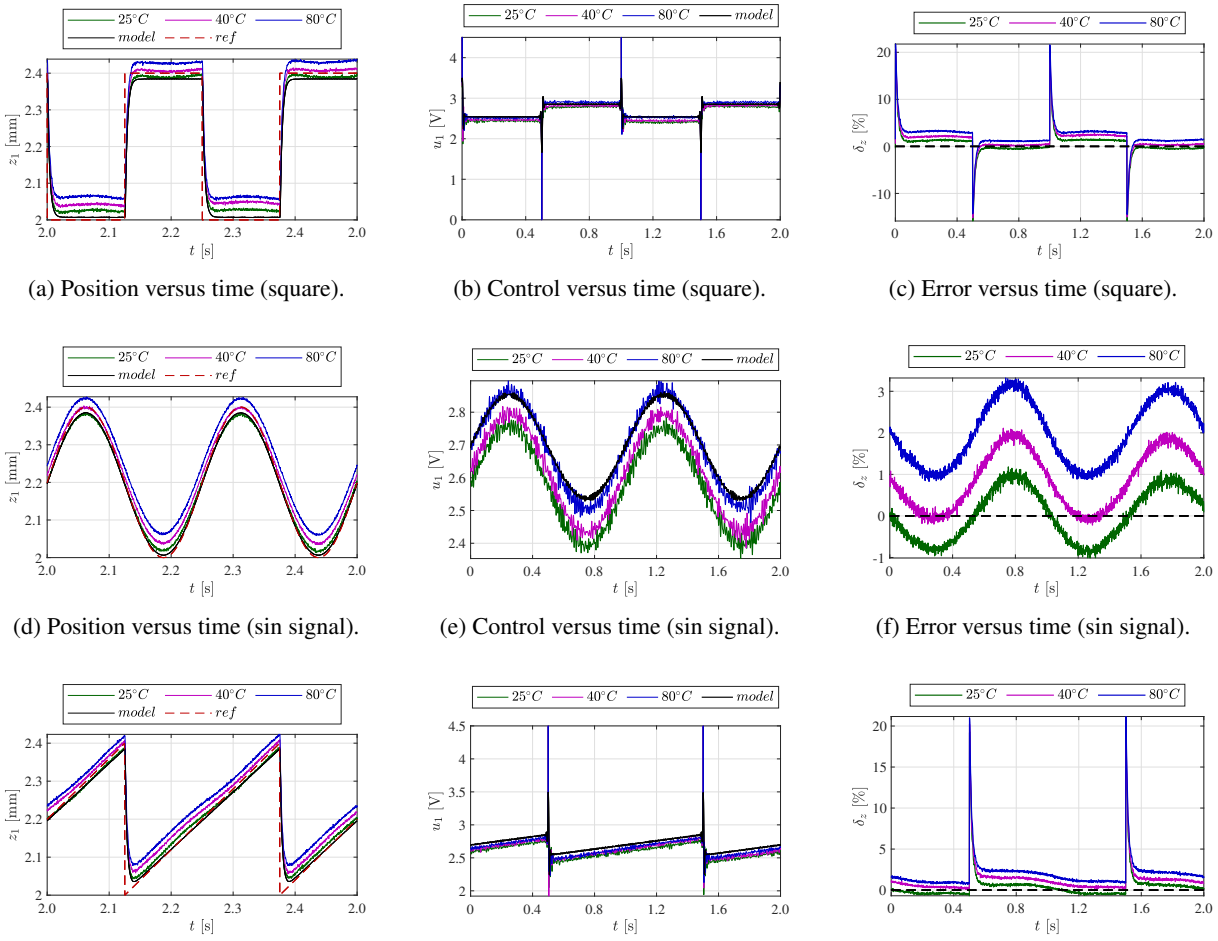

(a) Position versus time (square).
(b) Control versus time (square).
(c) Error versus time (square).
(d) Position versus time (sin signal).
(e) Control versus time (sin signal).
(f) Error versus time (sin signal).
(g) Position versus time (saw signal).
(h) Control versus time (saw signal).
(i) Error versus time (saw signal).

Fig. 12.15. Disc levitation for aperiodic PD regulator settings and a few operating temperatures of 6pAAMB.

For the aperiodic settings of the PD controller, a comprehensive comparison of the single-axis model with the experiment was made. Square, sine and saw-type reference signals were considered. Figure 12.15 shows the position control and the error between the given reference position and the measured one. Thermal calculation verification was a comparison of the above-mentioned experiments for temperatures 25°C, 40°C and 80°C. A significant position convergence of the single-axis model with the experiment may be observed (less than 1%) and the modeled control is shifted by approximately 4% with respect to the measured one. The reason for this is that the hardware current controller is not included in the proposed simplified model. The position and relative error increases along with higher temperature, reaching below 2% at maximum load compared to 25°C.

Table 12.13. Comparison of the damping cases on the basis of selected functions that approximate the step response of the levitating disk for different settings of the PD controller (damping case: w-weak, c-critically damped, s-strong).

P↓ D→	-0.97	-1.29	-1.62	-1.95	-2.27	-2.60	-2.93	-3.26	-3.58	-3.91
-130.94	s	s	s	c	c	s	s	s	s	s
-196.42	w	w	s	s	s	s	s	c	s	s
-229.16	w	w	w	w	c	s	s	s	s	s
-261.90	w	w	w	s	w	s	s	s	s	s
-294.64	w	w	w	s	s	c	s	s	s	s
-327.38	w	w	w	s	w	c	s	s	s	s
-360.12	w	w	w	w	w	w	c	c	s	s
-392.86	w	w	w	w	s	s	s	c	s	s
-425.60	w	w	w	w	w	s	s	s	c	s

Figure 12.16 presents the optimized step response characteristics for dynamic 6pAAMB operation. For computational purposes, the signals were offset so that z^{init} is the initial sample before the applied step and z^{end} equals 0. The following parameters were calculated based on the linear damped system:

- A_{peak} peak value of $|z_1(t) - z_1^{init}|$,
- δ_A percentage overshoot relative to the normalized response $||z_1(t)|| = (z_1(t) - z_1^{init})/(z_1^{end} - z_1^{init})$,
- T_{set} settling time, when the error $|z_1(t) - z_1^{end}| \leq 2\% \times |z_1^{end} - z_1^{init}|$ for $t \geq T_{set}$,
- T_{rise} rising time for the response from 10% to 90% of the rising edge from z_1^{init} to z_1^{end}.

The disc damping may exhibit oscillatory and decaying properties in several regimes (Table 12.13), i.e.: underdamped refers to a damping ratio ($0 \leq \zeta < 1, w$), overdamped with the solution being simply a sum of two decaying exponential with no oscillation ($\zeta > 1, s$) and critically damped - a desired border between the two cases mentioned above ($\zeta = 1, c$). Figure 12.17 provides the complete map of the optimal control settings to achieve the selected dynamic properties of the 6pAAMB actuator. A thorough data analysis shows that the system model requires higher-order functions. This confirms the limitation of the utilized approximation method, which the author are aware of, presenting only the selected parameters of the system step response. In the future, the 6pAAMB model should be extended to include transient nonlinearities.

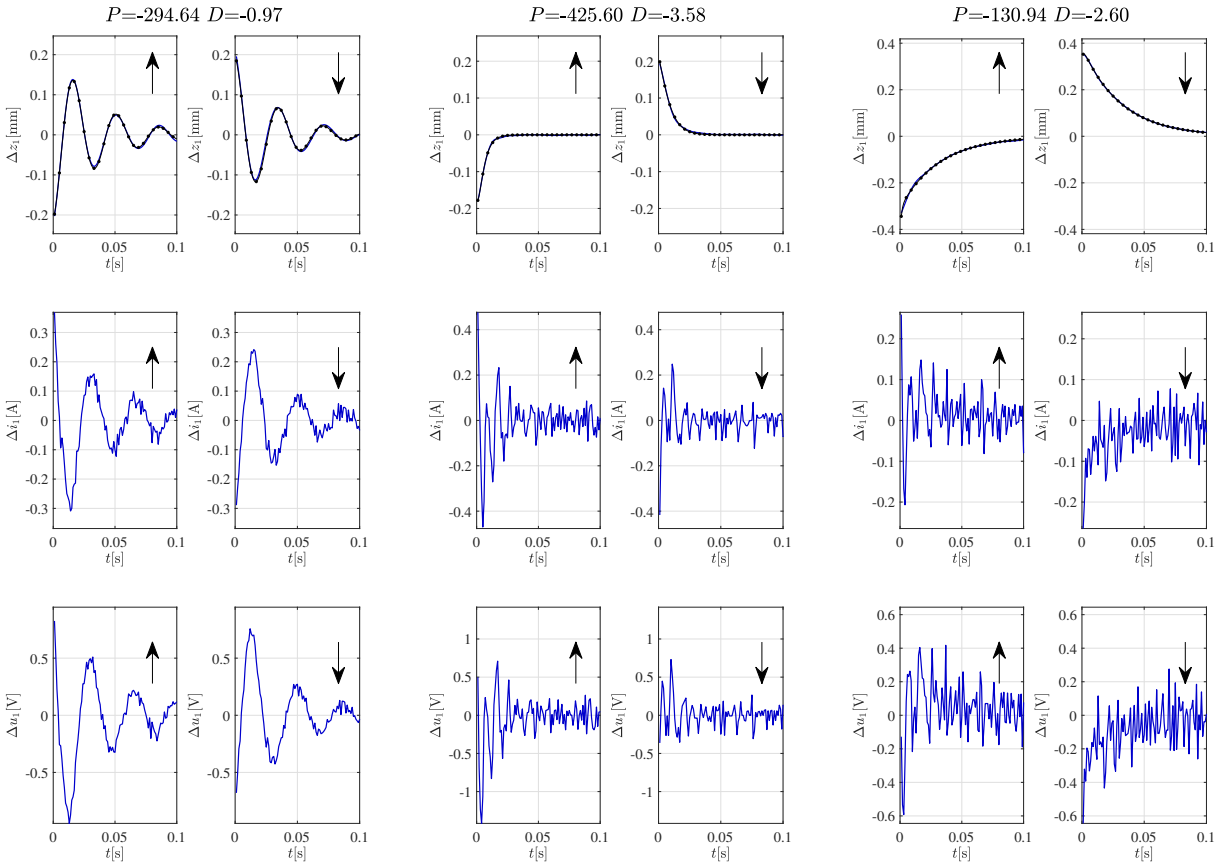

(a) Underdamped disc vibrations. (b) Critically damped disc vibrations. (c) Overdamped disc vibrations.

Fig. 12.16. Disc position, current and control errors for step response with 0.2 mm step amplitude and 2.2 mm levitating gap for different PD controller settings.

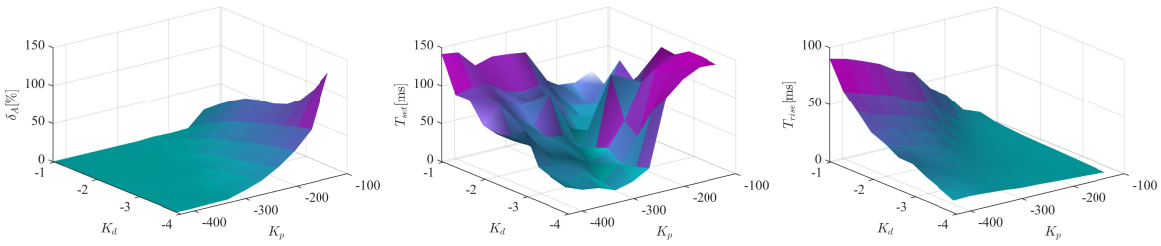

(a) Position overshoot. (b) Position settling time. (c) Position rising time.

Fig. 12.17. Comparison of parameters describing the step response of the levitating disc in a function of PD controller settings.

12.8. Dynamic force excitation investigation

Constant vibration and repeated shocks acting on an actuator surface are commonplace for many devices, such as active vibration isolators and magnetic suspension systems, as well as industrial electromagnetic grippers with automatic identification of the handled object and mobile robotics solutions.

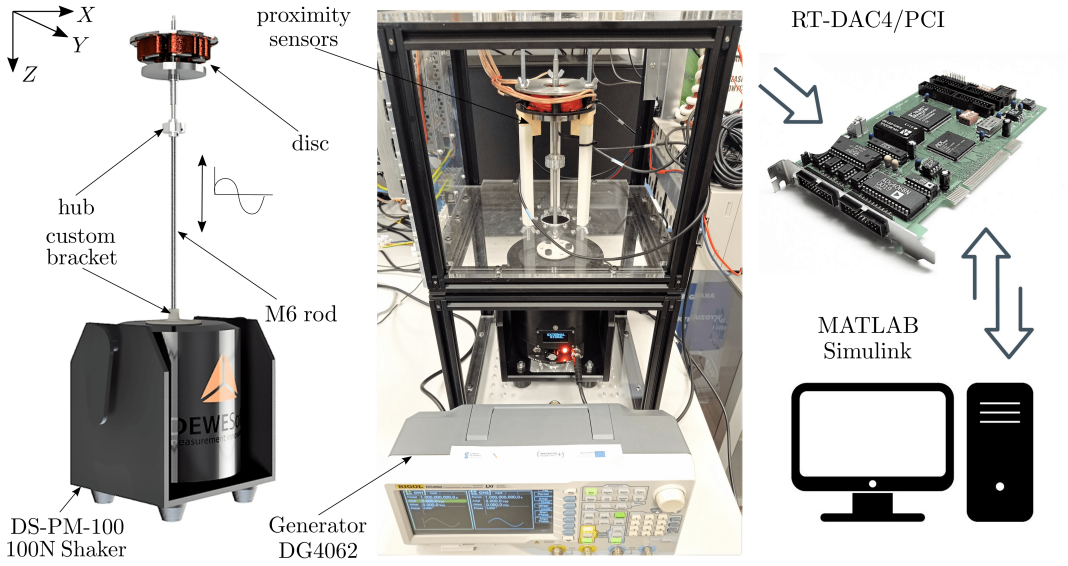

Fig. 12.18. Test stand with dynamic excitation for vibration testing of the 6pAAMB actuator.

To maintain desired performance under demanding conditions and present excellent operational quality for many years, a design, components and materials must be carefully considered and extensively tested. Identifications based on dynamic excitation are especially provided by manufacturers of small-sized mechanical structures in the field of robotics and mechatronics, whose working conditions or the work itself generate chaotic motion of a moving object and vibrations in various directions. It is essential that the actuators can withstand the load and still perform flawlessly. With this in mind, the test stand (Fig. 12.18) was assembled to identify the impact of a dynamic force input on the 6pAAMB actuator operation.

Table 12.14. Approximated sinusoidal waveforms for different excitation frequency - relative error comparison.

δ[%]	f[Hz]										
	1	2	4	6	8	10	12	14	16	18	20
δ_z	0.05	0.04	0.03	0.01	0	0.02	0.04	0.03	0.07	0.01	0.17
δ_i	0.79	0.86	1.53	1.86	2.38	2.29	2.08	1.92	1.88	1.65	3.00
δ_c	0.09	.07	0.70	1.00	1.71	0.10	3.23	3.67	0.84	0.53	0.74
δ_e	0.23	0.25	0.23	0.57	0.50	1.15	0.40	0.87	0.10	0.50	0.57

The test stand consists of the DS-PM-100 shaker from Dewesoft with a M6 threaded rod attached through an aluminum hub to the disc axis. The shaker generates sinusoidal excitation along the axial direction with a given amplitude and frequency from the Rigol DG4062 function generator. Signal acquisition is provided by the RT-DAC4/PCI control board and analyzed in MATLAB/Simulink. The disc excited by forced vibrations (Fig. 12.19a) is actuated by the PD controller with parameters three times higher compared to the aperiodic ones for 2.2 mm desired gap (K_p=-1624.02, K_d=-21.30) with a position change that affects the control and current value (Fig. 12.19b). The measured waveforms are approximated by the sinusoidal function, as shown in Table 12.14. Figure 12.19d illustrates the influence of vibrations on

the position of the disc with the regulator's objective of stabilization at the desired level. After a downward air gap violation, the regulator tries to return to the setpoint, while with the decreasing air gap, there is no possibility of the disc pushing back action due to the single-sided configuration of the actuator.

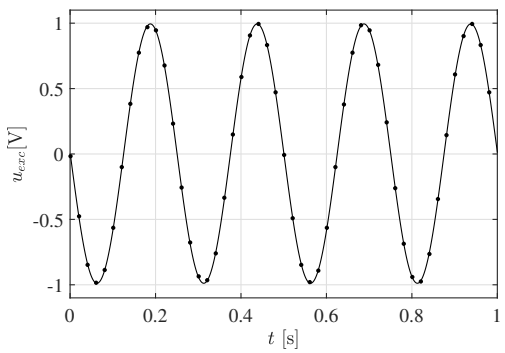

(a) Excitation voltage of the DS-PM-100 shaker.

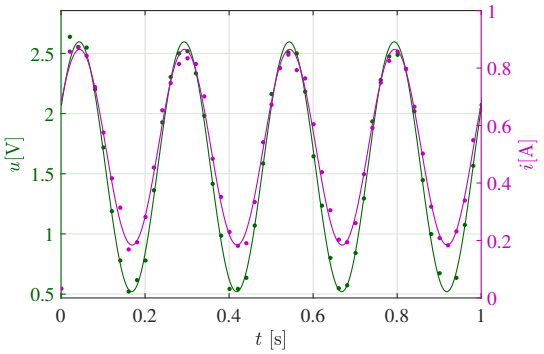

(b) PD control and current for f=4 Hz excitation signal.

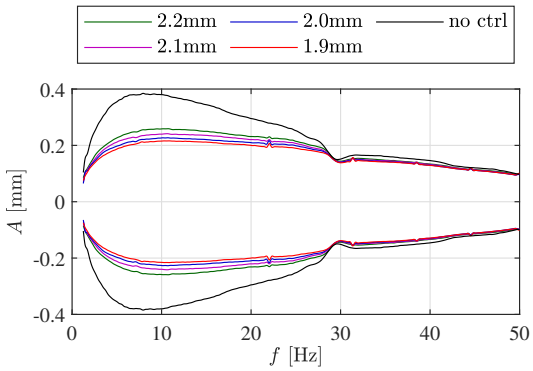

(c) Amplitude-frequency characteristic of the shaker.

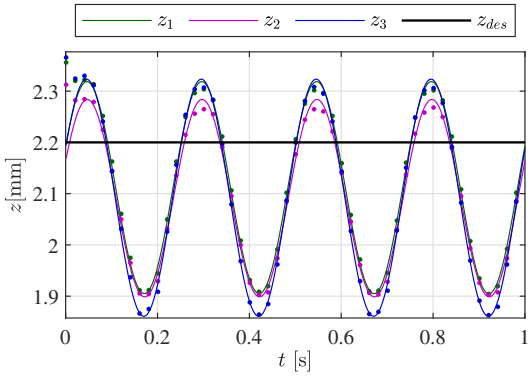

(d) Disc position excited by the shaker for f=4 Hz.

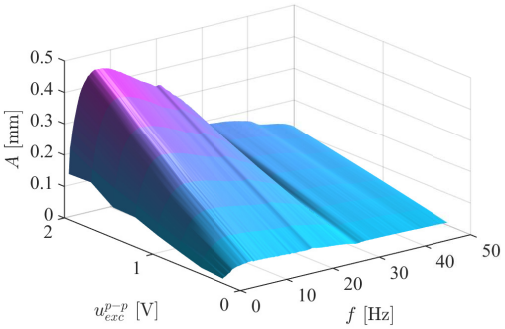

(e) Disc vibration amplitude versus frequency and excitation without the applied control.

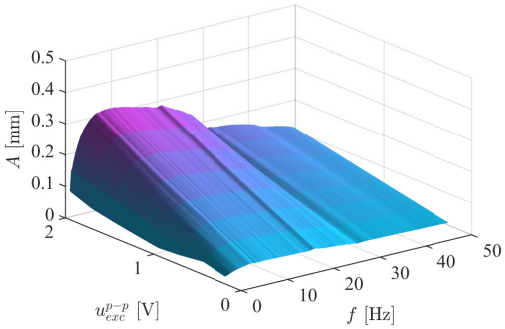

(f) Disc vibration amplitude versus frequency and excitation with the PD control for 2.2 mm.

Fig. 12.19. The 6pAAMB vibration testing and identification.

By performing shaker excitation through a wide frequency range, one can obtain the amplitude-frequency characteristics (Fig. 12.19c) of 6pAAMB with a regulator for a given operational mode, as well as the shaker itself for further identification. The vibration amplitude as a function of frequency and excitation is presented in Fig. 12.19e and Fig. 12.19f for 6pAAMB, respectively, without and with the applied control.

The integral element of a mechanical system dynamic analysis is its determination of the amplitude-phase characteristics. Figures 12.20a-12.20b show the convergent linear phase shift for each electromagnet between the current-to-control and the control-to-position signals. Figures 12.20c-12.20d present the ratio of control to displacement and excitation to control. Figure 12.20e shows the shaker excitation function for which the vibration amplitude (Fig. 12.20f) in the given range will be approximately constant. The operation of the regulator allows us to reduce the amplitude of vibrations by about 25% with the simultaneous increase of excitation by up to 50%.

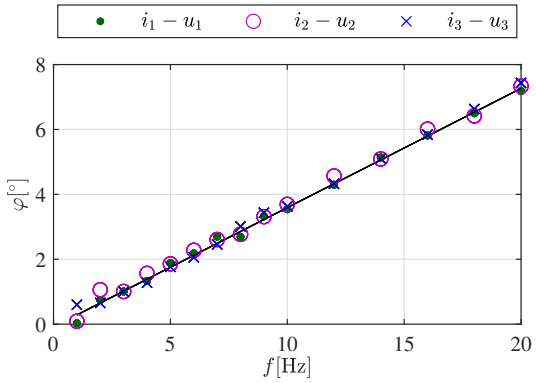

(a) Phase lag versus frequency between current - control.

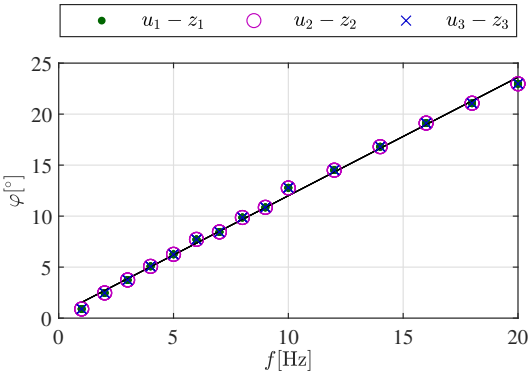

(b) Phase lag versus frequency between control - position.

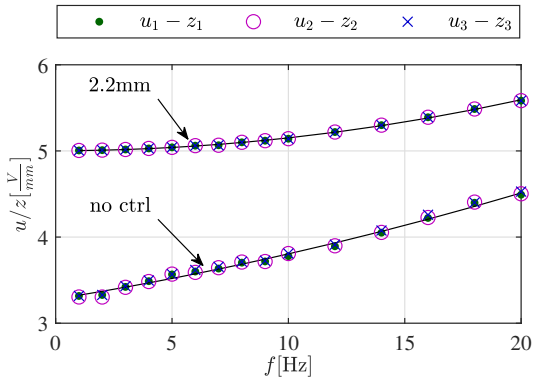

(c) Control to position amplitude ratio versus frequency.

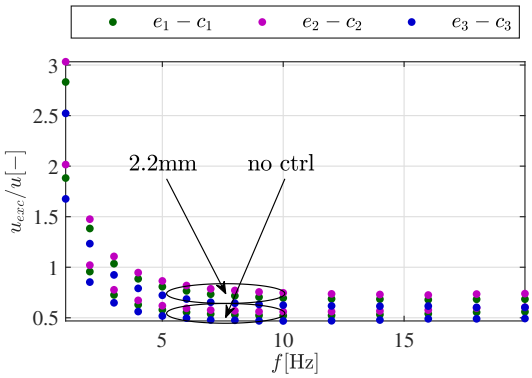

(d) Excitation to control amplitude ratio versus frequency.

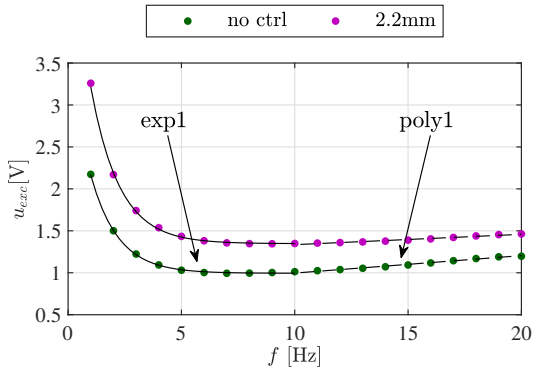

(e) Excitation amplitude versus frequency.

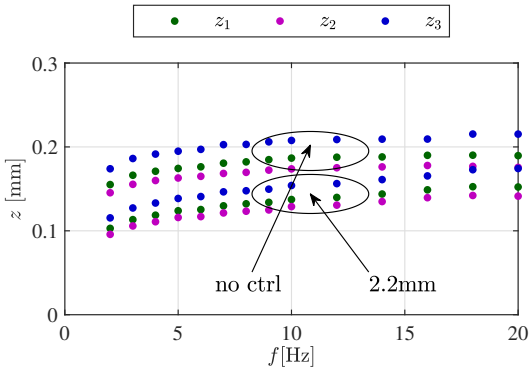

(f) Disc vibration amplitude versus frequency.

Fig. 12.20. The 6pAAMB amplitude and phase characteristics.

Summary of results

Research demonstrated a complete identification inspired by real system imperfections, leading to the verified model of the single-axis axial active magnetic bearing. This step states the starting point for a multivariate parametric optimization, which accelerates the complete 6-DoF global model of 6pAAMB. The paper presented a real prototype with the novel design applied in the custom test rig. The existing inaccuracies resulting from coil differences and assembly errors became a motivation to discuss in detail the identification process in a wide range of interdisciplinary methods. The problem of eccentricity was emphasized during the levitation of the tilted disc, which has a consequence in its chaotic motion. Discrepancies in the winding parameters were investigated with the RLC meter, the magnetic field probe and the oscilloscope, resulting in a slight uncertainty of the parameters related to the manual production of the coils.

Future investigations should include work on electromagnet's mutual inductance and cross-coupling modeling due to the adopted actuator configuration, external disturbances or system inaccuracies. The heating experiment has shown that the 6pAAMB thermal influence is acceptable even under operating conditions that significantly exceed the nominal ones. The study extended considerations concerning the measurement and calculation of the electromagnetic force through a few methods, i.e., indirect from the levitation experiment, direct with the uniaxial sensor measurement, analytical based on Maxwell's equations and from a numerical 3D model. The convergence between the applied methods was satisfactory and has been described in detail in Section 12.6. The 6pAAMB experiments were carried out with a much larger levitation gap compared to the dedicated applications.

The dynamic properties of the system in a broad frequency range were examined using the shaker DS-PM-100 with external harmonic excitation. The adjusted PD controller for 6pAAMB shows the desirable features of the magnetic levitation system in terms of the amplitude-phase characteristic. The conducted research forms a consistent methodology for the identification of electromagnetic actuators with particular emphasis on axial active magnetic suspension systems. In general, the designed 6pAAMB actuator could extend the stabilization range of rigid and flexible rotors. In the last chapter the author will prove that an axial magnetic bearing with multiple pole pieces may support the spatial orientation of the levitating object.

Chapter 13

Disc spatial orientation in six pole axial active magnetic bearing

The last chapter of the doctoral dissertation focuses on presenting the possibility of stabilizing the disc at a selected point in the active space of the bearing with the use of the developed axial actuator with six pole pieces. The experiments supporting the main statement are discussed below. The experimental data were used in numerical calculations to obtain model equations describing the disc in steady states. The skewing of the disc around the x axis with variable parameters of the PD controller illustrates the influence of the controller settings on the dynamics of the disc spatial orientation. The character of the lateral motion of the disc was presented. The chapter summarizes the interdisciplinary course of designing, manufacturing, identifying and controlling the levitation object by means of an axial active magnetic bearing with six pole pieces. The reader becomes acquainted with the possibilities and limitations of the proposed solution. Experimental research was carried out in the control system consisting of three local PID controllers.

13.1. Steady state analysis

13.1.1. Experimental research

Experimental research was carried out on the test stand shown in Figure 13.2. The reader can see the details of the 6pAAMB setup in the diagram below (Fig. 13.1). The adopted designations are consistent with previous studies. A number of experiments were performed to collect a database describing the states of the levitating rotor when varying the set parameters according to two scenarios:

1. all combinations of 11-element variables z_1, z_2, z_3,
2. all combinations of 11-element variables z_c, α, β

The axial displacement varied from 1.9 to 2.4 mm in steps of 0.05 mm; the tilt angles ranged from -0.01 rad to 0.01 rad in increments of 0.002 rad. Each variable reached 11 different states, which means 1331 simulations for each variant. There were 10 repetitions for each scenario. The distribution of the data is described in Table 13.1. It can be concluded that with assumed unknowns, such as the impossibility of perfect leveling of the test stand base surface, tolerances of the housing components and the varying

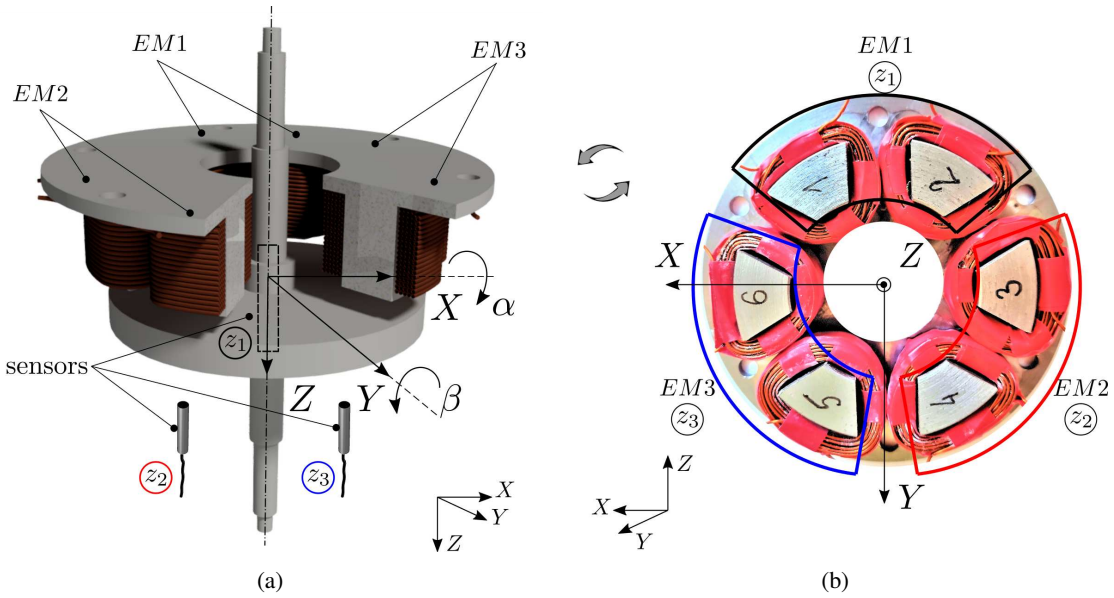

Fig. 13.1. Isometric cross-section of the 6pAAMB actuator with the adopted coordinate system (a) and top view of the stator after rotating it around the y axis by β=180° (b).

initial position of the disc at the beginning of the experiment, the dispersion of the obtained data confirmed the repeatability of the experiment with the relative error of disc stabilization in the inactive plane, respectively, 4.02% in the x axis, 6.37% in the y axis. All experiments in this section were performed in a closed loop with three local PID controllers (2.3) for settings K_p = -3300, K_d = -43.5, K_i = -500 with a sampling period T_0 equal to 1 ms.

Table 13.1. Relative difference in parameters for all measurement sets in the 2nd experimental scenario.

$\|\delta\|$[%]	x_m	y_m	i_1	c_1	z_c
min	1.821	4.185	0.350	0.537	0.004
max	2.197	6.367	0.813	0.990	0.005

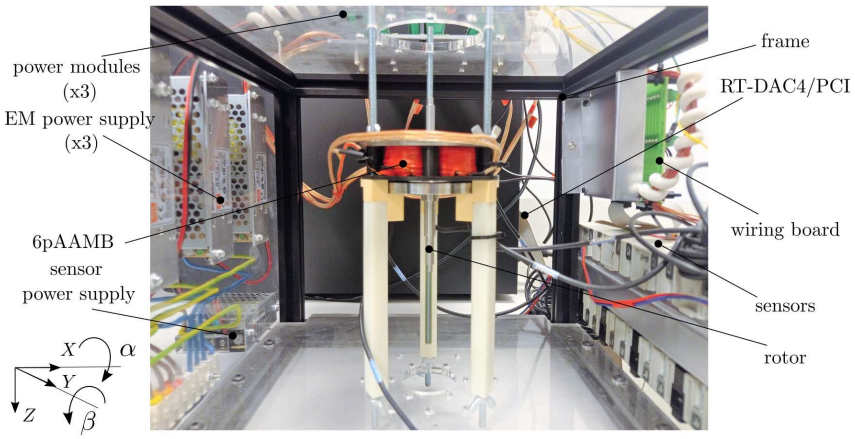

Fig. 13.2. Assembled laboratory test stand for testing 6pAAMB.

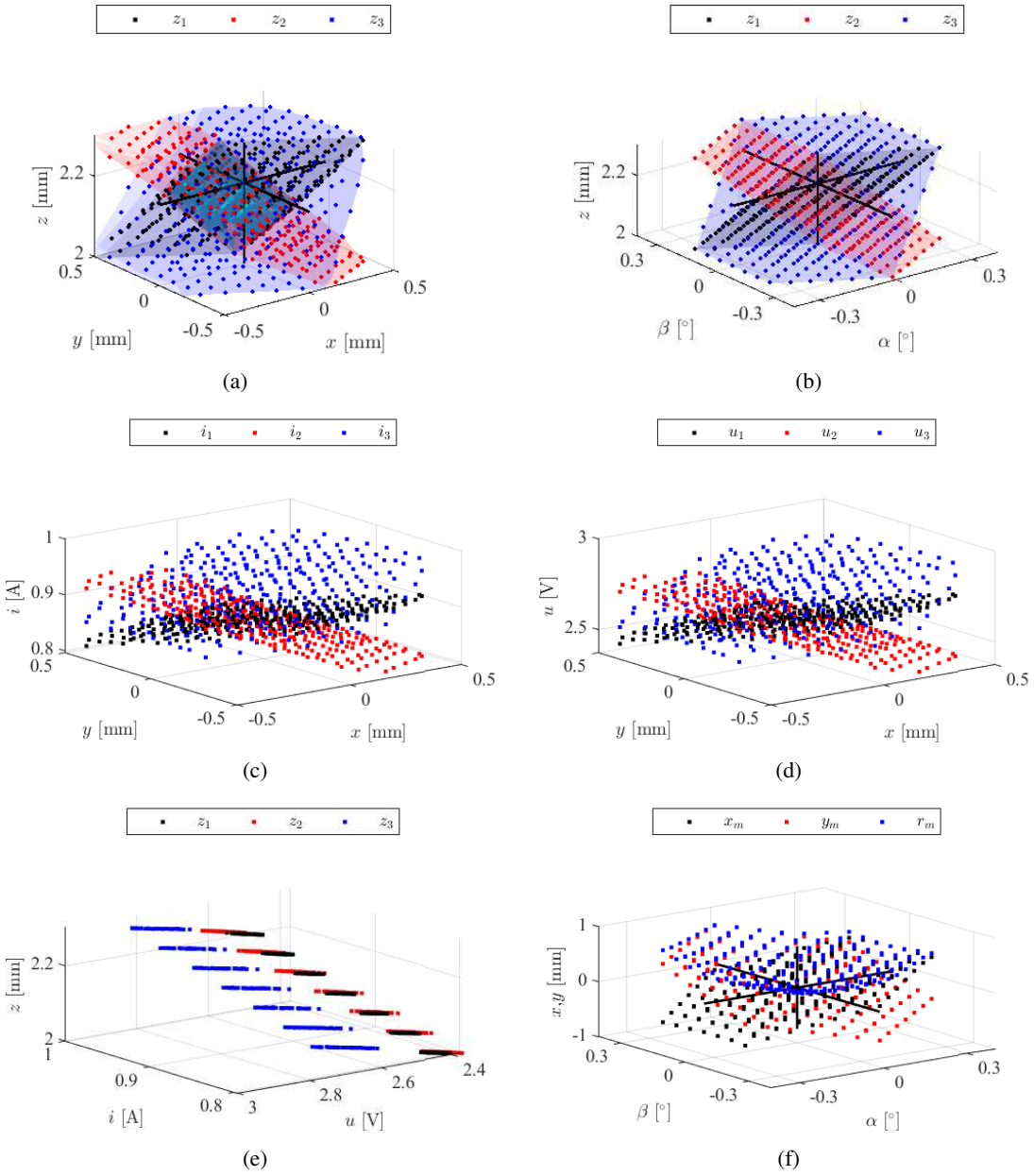

Fig. 13.3. Levitating disc steady states for the 1st experimental scenario (1st iteration).

Illustrative Figures 13.3a-13.3b show the measurement from three axial sensors as a function of the transverse position of the disc and the tilt angles. The data indicate that the individual measurement sets of the sensors form oblique spatial figures that have a certain set of common points (see turquoise color in Fig. 13.3a), where, while maintaining the axial position, the disc also occupies a position in the x-y plane close to the center of the coordinate system. Another conclusion is the shift of the disc stabilization point (x_c, y_c) relative to the adopted reference due to the aforementioned measurement and design uncertainties. Sets of measured steady currents and controls demonstrate discrepancies in the parameters of the electromagnets. Figure 13.3e shows the linear dependence of the measured axial positions of the disc as a function of current and control for individual levitation intervals.

The steady states x_0 and y_0 are approximated by equations (13.1) with a fit of $R^2[\%]$ equal 98.87% and 99.78%, respectively (RMSE: 0.02544, 0.01195). Radial displacement can be described by the equation of an elliptical cone with a 92% fit.

$$x_0(\alpha, \beta) = -0.009 + 1.497\alpha - 0.245\beta \tag{13.1a}$$

$$y_0(\alpha, \beta) = 0.096 - 0.234\alpha + 1.605\beta \tag{13.1b}$$

$$r(\alpha, \beta) = \sqrt{\frac{(\alpha - a_0)^2}{a^2} + \frac{(\beta - b_0)^2}{b^2}} \tag{13.2}$$

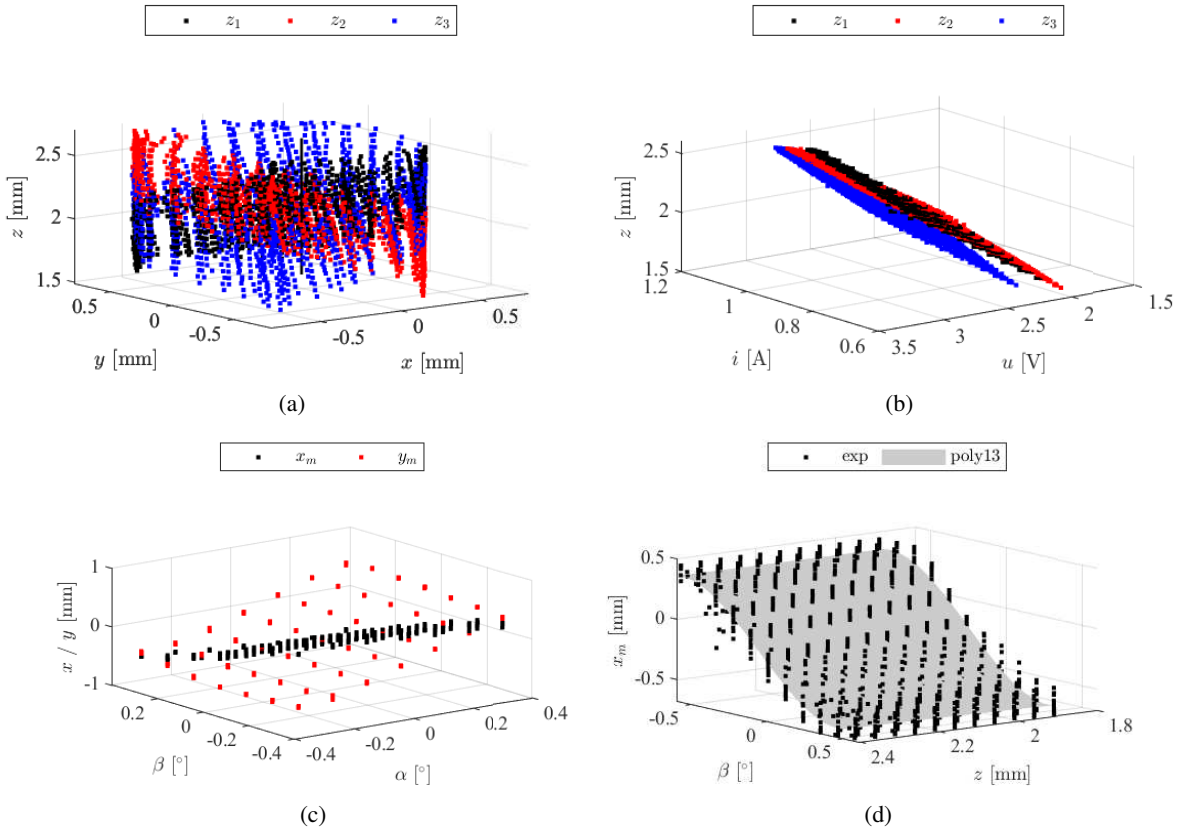

Fig. 13.4. Levitating disc steady states for the 2nd experimental scenario (1st iteration).

Figure 13.4 shows the sets of steady states obtained in the experiments according to the 2nd scenario. The analysis of the distribution of the measured axial positions will show the operational ranges of individual actuators. Figure 13.4b presents the almost linear nature (R^2=98.1%, *poly11*[1], RMSE=0.02661) of the axial position as a function of current and control for the individual electromagnets. Steady states of the rotor lateral position can be described as a function of tilt angles (Fig. 13.4c) or angle and axial position (Fig. 13.4d), where $y = f(z, \alpha)$ and $x = f(z, \beta)$ are approximated with an accuracy of, respectively, 95.90% and 94.37% for a polynomial of 3rd degree (*poly13*[2]).

[1] *poly11*: $f(x, y) = p_{00} + p_{10}x + p_{01}y$.
[2] *poly13*: $f(x, y) = p_{00} + p_{10}x + p_{01}y + p_{11}xy + p_{02}y^2 + p_{12}xy^2 + p_{03}y^3$.

13.1.2. Air gap volumes

The air gap volumes are the sum of the volumes limited by the individual pole pieces, between the reference plane of the 6pAAMB stator and the levitation plane of the rotor. They were calculated by adding the volume integrals from the functions that describe the geometry of the air gap corresponding to each pole piece (V_i, where $i \in [1, 6]$). The calculations were made in cylindrical coordinates with constraints resulting from the geometry of the pole pieces and the position of the levitating disc (13.3)[3]. The air gap volumes associated with the corresponding electromagnets as a function of the rotor tilt angles are presented in Figure 13.5.

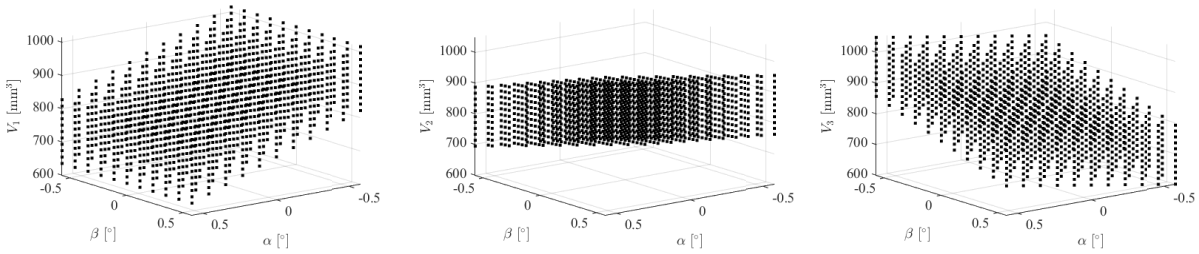

(a) (b) (c)

Fig. 13.5. Calculated volumes of air gaps associated with individual electromagnets.

$$\begin{cases} V_i & = \iiint_V f(r,\varphi,z)\,dz\,d\varphi\,dr = \int_{R_i}^{R_o}\int_{\varphi_{min}}^{\varphi_{max}}\int_{z_{min}}^{z_{max}} r\,dz\,d\varphi\,dr \\ z_{min} & = 0 \\ z_{max} & = \dfrac{-Ar\cos(\varphi) - Br\sin(\varphi) - D}{C} \\ \varphi^i_{min} & = \dfrac{\pi}{6} + \dfrac{6.979}{r - 0.1596} + \dfrac{\pi}{3}(i-1) \\ \varphi^i_{max} & = \dfrac{\pi}{6} - \dfrac{6.979}{r - 0.1596} + \dfrac{\pi}{3}i \end{cases} \tag{13.3}$$

The volumes obtained as a result of calculations according to formulas (13.3) can be approximated by the linear function depending on the central position of the levitating rotor and its tilt angles:

$$V = c_{01}z + c_{02} + c_1\alpha + c_2\beta \tag{13.4}$$

where the tilt angles of the rotor α and β are in [rad], the axial position of the rotor z is in [mm] and the resulting volume is in [mm^3]. For the ideal case[4], the coefficient c_{02} is equal to 0. Table 13.2 compares the coefficients obtained by volume calculation with the substitution of the desired and experimental parameter values. A graphical representation of these differences is provided in Figure 13.6. Due to the fact that this difference is less than 1%, the variant of calculations for ideal parameter values was used.

[3]The rational function describing half of the pole piece opening angle is an equation element of the determined limits of integration along the angular component; it depends on radius.

[4]Expected values for given vectors α, β, z.

Table 13.2. Coefficients of the volume functions based on ideal (left) and experimental (right) parameter values.

EM	c_{01}	c_{02}	c_1	c_2
1			-9348.3	0
2	383.68	0	4674.2	8095.9
3			4674.2	-8095.9

EM	c_{01}	c_{02}	c_1	c_2
1	383.66	-1.49	-9330.4	-42.1
2	383.20	-0.53	4675.3	8044.0
3	383.22	-0.49	4677.7	-8129.5

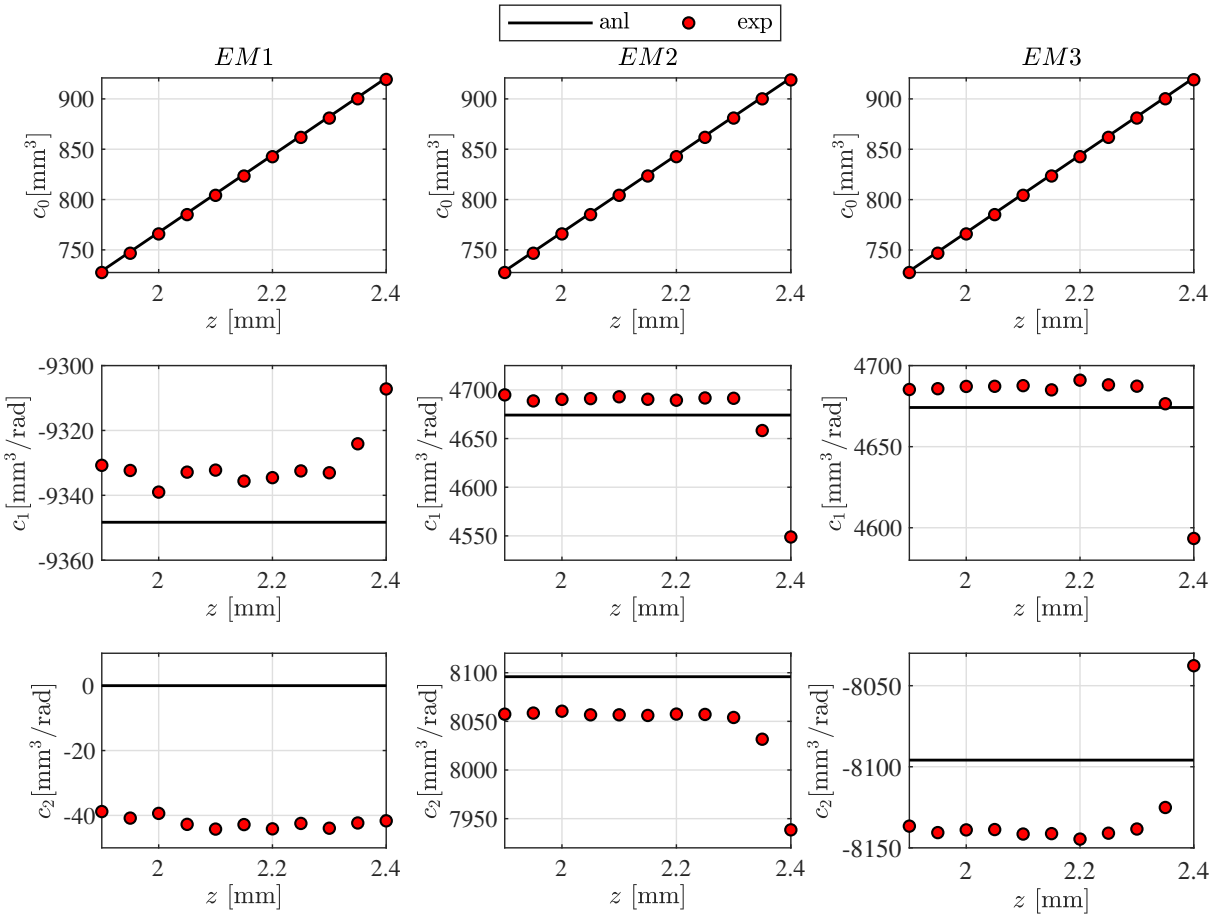

Fig. 13.6. Evaluation of volumes function coefficients approximated from ideal and measured values.

13.2. Numerical analysis for states identical to experimental results

The extended numerical verification of the obtained experimental data was carried out in COMSOL Multiphysics. The goal was to provide a reliable description of the distribution of electromagnetic forces and torques in the 6pAAMB active space. For the specified model and simulation details, refer to Section 10.3. The simulation output parameters in order are as follows:

– the electromagnetic forces: F_x, F_y, F_z, F_{x1}, F_{y1}, F_{z1}, F_{x2}, F_{y2}, F_{z2}, F_{x3}, F_{y3}, F_{z3},

– the electromagnetic torques: T_x, T_y, T_z, T_{x1}, T_{y1}, T_{z1}, T_{x2}, T_{y2}, T_{z2}, T_{x3}, T_{y3}, T_{z3}.

In total, 24 components of forces and torques were analyzed. The steady states measured from the levitating disc were imported into the developed 6pAAMB numerical model. Several simulations were performed according to the plan:

– *1st simulation*: specified combinations [α, β, z_c, i_1, i_2, i_3]; assumptions[5]: x = 0, y = 0; N_t = 125,
– *2nd simulation*: specified combinations [α, β, z_c, i_1, i_2, i_3, x, y], N_t is, respectively, 126, 129, 120 for the three electromagnets,
– *3rd simulation*: all combinations [α, β, z_c] for i=const., equal 1 A; assumptions from *1st simulation*.

Simulations were performed using the parametric sweep mode. For verification purposes, an extended iteration of *1st simulation* was calculated with the added values of the recorded steady states x, y. The obtained results were time consuming, but did not introduce a noticeable difference compared to the data from *1st simulation*, hence the assumption.

13.2.1. Axial electromagnetic force analytical expression

On the basis of the conducted 6pAAMB interdisciplinary analysis, the value of the axial electromagnetic force and its distribution for the three electromagnets is a key parameter of the 6pAAMB model.

$$F_z = \sum_{k=1}^{3} F_{z_k}(V_k, i_k) = \begin{cases} -\frac{1}{2} k_{L_k} i_k^2 \frac{2mg}{(a_k V_k \cdot 10^{-3} + b_k)^2} \\ a_k + b_k V_k + c_k i_k \\ a_k e^{(b_k V_t)} + c_k e^{(d_k V_t)} \end{cases} \tag{13.5}$$

where $k \in \{1, 2, 3\}$ and i_k, V_k, k_{L_k} denote, respectively, current, air gap volume under particular electromagnet and the given electromagnet share of the force factor based on the identified inductance differences; V_t is a total 6pAAMB air gap volume and a_k, b_k, c_k, d_k are coefficients. In the course of the axial electromagnetic force approximation, a few functions were proposed (13.5), of which the first provides the best fit. Other formulas included a linear relationship between volume and current or a reference to the total volume of the air gap $V_t = f(z_k, i_k)$ as a function of the position of the rotor and the currents of the electromagnets.

Table 13.3. The selected function of the electromagnetic axial force from *1st simulation* for different cases.

case	coeff/fit	EM_1	EM_2	EM_3
1 $z = var.$, α=β=0	a_k	1.071	1.077	1.046
	b_k	0.04349	0.04432	0.04098
	R^2	0.9994	0.9985	0.9998
	RMSE	0.0006772	0.0007158	0.0005068
2 $z = var.$, $\alpha = var.$, $\beta = var.$	a_k	1.073	1.080	1.045
	b_k	0.03929	0.04039	0.03957
	R^2	0.9901	0.9905	0.9928
	RMSE	0.002700	0.003188	0.003505
2 with a_k, b_k from **1**	R^2	0.9699	0.9836	0.9862
	RMSE	0.004717	0.004193	0.004868

[5]Core material in simulations: structural steel with imported B-H characteristiccftool (refer to Section 7.5).

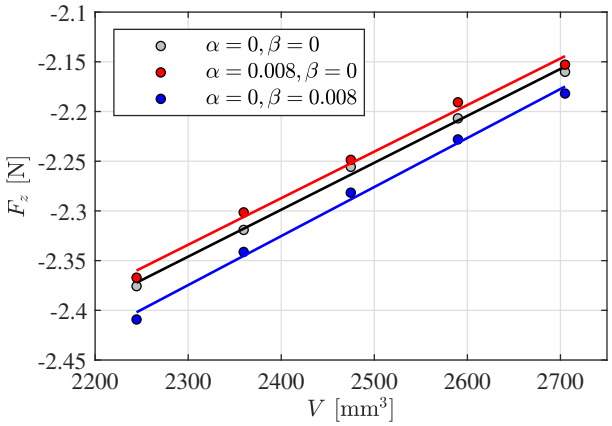

Fig. 13.7. The electromagnetic force versus air gap volume for different disc tilt angles (in [rad]).

A tabular summary of the approximation results of the selected function for several variants of parameters can be found in Table 13.3. To confirm the universality of the proposed formula describing the 6pAAMB axial electromagnetic force, the function was first fitted to the data at zero rotor inclination, then only for the case of various rotor tilt angles and finally the data from the fit of the first case were applied to the second. The results are satisfactory. The simulation used the same steady states and controls in which the rotor levitated during the experiments. This analysis indicated that the value of the axial electromagnetic force is directly related to the volume of the corresponding air gap (Fig. 13.7). The model to calculate the forces and torques of the rotor developed in MATLAB/Simulink did not achieve convergence of the results in the z axis until the force was related to the volume of the gap. This leads to the conclusion that a universal formula for the axial electromagnetic force requires correctly calculated and modeled air gap volumes.

13.2.2. Values and distribution of lateral forces

The identification was carried out on the basis of *2nd simulation*, which was a parametric sweep through specified combinations [α, β, z, i_1, i_2, i_3] and N_t equaled, respectively, 126, 129 and 120 for a particular electromagnet[6]. To approximate the 6pAAMB horizontal electromagnetic forces, several functions were proposed, among them polynomials, rational and custom functions, which approximate the data in the range of 77.5% to 94.8% and are represented by Fig. 13.8a.

$$F_{x_i} = p_{00} + p_{10} F_{z_i} \sin(\beta) \tag{13.6}$$

$$F_{y_i} = p_{00} + p_{10} F_{z_i} \sin(\alpha) \tag{13.7}$$

[6]The number of turns of the coils of individual electromagnets was adopted by optimization to experimentally estimated data in order to reflect the difference in the resistance and inductance of the coils, which translates into the appropriate distribution of the generated electromagnetic forces.

Table 13.4. Signs and ranges of electromagnetic force components in the horizontal rotor plane (*1st simulation*).

	α	β	F_x	F_y	F_{x_1}	F_{y_1}	F_{x_2}	F_{y_2}	F_{x_3}	F_{y_3}
sign	+	+	−	+	−	−	−	+	+	+
	−	+	−	−	−	−	−	+	+	+
	+	−	+	+	+	−	−	+	+	+
	−	−	+	−	+	−	−	+	+	+
$F_{\max}$			0.0329	0.0365	0.0087	-0.0149	-0.0106	0.0274	0.0417	0.0273
$F_{\min}$	[N]		-0.0264	-0.0253	-0.0065	-0.0409	-0.0370	0.0046	0.0099	0.0052
$\overline{F}$			0.0018	0.0020	4.82×10^{-6}	-0.0287	-0.0247	0.0150	0.0265	0.0158

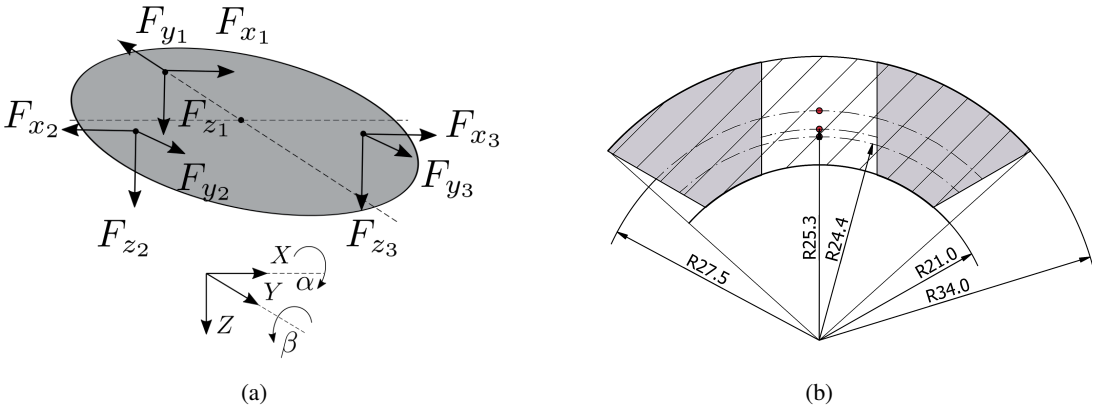

(a) (b)

Fig. 13.8. Force distribution diagram (a) and average radius of torques acting on the rotor (b).

Table 13.5. Approximated horizontal forces F_x, F_y based on the data from *2nd simulation*.

coeff	z[mm]	F_{x_1}	F_{x_2}	F_{x_3}	F_{y_1}	F_{y_2}	F_{y_3}
p_{00}	1.95	-0.0232×10^{-2}	-0.0237	0.0262	-0.0287	0.0156	0.0150
	2.05	0.0519×10^{-2}	-0.0240	0.0263	-0.0286	0.0151	0.0148
	2.15	-0.0035×10^{-2}	-0.0245	0.0263	-0.0289	0.0159	0.0140
	2.25	0.0180×10^{-2}	-0.0205	0.0264	-0.0291	0.0163	0.0148
	2.35	-0.0316×10^{-2}	-0.0252	0.0267	-0.0301	0.0170	0.0142
p_{10}	1.95	0.852	1.712	1.522	-1.675	-1.091	-1.141
	2.05	0.804	1.549	1.624	-1.719	-1.147	-1.079
	2.15	0.873	1.701	1.571	-1.637	-1.093	-1.017
	2.25	0.790	1.663	1.489	-1.655	-1.173	-1.035
	2.35	0.709	1.610	1.557	-1.742	-1.107	-1.001
p_{00}	all	5.031×10^{-5}	-0.0261	0.0243	-0.0291	0.0160	0.0146
p_{10}	all	0.821	1.657	1.552	-1.688	-1.149	-1.023
R^2	[%]	88.3	91.2	94.2	94.8	77.5	82.1

$$F_x = -0.001808 + 1.351F_z\sin(\beta) \approx 1.351F_z\sin(\beta) \tag{13.8}$$

$$F_y = 0.001385 - 1.282F_z\sin(\alpha) \approx -1.282F_z\sin(\alpha) \tag{13.9}$$

Table 13.4 presents the vector directions of the total lateral forces and their individual components along with the range of values. It can be seen that the resulting steady-state forces are up to 2% of the axial forces. Table 13.5 presents approximate values of coefficients of selected linear functions (13.6-13.7), which describe the distribution of lateral forces. Due to the negligible impact and the lack of a clear trend for the coefficients of lateral forces as a function of the rotor axial position, a single function was proposed for a given force component in the entire range of axial motion (13.8-13.9). Thus, the lateral forces are a function of the axial force F_z and the tilt angles α, β for F_y, F_x, respectively.

The applied functions were verified in the dataset from *3rd simulation*, which was the parametric sweep through all combinations [α, β, z], N_t=125 and current i_1=i_2=i_3=1 A. Both cases, with α=0 and β=0 were considered (see Tab. 13.6[7]). In addition to the previously utilized functions, the approximation with polynomials of first and second degree was listed for comparison.

Table 13.6. Verification of the horizontal forces F_x, F_y based on the data from *3rd simulation*.

case		α=0			β=0		
coeff		F_{x_1}	F_{x_2}	F_{x_3}	F_{y_1}	F_{y_2}	F_{y_3}
p_{00}		7.922×10^{-6}	-0.0264	0.0250	-0.0291	0.0158	0.0144
p_{10}		0.719	1.766	1.56	-1.590	-1.116	-1.067
R^2[%]	f^*	88.5	95.5	96.1	91.9	88.5	91.8
	poly1	87.5	97.2	94.8	96.0	89.0	91.4
	poly2	93.2	97.9	98.1	96.7	90.1	92.0

As a result of these considerations, a useful and verified formula was proposed, which describes the lateral forces in the steady state of the rotor with its variable orientation in the 6pAAMB active space.

13.2.3. Values and distribution of electromagnetic torques

In addition to the electromagnetic forces, the torques should also be described. It was assumed that the net force generated by a single electromagnet can be applied pointwise on a radius, which corresponds to a given torque.

Table 13.7. Signs and ranges of torque components in the horizontal disc plane (*1st simulation*).

	α	β	T_x	T_y	T_{x_1}	T_{y_1}	T_{x_2}	T_{y_2}	T_{x_3}	T_{y_3}
sign	+	+	−	+	+	+	−	−	−	+
	−	+	−	+	+	+	−	−	−	+
	+	−	−	+	+	−	−	−	−	+
	−	−	−	+	+	−	−	−	−	+
$T_{\max}$			$\to 0$	4.4763	19.7060	1.2718	-7.7015	-13.7940	-9.2021	19.2590
$T_{\min}$	[mNm]		-3.3896	$\to 0$	16.8990	-1.2528	-11.2460	-17.8950	-12.9540	16.2400
$\overline{T}$			-1.2718	1.6359	18.3380	0.0017	-9.3293	-16.1140	-10.2810	17.7480

[7] f^* is expressed by (13.6-13.7); poly1: $F_y = p_{00} + p_{10}\alpha + p_{01}F_z$; poly2: $F_y = p_{00} + p_{10}\alpha + p_{01}F_z + p_{11}\alpha F_z + p_{02}F_z^2$;

Discussion on average radius

The issue of how to determine the radius of the forces acting on the rotor was discussed. For this purpose, several cases have been considered, that is, the geometric center of the first electromagnet pole piece (0,-24.4) mm, its air gap cross-sectional area (0,-25.3) mm, as well as the average pole radius equal 27.5 mm. Figure 13.8b illustrates these cases well.

Table 13.7 and the kinematics of the forces described by the vectors, as in Figure 13.8a, provide enough information to describe the individual components of the electromagnetic torques generated by 6pAAMB. Rotor rotation was excluded, therefore, torque in the z axis is not considered. Electromagnetic torques are described by the following equations:

$$\begin{cases} T_{x_1}^{ANL} &= -(z_1 - z_m)F_{y_1} - r_m \cos(0^\circ)F_{z1} \\ T_{y_1}^{ANL} &= -(z_1 - z_m)F_{x_1} + r_m \sin(0^\circ)F_{z1} \\ T_{x_2}^{ANL} &= +(z_2 - z_m)F_{y_2} - r_m \sin(30^\circ)F_{z2} \\ T_{y_2}^{ANL} &= +(z_2 - z_m)F_{x_2} + r_m \cos(30^\circ)F_{z2} \\ T_{x_3}^{ANL} &= +(z_3 - z_m)F_{y_3} + r_m \sin(30^\circ)F_{z3} \\ T_{y_3}^{ANL} &= -(z_3 - z_m)F_{x_3} - r_m \cos(30^\circ)F_{z3} \end{cases} \tag{13.10}$$

Hypothesis: the electromagnetic torque components (13.10) derived from the kinematics of the levitating rotor, assuming that the electromagnetic forces components act as vectors originating at the center of gravity of the individual air gaps, are not equal to the entire electromagnetic torque due to the C-type electromagnet configuration, therefore, require the use of correction functions.

Table 13.8. The difference between the torque components obtained in the analytical and numerical approach (data from *2nd simulation*).

Δ_T	a_I	b_I	r_m	a_{II}	b_{II}	R^2	δ_{T_Δ}		
	[Nm/rad]		[mm]	[Nm/rad]		[%]	avg[%]	max[%]	min[%]
x_1	0.0132	$\to 0$	25.363	0.0135	$\to 0$	68.2	0.47	0.92	-1.40
x_2	-0.1001	0.0698	25.408	-0.1001	0.0699	98.3	5.83	18.11	-12.60
x_3	-0.0975	0.0639	25.383	-0.0977	-0.0642	98.5	5.84	18.17	-12.45
y_1	$\to 0$	-0.1337	25.295	$\to 0$	-0.1338	99.0	99.94	97.33	-101.42
y_2	0.0662	-0.0234	25.327	0.0662	-0.0233	97.3	1.98	5.07	-4.56
y_3	-0.0640	-0.0214	25.297	-0.0639	-0.0214	97.2	2.01	4.74	-4.34

$$\Delta_{T_{x/y_i}} = T_{x/y_i}^{3D} - T_{x/y_i}^{ANL} = a\alpha + b\beta + c \tag{13.11}$$

$$\delta_{T_\Delta} = \frac{T_{x/y_i}^{ANL} - T_{x/y_i}^{3D}}{T_{x/y_i}^{3D}} \tag{13.12}$$

Parametric optimization of electromagnetic torques was carried out on the basis of analytical equations (13.10). Table 13.8 summarizes the optimization results according to the following steps:

- the mean radius r_m was treated as a variable and a torque correction function (13.11) was subtracted to all the torque equations; the result was verified by data from *2nd simulation*,
- the minimum of function using derivative-free method was found by built-in *fminsearch* solver,
- the first optimization results[8] returned coefficients a_I, b_I and r_m; the mean radius as the geometric center of the single electromagnet air gap cross-section was confirmed, therefore, r_m=25.3 mm,
- the optimization was repeated to obtain a_{II}, b_{II},
- the relative error (13.12) was calculated; for 2nd and 3rd electromagnets is in the range of 2 to 6% (average value), while for 1st electromagnet, which is on the y axis of symmetry for the adopted coordinate system, the torque correction $\Delta_{T_{x_1}}$ is smaller than the others by an order of magnitude, therefore, may be omitted, while $\Delta_{T_{y_1}}$ is almost equal to T_{y_1} due to no influence of F_{z_1}, which is zeroed in the analytical equation of T_{y_1},
- varying axial position z did not affect the torque correction function $\Delta_{T_{x/y_i}}$[9].

$$
\begin{cases}
F_{x_0} = 1.351 F_{z_0} \sin(\beta_0) \\
F_{y_0} = -1.282 F_{z_0} \sin(\alpha_0) \\
F_{z_0} = \sum_{k=1}^{3} \left(-\frac{1}{2} k_{L_k} i_{k_0}^2 \frac{2mg}{(a_k V_k \cdot 10^{-3} + b_k)^2} \right) \\
T_{x_0} = (-(z_{10} - z_0) F_{y_{10}} + (z_{20} - z_0) F_{y_{20}} + (z_{30} - z_0) F_{y_{30}}) + \\
\qquad (-r_m \cos(0) F_{z_{10}} + r_m \sin(30^\circ) F_{z_{20}} + r_m \sin(30^\circ) F_{z_{30}}) - \sum_{i=1}^{3} \Delta T_{x_{i0}} \\
T_{y_0} = (-(z_{10} - z_0) F_{x_{10}} + (z_{20} - z_0) F_{x_{20}} - (z_{30} - z_0) F_{x_{30}}) + \\
\qquad (r_m \sin(0) F_{z_{10}} + r_m \cos(30^\circ) F_{z_{20}} - r_m \cos(30^\circ) F_{z_{30}}) - \sum_{i=1}^{3} \Delta T_{y_{i0}}
\end{cases}
\tag{13.13}
$$

The set of equations (13.13) represents the electromagnetic forces and torques of the 5-DoF 6pAAMB model[10] in experimentally determined steady states, verified by a series of numerical simulations. Despite the observed convergence of the axial position and tilt angles of the rotor in the dynamic model based on the electromagnetic force and the torques calculated from the steady states, the dynamics of the lateral forces in the transition state (see Subsection 13.3.1) is not described by equations (13.6)-(13.9). Obtaining convergence of the analytical model describing the 6pAAMB dynamic states with the experiments is the scope of current research.

[8] In (13.11) the offset is negligible, i.e. $c \to 0$.

[9] The influence of the axial displacement of the rotor is included in the axial electromagnetic force.

[10] Refer to Tab. 12.1 for parameters; see (13.5)-(13.11) for function details; all the variables are followed by "nought", i.e. the subscript 0 points out the limitation of the model analysis to steady states of the rotor.

13.3. Disc tilting around virtual axes

The following experimental studies demonstrated the possibility of arbitrarily orienting the rotor in the 6pAAMB levitation space. The proposed experiment was carried out in a closed loop with three local regulators, i.e. two electromagnets maintained the set position of 2.2 mm through the PID regulators[11] with settings K_p = -3300, K_d = -43.5, K_i = -500 and sampling period T_0 equal 1ms, which provided aperiodic control around the operating point for z = 2.2 mm. The tested electromagnet is controlled by the PD regulator with variable settings. The desired position is a sequence of numbers specified in a table of time-value pairs, i.e. t=[0, 40, 40+T_0, 80, 80+T_0, 120, 120+T_0, 160] s and z_{des}=[2.2, 2.2, 2.3, 2.3, 2.2, 2.2, 2.1, 2.1] mm. Figure 13.9 is the complementary description of the adopted experimental scenario. Further analysis was limited to the selected time period marked with a gray bar.

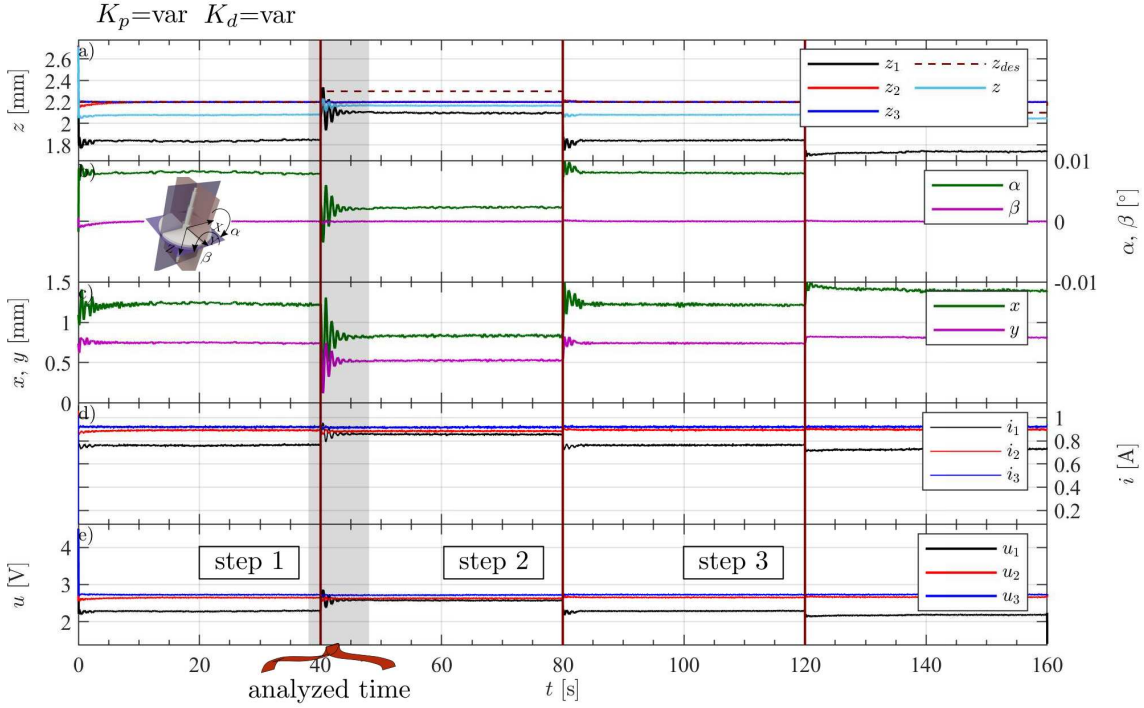

Fig. 13.9. Illustrative demonstration of the rotor tilting adopted scenario; example of the rotor tilt under 1st electromagnet throughout the entire 160 s experiment; K_p = -1200, K_d = -10.

13.3.1. Dynamics of disc tilting

In order to analyze the dynamic changes of the rotor state variables during its tilting, a series of experiments were performed for the values K_p = -[1200:150:3300], K_d = -[10:5:80], i.e. 225 experiments in a single iteration[12]. The repeatability of the observed dynamic properties was confirmed in the range below 5% of the relative error in relation to the first iteration of the experiment for its 5 datasets.

[11] Refer to Section 12.7 and (2.2)-(2.3) for details.

[12] 5 iterations of 225 experiments require 50 hours of the 6pAAMB operation.

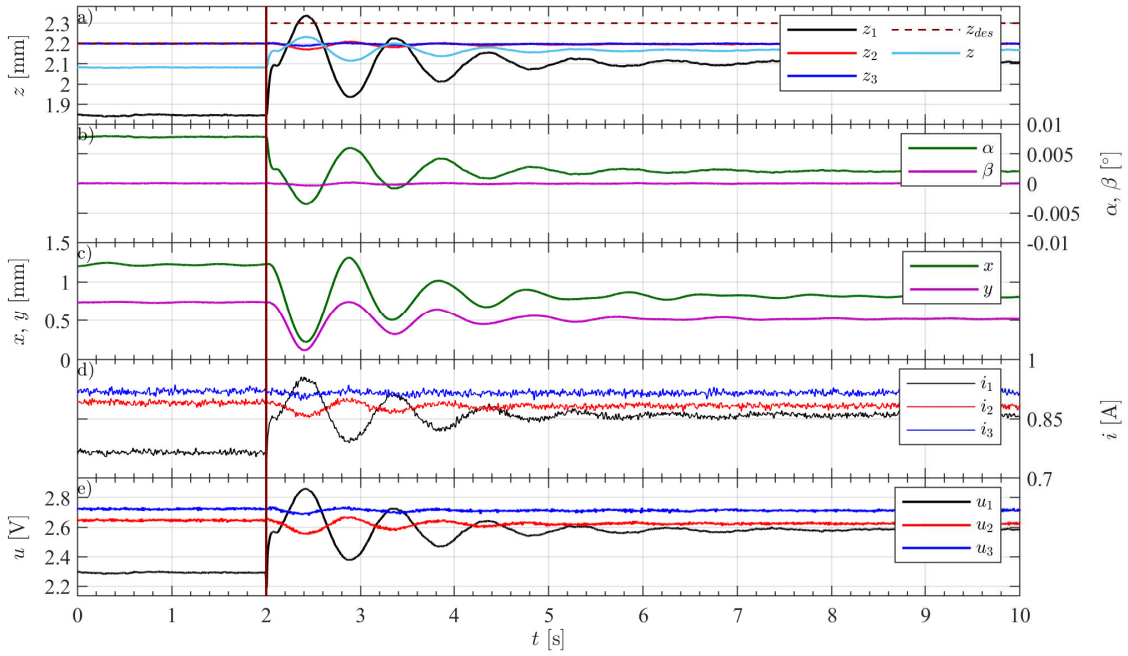

Fig. 13.10. The rotor tilt under 1st electromagnet according to the scenario; K_p = -1200, K_d = -10, 1st step.

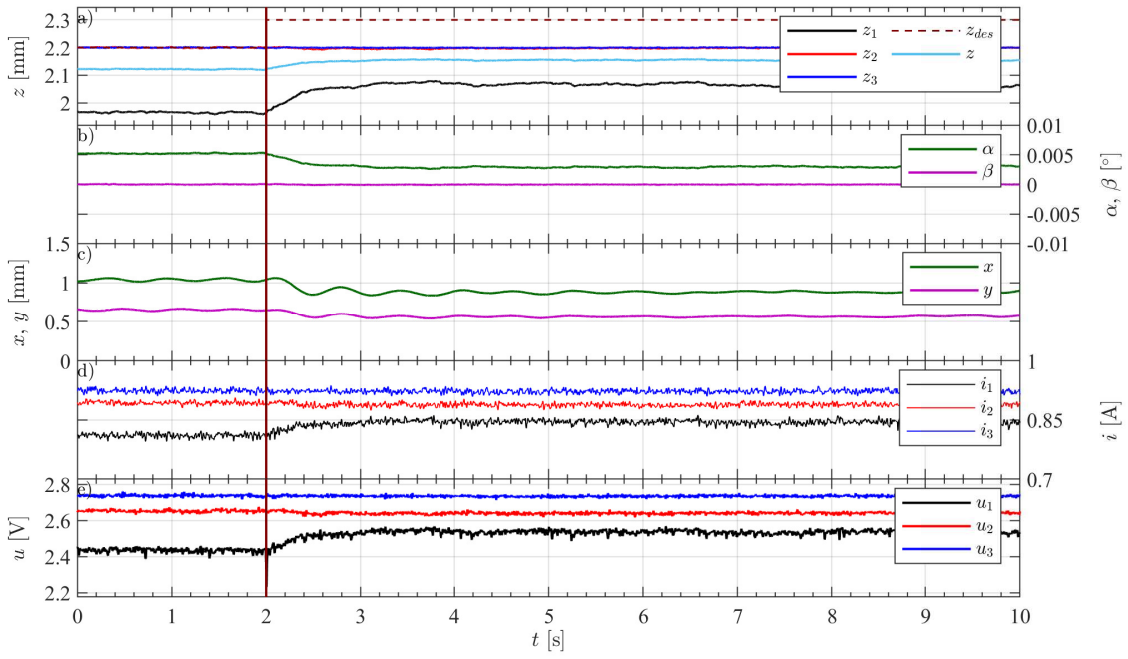

Fig. 13.11. The rotor tilt under 1st electromagnet according to the scenario; K_p = -1200, K_d = -80, 1st step.

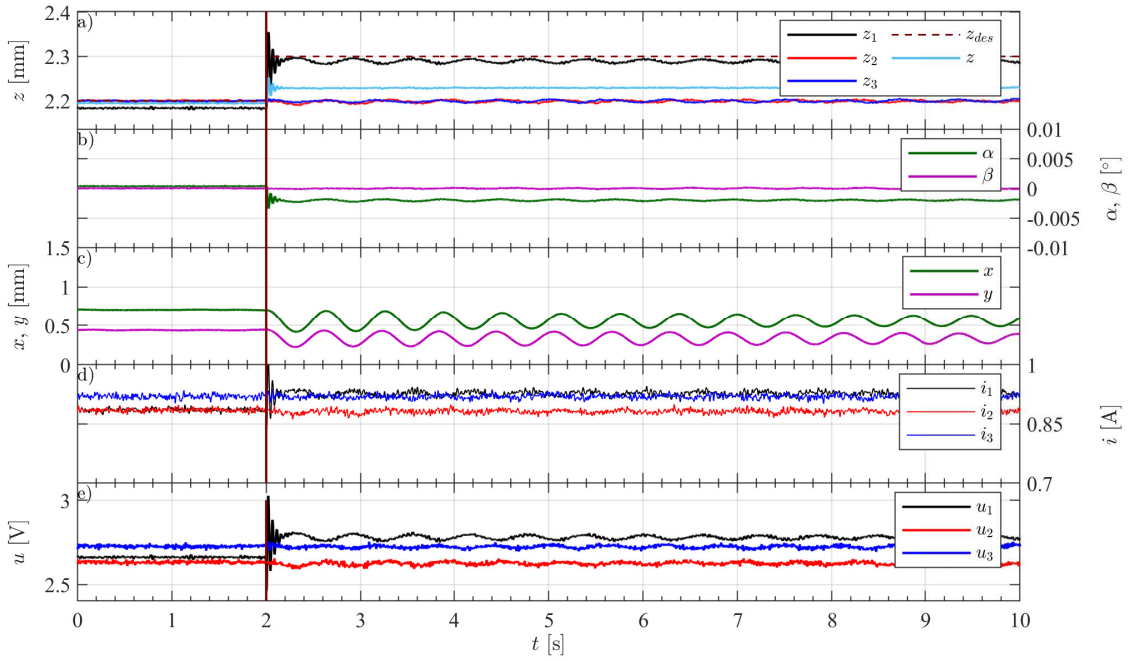

Fig. 13.12. The rotor tilt under 1st electromagnet according to the scenario; K_p = -3300, K_d = -10, 1st step.

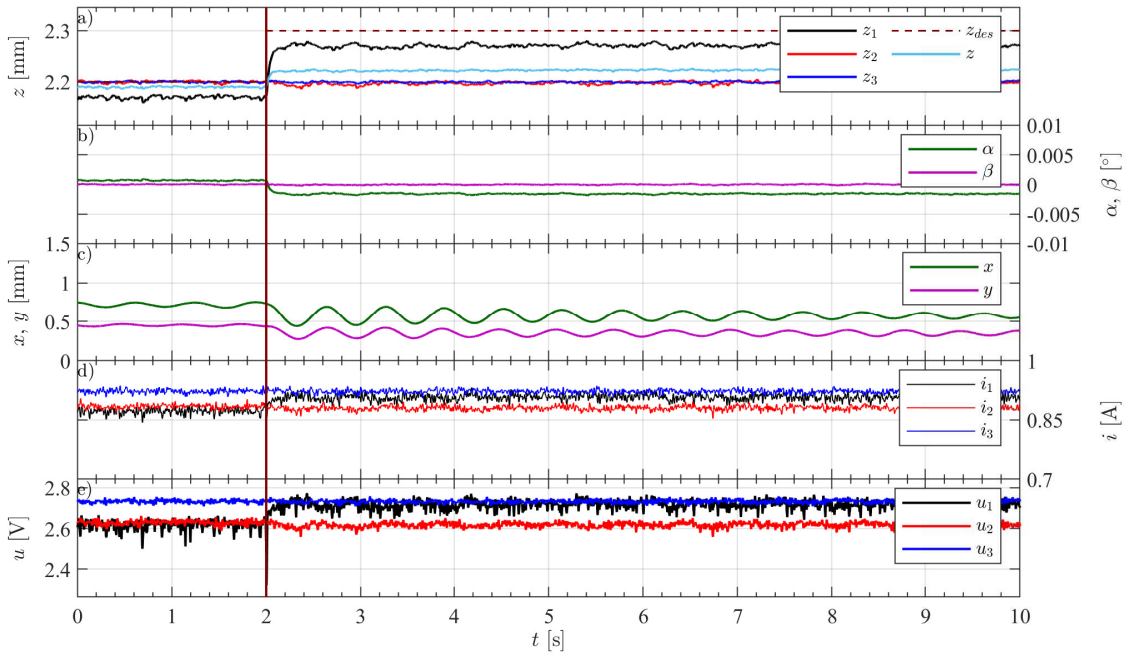

Fig. 13.13. The rotor tilt under 1st electromagnet according to the scenario; K_p = -3300, K_d = -80, 1st step.

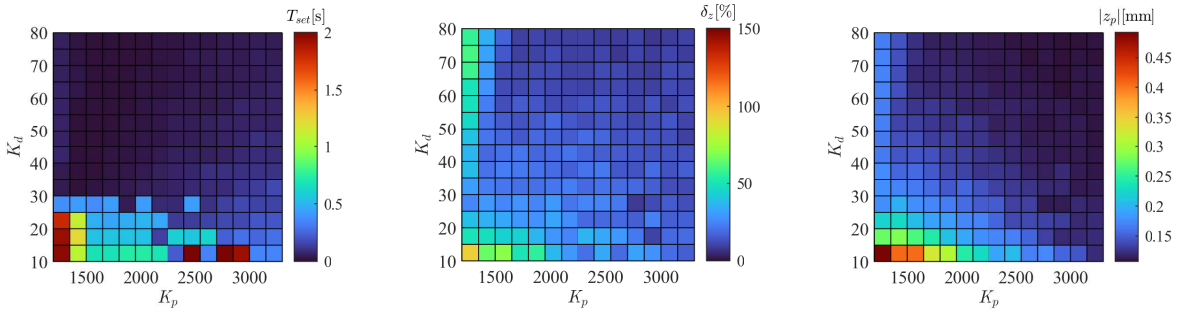

(a) Settling time, z. (b) Overshoot, z. (c) Peak value, z.

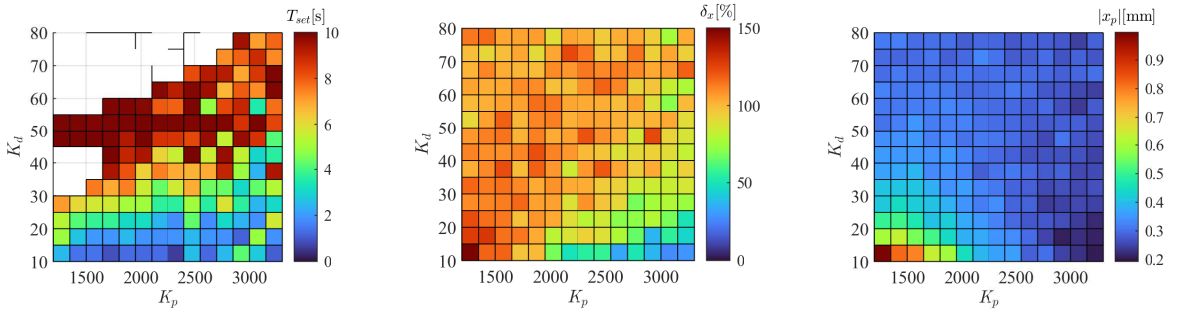

(d) Settling time, x. (e) Overshoot, x. (f) Peak value, x.

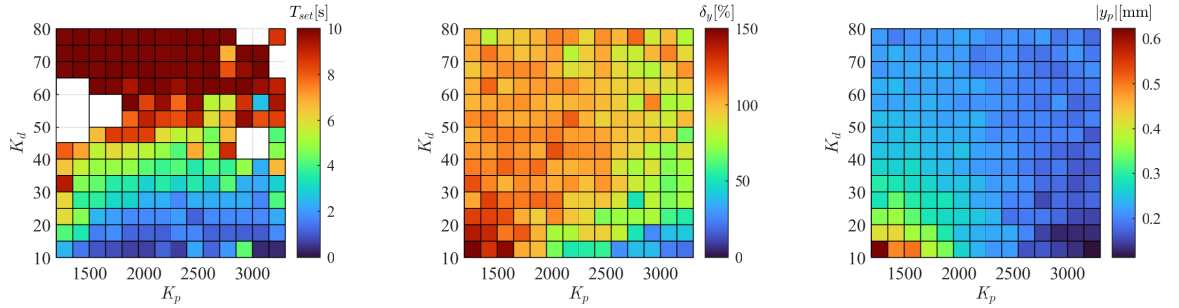

(g) Settling time, y. (h) Overshoot, y. (i) Peak value, y.

Fig. 13.14. Rotor tilting dynamics based on step response analysis (1st step).

Figures 13.10-13.13 show the borderline cases of the applied PD controller parameters. The reader can trace the given axial motion of the rotor, then its tilt angles α, β and the corresponding lateral displacements x, y. Currents i_1, i_2, i_3 and controls u_1, u_2, u_3 complete the overview of the proposed 6pAAMB solution from setting the desired position to the control signal.

Figure 13.14 shows a map of several parameters[13] of a step response characteristic for a dynamic system. The computation was done for a zero initial offset before the step occurs. The settling time T_{set} measures the time it takes for the error to remain below the assumed 10% threshold of $|z_{final}\text{-}z_0|$. The overshoot δ_z is calculated relative to the normalized response and is expressed as a percentage, i.e. $\max(z_{norm}(t)\text{-}1)$, where $z_{norm}(t)=z(t)/z_{final}$. The peak value $|z(t)|$ is also shown to indicate the maximum rotor displacement in a given axis.

[13]The expressions used in this paragraph, describing the individual dynamic parameters, are the same for x, y and z.

13.3.2. Disc position control with three local controllers

The last subsection contains the waveforms of rotor stabilization after step excitation for each of the 6pAAMB actuator electromagnets. Figures 13.15-13.17 show the experiment for the PD controller settings K_p = -1800 and K_d = -25. Individual electromagnets exhibit different performance under the same experimental parameters. The reader can assess the damping of the lateral vibrations, when controlling the axial position of the rotor in accordance with the given signal.

During experiments, the inclination of the rotor in a control system of three local regulators takes place around the so-called virtual axis[14], where the feedback comes from a sensor measuring the position of the rotor over the electromagnet under test while maintaining a constant position from the other two sensors. The experimental data demonstrate the potential of the proposed actuator, which allows for any positioning of the rotor in the air gap space. The maps of the selected dynamic step response parameters (see Fig. 13.14) clearly show that a compromise must be found between the stability in the z axis and the damping of lateral vibrations. Low values of K_p and K_d result in a displacement overshoot in individual axes and lower rotor stiffness, but, at the same time, support damping in all axes (Fig. 13.10). On the contrary, high values of the settings sustain lateral oscillations of the rotor with aperiodic control of the axial position (Fig. 13.13).

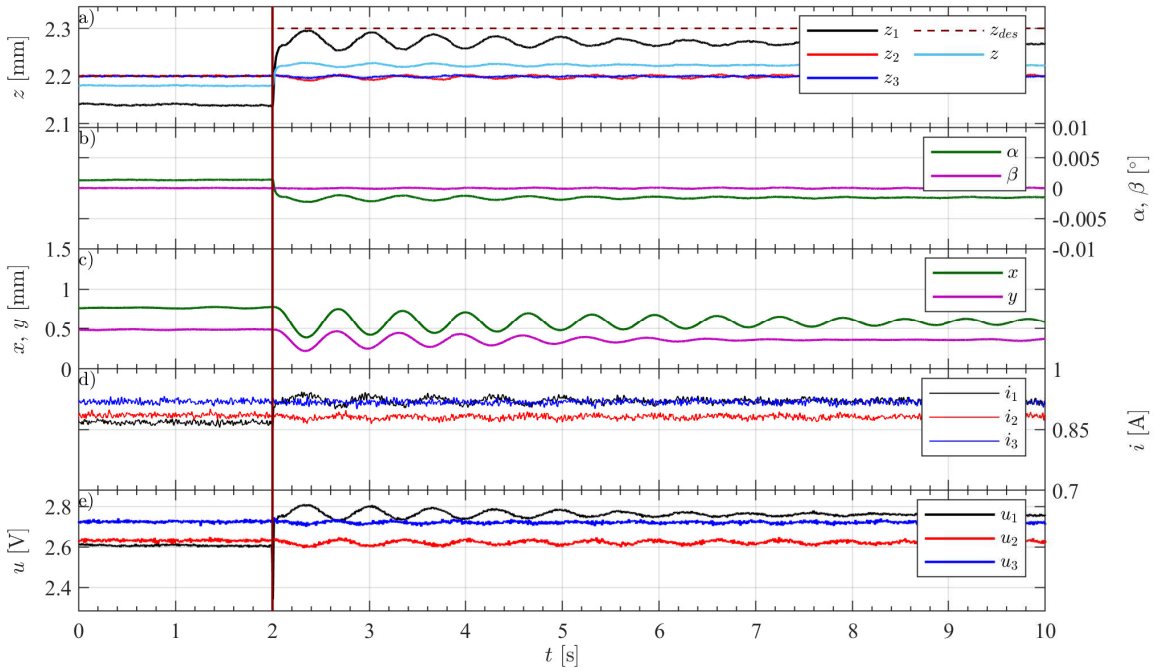

Fig. 13.15. The rotor tilt under 1st electromagnet according to the scenario; K_p = -1800, K_d = -25, 1st step.

[14]It passes through the line connecting the geometrical centers of the cross-section of the air gaps of the two electromagnets controlled by PID regulators.

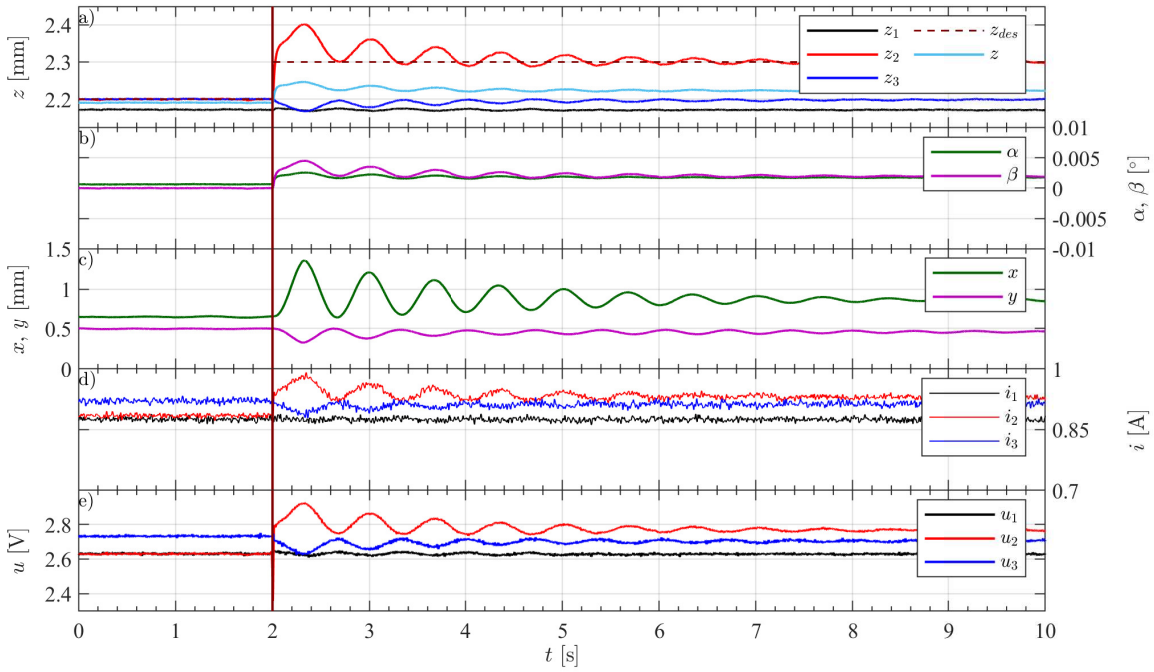

Fig. 13.16. The rotor tilt under 2nd electromagnet according to the scenario; K_p = -1800, K_d = -25, 1st step.

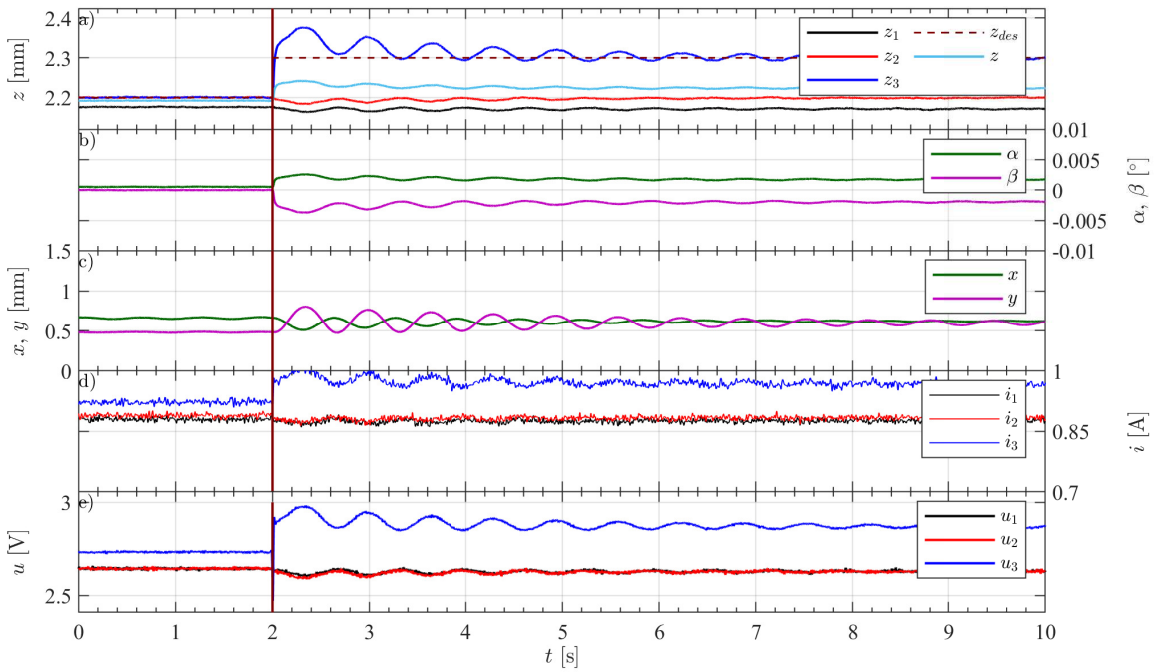

Fig. 13.17. The rotor tilt under 3rd electromagnet according to the scenario; K_p = -1800, K_d = -25, 1st step.

Chapter 14

Summary of results

In this doctoral dissertation, the author presented an innovative concept of an axial active magnetic bearing with six pole pieces. The proposed solution has application potential as a modern automation actuator. As a result of scientific research, the main statement was confirmed, showing the exclusive feature of 6pAAMB, which is the possibility of spatial positioning of the levitating object. The completed research that comprised this dissertation required an interdisciplinary approach to actuator design. Its scope covered numerous fields of science around the author's interests, the effect of which is the presented coherent line of reasoning leading from the application need and idea, through testing and verification of various concepts, to the design procedure, including numerical modeling, analytical calculations, manufacturing, quality check, identification and control application. A roadmap to prove the main statement of the dissertation led through a wide range of research, the effects of which were described in twelve modular chapters. Each of them was a separate milestone to achieve the set goal. The most important results and conclusions in relation to the individual chapters are briefly presented below.

Investigation of lateral motion in levitation system with opposite electromagnets

- This chapter demonstrated the possibility of minimizing an active magnetic levitation to the configuration with two electromagnets if the stretching forces are sufficient to stabilize the levitating object under external disturbances.
- The simplified single axis AMB allows to influence to some extent the position of the levitating object in the inactive axes.
- It is recommended to develop AAMB that can control the dynamics of axial motion to the extent that it can support the task of radial stabilization in a more controlled way.

Axial active magnetic levitation extended by heat transfer

- Long-term experiments indicated that increasing the temperature of the electromagnet causes a decrease in the value of the magnetic induction and the electromagnetic force, which, in consequence, influences the dynamic properties of the system.

- Understanding the influence of temperature on the dynamics of the system in connection with its geometry and electromagnet parameters provides important suggestions for improvements during the actuator design stage.
- The influence of the actuator core temperature on the inductance value was observed. The issue requires a separate analysis to draw verified conclusions.
- For the correct description of thermal effects in the electromagnetic actuator, a higher-order nonlinear model is required, introducing state variables in the form of coil, core and ambient temperature depending on the geometrical parameters of the actuator.

Porous core electromagnet design for levitation applications

- An original method was implemented for the rapid prototyping of the AAMB powder core.
- The manufactured electromagnet did not meet the expected requirements as a result of no access to industrial facilities that enable the powder core manufacturing process to be optimized.
- The efficiency of the powder core magnetic circuit depends on the degree of packing of the iron filings and the type of bonding agent.

Hybrid axial active magnetic bearing

- Power consumption was reduced using the PMs-biased configuration in the implemented concept of AAMB. At the same time, significant magnetic forces from PMs caused frequent disc tilting; thus, the task of radial stabilization requires the support of an active magnetic radial bearing.
- The appropriate configuration of PMs can provide close to linear characteristics of the axial electromagnetic force in a narrow range of axial levitation. The magnetic flux path of HAMB was adjusted to compensate for the gravity load at the desired operating point.
- 2D numerical models do not cover all the phenomena that occur in machines with axial magnetic flux flow, which is why it is recommended to develop the 3D numerical models.

Concept of axial active magnetic bearing with six poles

- The undoubted achievement presented in this chapter is the prototype of the actuator with six pole pieces manufactured in several iterations over the PhD timeline.
- A distinguished feature of the described prototype is the configuration of six pole pieces that allow the arrangement of at least three electromagnets generating separate vectors of the axial electromagnetic force.

Numerical model of axial magnetic bearing with six cylindrical poles

- The effect of this chapter was a virtual twin of 6pAAMB, from which the user can collect various characteristics.
- The numerical model consists of numerous elements, such as parameterized geometry, selected materials, meshing, solver configuration and study type. During the development of the model, material tests were performed to determine the magnetization curve of the utilized steel, which was then imported into the model. The model is a useful tool in the optimization and verification process of the actuator design. It is recommended to continue numerical research towards multidisciplinary models.

Quality performance of the axial magnetic bearing

- A tool was developed to detect defects in the assembly or operation of axial machines in situ.
- The open-ended procedure for semiautomatic identification of the axial actuator has been proposed. Current trends in the design of control and measurement systems for electromagnetic actuators are oriented toward self-monitoring or diagnostic systems.
- The quality assessment of the manufactured actuator was carried out using a proprietary algorithm, a coordinate measuring machine and a laser profiler, presenting and comparing the capabilities of selected tools.

Axial active magnetic bearing in rotor system[1]

- A reconfigurable magnetic bearing system was set up for flexible shaft machinery.
- Experimental scenarios were developed to assess cross-coupling between individual electromagnets in the actuator with several pole pieces.
- Considerations undertaken at that time and preliminary research on axial active magnetic bearing with six cylindrical poles resulted in the development of the latest actuator iteration.

Analytical modeling and experimental validation of six pole axial magnetic bearing

- The validated 6pAAMB analytical model was obtained, which is convergent with experiments and numerical simulation.
- Schwarz-Christoffel transformation was utilized in the study of the actuator end effect.
- The 3D complex permeance function, which represents the stator pole pieces, was provided and can be utilized to optimize the geometry of the slot or select a suitable location of the sensing element for identification or control feedback purposes.
- The computational time of the analytical model was significantly shorter than the numerical one.
- The mathematical model provides explicit formulae, which contribute valuable information about the magnetic field distribution in the 6pAAMB air gap.

Radial passive magnetic bearing in configuration with axial active magnetic suspension

- The developed RPMB prototype achieved its task of supporting the stabilization of the rotor in the x-y plane and can be extensively modified and miniaturized due to its simplicity.
- PMB, depending on the position of the rotating part in relation to the stationary part, can generate a negative or positive axial electromagnetic force component.
- It is a key issue and, at the same time, a nontrivial task to propose integrated force and dynamic characteristics for AMS with PMBs.
- The proprietary noncontact magnetic gear was developed to accelerate the rotor to a speed of 4000 rpm. As a result, a rotational motion of a fully levitated 6-DoF rotor was observed.

[1] As a reminder, this chapter was a transition stage of the doctoral dissertation at the time of the onset of the pandemic. It contains discussions of selected issues on AMBs in rotating machines, as well as inspiration for further research.

Interdisciplinary identification of six pole axial active magnetic bearing prototype

- Research demonstrated a complete identification inspired by real system imperfections, leading to the verified model of the single-axis axial active magnetic bearing.
- The problem of eccentricity was emphasized during the levitation of the tilted disc, which has a consequence on its chaotic motion.
- The dynamic properties of the system in a broad frequency range were examined using a shaker with external harmonic excitation. The adjusted PD controller for 6pAAMB shows the desirable features of the magnetic levitation system in terms of the amplitude-phase characteristic.
- In general, the 6pAAMB actuator could extend the stabilization range of rigid and flexible rotors.

Disc spatial orientation in six pole axial active magnetic bearing

- The chapter guided the reader through the analysis of an extensive set of experimental data supporting the main statement, describing the rotor steady states as functions of various parameters.
- Despite the assembly inaccuracies and the difference in the actuator electromagnet parameters, the repeatability of the rotor steady state in the inactive axes was confirmed.
- Extended numerical verification of the experimental data was carried out in COMSOL Multiphysics to provide a reliable description of the distribution of electromagnetic forces and torques in the 6pAAMB active space. The steady states measured from the levitating rotor were imported into the developed 6pAAMB numerical model.
- A global formula of the axial electromagnetic force requires precisely calculated air gap volumes.
- The 5-DoF actuator model was developed for steady states obtained experimentally and numerically verified. The model shows convergence with the experiment for the axial position and tilt angles of the rotor, whereas the equations of the lateral forces in steady state do not reflect their real dynamics due to the nonperiodic, chaotic or statistically unrepeatable nature of the 6pAAMB lateral motion.
- The possibility of arbitrarily orienting the rotor in the 6pAAMB levitation space was demonstrated.
- Analysis of the rotor dynamics in the control system with three local regulators indicates the need for a compromise between stability in the z axis and damping of lateral vibrations.

The issues presented in the above dissertation summarize the interdisciplinary course of designing, manufacturing, identifying and controlling the levitation object by means of an axial active magnetic bearing with six pole pieces. The reader may consider the above as the blueprint for the design of an axial actuator with a few pole pieces. Individual chapters outline the struggle with the subsequent stages of the 6pAAMB design and implementation procedure. Perhaps the key end result of the author's research is the motivation, inspiration and knowledge necessary to propose an industrial application of the developed actuator. Low-power wind farms, pumps, centrifuges and energy storage facilities are among the considered options.

References

[1] L. Hawkins, A. Filatov, R. Khatri, *et al.*, "Design of a compact magnetically levitated blower for space applications," in *Volume 10A: Structures and Dynamics. Turbo Expo: Power for Land, Sea, and Air*, 2020, pp. 1–6. DOI: *10.1115/GT2020-15090*.

[2] S. Y. Yoon, Z. Lin, W. Jiang, *et al.*, "Flow-rate observers in the suppression of compressor surge using active magnetic bearings," *Journal of Turbomachinery*, vol. 135, 041015 (11 pages), Jul. 2013. DOI: *10.1115/1.4007600*.

[3] B. Luan, X. Zhang, F. Xu, *et al.*, "High precision magnetic levitation actuator for micro-edm," *Actuators*, vol. 11, no. 12, 2022. DOI: *10.3390/act11120361*.

[4] H. Bangcheng, X. Qinjie, and Y. Qian, "Multiobjective Optimization of a Combined Radial-Axial Magnetic Bearing for Magnetically Suspended Compressor," *IEEE Trans. Ind. Electron.*, vol. 63, no. 4, pp. 2284–2293, 2016. DOI: *10.1109/TIE.2015.2509905*.

[5] B. Han, Z. Huang, and Y. Le, "Design aspects of a large scale turbomolecular pump with active magnetic bearings," *Vacuum*, vol. 142, pp. 96–105, 2017. DOI: *https://doi.org/10.1016/j.vacuum.2016.12.010*.

[6] J. Sun, H. Zhou, and Z. Ju, "Dynamic Stiffness Analysis and Measurement of Radial Active Magnetic Bearing in Magnetically Suspended Molecular Pump," *Sci. Rep.*, vol. 10, no. 1, pp. 1–16, 2020. DOI: *10.1038/s41598-020-57523-8*.

[7] C. Zwyssig, J. W. Kolar, and S. D. Round, "Megaspeed drive systems: Pushing beyond 1 million r/min," *IEEE/ASME Transactions on mechatronics*, vol. 14, no. 5, pp. 564–574, 2009.

[8] C. Zhang, K. J. Tseng, T. D. Nguyen, *et al.*, "Stiffness analysis and levitation force control of active magnetic bearing for a partially-self-bearing flywheel system," *International Journal of Applied Electromagnetics and Mechanics*, vol. 36, pp. 229–242, 3 2011. DOI: *10.3233/JAE-2011-1362*.

[9] M. Andriollo, R. Benato, and A. Tortella, "Design and modeling of an integrated flywheel magnetic suspension for kinetic energy storage systems," *Energies*, vol. 13, no. 4, 2020. DOI: *10.3390/en13040847*.

[10] Z. Qadir, A. Munir, T. Ashfaq, *et al.*, "A prototype of an energy-efficient maglev train: A step towards cleaner train transport," *Cleaner Engineering and Technology*, vol. 4, p. 100 217, 2021. DOI: *https://doi.org/10.1016/j.clet.2021.100217*.

[11] M. Schuck, D. Steinert, T. Nussbaumer, *et al.*, "Ultrafast rotation of magnetically levitated macroscopic steel spheres," *Science Advances*, vol. 4, no. 1, e1701519, 2018. DOI: *10.1126/sciadv.1701519*. eprint: *https://www.science.org/doi/pdf/10.1126/sciadv.1701519*.

[12] L. Yun, S. Jinji, and H. Bangcheng, "Modeling and Design of 3-DOF Magnetic Bearing for High-Speed Motor Including Eddy-Current Effects and Leakage Effects," *IEEE Trans. Ind. Electron.*, vol. 63, no. 6, pp. 3656–3665, 2016. DOI: *10.1109/TIE.2016.2530778*.

[13] M. R. Mehra, Y. Naka, N. Uriel, *et al.*, "A fully magnetically levitated circulatory pump for advanced heart failure," *New England Journal of Medicine*, vol. 376, no. 5, pp. 440–450, 2017. DOI: *10.1056/NEJMoa1610426*. eprint: *https://doi.org/10.1056/NEJMoa1610426*.

[14] N. O. Osinde, M. Etiévant, J. B. Byiringiro, *et al.*, "Calibration of a multi-mobile coil magnetic manipulation system utilizing a control-oriented magnetic model," *Mechatronics*, vol. 84, p. 102 774, 2022. DOI: *https://doi.org/10.1016/j.mechatronics.2022.102774*.

[15] X. Zhang, C. Trakarnchaiyo, H. Zhang, *et al.*, "Magtable: A tabletop system for 6-dof large range and completely contactless operation using magnetic levitation," *Mechatronics*, vol. 77, p. 102 600, 2021. DOI: *https://doi.org/10.1016/j.mechatronics.2021.102600*.

[16] K. D. Bachovchin, J. F. Hoburg, and R. F. Post, "Stable levitation of a passive magnetic bearing," *IEEE Transactions on Magnetics*, vol. 49, no. 1, pp. 609–617, 2013. DOI: *10.1109/TMAG.2012.2209123*.

[17] S. Jinji and F. Jiancheng, "A novel structure of permanent-magnet-biased radial hybrid magnetic bearing," *Journal of Magnetism and Magnetic Materials*, vol. 323, no. 2, pp. 202–208, 2011. DOI: *https://doi.org/10.1016/j.jmmm.2010.08.053*.

[18] G. Barbaraci, "Axial active magnetic bearing design," *Journal of Vibration and Control*, vol. 22, no. 5, pp. 1190–1197, 2016. DOI: *10.1177/1077546314534720*. eprint: *https://doi.org/10.1177/1077546314534720*.

[19] D. Wajnert, "Simulation for the determination of the hybrid magnetic bearing's electromagnetic parameters," *Przegląd Elektrotechniczny*, vol. 1, pp. 159–162, Feb. 2017. DOI: *10.15199/48.2017.02.34*.

[20] C. Weißbacher, H. Stelzer, and K. Hameyer, "Application of a tubular linear actuator as an axial magnetic bearing," *IEEE/ASME Transactions on Mechatronics*, vol. 15, no. 4, pp. 615–622, 2010. DOI: *10.1109/TMECH.2009.2031111*.

[21] K. Hijikata, S. Kobayashi, M. Takemoto, *et al.*, "Basic characteristics of an active thrust magnetic bearing with a cylindrical rotor core," *IEEE Transactions on Magnetics*, vol. 44, no. 11, pp. 4167–4170, 2008. DOI: *10.1109/TMAG.2008.2002628*.

[22] S. Xu and J. Fang, "A novel conical active magnetic bearing with claw structure," *IEEE Transactions on Magnetics*, vol. 50, 5 2014. DOI: *10.1109/TMAG.2013.2295060*.

[23] A. Piłat and B. Sikora, "Design and initial study of porous core electromagnet for levitation applications," *AIP Conference Proceedings*, vol. 2029, no. 1, p. 020 057, 2018. DOI: *10.1063/1.5066519*. eprint: *https://aip.scitation.org/doi/pdf/10.1063/1.5066519*.

[24] A. Piłat, "Analytical modeling of active magnetic bearing geometry," *Applied Mathematical Modelling*, vol. 34, p. 3805, 2010.

[25] W. Geng and Z. Zhang, "Investigation of a new ironless-stator self-bearing axial flux permanent magnet motor," *IEEE Transactions on Magnetics*, vol. 52, no. 7, pp. 1–4, Jul. 2016. DOI: *10.1109/TMAG.2016.2524649*.

[26] D. Eichenberg, C. Gallo, and W. Thompson, "Development and testing of an axial halbach magnetic bearing," NASA, Tech. Rep., 2006.

[27] A. Piłat, B. Sikora, and J. Źrebiec, "Investigation of lateral stiffness and damping in levitation system with opposite electromagnets*," in *2019 12th Asian Control Conf.*, 2019, pp. 1210–1215.

[28] Y. Ishino, T. Mizuno, M. Takasaki, *et al.*, "Development of a compact axial active magnetic bearing with a function of two-tilt-motion control," *Actuators*, vol. 6, 2 2017. DOI: *10.3390/act6020014*.

[29] A. Piłat, "Modelling, investigation, simulation, and pid current control of active magnetic levitation fem model," in *2013 18th International Conference on Methods Models in Automation Robotics (MMAR)*, Aug. 2013, pp. 299–304. DOI: *10.1109/MMAR.2013.6669923*.

[30] A. Hemeida, B. Hannon, H. Vansompel, *et al.*, "Comparison of three analytical methods for the precise calculation of cogging torque and torque ripple in axial flux PM machines," *Math. Probl. Eng.*, vol. 2016, 2016. DOI: *10.1155/2016/2171547*.

[31] C. Koechli and Y. Perriard, "Analytical model for slotless permanent magnet axial flux motors," *Proc. 2013 IEEE Int. Electr. Mach. Drives Conf. IEMDC 2013*, no. May 2013, pp. 788–792, 2013. DOI: *10.1109/IEMDC.2013.6556183*.

[32] D. Zarko, *A Systematic Approach to Optimized Design of Permanent Magnet Motors with Reduced Torque Pulsations*. University of Wisconsin–Madison, 2004.

[33] K. Boughrara, R. Ibtiouen, D. Zarko, *et al.*, "Magnetic field analysis of external rotor permanent-magnet synchronous motors using conformal mapping," *IEEE Transactions on Magnetics*, vol. 46, no. 9, pp. 3684–3693, 9 2010. DOI: *10.1109/TMAG.2010.2047508*.

[34] T. Lubin, S. Mezani, and A. Rezzoug, "Exact analytical method for magnetic field computation in the air gap of cylindrical electrical machines considering slotting effects," *IEEE Transactions on Magnetics*, vol. 46, no. 4, pp. 1092–1099, 4 2010. DOI: *10.1109/TMAG.2009.2036257*.

[35] K. Wang, D. Wang, Y. Shen, *et al.*, "Subdomain Method for Permanent Magnet Biased Homo-Polar Radial Magnetic Bearing," *IEEE Trans. Magn.*, vol. 52, no. 7, 2016.

[36] T. Wenming, W. Shuai, W. Shengnan, *et al.*, "A complete quasi-3-d analytical model of no-load magnetic field of double-sided slotted AFPMMs considering end effect," *IEEE Access*, vol. 6, pp. 59 557–59 566, 2018. DOI: *10.1109/ACCESS.2018.2875306*.

[37] B. Sikora, "Design and analysis of axial and radial active magnetic bearings," M.Sc., supervisor: A. Piłat, Ph.D., D.Sc, AGH University of Science and Technology, 2017.

[38] B. Sikora, "Simulation and experimental research into off-axis system for vibration elimination generated by unbalanced rotating machinery," B.Sc., supervisor: S. Pakuła, Ph.D. AGH University of Science and Technology, 2019.

[39] A. Piłat and B. Sikora, "Hybrid axial active magnetic bearing - design, modelling and prototype," in *ISMB16 -the 16th International Symposium on Magnetic Bearings*, 2018, pp. 1–6.

[40] B. Sikora and A. Pilat, "Numerical model of the axial magnetic bearing with six cylindrical poles," *Archives of Electrical Engineering*, vol. 68, pp. 195–208, 1 2019. DOI: *10.24425/aee.2019.125990*.

[41] B. Sikora and A. Piłat, "Analytical modeling and experimental validation of the six pole axial active magnetic bearing," *Applied Mathematical Modelling*, vol. 104, pp. 50–66, 2022. DOI: *https://doi.org/10.1016/j.apm.2021.10.024*.

[42] B. Sikora and A. Piłat, "Interdisciplinary identification of six pole axial active magnetic bearing prototype," *Mechatronics*, 2023, after first review.

[43] A. Pilat, "Testing performance and reliability of magnetic suspension controllers," *IFAC Proceedings Volumes*, vol. 42, no. 13, pp. 164 –167, 2009, 14th IFAC Conference on Methods and Models in Automation and Robotics.

[44] T. Mizuno, "Vibration isolation system using zero-power magnetic suspension," *IFAC Proceedings Volumes*, vol. 35, no. 1, pp. 25 –30, 2002, 15th IFAC World Congress.

[45] InTeCo, *Active magnetic levitation system MLS2EM - User's Guide*. INTECO, Krakow, Poland, 2006.

[46] A. Piłat, "Robotized set-up for the magnetic field investigation," *PAR Pomiary Automatyka Robotyka*, vol. 13, p. 18, 2009.

[47] C. Bojan-Dragos, S. Preitl, R. Precup, *et al.*, "Magnetic levitation system laboratory-based education in control engineering," in *3rd International Conference on Human System Interaction*, 2010, pp. 496–501.

[48] C. Bojan-Dragos, R. Precup, S. Hergane, *et al.*, "Fuzzy logic-based adaptive control scheme for magnetic levitation systems," in *2017 IEEE International Symposium on Robotics and Intelligent Sensors (IRIS)*, 2017, pp. 160–165.

[49] A. Pilat, "The programmable analog controller: Static and dynamic configuration, as exemplified for active magnetic levitation," *Electrical Review*, vol. Vol. 88, no. 4b, pp. 282–287, 2012.

[50] A. Pilat, "Modeling, simulation and control of dual electromagnet active magnetic levitation," in *Proceedings of the 2012 COMSOL Conference*, 2012.

[51] A. Bonfitto, L. M. Castellanos Molina, A. Tonoli, *et al.*, "Offset-free model predictive control for active magnetic bearing systems," *Actuators*, vol. 7, no. 3, 2018.

[52] H. Huang, H. Du, and W. Li, "Stability enhancement of magnetic levitation ball system with two controlled electomagnets," in *2015 Australasian Universities Power Engineering Conference (AUPEC)*, 2015, pp. 1–6.

[53] InTeCo, *Active magnetic levitation system MLS1EM - User's Guide*. INTECO, Krakow, Poland, 2005.

[54] M. Andriollo, E. Scaldaferro, and A. Tortella, "Design optimization of the magnetic suspension for a flywheel energy storage application," *5th International Conference on Clean Electrical Power: Renewable Energy Resources Impact, ICCEP 2015*, Aug. 2015.

[55] J. Rovers, M. Stöck, J. Jansen, *et al.*, "Real-time 3d thermal modeling of a magnetically levitated planar actuator," *Mechatronics*, vol. 23, pp. 240–246, 2 Mar. 2013. DOI: *10.1016/j.mechatronics.2012.04.004*.

[56] W. Yang, L. Queval, G. Ma, *et al.*, "A 3-d strong-coupled electromagnetic-thermal model for hts bulk and its uses to study the dynamic characteristics of a linear hts maglev bearing," *IEEE Transactions on Applied Superconductivity*, vol. 30, pp. 1–14, 6 Sep. 2020. DOI: *10.1109/TASC.2020.2982879*.

[57] L. Alloui, F. Bouillault, and M. Mimoune, *The European Physical Journal - Applied Physics*, 2. DOI: *10.1051/EPJAP/2009008*.

[58] H. Zhang, B. Kou, W. Zhao, *et al.*, *Conference Proceedings - EML 2014 17th International Symposium on Electromagnetic Launch Technology*, DOI: *10.1109/EML.2014.6920612*.

[59] Y. D. Tang, R. C. Flesch, C. Zhang, *et al.*, "Numerical analysis of the effect of non-uniformity of the magnetic field produced by a solenoid on temperature distribution during magnetic hyperthermia," *Journal of Magnetism and Magnetic Materials*, Mar. 2018.

[60] R. Pöllänen, J. Nerg, M. Rilla, *et al.*, "Transient thermal model for radial active magnetic bearing," Jan. 2006.

[61] C. Jin, Y. Zhu, L. Xu, *et al.*, "The thermodynamic properties of a new type catcher bearing used in active magnetic bearings system," *Applied Thermal Engineering*, vol. 82, pp. 253–263, May 2015. DOI: *10.1016/j.applthermaleng.2015.02.076*.

[62] L. Burdet, B. Aeschlimann, and R. Siegwart, *9th International Symposium on Magnetic Bearings*, Figure 1. DOI: *10.3929/ethz-a-010085459*.

[63] C. Liu, "Comprehensive prediction of magnetisation via temperature and magnetic field," *Materials Technology*, Nov. 2015.

[64] J. Chen, D. Wang, S. Cheng, *et al.*, *2015 IEEE International Magnetics Conference, INTERMAG 2015*, DOI: *10.1109/INTMAG.2015.7157644*.

[65] R. Zhou, S. Yan, Y. Zhou, *et al.*, "Effects of temperature on control performance of magnetically levitated planar actuators," *International Journal of Precision Engineering and Manufacturing*, vol. 16, pp. 43–51, 1 Jan. 2015. DOI: *10.1007/s12541-015-0005-5*.

[66] M. D. Noh, M. J. Gi, D. Kim, *et al.*, "Modeling and validation of high-temperature electromagnetic actuator," *IEEE Transactions on Magnetics*, Nov. 2015.

[67] K. Pancharoen, D. Zhu, and S. P. Beeby, "Temperature dependence of a magnetically levitated electromagnetic vibration energy harvester," *Sensors and Actuators, A: Physical*, Apr. 2017.

[68] S. Saeed, J. Garcia, M. S. Perdigão, *et al.*, "Evaluation of temperature effect on inductance computation in variable magnetic components for dual-active-bridge application," 2020.

[69] N. Doumit, B. Danoumbé, S. Capraro, *et al.*, "Temperature impact on inductance and resistance values of a coreless inductor (cu/al2o3)," *Microelectronics Reliability*, May 2017.

[70] K. Górecki and K. Detka, "Application of average electrothermal models in the spice-aided analysis of boost converters," *IEEE Transactions on Industrial Electronics,*, 2019.

[71] R. F. Krause, J. H. Bularzik, and H. R. Kokal, "A new soft magnetic material for ac and dc motor applications," *Journal of Materials Engineering and Performance*, vol. 6, no. 6, pp. 710–712, Dec. 1997. DOI: *10.1007/s11665-997-0070-8*.

[72] L. Liu, "Nicuzn ferrite cores by gelcasting: Processing and properties," *IEEE Transactions on Industry Applications - 2017*, vol. 54, p. 5728,

[73] A. Schoppa and P. Delarbre, "Soft magnetic powder composites and potential applications in modern electric machines and devices," *IEEE Transactions on Magnetics - 2014*, vol. 50,

[74] S. Lee, "Magnetic properties of pure iron soft magnetic composites coated by manganese phosphates," *IEEE Transactions on Magnetics-2017*, vol. 53,

[75] A. Chiba, *Magnetic Bearings and Bearingless Drives* (Electronics & Electrical). Elsevier/Newnes, 2005.

[76] J. Fang, J. Sun, H. Liu, *et al.*, "A novel 3-dof axial hybrid magnetic bearing," *Magnetics, IEEE Transactions on*, vol. 46, pp. 4034 –4045, Jan. 2011. DOI: *10.1109/TMAG.2010.2074206*.

[77] J. Fang, J. Sun, Y. Xu, *et al.*, "A new structure for permanent-magnet-biased axial hybrid magnetic bearings," *IEEE Transactions on Magnetics*, vol. 45, no. 12, pp. 5319–5325, 2009. DOI: *10.1109/TMAG.2009.2024687*.

[78] H. Lv, H. Geng, J. Zhou, *et al.*, "Structure design and optimization of thrust magnetic bearing for the high-speed motor," in *2017 IEEE International Conference on Mechatronics and Automation (ICMA)*, 2017, pp. 805–809. DOI: *10.1109/ICMA.2017.8015919*.

[79] J. Tang, J. Sun, J. Fang, *et al.*, "Low eddy loss axial hybrid magnetic bearing with gimballing control ability for momentum flywheel," *Journal of Magnetism and Magnetic Materials*, vol. 329, pp. 153–164, 2013. DOI: *https://doi.org/10.1016/j.jmmm.2012.10.006*.

[80] D. Wajnert and B. Tomczuk, "Two models for time-domain simulation of hybrid magnetic bearingrsquo;s characteristics," *Sensors*, vol. 22, no. 4, 2022. DOI: *10.3390/s22041567*.

[81] B. Guo, Y. Huang, and F. Peng, "An improved conformal mapping method for static angular eccentricity analysis of axial flux permanent magnet machines," *J. Magn.*, vol. 23, no. 1, pp. 27–34, 2018.

[82] D. Meeker, *Finite element method magnetics*, (28Feb2018 Build), Feb. 2018.

[83] N. Paudel, *How to model magnetic bearings in comsol multiphysics*, Jul. 2015.

[84] J. Pérez-Loya, J. Abrahamsson, and U. Lundin, "Demonstration of active compensation of unbalanced magnetic pull in synchronous machines," *CIGRE*, Jun. 2017.

[85] H. Neubert, J. Ziske, T. Heimpold, *et al.*, "Homogenization approaches for laminated magnetic cores using the example of transient 3 d transformer modeling," 2013.

[86] D. Marcsa and M. Kuczmann, "Modeling of radial magnetic bearing by finite element method," *Pollack Periodica*, vol. 6, no. 2, pp. 13–24, 2011. DOI: *10.1556/pollack.6.2011.2.2*.

[87] D. Wajnert, "Comparison of magnetic field parameters obtained from 2d and 3d finite element analysis for an active magnetic bearing," in *2013 International Symposium on Electrodynamic and Mechatronic Systems (SELM)*, 2013, pp. 73–74. DOI: *10.1109/SELM.2013.6562986*.

[88] B. Tomczuk and D. Wajnert, "Field–circuit model of the radial active magnetic bearing system," *Electrical Engineering*, vol. 100, no. 4, pp. 2319–2328, 2018. DOI: *10.1007/s00202-018-0707-7*.

[89] J. Sun, G. Bai, Y. Le, *et al.*, "Analysis and design of permanent magnet biased magnetic bearing based on hybrid factor," *Advances in Mechanical Engineering*, vol. 8, no. 3, p. 168 781 401 663 362, 2016. DOI: *10.1177/1687814016633623*.

[90] D. Wajnert, "A field-circuit model of the hybrid magnetic bearing," *Archive of Mechanical Engineering*, vol. vol. 66, no. No 2, pp. 191–208, 2019. DOI: *10.24425/ame.2019.128444*.

[91] X. Ye, Y. Yan, C. Jia, *et al.*, "Modeling and design of a novel 5-dof ac/dc hybrid magnetic bearing," *Applied Sciences*, vol. 12, no. 18, 2022. DOI: *10.3390/app12188931*.

[92] A. Nakajima, K. Hirata, N. Niguchi, *et al.*, "Dynamic characteristics of triaxial active control magnetic bearing with asymmetric structure," *Open Physics*, vol. 16, no. 1, pp. 9–13, 2018. DOI: *10.1515/phys-2018-0002*.

[93] S. Saha and M. Nabi, "Finite element modelling and analysis of axial active magnetic bearing," in *2018 IEEE 13th International Conference on Industrial and Information Systems (ICIIS)*, IEEE, 2018. DOI: *10.1109/iciinfs.2018.8721385*.

[94] H. Spece, R. Fittro, and C. Knospe, "Optimization of axial magnetic bearing actuators for dynamic performance," *Actuators*, vol. 7, no. 4, p. 66, 2018. DOI: *10.3390/act7040066*.

[95] R. Bjørk and C. R. H. Bahl, "A conical passive magnetic bearing with constant stiffness," *Scientific Reports*, vol. 12, no. 1, p. 4130, 2022. DOI: *10.1038/s41598-022-07988-6*.

[96] M. Aenis, E. Knopf, and R. Nordmann, "Active magnetic bearings for the identification and fault diagnosis in turbomachinery," *IFAC Proceedings Volumes*, vol. 33, no. 26, pp. 1079–1084, 2000, IFAC Conference on Mechatronic Systems, Darmstadt, Germany, 18-20 September 2000. DOI: *https://doi.org/10.1016/S1474-6670(17)39290-X*.

[97] N.-C. Tsai, Y.-H. King, and R.-M. Lee, "Fault diagnosis for magnetic bearing systems," *Mechanical Systems and Signal Processing*, vol. 23, no. 4, pp. 1339–1351, 2009. DOI: *https://doi.org/10.1016/j.ymssp.2008.08.012*.

[98] A. Piłat, "Active magnetic bearing and control system for active magnetic bearing," European pat. WO2011074996A3, 2011.

[99] Y. Huang, B. Guo, A. Hemeida, *et al.*, "Analytical modeling of static eccentricities in axial flux permanent-magnet machines with concentrated windings," *Energies*, vol. 9, no. 11, 2016. DOI: *10.3390/en9110892*.

[100] S. M. Mirimani, A. Vahedi, F. Marignetti, *et al.*, "Static eccentricity fault detection in single-stator–single-rotor axial-flux permanent-magnet machines," *IEEE Transactions on Industry Applications*, vol. 48, no. 6, pp. 1838–1845, 2012. DOI: *10.1109/tia.2012.2221673*.

[101] S. M. Mirimani, A. Vahedi, F. Marignetti, *et al.*, "An online method for static eccentricity fault detection in axial flux machines," *IEEE Transactions on Industrial Electronics*, vol. 62, no. 3, pp. 1931–1942, 2015. DOI: *10.1109/tie.2014.2360070*.

[102] B. Liu, W. Wang, Y. Zhang, *et al.*, "Investigation on axial displacement fault mechanism based on dynamic characteristic coefficients identification of tilting-pad thrust bearing," *Journal of Failure Analysis and Prevention*, vol. 18, no. 2, pp. 330–341, 2018. DOI: *10.1007/s11668-018-0420-x*.

[103] X. Yan, Z. Sun, J. Zhao, *et al.*, "Fault diagnosis of active magnetic bearingrotor system via vibration images," *Sensors (Basel)*, vol. 19, no. 2, p. 244, Jan. 10, 2019. DOI: *10.3390/s19020244*.

[104] Q. Chao, H. Gao, J. Tao, *et al.*, "Fault diagnosis of axial piston pumps with multi-sensor data and convolutional neural network," *Frontiers of Mechanical Engineering*, vol. 17, no. 3, 2022. DOI: *10.1007/s11465-022-0692-4*.

[105] A. Mlot and J. González, "Performance assessment of axial-flux permanent magnet motors from a manual manufacturing process," *Energies*, vol. 13, no. 8, p. 2122, 2020. DOI: *10.3390/en13082122*.

[106] R. Z. Haddad, "Detection and identification of rotor faults in axial flux permanent magnet synchronous motors due to manufacturing and assembly imperfections," *IEEE Transactions on Energy Conversion*, vol. 35, no. 1, pp. 174–183, 2020. DOI: *10.1109/TEC.2019.2951659*.

[107] J. Wang, G. Du, Z. Zhu, *et al.*, "Fault diagnosis of rotating machines based on the emd manifold," *Mechanical Systems and Signal Processing*, vol. 135, p. 106 443, 2020. DOI: *https://doi.org/10.1016/j.ymssp.2019.106443*.

[108] A. Piłat, "Systemy aktywnej lewitacji magnetycznej," *AGH University of Science and Technology Press: Krakow, Poland*, 2013.

[109] A. Piłat, "Testing of the programmable amb spring and damping forces in a flexible rotor test-rig mode," in *ISMB12*, 2010.

[110] E. Maslen, G. Schweitzer, H. Bleuler, *et al.*, *Magnetic Bearings—Theory, Design and Application to Rotating Machinery*. Jan. 2009. DOI: *10.1007/978-3-642-00497-1*.

[111] A. Piłat, "An synergistic dynamic model of an active magnetic bearing with three electromagnets," in *2013 International Symposium on Electrodynamic and Mechatronic Systems (SELM)*, IEEE, 2013, pp. 23–24.

[112] A. Piłat, "Electromagnetic force components analysis in an active magnetic bearing numerical model," in *2013 International Symposium on Electrodynamic and Mechatronic Systems (SELM)*, IEEE, 2013, pp. 21–22.

[113] J. Burcan, *Łożyska wspomagane polem magnetycznym*. Warszawa: WNT, 1996.

[114] R. Gryboś, "Dynamics of rotating machinery," *PWN, Warszawa*, 1994.

[115] M. I. Friswell, J. E. T. Penny, S. D. Garvey, *et al.*, *Dynamics of rotating machines*. Cambridge university press, 2010.

[116] Z. Gosiewski, *Łożyska magnetyczne dla maszyn wirnikowych. Cz. 1, Podstawy teoretyczne*. Wyższa Szkoła Inżynierska, 1993.

[117] A. Piłat and W. Grega, "Reconfigurable test-rig for amb control," in *7th Conference on Active Noise and Vibration Control Methods, Wigry (Poland)*, 2005, pp. 8–12.

[118] D. Kozanecka, Z. Kozanecki, and T. Lech, "Experimental identification of dynamic parameters for active magnetic bearings," *Journal of Theoretical and Applied Mechanics*, vol. 46, no. 1, pp. 41–50, 2008.

[119] A. Mystkowski and Z. Gosiewski, "Uncertainty modeling in robust control of active magnetic suspension," in *Solid State Phenomena*, vol. 144, Trans Tech Publ, 2009, pp. 22–26.

[120] L. Y. Pao, "Minimum-time control characteristics of flexible structures," *Journal of Guidance, Control, and Dynamics*, vol. 19, no. 1, pp. 123–129, 1996.

[121] A. Piłat and J. Klocek, "Programmable analog hard real-time controller," *Przegląd Elektrotechniczny*, vol. 89, no. 3a, pp. 38–46, 2013.

[122] T. Mashimo, X. Huang, T. Osakabe, *et al.*, "Advanced high-temperature ultracentrifuge apparatus for mega-gravity materials science," *Review of Scientific Instruments*, vol. 74, pp. 160 –163, Feb. 2003. DOI: *10.1063/1.1527718*.

[123] J. M. Curtin, "Development and Testing of an Development and Testing of an," vol. 44, no. August, pp. 695–703, 2007.

[124] A. Tessarolo and M. Olivo, "A new method for the analytical determination of the complex relative permeance function in linear electric machines with slotted air gap," *2016 Int. Symp. Power Electron. Electr. Drives, Autom. Motion, SPEEDAM 2016*, pp. 1330–1335, 2016.

[125] Z. J. Liu and J. T. Li, "Analytical solution of air-gap field in permanent-magnet motors taking into account the effect of pole transition over slots," *IEEE Trans. Magn.*, vol. 43, no. 10, pp. 3872–3883, 2007.

[126] T. Lubin, S. Mezani, and A. Rezzoug, "Surface-mounted pm motors considering slotting effects and armature reaction," 2011.

[127] Z. Q. Zhu and D. Howe, "Instantaneous magnetic field distribution in brushless permanent magnet dc motors, Part II: Armature Reaction Field," *IEEE Trans. Magn.*, vol. 29, no. 1, pp. 143–151, 1993. DOI: *10.1109/20.195559*.

[128] A. Egea, G. Almandoz, J. Poza, *et al.*, "Axial-flux-machine modeling with the combination of FEM-2-D and analytical tools," *IEEE Trans. Ind. Appl.*, vol. 48, no. 4, pp. 1318–1326, 2012. DOI: *10.1109/TIA.2012.2199450*.

[129] T. Myint-U and L. Debnath, *Linear Partial Differential Equations for Scientists and Engineers*. Jan. 2007. DOI: *10.1007/978-0-8176-4560-1*.

[130] A. Hemeida, A. Lehikoinen, P. Rasilo, *et al.*, "A Simple and Efficient Quasi-3D Magnetic Equivalent Circuit for Surface Axial Flux Permanent Magnet Synchronous Machines," *IEEE Trans. Ind. Electron.*, vol. 66, no. 11, pp. 8318–8333, 2019. DOI: *10.1109/TIE.2018.2884212*.

[131] H. Zhu, S. Ding, and J. Jv, "Modeling for three-pole radial hybrid magnetic bearing considering edge effect," 2016. DOI: *10.3390/en9050345*.

[132] J. P. Yonnet, "Passive magnetic bearings with permanent magnets," *IEEE Transactions on Magnetics*, vol. 14, no. 5, pp. 803–805, 1978. DOI: *10.1109/TMAG.1978.1060019*.

[133] T. S. Slininger, W. Chan, E. L. Severson, *et al.*, "An overview on passive magnetic bearings," in *2021 IEEE International Electric Machines Drives Conference (IEMDC)*, 2021, pp. 1–8. DOI: *10.1109/IEMDC47953.2021.9449571*.

[134] M. Alizadehtir, F. Marignetti, and S. Deaconu, "Passive magnetic bearings," in Jul. 2018, ch. 4.

[135] *Upwingenergy. passive magnetic radial bearings*, *https://www.upwingenergy.com*, Accessed: 2022-12-11.

[136] *Calentixtechnologies. passive magnetic bearings*, *https://www.calnetix.com*, Accessed: 2022-12-11.

[137] A. Hamler, V. Gorican, B. Štumberger, *et al.*, "Passive magnetic bearing," *Journal of Magnetism and Magnetic Materials*, vol. 272-276, pp. 2379–2380, 2004, Proceedings of the International Conference on Magnetism (ICM 2003). DOI: *https://doi.org/10.1016/j.jmmm.2003.12.972*.

[138] N. Tănase, A. M. Morega, I. Chiriță, *et al.*, "Passive magnetic bearing – design and numerical simulation," in *2019 11th International Symposium on Advanced Topics in Electrical Engineering (ATEE)*, 2019, pp. 1–5. DOI: *10.1109/ATEE.2019.8724949*.

[139] D. Vokoun, M. Beleggia, L. Heller, *et al.*, "Magnetostatic interactions and forces between cylindrical permanent magnets," *Journal of Magnetism and Magnetic Materials*, vol. 321, no. 22, pp. 3758–3763, 2009. DOI: *https://doi.org/10.1016/j.jmmm.2009.07.030*.

[140] K. Asami, A. Chiba, M. A. Rahman, *et al.*, "Stiffness analysis of a magnetically suspended bearingless motor with permanent magnet passive positioning," *IEEE Transactions on Magnetics*, vol. 41, no. 10, pp. 3820–3822, 2005. DOI: *10.1109/TMAG.2005.854933*.

[141] T. M. Premkumar, T. Mohan, and S. Sivamani, "Design and analysis of a permanent magnetic bearing for vertical axis small wind turbine," *Energy Procedia*, vol. 117, pp. 291–298, 2017, "First International Conference on Power Engineering Computing and CONtrol (PECCON-2017) 2nd -4th March .2017." Organized by School of Electrical Engineering, VIT University, Chennai, Tamil Nadu, India. DOI: *https://doi.org/10.1016/j.egypro.2017.05.134*.

[142] L. Matuszewski and K. Falkowski, "Mathematical model of radial passive magnetic bearing," *Polish Maritime Research*, vol. 17, no. 3, pp. 37–44, 2011. DOI: *doi:10.2478/v10012-010-0026z*.

[143] A. Mystkowski and L. Ambroziak, "The dynamic stability of a rotor passive magnetic bearing with an halbach-array," *Mechanics and Control*, vol. 31, p. 40, Jan. 2012. DOI: *10.7494/mech.2012.31.1.40*.

[144] K. Li and J. Z. Bird, "A 3-d analytical model of a halbach axial magnetic coupling," Jun. 2016, pp. 1448–1454. DOI: *10.1109/SPEEDAM.2016.7525881*.

[145] F. Marignetti, A. Vahedi, and S. M. Mirimani, "An analytical approach to eccentricity in axial flux permanent magnet synchronous generators for wind turbines," *Electric Power Components and Systems*, vol. 43, no. 8-10, pp. 1039–1050, 2015. DOI: *10.1080/15325008.2015.1024356*. eprint: *https://doi.org/10.1080/15325008.2015.1024356*.

[146] R. Holehouse, K. Atallah, M. Michon, *et al.*, "Unbalanced magnetic pull in permanent magnet machines," vol. 2014, Jan. 2014, pp. 2.1.01–2.1.01. DOI: *10.1049/cp.2014.0277*.

[147] A. A. Hattangadi, "Failures of stator coils in rotating machines," en, in First edition., New York: McGraw-Hill Education, 2004.

[148] L. Sung, B. Jaenam, and K. Won-ho, "Study on the axial leakage magnetic flux in a spoke type permanent magnet synchronous motor," *IEEE Transactions on Industry Applications*, vol. PP, pp. 1–1, Sep. 2019. DOI: *10.1109/TIA.2019.2939743*.

[149] W. Wang, H. Wang, and H. Karimi, "Study on the characteristics of electromagnetic noise of axial flux permanent magnet synchronous motor," *Abstract and Applied Analysis*, vol. 2014, pp. 1–8, Feb. 2014. DOI: *10.1155/2014/764105*.

[150] W. S. Ma, W. Zhang, and Y. F. Zhang, "Stability and multi-pulse jumping chaotic vibrations of a rotor-active magnetic bearing system with 16-pole legs under mechanical-electric-electromagnetic excitations," *Eur. J. Mech. A/Solids*, vol. 85, no. April 2020, 2021. DOI: *10.1016/j.euromechsol.2020.104120*.

[151] R. Q. Wu, W. Zhang, and M. H. Yao, "Nonlinear dynamics near resonances of a rotor-active magnetic bearings system with 16-pole legs and time varying stiffness," *Mech. Syst. Signal Process.*, vol. 100, pp. 113–134, 2018. DOI: *10.1016/j.ymssp.2017.07.033*.

[152] W. Zhang, R. Q. Wu, and B. Siriguleng, "Nonlinear Vibrations of a Rotor-Active Magnetic Bearing System with 16-Pole Legs and Two Degrees of Freedom," *Shock Vib.*, vol. 2020, 2020. DOI: *10.1155/2020/5282904*.

[153] D. Wajnert and B. Tomczuk, "Analysis of spatial thermal field in a magnetic bearing," *Open Physics*, vol. 16, no. 1, pp. 52–56, 2018. DOI: *doi:10.1515/phys-2018-0010*.